The modulation of myosin function:

How small molecules and sarcomeric mutations impact actomyosin interactions

Saffie Mohran

A dissertation

submitted in partial fulfillment of the

requirements for the degree of

Doctor of Philosophy

University of Washington

2023

Reading Committee:

Michael Regnier, Chair

David Mack

Jennifer Davis

Program Authorized to Offer Degree:

Bioengineering

University of Washington

ABSTRACT

The modulation of myosin function:
How small molecules and sarcomeric mutations impact actomyosin interactions

Saffie Mohran

Chair of the Supervisory Committee:
Michael Regnier
Department of Bioengineering

The subcellular mechanisms that regulate striated muscle function have been studied by biophysicists and physiologists for over a century. Numerous scientists have made significant findings in the field of muscle biology with fundamental discoveries regarding sarcomeric specific proteins, lattice-spacing architecture, and mechanisms of sarcomeric regulation. With these essential findings as the foundation of our field, there are still many sarcomere-based mechanisms of regulation that remain unresolved. The body of work presented here is aimed at extending the knowledge of sarcomeric contraction and regulation by leveraging recent advances in structural, mechanical, and biochemical assays utilized in the field of muscle biology. Specifically, the presented studies demonstrate an integrated approach to elucidating the myofilament specific processes that underlie striated muscle function by addressing (1) the underlying regulatory role of myosin through differences in structural recruitment and biochemical cycling, (2) the structural and biochemical pathways that small molecules alter sarcomeric

proteins as mechanisms of therapy for individuals with congenital heart failure, and (3) underlying mechanisms of dysfunction in hypercontractile models of striated muscle diseases.

The presented work focuses primarily on the thick filament protein myosin and the regulatory role the protein plays in sarcomeric function. In comparison to the vastly studied thin filament, significantly less is known about the modulation of sarcomeric function through myosin. First, we assessed the structural organization and position of myosin within the sarcomere and compared those results to sophisticated biochemical measurements of nucleotide turnover kinetics. We show that the diffraction-based measurements of myosin recruitment as a parameter for myosin regulation is independent from biochemical regulation of myosin head cycling kinetics. Second, we determined the mechanistic pathway of a novel myosin-specific small molecule as a therapeutic agent in hypo-contractile models of cardiac diseases. We show how inotropic interventions can modulate myosin cycling and recruitment through product release inhibition; a mechanistic pathway that can rescue a transgenic murine model harboring a loss-of-function troponin mutation that causes dilated cardiomyopathy. Lastly, we utilize a transgenic porcine model harboring the first reported familial hypertrophic cardiomyopathy mutation to describe how perturbations in specific regions of myosin can lead to sarcomeric dysfunction. We show that isolated protein measurements do not fully recapitulate the phenotypic disease expression observed in myofibril-level and tissue-level preparations, suggesting that certain myosin mutations require the interaction of other sarcomeric proteins to manifest.

To summarize, the work presented here expands the understanding of sarcomeric regulation though myosin specific pathways. We address topics ranging from basic molecular regulation of sarcomeric function to fundamental mechanistic pathways of different diseases and novel sarcomere-specific therapeutic agents.

ACKNOWLEDGEMENTS

The work presented in this thesis would not have been possible without the incredible support, mentorship, and guidance of several special indivuduals. First and foremost, I want to share my deep appreciation to my advisors Mike Regnier and David Mack. I could not have asked for better role models and leaders to guide me through my doctoral degree. Mike offered me the incredible opportunity to join the Ph.D program, and persue my interests in studying the fundamental aspects of striated muscle diseases. I am forever grateful for the incredible freedom you allowed me to achieve my degree, and the ability to learn any assay or technique that I wanted. David offered me the opportunity to understand my research towards theraputic intervention. Through the incredible projects related to gene therapy development and treatment of muscle diseases, David has been an incredible role model in understanding the translational approach of muscle research, and the application of research discoveries to the clinic.

In addition to my primary mentors, I want to thank all the incredible supportive faculty at UW and around the world that have guided my scientific growth. To my committee members Tom Daniel, Jen Davis, and April Stempien-Otero, you all provided me with incredible support throughout my doctural tenure. I truly appreciate all of the one-on-one meetings that we had to discuss the direction of my disseration and myself as a scientist. To all of my external collaboatorive adivsiors including Farid Moussavi-Harami, Alec Smith, Weikang Ma, Thomas Irving, Bert Tanner, Corrado Poggesi, Manuel Pioner, Mike Geeves, Neil Kad, Dave Marcinek, and Beth Pruitt, thank you so much for the incredible support and collaborative work we have conducted over the years of my doctural tenure. Working with all of you on a variety of projects has been an incredible experience, and has significantly helped me grow as a scientist.

To my undergraduate mentors Steven Goldman, Elizabeth Juneman, and Jordan Lancaster, thank you so much for instilling the foundation of science in me. Each of you played a significant role in building my scientific foundation, and teaching me how to perform correct

science. I was able to utilize all the skills from my undergraduate studies to my graduate degree, and I am extremely grateful for the opportunities and mentorship.

To my friends and family, I am extremely thankful for the contributions you played in my life as both a professional scientist and as a person. To my friends and colleagues Nisa, Christian, Travis, Andy, Bonnie, Alec, Jon, Meredith, Samantha, Michael, Ian, Audrey, Elisa, Sonette, Kerry, Matt, Kristi, Tim, Galina, Abby, Kalen, Phil, SiWei, Shawn, and Joe, thank you all so much for making my time in graduate school enjoyable. Each one of you played a significant role in my life here in Seattle, and I will forever grateful for the fond memories and experiences we all share together. To my family: Mom, Dad, Rouna, Rhyaan, Steph, Diana, and Mark, I will forever cherish the love and support that you given me throughout my doctoral tenure.

TABLE OF CONTENTS

I. Background

i. Overview and Significance

Striated muscles are highly organized tissues that serve fundamental roles for human life and mobility. Skeletal and cardiac muscle are two different types of striated muscle, and exhibit significant differences in regulatory mechanisms, size, and protein composition. These striated muscle types, however, also share numerous structural and functional characteristics, as well as the potential for muscle dysregulation and dysfunction. Through causations of injury, aging, and protein mutations, the consequences of dysregulation in striated muscle can have a devastating impact on an individual's health (Shadrin et al., 2016). To comprehend how dysfunctional muscles operate differently from normal conditions, it is critical to understand the many fundamental underlying mechanisms that regulate muscle function. This information is essential to our ability to prevent dysfunction and/or restore proper muscle function in individuals with life-threatening muscular diseases. The studies presented here demonstrate an integrated approach to elucidating the myofilament-specific processes that underlie the regulation of cardiac and skeletal muscle performance. This work is aimed to address (1) unknown regulatory mechanisms of striated muscle myosin structure and function, (2) the structural and biochemical pathways that small molecules alter sarcomeric proteins as mechanisms of therapy, and (3) underlying mechanisms of dysfunction in hypercontractile models of striated muscle diseases.

ii. Striated Muscle Morphology and Excitation-Contraction Coupling

Striated muscle has distinctive structural, molecular, and functional properties that are expressed in both skeletal and cardiac types. Cardiac muscle makes up the thick middle layer of the heart, surrounded by the exterior epicardium and interior endocardium layers. It is composed of individual cardiac muscle cells, called cardiomyocytes, which are short, branched, centrally-mononucleated cells that are joined together at their ends by intercalated disks (Saxton et al., 2022). Within the intercalated disc, there are distinct types of cell junctions that enable the

cardiomyocytes to communicate and facilitate the rapid transmission of action potentials to produce synchronized contraction (Hong & Shaw, 2017). In comparison, skeletal muscle is composed of long uniformly aligned multinucleated myocytes surrounded by a thin layer of connective tissue called the endomysium. These skeletal fibers are highly organized in structure, span the entire length of the muscle, and do not feature any cell-cell junctions (Mukund & Subramaniam, 2020; Rossi et al., 2022). Despite the morphological differences described, both skeletal and cardiac muscle are composed of myofibrils, which are the smallest spatially organized organelles of contraction.

The lack of gap junctions in skeletal muscle is highlighted by the significant differences in excitation-contraction (EC) coupling between the two striated muscles (Calderón et al., 2014; Lamb, 2000). EC coupling is a term first introduced by Alexander Sandow in 1952, describing the rapid electrical mechanism of inducing calcium release from the sarcoplasmic reticulum (SR) into the sarcoplasm and the subsequent generation of muscle contraction. In skeletal muscle, the sarcolemma (plasma membrane of the muscle cell) form regular invaginations which insert between myofibrils (Rossi et al., 2022). These invaginations are termed transverse tubules (t-tubules) and are tightly associated with the SR in regions called terminal cisternae. Each t-tubule interacts with an SR on either side, forming a triad (Al-Qusairi & Laporte, 2011). EC coupling begins when an action potential travels across the sarcolemma, down the t-tubules, and changes the structural conformation of dihydropyridine receptor (DHPR). DHPR is a voltage gated L-type calcium channel located on the t-tubule and is physically connected to a ryanodine receptor (RyR1). RyR1 is a calcium release channel localized on the junction face of the SR, and serves as the “gate” blocking all the stored calcium inside of the SR. The structural alteration to DHPR induced by the action potential directly opens the RyR1 “gate”, releasing calcium in the sarcoplasm and initiating a cascade of events leading to muscle contraction. After activation,

calcium is pumped back into the SR by the sarcoendoplasmic reticulum calcium ATPase (SERCA1) pump (Xu & Van Remmen, 2021).

The mechanism of EC coupling in cardiac muscle has two main differences when compared to skeletal muscle. These differences are (1) the t-tubule complex and (2) the mechanism of inducing calcium release from the SR. Unlike skeletal muscle, the t-tubules along the myofibrils interact with only one SR terminal cisternae, forming a diad complex (Lu & Pu, 2020). As the action potential propagates across the sarcolemma and into the t-tubules, activated L-type calcium channels allow a small influx of calcium into the sarcoplasm. This calcium binds to a ryanodine receptor (RyR2) on the SR, inducing calcium release from the SR. This mechanism is termed calcium induced calcium release (CICR) and is different than the physical gating described above for skeletal muscle (Eisner et al., 2017). The reuptake process of calcium back into the SR for cardiac muscle follows the same mechanism in skeletal muscle, utilizing a

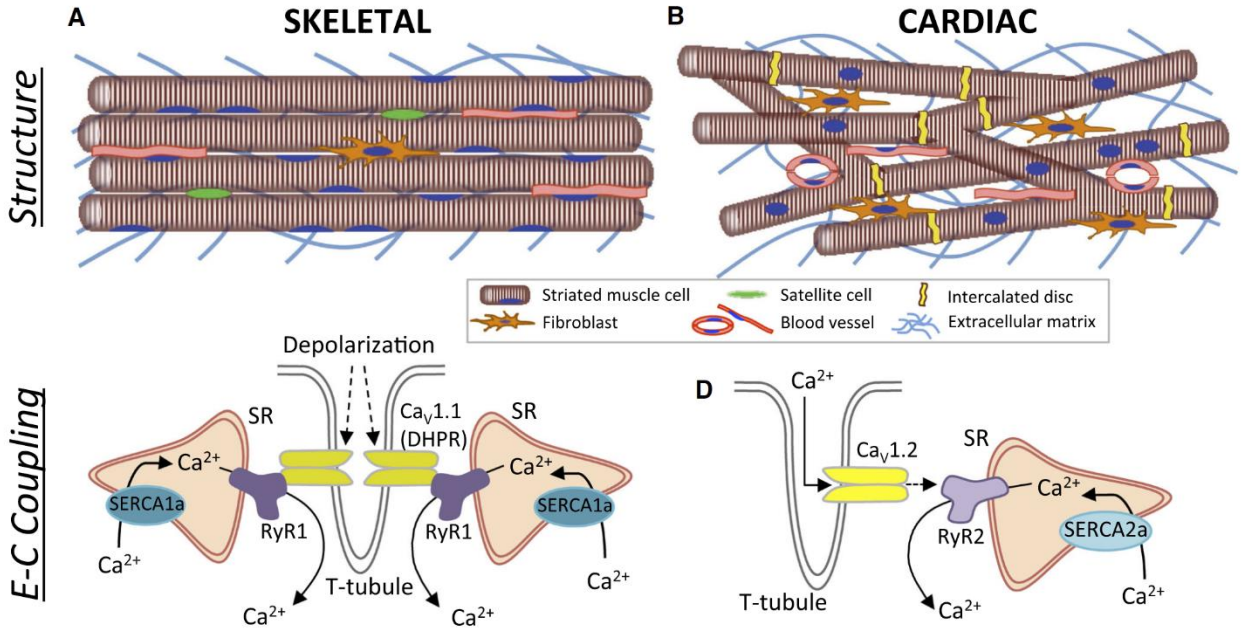

cardiac (B) muscle. In addition to the visual branching of cardiomyocytes, the significant number of intercalated disks play an enormous role in synchronous muscle contraction, compared to skeletal muscle with none. This difference is highlighted by the mechanism for E-C couple, where cardiac muscle utilizes CICR to activate Ca^{2+} release and muscle contraction. Image adapted from (Shadrin et al., 2016).

different isoform of SERCA, SERCA2, to transport the calcium out of the sarcoplasm and back into the SR.

iii. Subcellular Structure and Regulation

Although the mechanism to induce calcium influx into the sarcoplasm is different between cardiac and skeletal muscle, the complex subcellular protein machinery that has evolved to utilize calcium and generate muscle contractures shares several commonalities regarding both structure and function. In striated muscle, each myofibril is composed of a dense network of repeating protein structures called sarcomeres (Cooper, 2000). Sarcomeres are the structural unit of a myofibril, and consist of three myofilaments: thick, thin, and elastic. Both the thick and thin filament are decorated with various regulatory and structural proteins. The thick filament is primarily constituted of myosin (organized in a three-dimensional helical structure) (Liu et al., 2020) and myosin-binding protein-C (localized to the C-zones of striated muscle sarcomeres) (Previs et al., 2012). The thin filament consists of three proteins, a helical backbone of F-actin molecules regulated by tropomyosin and calcium-sensitive troponin complexes. Finally, the elastic filament utilizes the protein titin to anchor the thick-filament to the z-line and acts as a protective spring mechanism within the sarcomere.

The myofilaments within the sarcomere are highly ordered in structure, and visual illustrations of a myofibril under a microscope depicts a repeating series of dark and light bands (Pinotsis et al., 2009). These bands are called A-bands and I-bands, respectively, and encompass different regions of the sarcomere. The A-band of the sarcomere consists of both thick and thin filaments, whereas the I-band only consists of thin and elastic filaments. In addition to the repeating visual bands, another prominent feature of the sarcomere is the z-line. The z-line is a network of proteins that the thin filament and titin are anchored to. Key properties of the thick and thin filaments, along with the various regulatory proteins that decorate them, are described in more detail in the sections below.

- *The Thin Filament: Actin, Troponin, and Tropomyosin*

Within the sarcomere, the main site for calcium-based regulation of muscle function is the thin filament. The thin filament is composed primarily of small globular actin monomers (G actin), that are polymerized into a long fibrous actin (F-actin) strand and formed into a coiled-coil structure. Alone, the bare coiled-coil F-actin structures would be continuously exposed to myosin, and there would be no mechanism to control actin-myosin binding. This highlights the importance of regulatory proteins tropomyosin (a long, filamentous protein) and calcium-sensitive troponin complex (composed for three subunits: troponin C, I, and T) (Chou & Pollard, 2019; Cooper, 2000). Uniformly spaced along the coiled-coil F-actin microfilament, the decorated regulatory proteins interact with each other and position tropomyosin on actin, blocking the myosin-binding sites until EC-coupling releases calcium into the sarcoplasm.

As calcium saturates into the cytosol, it interacts with the calcium-sensitive troponin complex, and more specifically the subunit troponin C (TnC). This subunit is the calcium receptor on the thin filament and is present in both skeletal and cardiac muscle (Li & Hwang, 2015). There are two different isoforms of TnC expressed in striated muscle. The first isoform is a fast skeletal TnC subcomplex, found in specific types of fast twitch skeletal muscle fibers. These isoforms of TnC contain two binding sites within the subunit. In comparison, the second isoform is termed slow cardiac TnC, and can be found in both cardiac and slow twitch skeletal muscle fibers. Cardiac TnC isoforms only contain a single calcium binding site (Hartner & Pette, 1990; Palmer & Kentish, 1994; Sogah et al., 2010). Conserved between the two different isoforms however is the mechanism of calcium regulation, where upon binding of calcium to TnC, a conformation change in the structure of the entire troponin complex occurs. This changes in troponin induce a change in position of tropomyosin on actin, and result in tropomyosin exposing the myosin binding sites on actin (Cheng & Regnier, 2016).

- *The Thick Filament: Myosin, Light Chains, and Myosin-Binding Protein C*

Most of the thick filament in the sarcomere is composed of myosin motor proteins, specifically myosin II. Myosin II, also known as conventional myosin, is responsible for the production of muscle contraction (Hodge & Cope, 2000; Smerdu et al., 1994). Structurally, myosin II contains two heavy chains, each approximately two thousand amino acids in length, and constitute both a head and tail domain (N-terminal and C-terminal, respectfully). The C-terminals of myosin interact to form a coiled-coil structure, holding the two head domains together (and forming the signature structure of myosin) (Heissler et al., 2021). Within the neck region of the myosin motor protein reside two sets of (four total) myosin light chains. The first set of light chains are regulatory light chains (RLC), and actively participate in the regulation and mechanism of muscle contraction (Markandran et al., 2021). The second set of light chains are essential light chains (ELC). Although the exact function of ELC's remain unclear, current studies have hypothesized that ELC's contribute to the structural stability of the myosin head (Hernandez et al., 2007). The organization of the six polypeptide chains can be fragmented into different regions. The S1 subfragment describes the head region of myosin, while the S2 subfragment is a short 54k-Da coiled-coil fragment (Blankenfeldt et al., 2006). Combining S1 and S2 creates heavy meromyosin (HMM), while the remaining tail region is called light meromyosin (LMM) (Boland et al., 2019).

Fully constructed with both HMM and LMM regions, myosin proteins polymerize together and form a bipolar filament that is helical in structure (Liu et al., 2020). This polymerization positions the coiled-coil tail of the myosin motor protein along the backbone of the thick filament, and extending the myosin heads outwards, in a radial manner. The precise structure and orientation of the myosin along the thick filament is critical for function, as the myosin heads form "crowns" (Squire, 2009). A "crown" consists of three myosin heads, spanning the circumference of the thick filament exactly 120° from each other. Subsequent crowns along the thick filament are separated

by ~14.3nm and are rotated by 40°. This organization gives the thick filament a helical periodicity of ~43 nm (Reconditi, 2006).

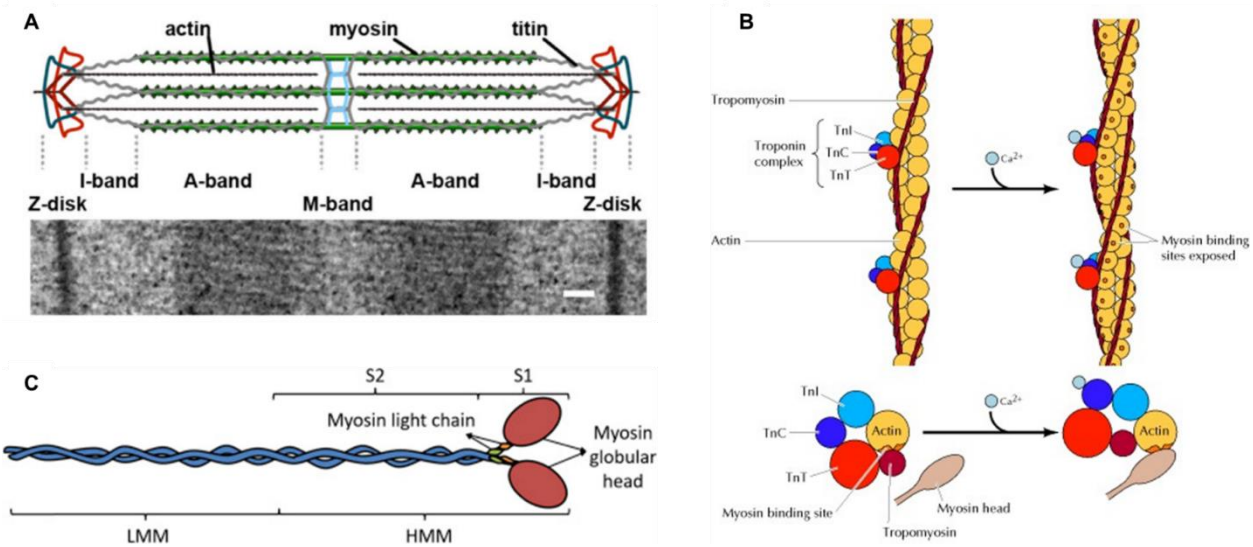

Figure 1.2 Subcellular composition of the sarcomere

Even with significant differences in macroscope structure, skeletal and cardiac muscle share significant organization and protein composition within the sarcomere. The composition of a sarcomere (A | (Crocini & Gotthardt, 2021)) consists of interlacing thick and thin filaments. The degree of overlap alters the size of the I-band; however, the A-band remains constant. On the thin filament (B | (Cooper, 2000)), the polymerized actin is decorated with regulatory protein complexes that are calcium dependent. The thick filament, composed of mostly myosin (C | (Boland et al., 2019)), interact with actin when activated by calcium.

Along with myosin, the composition of the thick filament includes a protein called myosin-binding protein-C (MyBP-C). MyBP-C is a regulatory protein the resides on the thick filament and regulates contraction of striated muscle. There are three isoforms of MyBP-C, and they are specific for slow-skeletal, fast-skeletal, and cardiac muscle. Each isoform of MyBP-C is always located in the C-zone of the sarcomere, which is the central third region of the A-band. The exact functional role of MyBP-C is dependent on the isoform; however, it is generally accepted that all isoforms link the thin and thick filaments together (Lin et al., 2018). Cardiac MyBP-C is the most characterized isoform, with publications describing how it interact with both myosin and actin

(Previs et al., 2012). Recent publications have shown that the regulatory region on cardiac MyBP-C shifts the structural position of tropomyosin, exposing the myosin-binding sites on the F-actin (Mun et al., 2014). This mechanism is like the previously described calcium regulated activation of the thin filament by troponin, however, instead of the entire thin filament, the conformation changes to tropomyosin only occur within the C-zone boundary.

iv. Mechanisms of Sarcomeric Contraction

With the composition and structure of the thick and thin filament described above, it becomes important to understand how they interact within the sarcomere, and what are the underlying mechanisms utilized to achieve force production. These underlying mechanisms of striated muscle contraction was first introduced in 1954, as pioneers in the field of muscle physiology Andrew Huxley and Hugh Huxley published two independent papers in Nature (Huxley & Niedergerke, 1954; Huxley & Hanson, 1954), providing a hypothesis that myosin slides the thin filament towards the center of the thick filament during contraction, shortening the sarcomere length (SL, distance between z-disks) and in-turn, the muscle fiber, during contraction. As the sliding filament theory evolved over the subsequent years, another fundamental mechanism for muscle function was published by Lymn and Taylor in 1971 (Lymn & Taylor, 1971) regarding a revolutionary 4-state actomyosin cross-bridge cycle. In their publication, they provided two fundamental findings: (1) evidence that hydrolysis of ATP occurs in the detached state when myosin is not bound to actin, and (2), that the addition of ATP to myosin results in a burst of ATP hydrolysis that was nearly stoichiometric with the myosin heads (Szent-GyöRgyi, 2004). Both the crossbridge cycling and sliding filament mechanisms are described in more detail below.

- *The Sliding Filament Theory & Length-Tension Relationship*

Hugh Huxley generated the first x-ray diffraction image from live relaxed muscle, and through years of protocol optimization, was able to show how basic meridional periodicities in muscle remained constant at various lengths while equatorial reflections indicated the presence of two

filamentous structures (H. E. Huxley, 1971; Huxley, 2004b). In addition to x-ray diffraction, work done by electron microscopy highlighted the presence of A- and I-bands within the sarcomere, along with Z-bands and the H-zone. At the same time as Hugh Huxley's experimentation, Andrew Huxley aimed to address sarcomeric structure and function by conducting experiments on intact frog muscles using interference microscopy. Andrew was able to visualize the different regions of the sarcomere in stretch, isometric twitch, and isotonic contractions. Both independent researchers were able to derive a similar hypothesis for sarcomeric contraction, stating that the A-band, myosin, would pull the I-band, actin, towards the center of the sarcomere, decreasing the SL, but also reducing the size of the I-band (as it began to overlap the A-band) (Huxley, 1969, 2004a).

After the coordinated publication of both articles by Andrew and Hugh Huxley, many subsequent research papers have utilized the sliding filament theory to evaluate how SL can impact the functional output of different striated muscle types. In contrast to the structural similarities that skeletal and cardiac muscle share at the sarcomere level, the functional relationship between muscle types and SL regulation are drastically different. A direct quantification of this relationship can be expressed as the length-tension relationship, where values in passive and active force generation in cardiac and skeletal muscle do not respond equally to the same changes in SL. These muscle specific length-tension relationships provide valuable information regarding muscle specific isoforms and regulatory mechanisms and was first introduced into the field by Albert Gordon and colleagues in 1966 (Gordon et al., 1966b). By performing experiments on isolated frog skeletal muscle fibers, Gordon argued that the length-tension relationship consisted of three phases. The initial phase constituted of an ascending length-tension relationship, where the frog skeletal muscle fiber rose from minimal isometric tension to maximum tension (described to be between ~1.25 and 2.0um in SL). The second phase, called the plateau phase, ranged between 2.0 and 2.25 um in SL, and exhibited no change

in maximal isometric tension generation. The third phase of the length-tension relationship encompassed any length greater than 2.25um, leading to a proportional reduction in tetanic force production. Gordon argued that the observed results were related to the sliding filament theory, and that each region described the optimal overlay of the thick and thin filaments (Gordon et al., 1966a). The optimal length for tension generation was observed to be during the plateau phase, where the force generated was due to the optimal degree of inter-myofilament overlaps for this range of SL.

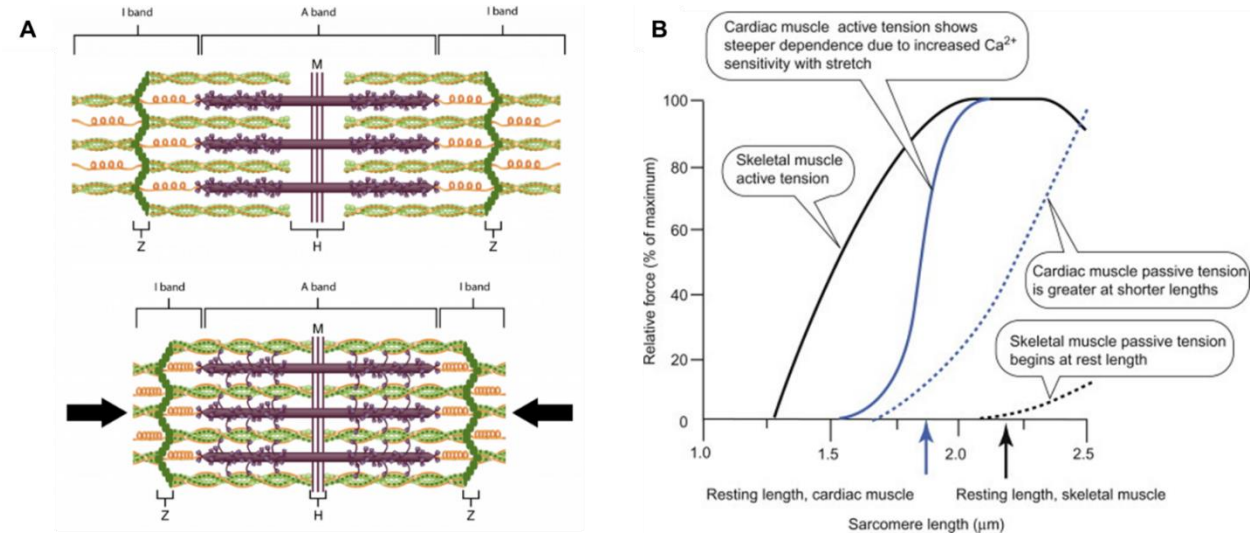

Figure 1.3 Illustration of the sliding filament theory and length-tension relationship

Although the sliding filament theory is conserved between cardiac and skeletal muscle (A | (Biga, 2019)), the relationship of stretch to tension in cardiac and skeletal muscle are completely different. Shown in relative force (%) to sarcomere length (B | (Feher, 2012), skeletal muscle normally operates at 100% myosin recruitment and 100% Ca^{2+} saturation. This is compared to cardiac tissue where muscle is normally not saturated with Ca^{2+} and operates at a sub-maximal. Stretching the muscle at short lengths increases sensitivity to Ca^{2+} which alters both the force due to the number of active cross bridges as well as filament overlap.

Like skeletal muscle, cardiac muscle also expresses a length-tension relationship, however, the values are drastically different due to how the heart functions as an organ. The Frank Starling Law is a description of cardiac hemodynamics, and relates cardiomyocyte stretch and contractility (SL to tension). The Frank-Starling law states that the stroke volume of the left ventricle will

increase as the left ventricular volume increases. This is due to the myocyte stretch causing a more forceful systolic contraction. In terms of the length-tension relationship, cardiac muscle rise steadily between SL 1.8 and 2.3 um (Brady, 1967a, 1967b). Any stretching beyond 2.3 um causes a steep rise in passive force, and a reduction in the active force generated by the muscle. This means that the heart normally operates only on the ascending limb of the length tension curve (Feher, 2012).

- *The Crossbridge Cycle, Super-Relaxed State, & Inhibited Heads Motif*

Even with the introduction of the sliding filament theory in 1954, the underlying mechanism of cross-bridge cycling, and the order of interactions that governed how myosin was able to interact with actin was not fully described until much later. The preliminary four state model by Lymn and Taylor (Lymn & Taylor, 1971) proposed the following: (1) ATP binds myosin, M.ATP, (2) ATP is hydrolyzed into ADP and inorganic phosphate (P_i) causing a structural change to the myosin head, M.ADP.Pi, (3) the myosin head with ADP and P_i bind to actin, AM.ADP.Pi, (4) finally followed by the product release of ADP and P_i, causing the myosin head to perform the power stroke. The recovery to the resting state structure of unbounding myosin from actin by a newly bound ATP molecule.

This simplified crossbridge cycle serves as the backbone for the crossbridge cycle currently used today. Recent discoveries in the field have grown the cross-bridge cycle to seven different myosin states, including separate states for ATP hydrolysis product releases (ADP and P_i) as well as the most recently discovered super relaxed state (SRX) (Geeves et al., 2019; Hooijman et al., 2011a; Stewart et al., 2010; Tyska & Warshaw, 2002; Walklate et al., 2022b). The introduction of the SRX state by Roger Cooke and colleagues in 2010 demonstrated a new functional state of myosin molecules in the crossbridge cycle. A hallmark of the SRX state is the significantly slower release of ATP hydrolysis products relative to the other states of myosin. With this discovery, Cooke proposed that myosin existed in three distinct functional states within the sarcomere. The

first state was the active cycling state of myosin, where actin binding is involved for ATP hydrolysis, and the myosin cycles through ATP turnover in less than one second. The second state, termed the disordered relaxed (DRX) state, is a function state of myosin ATP turnover in the absence of actin. This state has a functional ATP turnover time of less than thirty seconds. The final state, SRX, is a state of significantly prolonged ATP turnover, and can take an excess of one hundred seconds to complete the cycle (Nag & Trivedi, 2021).

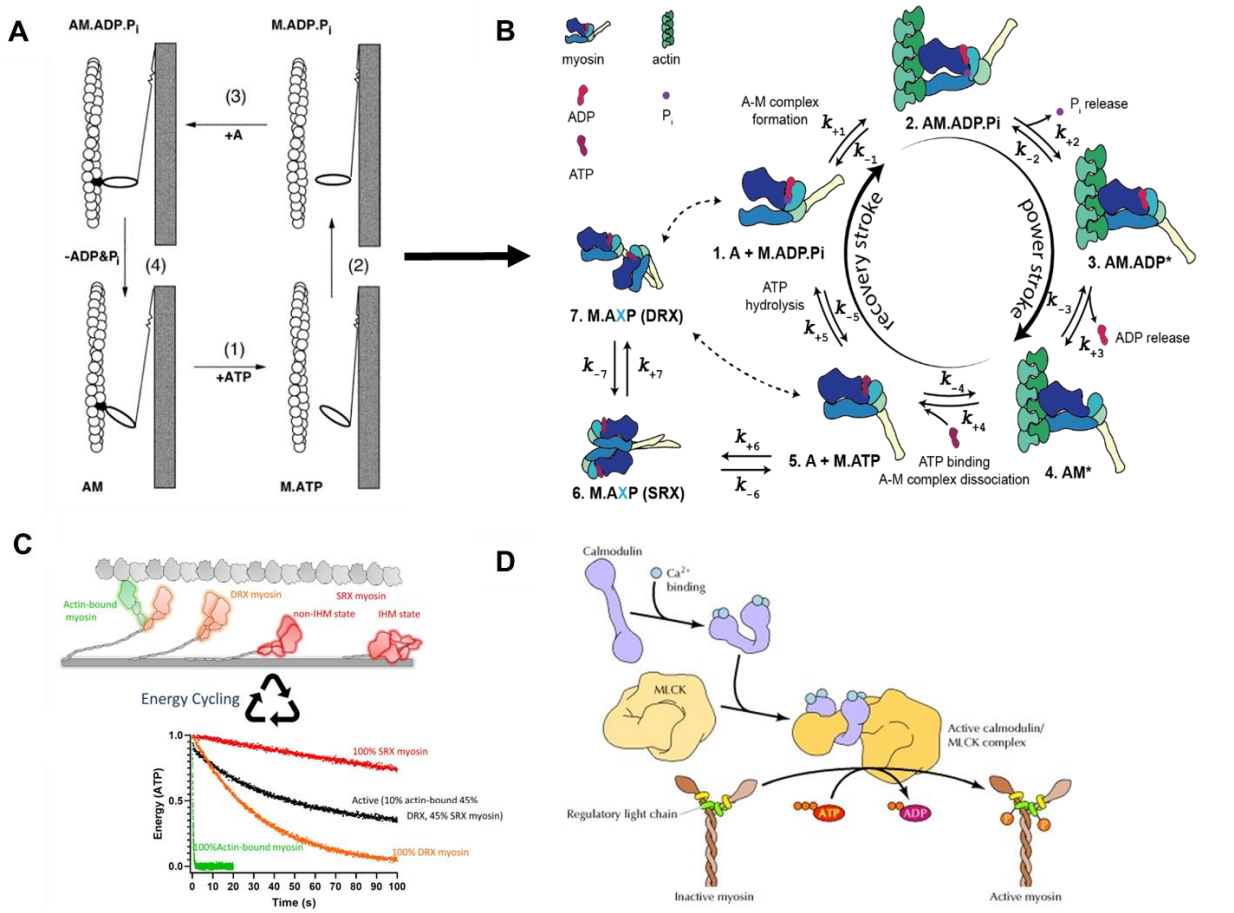

Figure 1.4 Evolution of the crossbridge cycling mechanism and SRX regulation

The evolution of the crossbridge cycle increases the number of myosin interaction states from 4 (A | (Szent-GyöRgyi, 2004)) to 7 (B | Image designed by Dr. Matthew Childers UW) where the DRX and SRX conformations are also considered. The function and energy consumption of myosin is illustrated (C | (Nag & Trivedi, 2021) in the three states, showing the amount of energy and duration each myosin conformation consumes. The regulation of SRX has been shown associated with RLC phosphorylation (D | (Cooper, 2000)) where activation of the RLC inhibits SRX conformation.

The introduction of the SRX state not only described a revolutionary state of ATP-turnover, but also proposed a new conformational structure of myosin. The proposed structure describes how the myosin heads interact with each other to form the “interactive heads motif” (IHM), where the myosin heads fold back onto its structure and interact with S2 domain (Alamo et al., 2016; Sami Chu et al., 2021; Mcnamara et al., 2015) as well as MyBP-C (Mcnamara, Li, Smith, Lal, Graham, Kooiker, Van Dijk, Remedios, et al., 2016). The formation of the IHM inhibited head activity and was associated with the decreased ATP-turnover activate observed in the SRX state. The IHM structure in turn conserved ATP consumption by the muscle until necessary. Regulatory mechanisms including the phosphorylation of RLC have been described to play a role in both cardiac and skeletal muscle myosin head recruitment (Toepfer et al., 2013; Christopher N. Toepfer et al., 2020). These fundamental principles revolutionized the study of myosin and serve as a significant mechanistic contributor when investigating myosin specific mutations in striated muscle.

v. Myosin Mutations in Striated Muscle

The described structure and mechanisms of myosin play a significant role in the dysfunction and dysregulation observed in a substantial number of sarcomeric related myopathies. Unfortunately, myosin (like all other proteins), is susceptible to disease causing missense mutations, with over one thousand different mutations being discovered. Mutations are found in all isoforms of striated muscle myosin and are expressed in β-myosin, α-myosin, embryonic, fetal, and adult fast myosin. Within the structure of myosin, most of the identified mutations exist in the S1 domain compared to S2 and LMM in all isoforms, however, the phenotypic expression and severity can vary dramatically (Parker & Peckham, 2020).

- *Mutations in embryonic myosin and disease*

Although mutations in skeletal muscle isoforms are uncommon, there are approximately thirty-four known embryonic myosin with 76% found in the S1 domain (Parker & Peckham, 2020).

Embryonic myosin plays a critical role in early muscle development, and mutations in embryonic myosin are associated with Freeman-Sheldon (FSS) and Sheldon-Hall (SHS) syndromes. These syndromes express a conditional termed distal arthrogryposis (DA), also known as congenital contractures, in identified persons (Toydemir et al., 2006). These two syndromes exhibit strongly in the distal appendages and orofacial muscles and are part of ten different conditions of arthrogryposis. Previous studies utilizing recombinant embryonic myosin showed that the three most prevalent mutations of FSS decreased the rate of ATP hydrolysis and of ATP binding to myosin (Walklate et al., 2016).

- *Mutations in cardiac β-myosin and disease*

In a 2020 review publication discussing disease mutations in striated muscle myosin, Parker and colleagues estimated that 73% of the missense mutations identified in β-cardiac developed hypertrophic cardiomyopathy (HCM) while 14% accounted for dilated cardiomyopathy (DCM) (Parker & Peckham, 2020). HCM is a disease in the heart that develops ventricular wall thickening, known as concentric hypertrophy. This remodeling decreases the total volume available for the heart to fill with blood during diastole filling. In contrast, DCM expresses eccentric remodeling, where the ventricular wall becomes thin and elongated, increasing the volume of the chambers, making it more difficult for the heart to pump blood into the body (Lowey et al., 2008; Ujfalusi et al., 2018; Van Heerebeek et al., 2008). These developed disease phenotypes are a direct compensatory mechanism of the mutation, and it becomes imperative to study and understand how the structural alterations in myosin impact the different regulatory and functional mechanisms. Previous studies have shown that myosin variants can alter myosin ATPase rate, actin detachment rate, the actin-myosin duty ratio, and destabilize the super relaxed state of myosin on the thick filament backbone (Adhikari et al., 2019; Fatkin et al., 2000; Gupte et al., 2015; Morck et al., 2022; Nag et al., 2017; Sommese et al., 2013; Tang et al., 2021; Christopher N. Toepfer et al., 2020; Trivedi et al., 2018; Ujfalusi et al., 2018; Vander Roest et al., 2021). These

findings are consistent with studies conducted on the first mutation linked to HCM, R403Q mutation. In addition to developing concentric remodeling, the myosin dysfunction impacted myosin recruitment, myosin activation, and myosin relaxation (Blanchard et al., 1999; S. Lowey et al., 2018; Lowey et al., 2008; Witjas-Paalberends et al., 2014). These dysfunctions were associated with the location of the mutation in the motor domain where the change in amino acid significantly reduced the population of heads in the IHM state.

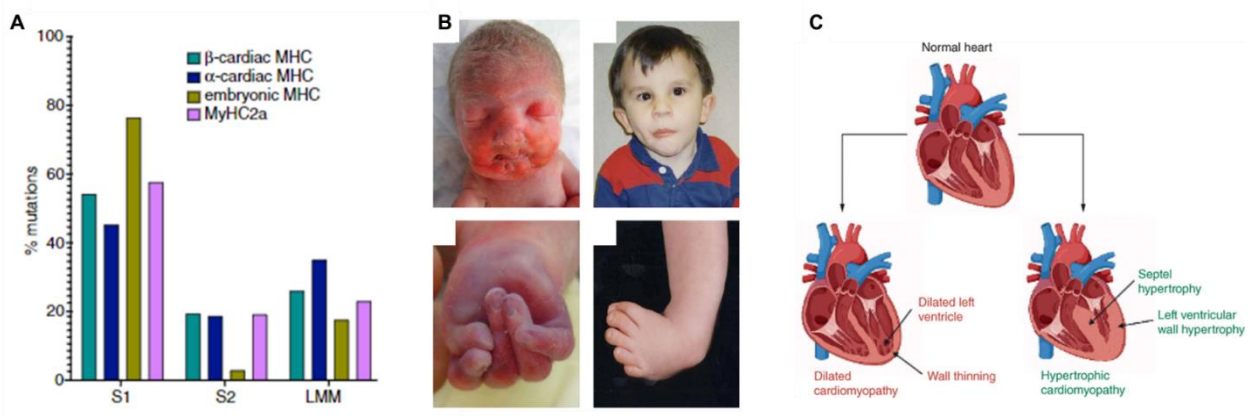

Figure 1.5 The prevalence and dysfunction of myosin mutations in skeletal and cardiac muscle

With over 1000 discovered myosin mutations, a significant population have been identified to reside in the S1 (A | (Parker & Peckham, 2020) domain. These mutations have been associated with myosin head dysfunction impacting different states of myosin throughout the crossbridge cycle. Phenotypic example of FSS and SHS syndrome (B (Toydemir et al., 2006)) due to embryonic skeletal mutations. The progression of cardiac remodeling (C | Designed in Biorender) illustrating eccentric (DCM) and concentric (HCM) remodeling.

vi. Myosin Specific Small Molecule Therapies for Sarcomeric Mutations

The consequences of mutated myosin structures, and the resulting compensatory phenotypes developed in the impacted muscle, bare an enormous burden both financially and on individual's quality of life. In the clinic, current intervention strategies for HCM increased wall thickness can range surgical myectomy to heart transplants. Patients are traditionally also given medications to manage symptoms and reduce cardiac function with β-blockers and Ca^{2+} channel blocker (Garcia-Pavia et al., 2019; Mortara et al., 2014). For DCM patients however, treatment

techniques focus on managing symptoms while preserving myocardial function. Traditional inotropic agents improve cardiomyocyte contractility via increased intracellular cyclic adenosine monophosphate (cAMP) and calcium levels (Lakdawala et al., 2010; McNally & Mestroni, 2017). Medical management for these diseases can prove insufficient to prevent disease progression, and current levels of care for end stage heart failure require heart transplantation or the implementation of ventricular assist devices. For this reason, there is a significant unmet clinical need in developing new therapeutic techniques that allow clinicians to modulate cardiac contractility without negative system effects on other organs.

The development of cardiac specific myosin modulating compounds has provided several successful clinical trials in patients with HCM and DCM diseases. By altering the cardiac myosin motor directly, small molecules can increase or reduce protein function, altering mechanisms such as ATPase activity and cardiac outputs functions like contractility (Spudich, 2014). During the initial screening process small-molecule compounds are separated into two distinct groups, (1) activators and (2) inhibitors. One important distinction is that even though these molecules are designed to specifically modulate myosin function, studies have shown that similar therapeutic efficiency patients with genetic variants in other sarcomeric proteins, as well as in patients with genetic variants in non- sarcomeric proteins (Sarah J. Lehman et al., 2022).

- *Myosin Inhibitors*

Small molecule myosin inhibitors are primarily designed to reduce myosin function by modulating protein availability and/or crossbridge cycling. A standout small molecule candidate, Mavacamten (MYK-461 | Bristol Myers Squibb) was identified as a potential myosin modulator that reduced sarcomere contractility. After initial screening, in-depth studies showed that Mavacamten decreased the rate of inorganic phosphate release during ATP hydrolysis and was able to stabilize the SRX conformation in myosin (R. Anderson et al., 2018; Robert L. Anderson et al., 2018; Gollapudi, 2020; Olivotto et al., 2020). Further reductional experimentation also

showed that the compound increased ADP release from myosin, increased ATP attachment to myosin, and increased crossbridge detachment. Experiments were performed on sarcomeric proteins isolated from distinct species (mouse, cow, rat, dog, minipig, and human) in a variety of assays, all showing different yet remarkable results to prove the compounds efficacy and efficiency (Scellini et al., 2021; Walklate et al., 2022b). Cumulatively, the mechanistic impact of Mavacamten showed reduced diastolic stiffness, and preclinical studies of HCM showed that Mavacamten treatment reduced fractional shortening, cardiac fibrosis, and cardiomyocyte disarray.

- *Myosin Activators*

In contrast to myosin inhibitors, myosin activators are associated with augmented ATPase activity, increased myosin head recruitment, and a decrease in the population of myosin heads in SRX; all developing an increase in contractility. An extensively studied example for myosin activators is Omecamtiv Mecarbil (OM), which was discovered by Cytokinetics in 2010 through a high screening process. The initial mechanism for OM was described to directly accelerate the actin-activated rate of phosphate release in myosin, and structurally prime the protein for interactions with myosin(Sarah J. Lehman et al., 2022). This initial hypothesis however was disproven, as reductionist assays showed that OM inhibited myosin crossbridge cycling and stabilized the SRX state (Liu et al., 2015; Nagy et al., 2015; Shen et al., 2021; Teerlink, Diaz, Felker, McMurray, Metra, Solomon, Adams, et al., 2021; Teerlink, Diaz, et al., 2021a; Woody et al., 2018). The underlying mechanism for OM (which expressed mechanistic attributes associated with myosin inhibitors) was related to increasing the cooperative activation of the thin filament through delayed ADP release. By keeping the myosin head bound to actin longer, a greater level of myosin head recruitment was achieved during activation. This mechanism however, showed to be sensitive to dosage, developing significantly adverse effects in studies dosed with high concentrations.

As an alternative to synthetic compounds, the Regnier laboratory at UW is developing a naturally occurring small molecule therapeutic called 2-deoxy-adenosine triphosphate (dATP) to increase myosin activity and force generation. In contrast to OM, dATP not only increases force generation in treated cardiac muscle, but also does not exhibit the detrimental delay in relaxation or increased systolic ejection time (Kolwicz et al., 2019; Lundy et al., 2014). Significant effort in computational and experimental approaches have shown that straited muscle with dATP exhibits a positive inotropic effect at increasing concentrations and is able to increase both myosin head recruitment and crossbridge cycling kinetics in nucleotide pools expressing ~1-2% dATP (Childers et al., 2020; Ma et al., 2020; McCabe et al., 2020). Recent publications demonstrated that dATP increases weak binding of myosin with actin through electrostatic interactions, lifting the myosin heads off the thick filament and closer to actin (in a primed position for binding) (Powers et al., 2019). These mechanistic attributes of dATP have provided significantly positive results in murine and porcine models of ischemic heart failure, recovering cardiac function in post myocardial infarction (MI) animals.

II. Unknown Mechanisms of Striated Muscle Function and Work Motivation

Decades of research in muscle physiology has enabled scientists to discover lifesaving therapeutics by understanding the underlying mechanisms of diseases. The fusion of biophysics, biology, and biochemistry provides the necessary tools to discover the unknown and learn new fundamental principles that govern life and how the human body functions. The journey as scientists remains unfinished however, as both old and new diseases remain untreated and misunderstood to this day, burdening those impacted by the phenotypes those mutations express. In my work, the aim of my research is to identify and diagnosis new mechanisms that regulate how normal and dysfunction muscles operate. This information is essential to our ability to prevent dysfunction and/or restore proper muscle function in individuals with life-threatening muscular diseases. The presented studies demonstrate an integrated approach to elucidating the myofilament specific processes that underlie cardiac muscle performance. This work is aimed to address (1) the underlying regulatory role of myosin through differences in structural recruitment and biochemical cycling, (2) the structural and biochemical pathways that small molecules alter sarcomeric proteins as mechanisms of therapy for individuals with congenital heart failure, and (3) underlying mechanisms of dysfunction in hypercontractile models of striated muscle diseases.

i. Aim 1: Determining the differences between the structural and biochemical functions of striated muscle myosin regulation

As described above, the introduction of the SRX state by Roger Cooke and colleagues in 2010 demonstrated a new functional state of myosin molecules in the crossbridge cycle (Nag & Trivedi, 2021). This *biochemical* definition of myosin described the significantly slower release of ATP hydrolysis products relative to the other states of myosin. As a third subset of the myosin population, the SRX-DRX states became a hallmark concept in the characterization of diseases and sarcomeric targeting small molecules. These *biochemical* definitions of myosin however have

become confused with other *structural* definitions of myosin. Characterization of muscle structure through small angle x-ray diffraction experimentation has reported the position of myosin relative to the thick and thin filament. These static images report the average mass of the myosin heads that diffract the x-ray beam relative to the thick and thin filament position. Myosin heads closer to the thick filament backbone are considered OFF myosin, while myosin heads elevated towards the thin filament are described as ON myosin.

It is important to note that the *biochemical* SRX-DRX and *structural* OFF-ON states of myosin report significantly different characteristics of myosin. By definition, the SRX-state only observes cycling kinetics of myosin while the OFF-state only observes myosin head order and position. Within the field however, these two definitions have become interchangeable, and utilized to describe a singular "sequestered" state of myosin. The purpose of my first aim is (1) to test the null hypothesis that the SRX and OFF states of myosin describe a correlative phenomenon of myosin function and (2), determine if the current method of calculating the SRX population is valid in conditions of isolated myosin proteins.

ii. Aim 2: Determine how myosin-targeting small molecules alter sarcomeric protein function and biochemical interactions

As myosin-targeting small molecules become more prevalent as therapeutic pathways to treat sarcomeric dysfunction and dysregulation, understanding what mechanistic pathways these compounds alter becomes even more important. As discussed above, OM was initially characterized to directly accelerate the actin-activated rate of phosphate release in myosin. Later reductionist experiments showed that OM inhibited myosin crossbridge cycling, expressing a positive inotropic response by increasing the cooperative activation of the thin filament through delayed ADP release. For my second project aim, I have selected a novel myosin activator, Danicamtiv, (Bristol-Myers Squibb) to identify what underling mechanisms produced such promising results in the recently published clinical trials (Voors et al., 2020). Briefly, reported

findings showed increased Ca^{2+} sensitivity and myofibril ATPase activity, resulting in canines with heart failure expressing improved LV stroke volume and LA emptying fraction. Through our reductionist assays, I aim to identify where on the crossbridge cycle Danicamtiv impacts myosin function, and how it alters the population of OFF myosin compared to untreated controls.

iii. Aim 3: Determine how myosin mutations impact myofibril structure and function in a model of hypercontractile familial cardiomyopathy

With over a thousand disease-causing missense mutations found in striated muscle myosin, it is imperative to understand how the alterations in structure impede myosin function. Within the scope of my research, I have selected a mutation that expresses hypercontractility in cardiac muscle. In this aim, I will utilize the hypercontractile familial cardiomyopathy R403Q to determine how the mutation alters the structural and mechanical function of myosin. Briefly, R403Q has been described to reduce the contractile function of myosin at the molecular and myofibril level while increasing crossbridge cycling rate and tension cost in β-myosin (S. Lowey et al., 2018; Witjas-Paalberends et al., 2014). Through single molecule force measurements, *in-vitro* motility assay, and single ATP turnover experiments, previous publications argued that the hypercontractility phenotype associated with R403Q was associated with an increased number of myosin heads functionally available for interaction with actin (Saswata S. Sarkar et al., 2020).

As a HCM mutation, the initial treatment pathway would be through a myosin inhibitor, such as Mavacamten, to reduce the population of functional myosin heads, and push the population further into the SRX conformation of myosin (Robert L. Anderson et al., 2018). This treatment however would further reduce the contractile performance of the myofibrils, potentially leading other downstream compensatory mechanisms to regain the lost function. As a therapeutic alternative, I aim to investigate the mechanistic impact of dATP and Mavacamten on R403Q and how these small molecules may address the dysfunctional contractile and structural phenotypes expressed by the disease.

III. Chapter 1: The structurally defined OFF and ON states can be decoupled from the biochemically defined super-relaxed and disordered-relaxed states of myosin

This chapter represents the latest version of a co-first author manuscript in preparation.

Saffie Mohran†, Vivek Jani †, Peter O. Awinda, Taejeong Song, Chengqian Gao, Henry Gong, Sakthivel Sadayappan, Michael Regnier, Bertrand C. W. Tanner, David A. Kass, Weikang Ma, Thomas Irving

†: Contributed equally.

i. Abstract

There is growing awareness that thick filament along with classical thin filament regulation play central roles in modulating muscle contraction. Biochemical assays have demonstrated that under relaxed conditions, myosin may reside in either a high energy-consuming disordered-relaxed (DRX) state available for binding actin to generate force, or in an energy-sparing super-relaxed (SRX) state unavailable for actin binding. X-ray diffraction studies have shown the majority of myosin heads are in a quasi-helically ordered OFF state in a resting muscle and that this helical ordering is lost when myosin heads are turned ON to participate in contraction. It has been assumed that myosin heads in SRX and DRX states are equivalent to the OFF and ON state respectively and the terms have been used interchangeably. Here we use X-ray diffraction and ATP turnover assays to track the structural and biochemical transitions of myosin heads respectively induced by either omecamtiv mecarbil (OM) or piperine in relaxed porcine myocardium, showing that while OM and piperine induce dramatic shifts of myosin heads from the OFF to ON states, there are no appreciable changes in the population of myosin heads in the SRX and DRX states. Our results show that biochemically defined SRX and DRX can be decoupled from structurally defined OFF and ON states. While SRX/DRX and OFF/ON transitions may be correlated in some cases, these two phenomena are not synonymous, measured using different approaches, and should be investigated and interpreted separately.

ii. Significance

Myosin based thick filament regulation is now known to be critical for muscle contraction and its dysregulation is found in hypertrophic and dilated cardiomyopathies. While previously thought to be synonymous, this study shows biochemical and structural thick filament disengagement are distinct properties to be investigated as independent phenomena. Understanding the details of thick filament regulation will be of great relevance to defining

sarcomere-level dysfunction in the myopathies and better designing therapies aimed at reversing them to treat these diseases.

iii. Introduction

Regulation of vertebrate striated muscle contraction has been regarded as a calcium (Ca^{2+}) mediated thin filament-based mechanism. Upon excitation signaling, Ca^{2+} enters the cytosol to bind to troponin-C on the thin filament triggering conformational changes to displace tropomyosin from myosin-binding sites on actin, allowing actin-myosin cross bridges and thus force generation. Initial binding of myosin to the unblocked sites results in a full cooperative activation of the thin filament (Lehman et al., 1994; Risi et al., 2021) to augment force. This classical Ca^{2+}-mediated thin filament-based regulation mechanism assumes that all myosin heads are free to bind actin once the actin binding sites are available. However, this picture appears incomplete, and we now realize that muscle regulation requires both thick and thin filament based mechanisms to fully activate the sarcomere (Irving, 2017).

Thick filament based regulation in vertebrate muscle was first bought to our attention when Roger Cooke and colleagues discovered that under resting conditions, myosin can exist either in a disordered-relaxed (DRX) state with a higher ATP consumption rate (~0.03 s^{-1}) or in an energy-sparing, low ATP consumption (~0.003 s^{-1}) state, known as the super-relaxed (SRX) state (Cooke, 2011; Hooijman et al., 2011b). This is considered a biochemical characterization related to ATP consumption. Subsequent studies suggested that myosin heads in the SRX state might be sequestered on the surface of thick filament making them unlikely or unavailable for acting binding and force generation, whereas heads in the DRX state could and would bind to generate force (R. L. Anderson et al., 2018a; Craig & Padron, 2022; Rohde et al., 2018; Spudich, 2019). The relative proportions of myosin heads in SRX and DRX states under resting conditions, estimated to exceed 50%) are related to the amount of force produced during activated state (Ma , W et al., 2023; Yuan et al., 2022a) and an imbalance of SRX/DRX states proposed to underlie

a substantial component of hypo- and hyper-contractility observed with cardiomyopathies (Kawana et al., 2022; Nag & Trivedi, 2021; Spudich, 2019; Yuan et al., 2022a, 2022b).

Another aspect of thick filament activation was brought to the forefront by Linari and colleagues, who proposed a mechano-sensing based thick filament activation model (Linari et al., 2015). In the resting state, most of the myosin heads are quasi-helically ordered on the surface of the thick filament backbone. These myosin heads, defined to be in the OFF state, produce the characteristic myosin-based layer line reflections in X-ray fiber diffraction patterns (Huxley, 1973; Ma & Irving, 2022b; Reconditi et al., 2005). The helical ordering is lost when myosin heads are turned ON to participate in contraction(H.E. Huxley, 1971; Huxley & Brown, 1967; Linari et al., 2015). In the mechano-sensing model, once the thin filament is turned on by influx of Ca^{2+}, a small portion of constitutively ON heads, assumed to be constantly searching for binding sites on actin, will bind to actin and generate small amounts of force that strain the thick filament. This strain then results in converting more myosin heads from the OFF state to the ON state (Irving, 2017; Linari et al., 2015).

It has been generally assumed that myosin heads in the biochemically-defined SRX and DRX state are equivalent to the structurally-defined OFF and ON state respectively (Craig & Padron, 2022; Irving, 2017; Wilson et al., 2014) so that terms SRX state and OFF state are often used interchangeably. Here we used X-ray diffraction and ATP turnover assays to track the structural and biochemical transitions involved in thick filament regulation induced by either omecamtiv mecarbil (OM) or piperine (PIP) respectively under resting conditions. We show that while OM and PIP induce dramatic shifts of myosin heads from the OFF to the ON states, there are no appreciable changes in the populations of myosin heads in the SRX and DRX states. These results reveal that biochemically defined SRX and DRX states can be decoupled from the structurally defined OFF and ON states, indicating the behaviors reflect different phenomena. In the presence of PIP, it is the structural OFF to ON transitions rather than the changes in SRX/DRX states that occur with increased steady-state force. We propose that the structure of the myosin

heads in the absence of perturbations that might alter actin-activated myosin ATPase activity, determine the functional output of muscle.

iv. Material and Methods

- *X-ray diffraction*

X-ray fiber diffraction patterns were obtained from permeabilized porcine left ventricular muscle bundles as described previously (Ma, Gong, et al., 2022; Ma, Nag, et al., 2022). Briefly, pieces of frozen porcine left ventricle wall were thawed and permeabilized with 1% Triton-X100 for 3 h at room temperature. Fiber bundles (~5 mm long at ~ 200 µm in diameter) were attached to aluminum T-clips at both ends for the X-ray experiments. X-ray diffraction patterns were collected on a MarCCD 165 detector (Rayonix Inc., Evanston IL) with a 1 s exposure time as a function of five increasing Omecamtiv mecarbil OM (0 µM, 0.1 µM, 0.5 µM, 1 µM, and 10 µM) and piperine (0 µM, 2 µM, 7 µM, 15 µM, and 50 µM) concentrations. The X-ray data were analyzed using the MuscleX software package developed at BioCAT (Jiratrakanvong et al., 2018).

- *Muscle mechanical experiments*

For the steady state tension vs. pCa experiments, permeabilized cardiomyocytes were prepared as described above. Force-Ca^{2+} relationships were obtained by subjecting CMs to increasing Ca^{2+} concentration (from 0.0–46.8 µM). Force was normalized to the cross-sectional area to obtain tension (mN/mm^2). Steady-state tension versus the log [Ca^{2+}] plots (T-Ca^{2+} plots) were fit to the three-element Hill equation to calculate T_{max}, EC50 and n_h. The cardiomyocytes were then incubated in relaxing solution with 1 µM OM and 7 µM piperine for 10 min, and the post-exposure tension-Ca^{2+} relation obtained. Myofibril preparations were isolated from previously frozen porcine left ventricle tissue as previously described (Moussavi-Harami et al., 2015). Briefly, the cardiac tissues were homogenized to generate myofibrils that were then mounted between a force transducer and a motor. Activation and relaxation were achieved by

rapid solution switching via double barreled pipette containing activating and relaxing solutions respectively.

- *ATP turnover assays*

Samples for unloaded ATP turnover assays from permeabilized porcine cardiac fiber bundles tissue were prepared as described previously (McNamara et al., 2017; McNamara, Li, Smith, Lal, Graham, Kooiker, van Dijk, dos Remedios, et al., 2016). Permeabilized cardiac tissue was further cut into small bundles of fibers and secured with double sided tape in a flow chamber (thickness ~270 μm) as described previously (McNamara, Li, Smith, Lal, Graham, Kooiker, van Dijk, dos Remedios, et al., 2016). ATP turnover assays from permeabilized single CMs under loaded conditions were conducted as described (Jani et al., 2022). Frozen porcine myocardium was cut into 10-15 μg pieces and permeabilized on ice before being homogenized for single CM extraction. CMs were affixed to a force and length transducer and the sarcomere length set to 2.1 μm. Samples were incubated in rigor buffer containing mant-ATP for 5 min before chasing with relaxing buffer containing ATP (See SI for details). All the results were fit to a double exponential decay function $I = 1 - P_1\left(1 - e^{\frac{-t}{T1}}\right) - P_2(1 - e^{\frac{-t}{T2}})$ where I is the fluorescence intensity at any given time (t)) to calculate P1, P2, T1 and T2. The proportion of the SRX myosin is 2 × P2.

v. Results

- *Structural changes of permeabilized porcine myocardium with OM and piperine.*

We studied X-ray diffraction patterns obtained from relaxed permeabilized porcine myocardium at different concentrations of OM and PIP. Qualitatively, permeabilized porcine myocardium showed characteristic relaxed myosin-based layer lines (MLL1 and MLL2) in the absence of myosin activators, that diminished in intensity with increasing activator concentration until they were no longer visible in the presence of the highest concentrations of OM and PIP

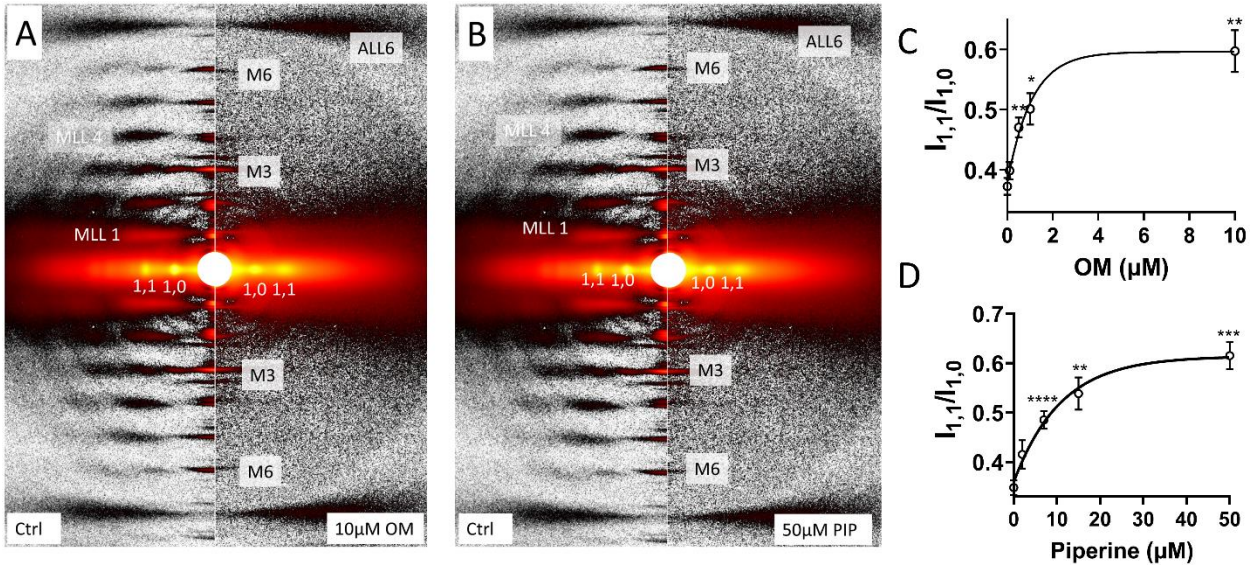

Figure 1. X-ray diffraction patterns from permeabilized porcine myocardium in relaxing solution in the absence and presence of myosin activators.

(**A**), X-ray diffraction patterns from relaxed muscle in the absence (left panel) and presence (right panel) of 10 μM omecamtiv mecarbil (OM). (**B**), X-ray diffraction patterns from relaxed muscle in the absence (left panel) and presence (right panel) of 50 μM piperine (PIP). Equatorial intensity ratio ($I_{1,1}/I_{1,0}$) at different concentration of omecamtiv mecarbil (OM) **(C)** and piperine **(D)**. Myosin heads moves radially closer to actin as OM and piperine concentration increases. The results are given as mean ± SEM with *p* values were calculated from RM one-way ANOVA with Dunnett's multiple comparisons test compared to control.

used in this study as shown in figure 1A and figure 1B respectively. The equatorial intensity ratio ($I_{1,1}/I_{1,0}$), an indicator of the proximity of myosin heads to actin in relaxed muscle (Ma & Irving, 2022b), increased monotonically as a function of either OM (Fig 1C, Table S1) or piperine (Fig 1D, Table S2) concentrations, indicating a shift of myosin heads away from the thick-filament backbone towards the thin filament at increased concentration of each activator.

In the OM experiments, we showed that both I_{MLL1} and I_{M3} decreased slightly at 0.1 μM OM (p = 0.22, p = 0.53 respectively), and further decreased monotonically at higher concentrations (Fig 2A & 2C, Table S1). Similarly, in the piperine experiments, both I_{MLL1} and I_{M3} decreased slightly at 2 μM piperine (p = 0.08, p = 0.29 respectively), and further decreased monotonically at higher concentrations (Fig 2B & 2D, Table S1). The intensity of the sixth order myosin-based meridional

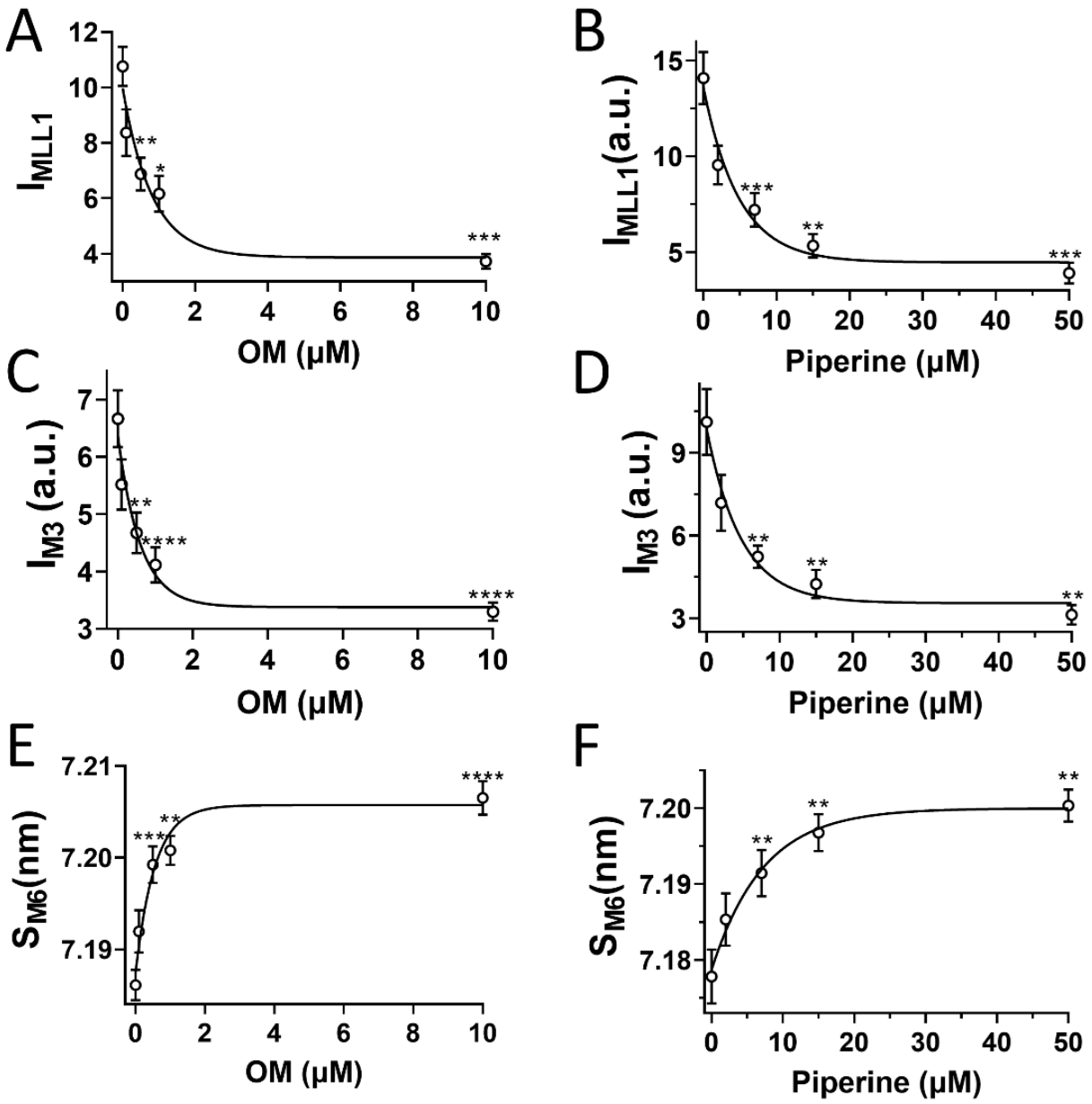

Figure 2. Thick filament structural changes in the presence of myosin activators.

The intensity of the first order myosin-based layer line (I_{MLL1}) in different concentrations of OM (**A**) and piperine (**B**). The third order myosin based meridional reflection (I_{M3}) in different concentrations of OM (**C**) and piperine (**D**). The spacing of the sixth order myosin based meridional reflection (S_{M6}) in different concentrations of OM (**E**) and piperine (**F**) Myosin heads moves from the helically ordered OFF states to disordered ON states as activators concentration increase. Results are given as mean ± SEM with *p* values calculated from RM one-way ANOVA with Dunnett's multiple comparisons test compared to ctrl (0 μM compound).

reflection (M6) arises primarily from the thick filament backbone. The spacing of M6 reflection (S_{M6}), reflecting the thick filament backbone periodicity (Ma & Irving, 2022b), increases as the concentration of either OM and piperine increases (Fig 2E & 2F, Table S1) . An increase in the thick filament backbone periodicity, indicated by the increases of S_{M6}, and a reduction in the degree of the helical ordering of the myosin heads, indicated by the decrease of I_{MLL1} and I_{M3}, are the characteristic signatures of the structurally-defined OFF to ON transition of myosin (Irving, 2017; Jani et al., 2022; Ma & Irving, 2022b). Taken together, these findings show both OM and piperine result in substantial disruption of the helical ordering of myosin heads on the surface of the thick filament backbone allowing for release of myosin heads to move closer to actin; an OFF to ON transition.

- *Effects of OM and piperine on steady-state isometric calcium concentrations vs. force relationship.*

We then investigated how the structural changes induced by OM and piperine under relaxing conditions can translate to functional differences in the activated state. We first interrogated the active tension versus calcium concentration (pCa) relationships. A classic sigmoidal tension vs. pCa relationship was observed in the control preparations. Upon the addition of OM, a left-upward shift in the tension/pCa relationship was observed, significantly increasing the calcium sensitive of the tissue preparations in a paired wise comparison. Interestingly, piperine did not show any significant change. The left-upward shift of the tension vs. the pCa relationship after OM treatment matched previously reported results (Kieu et al., 2019) while exhibiting a significant increase in tension generation at lower Ca^{2+} concentrations, a paired phenomenon with a lower hill coefficient value. At maximal Ca^{2+}, OM significantly reduced the tension generation compared to paired control. In comparison, piperine did not exhibit a decrease in calcium sensitivity or a drop in tension generation. Tissue preparations treated with piperine however did show a small increase in tension generation at lower (6.4 and 6.2) calcium

concentrations, which resulted in a significant decrease in the hill coefficient value. Both treatments significantly inhibited the maximal tension redevelopment rate of myosin during a slack re-stretch protocol, suggesting that each compound is impacting the function of myosin cycling mechanistically.

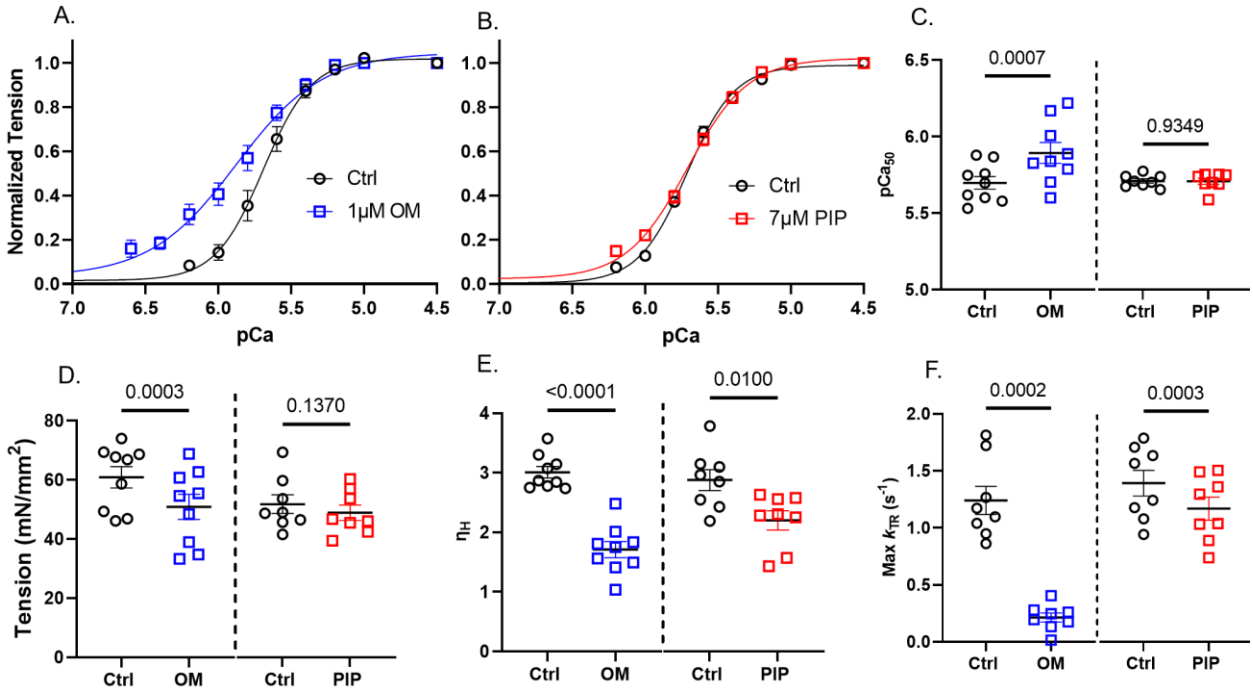

Figure 3. Steady state tissue mechanics in the presence of myosin activators.

The normalized tension curves as a relationship to calcium concentration for shows paired comparisons for OM (**A**) and piperine (**B**). The calculated calcium EC_{50} of the treated tissue compared to control (**C**) for both compounds. The maximal generated tension (**D**), hill coefficient (**E**) and tension redevelopment rate (k_{TR}) (**F**). Results are given as mean ± SEM with *p* values were calculated from student paired t-tests compared to paired control (0 μM compound).

- *Effects of OM and piperine on myofibril activation and relaxation kinetics.*

After obtaining the effects of OM or piperine on steady-state force production, we then did mechanical experiments on isolated myofibrils to study the effects of OM or piperine on the activation and relaxation kinetics by rapid solution switching via double barreled pipette before

and after treatment with OM or piperine. In OM treated myofibrils, the force development rate constant (k_{ACT}), the slow linear phase relaxation constant ($k_{REL(slow)}$) and the fast exponential relaxation constant ($k_{REL(fast)}$) are all significantly decreased (Fig 4 E-G) indicating that OM slows down cross-bridge cycling. There were no significant differences in k_{ACT} and $k_{REL(slow)}$ before and after piperine treatment (Fig 4E and 4G). There was, however, a slight, but statistically significant, decrease in $k_{REL(fast)}$ (18.85 ± 0.78 s^{-1} vs 17.57 ± 0.85 s^{-1}, p = 0.03, Fig 4F) before and after piperine treatment.

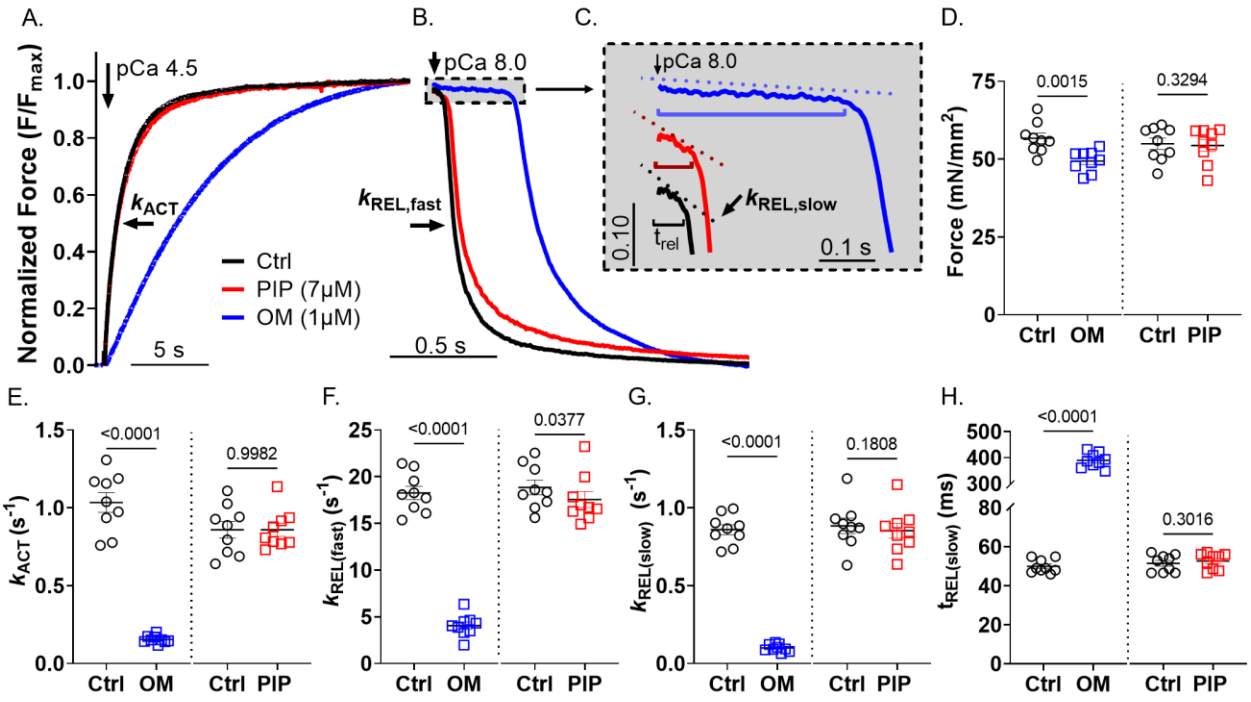

Figure 4. Myofibril mechanics to assess activation and relaxation kinetics in the presence of myosin activators.

The normalized tension curves of the myofibril activations **(A)** for control (black), OM (blue), and piperine (red), as well as fast and slow phases of relaxation **(B, C)**. Each compound treatment was done in a pairwise comparison to untreated control. Measurements myofibril force **(D)** activation kinetics, fast phase of relaxation **(F)**, slow phase relaxation kinetics **(G),** and duration **(H)** all showed significant dysfunction with OM with only some changes with treatment of piperine. Results are given as mean ± SEM with p values were calculated from student paired t-tests compared to paired control (0 μM compound).

- *Changes in ATP turnover rate in permeabilized porcine myocardium with OM and piperine.*

To test the hypothesis that the structurally defined OFF/ON states myosin heads are strongly correlated if not equivalent to biochemically defined SRX/DRX states, we next examined the proportion of myosin heads in SRX and DRX states with and without both activators. Utilizing a recently developed loaded ATP turnover procedure (Jani et al., 2022) in permeabilized single cardiomyocytes (CMs) and measured the proportions of myosin heads in the SRX/DRX states in a paired manner. Both OM (1 μM) and piperine (7 μM) were applied to permeabilized cardiomyocytes under unloaded conditions, and the decay rate of fluorescent MANT-ATP

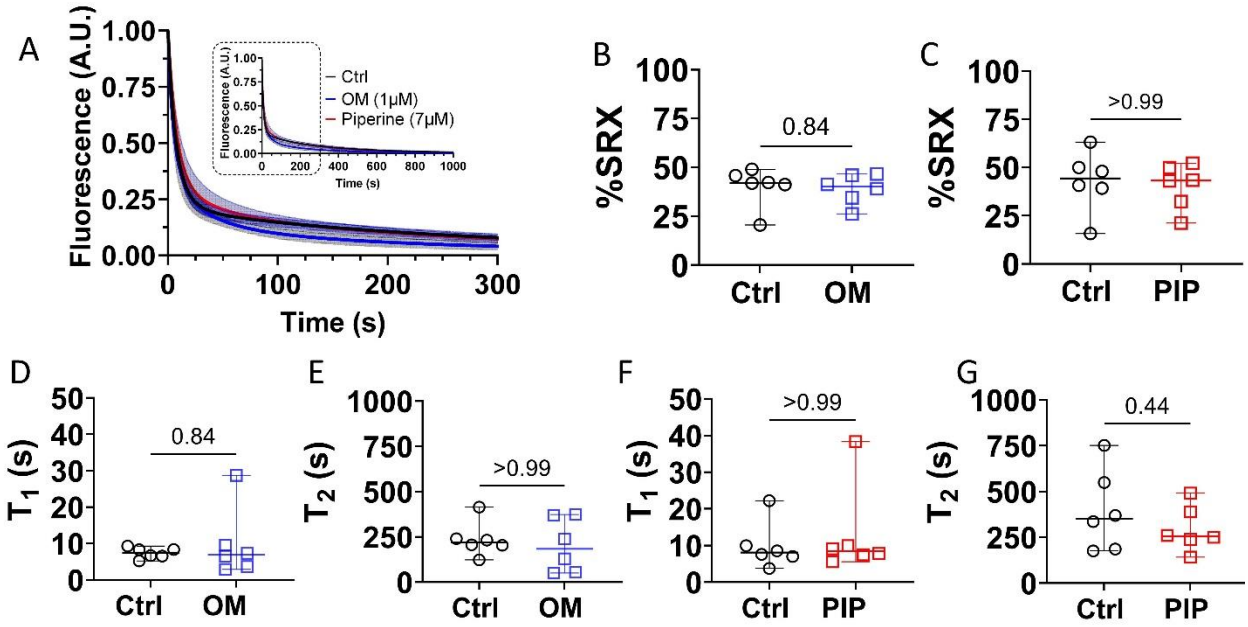

Figure 4. ATP turnover assays of loaded permeabilized porcine CMs before and after OM and piperine (PIP) treatment.

Mant-ATP dissociation over time curves **(A)** in control (black), 1 μM OM (blue) and 7 μM piperine (red). The percentage of myosin heads in the SRX state (% SRX) before and after OM (**B**) and piperine (**C**) treatment. The time constant of the fast phase (T_1) before and after the OM (**D**) and piperine (**E**) treatment. The time constant of the slow phase (T_2) before and after the OM (**F**) and piperine (**G**) treatment. The results are given as mean ± SEM with *p* values calculated from Wilcoxon matched pairs signed rank t tests.

provided a measure of ATP turnover rate. We found this fluorescence decay signal indistinguishable between control (un-treated) and OM/piperine treated tissues. The relative proportions of the myosin heads in the DRX and SRX states and the time constant of the fast phase (T1) and the slow phase (T2) were calculated by fitting the fluorescence decay profile with a 2-phase exponential decay function (see methods). Neither the fraction of the myosin heads in the SRX state nor the T1 and T2 values change significantly in the presence of either OM or piperine (Fig 5).

vi. Discussion

- *Structurally defined OFF and ON states can be decoupled from the biochemically defined SRX and DRX states.*

It has been often observed that the structurally-defined OFF and ON states of myosin are correlated with the biochemically defined SRX and DRX states (R. L. Anderson et al., 2018a; Craig & Padron, 2022; Irving, 2017; W. Ma, M. Henze, et al., 2021; Nag & Trivedi, 2021; Ranu et al., 2022) and, consequently, are widely assumed to reflect the same underlying phenomena. The structural basis for the SRX has been hypothesized to be the interacting head motif (IHM), in which a pair of the myosin heads interact with each other and the S2 segment causing them to be held close to the thick filament backbone (S. Chu et al., 2021; Craig & Padron, 2022; Padron et al., 2020). While our definition of the helically ordered OFF state does not address the precise configuration, and possible heterogeneity, of the OFF-state myosin heads, recent EM studies on isolated native cardiac thick filaments showed that myosin heads in the IHM configuration are indeed helically ordered on the surface of the thick filament. However, not all IHM configurations were observed to be exactly the same with three distinct forms identified in the presence of mavacamten (Dutta et al., 2023). Thus, a substantial fraction of the myosin heads in the structurally defined OFF state in resting muscle are likely to be in one of these IHM states. Here, our X-ray diffraction data showed that increased concentration of OM and piperine induce a

dramatic reduction in the helical ordering of the myosin heads (Fig 2) accompanied with a radial movement of the myosin heads towards actin (Fig 1) at pCa 8. These data strongly indicate an OFF to ON transition of myosin heads induced by OM and piperine. ATP turnover assays using both unloaded porcine fiber bundles and loaded cardiomyocytes, however, showed that OM and piperine did not significantly alter the relative portion of the myosin heads in the SRX and DRX states. These findings refute the notion that biochemically defined SRX and DRX are manifestations of structurally defined OFF and ON states, but rather that these behaviors are distinct.

It is worth noting that multiple hints of possible disconnects between the biochemical and structural states of myosin have previously appeared in the literature. It has been shown that the structural OFF to ON transitions induced by dATP in relaxed porcine myocardium were not equivalent to the biochemical SRX to DRX transitions (Ma, W et al., 2023). Chu and colleagues showed that Mavacamten, a small molecule myosin inhibitor, has a greater effect on the increase of population of myosin in the SRX state than the increase in number of myosin heads in the IHM state (S. Chu et al., 2021). Additionally, Anderson et al showed that isolated myosin S1 can adopt the SRX state without the possibility of forming the IHM (R. L. Anderson et al., 2018a).

- *Functionally accessible heads and contractile force*

The primary function of muscle is to generate force by cyclic interactions between myosin-containing thick filaments and actin-containing thin filaments. Spudich has proposed that the total force in a sarcomere is dependent, in part, on the number of functional accessible heads, N_a, defined as those capable of force generation (Spudich, 2019). Change in N_a is considered an important regulator in determining muscle force and too much change a contributor to sustained hypo- and hyper-contractility found in various myopathies (Kawana et al., 2022; S. S. Sarkar et al., 2020; Spudich, 2019). Details of the mechanisms determining N_a, however, have been

elusive. It is generally assumed that sequestered OFF state heads, presumably in the SRX state, are unavailable to bind actin and that the number of myosin heads in disordered states, either biochemically and structurally defined, determine N_a and thus contractile force. In this context, our findings that SRX/DRX and OFF/ON do not necessarily behave in lockstep have important implications. It has been shown that the structural OFF to ON changes induced by dATP under relaxing conditions is a better predictor of activated force than the degree of SRX to DRX transitions induced by dATP (Ma, W et al., 2023). In this study, both OM and piperine cause a leftward shift of the tension/pCa curve resulting in an increase in calcium sensitivity (EC_{50}) and a significant increase in the tension developed at sub-maximal activation without significantly affecting T_{max}. It has been shown that thick filaments can be directly activated by calcium (Ma, Nag, et al., 2022) and if thick filaments are partially turned ON by OM or piperine, one would expect that less calcium would be required to activate the muscle at intermediate levels of activation. At full activation, the effect of OM or piperine will be offset by the saturating level of calcium, so the effects of OM or piperine on T_{max} would be expected to be minimal, as demonstrated here. Given the lack of change of the populations of myosin heads in the SRX and DRX states, we conclude that it is the structural, rather than the biochemical states, of the myosin heads that ultimately determines muscle functional output.

There is also evidence that not all OFF to ON structural transitions have equivalent effects on force output. The helical ordering of myosin heads under resting conditions can be disrupted in multiple ways. It has been shown that lowering of temperature can disrupt the helical ordering of the myosin heads accompanied by a radial movement of the heads towards actin (Caremani et al., 2019; W. Ma, S. Duno-Miranda, et al., 2021; Xu et al., 2003), but all of these nominally OFF to ON transitions in the myosin heads lead to decreased active force. The lower temperature slows down the ATPase activity of myosin thus trapping the myosin in the ATP state so that the heads are incapable of binding to actin and producing force (Caremani et al., 2019). In contrast,

N-benzyl-p-toluene sulphonamide (BTS) does not appreciably affect the resting myosin configuration in intact skeletal muscle (Ma, Gong, & Irving, 2018) but significantly inhibits muscle contractility, in this case by inhibiting the myosin ATPase (Cheung et al., 2002). In the current study, we show that piperine does not appreciably change cross-bridge kinetics (Fig 6 and Fig 7) implying that it is the structural OFF to ON transitions, in the presence of unchanged populations of myosin heads in the SRX/DRX states, that are responsible for the increased steady-state force in the presence of piperine (Fig 5). We propose, therefore, that the structure of the myosin heads, in the absence of perturbations that might affect actin-activated myosin ATPase activity, determine the functional output of muscle.

- *Implications for sarcomere targeted treatment of cardiomyopathies.*

With this new concept that SRX/DRX and structural OFF/ON transitions represent different underlying phenomenon. While biochemical SRX/DRX states of myosin may correlated to the structural OFF/ON state to some extent under normal physiological conditions, these correlations can break down in pathological conditions or in the presence of chemical compounds, so it is critical to understand the precise causes of these diseases in order to design tailored therapies. Myosin inhibitors have been proposed to be a therapeutic strategy to curb the excessive contractile properties and impaired relaxation seen in hypertrophic cardiomyopathy (HCM). Indeed, this hypothesis has culminated in the FDA approval of Mavacamten, a myosin binding small molecule that shift more myosin heads to the structural OFF state and the biochemical SRX state (R. L. Anderson et al., 2018a; W. Ma, M. Henze, et al., 2021), to treat obstructive HCM (R. L. Anderson et al., 2018b; Ho et al., 2020). Mavacamten treated myocardium is one case where SRX/DRX and OFF/ON transitions are well correlated and mitigating both changes restore, at least partially, normal physiological conditions.

Another class of cardiomyopathies are associated with heart failure which is typically accompanied by depressed muscular contractile properties. It has been shown that, at least in one cohort of right ventricle heart failure patients, increases in the population of myosin heads in the biochemical SRX state and structural OFF state might be the underlying cause of depressed contractile forces. So far, only deoxy-ATP (Ma, W et al., 2023; Walklate et al., 2022a) and EMD-57033(Jani et al., 2022) have been shown, when used as tool compounds, to be able to recruit myosin from the OFF and SRX states and enhance muscle contractility, but these compounds have not been used for clinical studies due to other limitations (Kieu et al., 2019; Mamidi et al., 2017). OM was the first myosin activator to undergo, ultimately unsuccessful, clinical trials as a myosin activator. Surprisingly, there have been no previous published studies of the effects of OM on SRX/DRX. Here we show that OM disorders the myosin heads (promotes OFF to ON transitions) without changing SRX/DRX. While OM is able to increase the contractile force at systolic calcium concentration (Fig 3) it does it, not by recruiting myosin heads from the SRX state, but by increasing the phosphate release rate and stabilizing myosin in the pre-power stroke configuration (Woody et al., 2018) leading to severely impaired activation relaxation kinetics as demonstrated by our kinetics results (Fig 4) as well as in previous studies (Kieu et al., 2019; Mamidi et al., 2017).

Our piperine data suggests another avenue for searching for myosin activators. We showed that piperine was able to increase the active tension of permeabilized porcine CMs in the relevant systolic calcium concentration range (Fig 3) without significantly compromising cross-bridge cycling kinetics (Fig 4). More importantly, piperine activated myosin by shifting the heads from the structural OFF state to the ON state without affecting the equilibrium of heads in the SRX and DRX state indicating that piperine might be able to enhance systolic contractility without increasing diastolic ATP consumption which could be metabolic advantageous. Piperine would seem a far superior muscle activator from a purely biophysical perspective as compared to OM.

While piperine is not a suitable drug candidate for enhancing cardiac contractility due to its pleiotropic effects on the human body (Tripathi et al., 2022), it might be worth exploring the feasibility of similar, but more selective compounds that target the RLC of myosin (Tolkatchev et al., 2018) in a similar manner to piperine.

The current study shows that the biochemically defined SRX and DRX states can respond differently to physiological perturbations and experimental interventions than the structurally defined OFF and ON states and should not be considered the same underlying phenomena. Our study also allows us to propose that it is the structural state of the myosin heads, in the absence of perturbations that might affect actin-activated myosin ATPase activity, that determines the functional output of muscle. Our findings provide a fresh look at thick filament regulation mechanisms that can aid our understanding of the dysregulations of actomyosin interactions found in myopathies that can aid in targeting pharmaceutical interventions for these diseases.

vii. Acknowledgements

W.M, designed the experiments; S.M, V.J, P.O, T.S, B.T, W.M, and H.G performed the experiments; S.M, V.J, P.O, T.S, W.M, B.T, H.G, and C.G analyzed the data; W.M, S.M, S.S, M.R, B.T, D.K, and T.C.I. wrote the manuscript.

IV. Chapter 2: The biochemically defined SRX state of myosin – a paradox

This chapter represents the latest version of a second author manuscript in preparation.

Saffie Mohran[†], Kristina Kooiker[†], Max Mahoney-Schaefer[†], Christian Mandrycky, Kerry Kao, An-Yue Tu, Jeremy Freeman, Farid Moussavi-Harami, Michael Geeves & Michael Regnier

i. Abstract

The SRX (super relaxed) state of myosin has been defined as a low ATPase activity state which can conserve energy when the myosin is not required for muscle contraction. It has been correlated with a structurally defined ordered (vs disordered) state of muscle thick filaments. The two states may be linked via a common interacting head motif (IHM) in which the two heads of heavy meromyosin (HMM) or myosin fold back onto each other and form additional contacts with S2 and the thick filament. However, experimental observations of the SRX, IHM and the ordered form of thick filaments do not always agree. We have reexamined the measurements of the SRX state for porcine cardiac HMM to try to resolve the differences in the assays, and because current assays of the SRX result in series of paradoxes which are unresolved. In our hands we find little direct evidence of the SRX state using the commonly employed mant.ATP displacement assay. This means that while the structurally defined IHM and ordered thick filaments clearly exist, great care must be taken in use of the mant.ATP displacement assay to define the SRX. A combination of theory and experimental observations suggest this is not a reliable assay.

ii. Introduction

Current views suggest that the actomyosin interaction of muscle function is regulated by both thin and thick filament mechanisms. Thin filament activation is well studied and describes how the presence of calcium modulates the access of myosin binding sites on actin through troponin and tropomyosin interactions (Gordon et al., 2000). The regulation of myosin, and the availability of actively cycling heads within the thick filament system remains a subject of intense study. Evidence for myosin regulation comes from structural studies of isolated myosin and full thick filaments. These studies suggest an order-disorder transition of the thick filament as myosin heads transition between the OFF (sequestered) and ON (free) states along the thick filament surface (Craig & Padrón, 2022; Schmid & Toepfer, 2021). Similarly, biochemical assays observing the rate of ATP turnover by myosin heads in a variety of preparation including HMM, full-length myosin, synthetic thick filaments, myofibrils, and cells, have led to the definition of a super-relaxed state (SRX) (R. L. Anderson et al., 2018a; Sampath K. Gollapudi et al., 2021; Weikang Ma et al., 2021; C. N. Toepfer et al., 2020; Toepfer et al., 2019; Walklate et al., 2022b). This state describes an ATP turnover rate less than $1/10^{th}$ of the normal myosin state (the disordered relaxed state, DRX) (Craig & Padrón, 2022). Transition of myosin within populations of the SRX/DRX states or in the structural OFF/ON conformations can be manipulated by temperature, changes in ionic strength, phosphorylation of sarcomeric proteins (RLC, MyBP-C and TnI), and various small molecules (e.g. Mavacamten, blebbistatin, dATP) (Nag & Trivedi, 2021; Walklate et al., 2022b).

The degree of activation in myofibril or myocyte preparations can be modulated by the exposure of calcium and/or phosphorylation of thick and thin filament proteins including RLC, MyBPC, and TnI (van der Velden & Stienen, 2019). Modulators like calcium and phosphorylation have a direct impact on the population of myosin heads in the interacting head motif (IHM), a state of myosin where the two heads interact with each other in the M.ADP.Pi state, becoming sequestered along the thick filament. This state is central to thick filament regulation, and recent

cryo-EM studies have resolved the structure of the IHM for isolated human cardiac HMM and in the C-zone of relaxed muscle fibers (Grinzato et al., 2023). The IHM has been identified in almost all isolated 2-headed myosin isoforms and within thick filaments. The IHM has also been well studied in smooth muscle and molluscan striated muscle myosin (Craig & Padrón, 2022; Dutta et al., 2023; Yang et al., 2020).

A major debate within the field questions asks if the IHM conformation, the biochemically defined SRX-state, and the structurally defined OFF-state of myosin are all manifestations of the same regulatory mechanism of striated muscle myosin. In a recent review, Craig & Padron concluded that they were similar, however, several recent publications have described discrepancies between populations of myosin in the biochemically defined SRX/DRX and the structurally defined OFF/ON states (Ma et al., 2023; Walklate et al., 2022b). These reports have led to speculation about different subtypes of myosin head conformations and potential differences in the IHM position where one myosin head remains sequestered along the S2/thick filament backbone while the second is liberated into the pool of cycling myosin heads. These unknowns leave the field in a state of confusion, as different experimental assays measure different aspects of myosin structure and function. It is important to understand what each assay observes, and how comparable *in-vitro* studies of purified myosin proteins are to intact myofibril and myocyte preparations.

The standard biochemical SRX assay (single-nucleotide turnover) mixes the fluorescent ATP analogue mantATP with myosin in preparations ranging from purified S1/HMM to whole myocytes (S. Chu et al., 2021; Jani et al., 2022; Padron et al., 2023; Pilagov et al., 2023). Once steady state is established, a large excess of unlabeled ATP is utilized to chase off the mantATP. Previous reports have described this reaction as a double exponential relationship. The first phase of the fluorescence decay is a fast phase (~ 0.02 to 0.05 s-1), which is consistent with the ATPase rate of isolated myosin heads (Walklate et al., 2022b). The second component of the reaction is

described as the slow phase (~0.002 to 0.005 s-1) which is assumed to be the sequestered, or blocked, state of myosin designated as the SRX population.

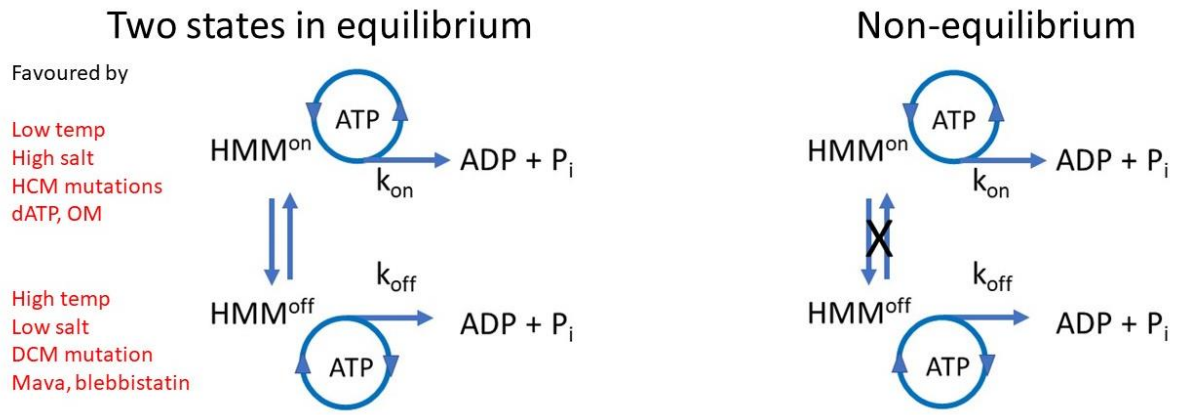

Schematic 1. The differences between the two states in equilibrium, as described by thermo-equilibrium, or a non-equilibrium state of myosin.

In this paper, we discuss the set of paradoxes associated with the definition of the SRX state through the single nucleotide turnover assay in purified myosin motor proteins. The SRX/DRX transition is assumed to be at thermodynamic equilibrium, a steady-state condition where the equilibrium position of the myosin population can be readily manipulated through conditions described in scheme 1. This definition, however, contradicts the reported experimental data. A model with the SRX and DRX at equilibrium (figure 1) would be expected to generate a single exponential relationship for mantATP displacement, as seen in scallop myosin which is regulated by calcium binding to the essential light chain (ELC). The expected single exponential decay is because the nucleotide bound in the SRX can escape via the turnover of the SRX state ([SRX] $k_{cat,SRX}$) or via a return to the DRX state. A double exponential can only be generated if the interconversion of the DRX and SRX are slower than the turnover of the SRX ($k_{cat,SRX}$). This would mean that the two populations are kinetically isolated on the time scale of the slow phase of the turnover assay. Such a condition has been described in smooth muscle myosin, where a mixture

of phosphorylated and dephosphorylated populations of myosin do not interconvert in the absence of a kinase/phosphatase.

A second paradox of the single nucleotide assay and the SRX state in isolated myosin preparations is that rarely do steady-state ATPase assays agree with the predictions of the SRX and DRX properties. For example, the basal ATPase rates measured for bovine cardiac S1, HMM and synthetic thick filaments (~0.015-0.017 s-1) are inhibited to the same extent by Mavacamten, a small molecule shown to structurally modulate the myosin head population into the OFF state (Weikang Ma et al., 2021) and to stabilize myosin into the biochemical SRX state (inhibition to ~30% of zero Mavacamten values, K_i ~0.6-0.8 μM) (R. Anderson et al., 2018; S. K. Gollapudi et al., 2021; Scellini et al., 2021). A previous report by Gollapudi et al. however suggests that different experimental preparations of myosin interact differently to Mavacamten and express different SRX population percentages at specific dosages (Sampath K. Gollapudi et al., 2021). In a follow up study, Gollapudi et al (S. K. Gollapudi et al., 2021) had the same ~ 3 fold inhibition of bovine synthetic thick filaments by mavacamten yet mavacamten increased the SRX population from 10 to 100% in which the ATPase is < 10% of the DRX ATPase (predicted ATPase at mavacamten > 2 uM, 100% SRX x $k_{cat.SRX}$)

A third issue is how rapidly the SRX is formed. In myofibril measurements performed in Walklate et al., the SRX state was formed within 200 ms of mantATP binding to myosin in rigor conditions. The SRX is therefore formed very quickly yet is stable for hundreds of seconds and yet only ~ 30 % of the myosin heads are in the SRX. This is not compatible with an equilibrium mixture of SRX & DRX.

While these paradoxes remain unresolved, the interpretation of this assay remains in doubt. To address this, we returned to the original mantATP chase assay using HMM isolated from porcine ventricle myosin. To our surprise we found no evidence of a secondary slow phase in our assays. The introduction of Mavacamten and other myosin modulators did not introduce a

second phase either, with all reactions expressing a single exponential decay in mantATP fluorescent decay. With a single exponential, there is no interpretation of the SRX to DRX ratio within the HMM population as it is currently defined. It is important to state here that we do not dispute the structural evidence that myosin alone and in thick filaments can exist in two forms, as originally defined for scallop HMM and smooth muscle HMM, but the current mantATP displacement assays of the SRX requires careful re-evaluation.

iii. Methods

- *Protein preparations*

Striated cardiac and skeletal muscle heavy meromyosin was isolated as previously described (Racca et al., 2016). In brief, porcine left cardiac ventricular muscle and rat back muscle muscle was roughly minced on ice. Minced tissue was then added to extraction buffer (0.3 mM KCl, 0.15 mM Imidazole, 10 mM $Na_2P_2O_7$, 1 mM $MgCl_2$, 2 mM DTT, pH 6.8) and stirred on ice for approximately 30 minutes in a small beaker. Excess muscle residue and actin filaments were then removed by centrifugation at 260,000 X g for 1 hour. The supernatant was then diluted 10-15-fold with 4°C water containing 2mM DTT and left on ice for 1.5 hours to allow for myosin precipitation. Samples were then spun at 44,000 X g to pellet precipitated myosin. Myosin was then dissolved in a high salt solution (0.6 M KCl, 2 mM $MgCl_2$, 2 mM DTT, 10mM, pH 7.0). For porcine cardiac heavy meromyosin (pc-HMM), dissolved myosin was then digested by chymotrypsin digest (TLCK treated, Sigma C3142) (50 µg/mL) at 25°C for 10 minutes. For rat skeletal heavy meromyosin (rs-HMM), dissolved myosin was digested by chymotrypsin digest (25 µg/mL) at 25°C for 10 minutes. Each digestion was stopped by adding 4-fold PMSF solution (2 mM MgCl2, 5 mM EGTA, 5 mM DTT, 10 mM Imidazole, 0.2 mM PMSF, pH 7.4) and left on ice for 1 hour. Precipitated light meromyosin (LMM) was removed by spinning at 45,000 X g for 20 minutes. Striated HMM was stored at -80C with the addition of 1% sucrose and 1% protease inhibitor (Sigma-Aldrich, St.

Louis, MO). *Note throughout the manuscript all concentrations of HMM refer to the concentration of heads (~170kDa).*

Porcine cardiac sub-fragment 1 (pc-S1) was isolated as previously described (Mathern & Burke, 1986). Starting with porcine cardiac myosin, add high salt solution (120 mM NaCl, 12.3 mM NaH_2PO_4, 7.7 mM Na_2HPO_4, 1 mM EDTA, pH 7.0) to achieve a myosin concentration of 10 mg/mL. Once dissolved, add chymotrypsin to a 30 µg/mL final concentration. Digest for 15 minutes before stopping with PMSF (0.4 mM final concentration in solution), and then 1.5x volume of BED solution (0.1mM $NaCO_3$, 0.1 mM EGTA, 1 mM DTT, pH 7.0) and 6 mM $MgCl_2$. Centrifuge at 620,000 x g for 20 minutes to isolate the pcS1 from the residual precipitate LMM and undigested myosin and store at -80°C with the addition of 1% sucrose and 1% protease inhibitor.

Actin filaments for multi-turnover assessment were generated as previously described (Racca et al., 2013). Briefly, bovine cardiac G-actin was incubated in polymerization buffer (50 mM KCl, 2 mM $MgCl_2$, 1 mM ATP) and allowed to assemble for 2 hours at 4°C. The polymerized actin was then dialyzed against 500x volume of working buffer (50 mM Tris-HCl, 100 mM KCl, 5 mM $MgCl_2$, 1 mM EDTA, pH 7.2 at 4°C) overnight. The next day, the actin was stabilized with unlabeled phalloidin by adding a 1:1 molarity concentration of phalloidin to actin and incubated overnight at 4°C. Actin was stored at 4°C for up to 3 weeks.

- *Recombinant regulatory light chain production*

The human cardiac RLC in pET3d vector was originally gifted by Dr. Szczesna-Cordary's lab at the University of Miami Health System. Further subcloning into pET24a expressing vector with the addition of a flag-tag at its C-terminal was done following the standard molecular biological techniques. Site directed mutagenesis was performed using the QuikChange II Site-Directed Mutagenesis Kit (Stratagene, La Jolla, CA) to substitute Serine 15 in RLC (Wildtype) with Aspartic acid (S15D). The DNA sequences of these two expressing constructs were verified by DNA

sequencing. The expression of the recombinant proteins in Escherichia coli (BL21) was done following the protocols previously developed in our lab (Chabes et al., 2003; Wang et al., 2013). The expressed recombinant proteins were extracted from bacterial cells and purified on DEAE Fast column equilibrated by 6 M Urea, 25 mM Tris at pH 8.0, 1 mM EDTA and 1 mM DTT. Proteins were eluted with a salt gradient washing in the same buffer from 0 to 0.25 M NaCl. The fractions containing the desired purified protein and their concentrations were monitored by SDS polyacrylamide gel electrophoresis and DU 800 Spectrophotometer. The super pure proteins were aliquoted and saved in -20°C freezer before use.

- *Regulatory light chain exchange*

Recombinant RLC^{WT} and RLC^{S15D} were exchanged into pc-HMM as previously described (Nayak et al., 2020). Briefly, both pc-HMM and recombinant RLC were dialyzed overnight against exchange buffer (50 mM HEPES, 500 mM NaCl, 10 mM EDTA, 10 mM DTT, pH 7.6). The molarity of pc-HMM (per head ~170kDa) and RLC wer, and then combined in exchange buffer at a 10-fold molar excess of RLC to pc-HMM and incubated at 30°C for 30 minutes. The reaction was stopped by adding 12 mM final concentration of $MgCl_2$ and placed on ice for 30 minutes. Excess RLC protein was removed by dialyzing overnight against wash buffer (5 mM NaH_2PO_4, 10 mM sodium acetate, 4 mM magnesium acetate, 2 mM DTT, pH 7.0). The exchanged pcHMM-RLC was stored at 4°C and used within 2 days.

- *Single nucleotide experimentation and analysis*

All kinetic assays were performed using a HiTech Scientific Stopped Flow system (Bradford upon Avon, UK) equipped with a Hg/Xe lamp and monochromator. Tryptophan fluorescence at 297 nm was utilized as a fluorescence resonance energy transfer (FRET) mechanism to excite mantATP, which was observed at above 400 nm at 90° to the incident light through a KV400 optical filter. This technique was utilized instead of direct 365 nm excitation of mantATP due to

the large excess of mantATP:protein (16:1) which resulted in a significant fluorescence bleaching over the collected measurement time scale. This means that all measurements only monitor mantATP bound to the protein and not the large excess mantATP free in solution. To correct for lamp variability and drift over the >3 min observation period, a beam splitter was introduced into the exciting light path and was recorded as a lamp reference channel. This dual light beam recording setup provided a reference signal of lamp stability and recorded the fluorescence signal normalized against the reference channel. Data was stored as 500 time points for each transient and each point represents the average of 48 individual reading of the photomultiplier output. This combination of conditions resulted in fluorescent signals with very low signal noise over the complete time course along with very stable baselines and minimized photobleaching. For each transient, the data was collected on a 300 s time base to allow accurate definition of the transient, followed by a further 300 s recording to allow accurate definition of the baseline signal. In all cases the base line was flat and stable over 300 s. The low noise on each transient meant that there was no advantage in averaging individual transients as is the normal practice. Instead, each transient was analyzed individually and the k_{obs} values reported as mean ± SEM of transients.

Data was analyzed using the software supplied with the equipment. This provides a least-squares best fit of the data with a range of functions including a single exponential ($Fl_t = Fl_{0.}exp^{-kobs.t}$ + baseline), as used here. In addition, a plot of the difference between the observed signal and the fitted function is provided in each plot to allow evaluation of the quality of the fitted function. In all cases the fitted line can describe > 99% of the signal change observed.

- *Statistics*

All groups were assessed for population normality. Statistical analysis of mean k_{obs} values used one-way Anova analysis.

iv. Results

We repeated the standard mantATP single nucleotide displacement assay using porcine cardiac HMM with stopped flow. Note, all concentrations refer to the concentrations after final mixing in the stopped flow observation chamber. 125 nM HMM was mixed with 2 µM mantATP and allowed to react for 1 min to achieve steady state before rapidly mixing with an excess of unlabeled ATP (125 µM) in a stopped flow fluorimeter. Figure 2A presents a typical transient observed for the reaction. Note the transient shows both the data collected over 300 seconds after mixing and data collected over the subsequent 300 seconds superimposed. Displaying this 300-600 second recording on an expanded y-scale indicated the signal change over this time to be < 1% of the change over the first 300 sec. The transient was therefore fitted to a single exponential with the best fit superimposed on the data (k_{obs} = 0.021 s^{-1}). The residual plot (experimental data subtracted from the best fit line) had random noise of < ± 0.1% of the total signal strength. The deviation from a flat line was < ±0.2% of the signal or < 1% of the observed fluorescence change (ΔFl). The fitted single exponential can therefore account for 99% of the observed fluorescens signal change. There was no evidence of a second component bigger than 1% observed in the fit. Note, Figure 1A displays a single transient as averaging of multiple transients gave no advantage to signal quality. Collecting repeated transient yields k_{obs} = 0.0200 ± 0.0004 s^{-1} (mean ± SEM, n=29). Our analysis gives high confidence that the data can be described by a single exponential with a stable end point.

Based on the extensive literature of this mantATP displacement reaction this single exponential was not expected. It is important therefore to establish the confidence with which we see a single exponential transient. We therefore undertook a series of controls shown in Figure 1B-D and Figure 2.

Generating HMM by proteolysis of myosin can result in the loss or clipping of some regulatory light chains (RLC). RLC has been described to play a fundament role in myosin head

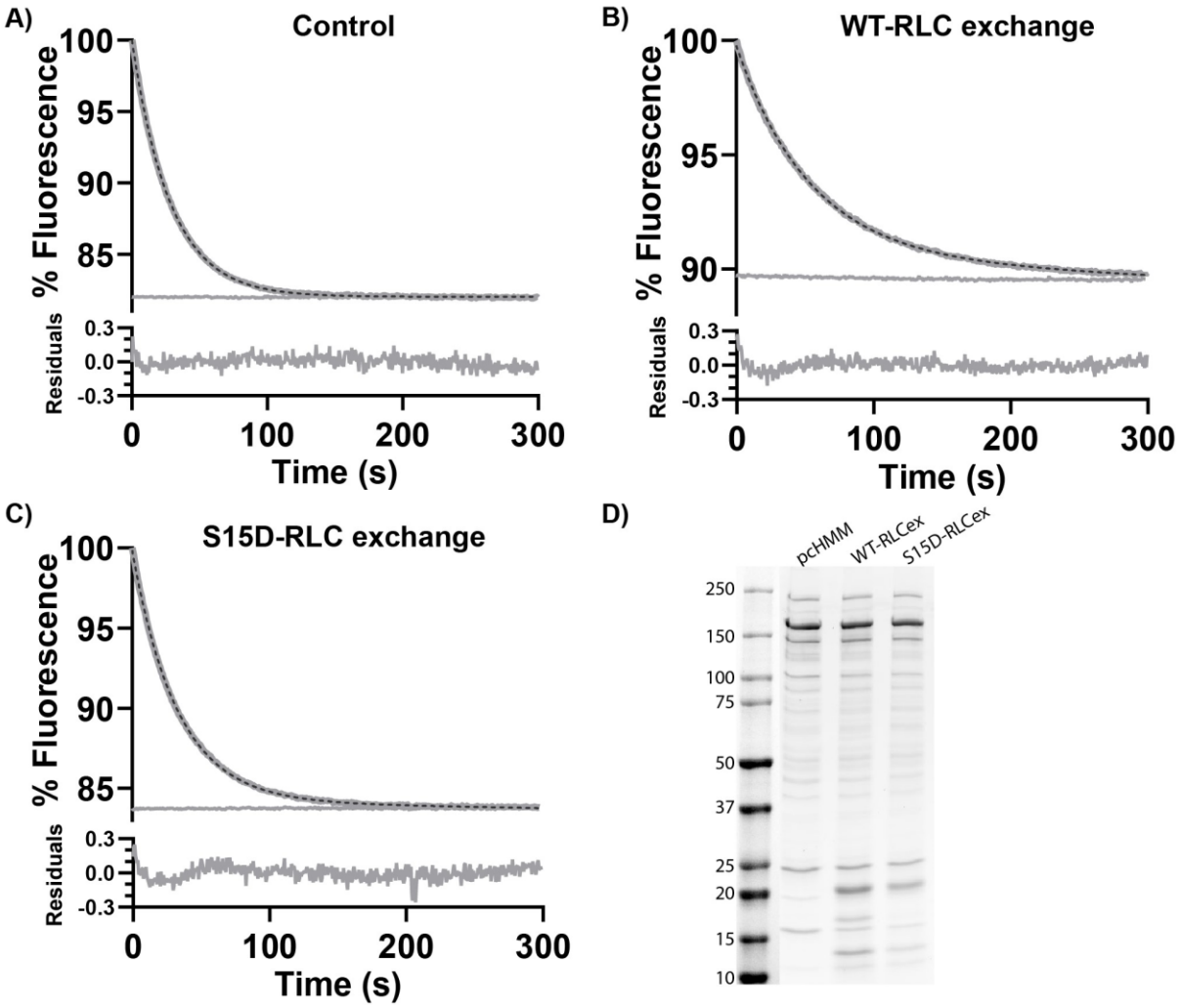

Figure 1. Fluorescence changes following displacement of mantATP from pc-HMM by an excess of ATP.

Pig cardiac HMM (125 nM) was preloaded with mantATP (2 µM), allowed to reach steady state (~ 1 min), then rapidly mixed in the stopped flow with an excess of unlabeled ATP (250 µM). Each panel is a single transient with the best fit single exponential superimposed (dashed line). Subsequent 300-600 s recording is superimposed. The residual plot is shown below the main plot on an expanded y-scale. **A)** Control conditions, k_{obs} = 0.021 s^{-1} **B)** The same experiment after exchange of RLC on HMM by WT, k_{obs} = 0.0163 s^{-1} or **C)** S15D human, k_{obs} = 0.0181 s^{-1} RLC. D) SDS-PAGE of HMM pre and post exchange of the RLC.

recruitment, as they are located at the hinge around which the IHM structure folds. By clipping or removing the RLC during HMM isolation, it is possible that either loss of the RLC or clipping of the RLC could impair the ability of the HMM to form the folded back IHM/SRX conformation. Similarly, phosphorylation of the RLC has also been reported to reduce the presence of the SRX. Protein assessment showed clipping of the RLC in our porcine HMM preparation. We therefore replaced the native RLC present in HMM with bacterial expressed RLC which is fully dephosphorylated (Fig 1B). This control corrects for both the loss of any native RLC and ensures we have no phosphorylation limiting the formation of the SRX conformation. In addition to RLC^{WT} exchanges, we also replaced the native RLC with the phospho-mimetic RLC^{S15D} (Fig 1C) which is reported to be a good mimic of phosphorylated RLC (Muthu et al., 2014). SDS-PAGE gels of the HMM with replaced RLC are shown (Fig 1D).

The results of mantATP single nucleotide displacement for both the WT and S15D exchanges (Fig 1B & 1C) indicated that the transients are still described by single exponentials with the same level of confidence as the original transient. The mean values of k_{obs} are summarized in Table 1 and for both WT and S15D k_{obs} values were decreased by 10% compared to controlled values but did not differ between WT RLC and the phospho-mimetic RLC.

Modulation of myosin head interaction by ionic strength is reported to influence the ability of HMM and myosin to form the SRX with low salt stabilizing the SRX state. We therefore repeated the assay of Fig 1 (100 mM KCL) at 20 mM KCl (Fig 2A). The decrease in ionic strength significantly increased the mean rate constant, k_{obs} = 0.0245 ± 0.0008 s^{-1}, but the decay transient remained a single exponential decay. The RLC is also known to bind calcium, and this could influence the formation of the SRX state. The transient of Fig 1A was repeated with high calcium (2 mM Ca^{2+}, ~30 µM EGTA) in solution (Fig 2A). A single exponential with a mean k_{obs} = 0.0217 ± 0.0008 s^{-1} was not significantly different from control values.

To test if the result with pc-HMM was the result of a specific issue with our HMM we tested different HMM and S1 proteins from different sources. We tried HMM from rat back muscle (longissimus and iliocostalis lumborum, rs-HMM) and porcine cardiac S1 (pc-S1). In all cases, we observe fluorescence transients that were well described by a single exponential. An example of transient data from a fast rat skeletal muscle, rs-HMM and pc-S1 are displayed in Fig 2C & D. The

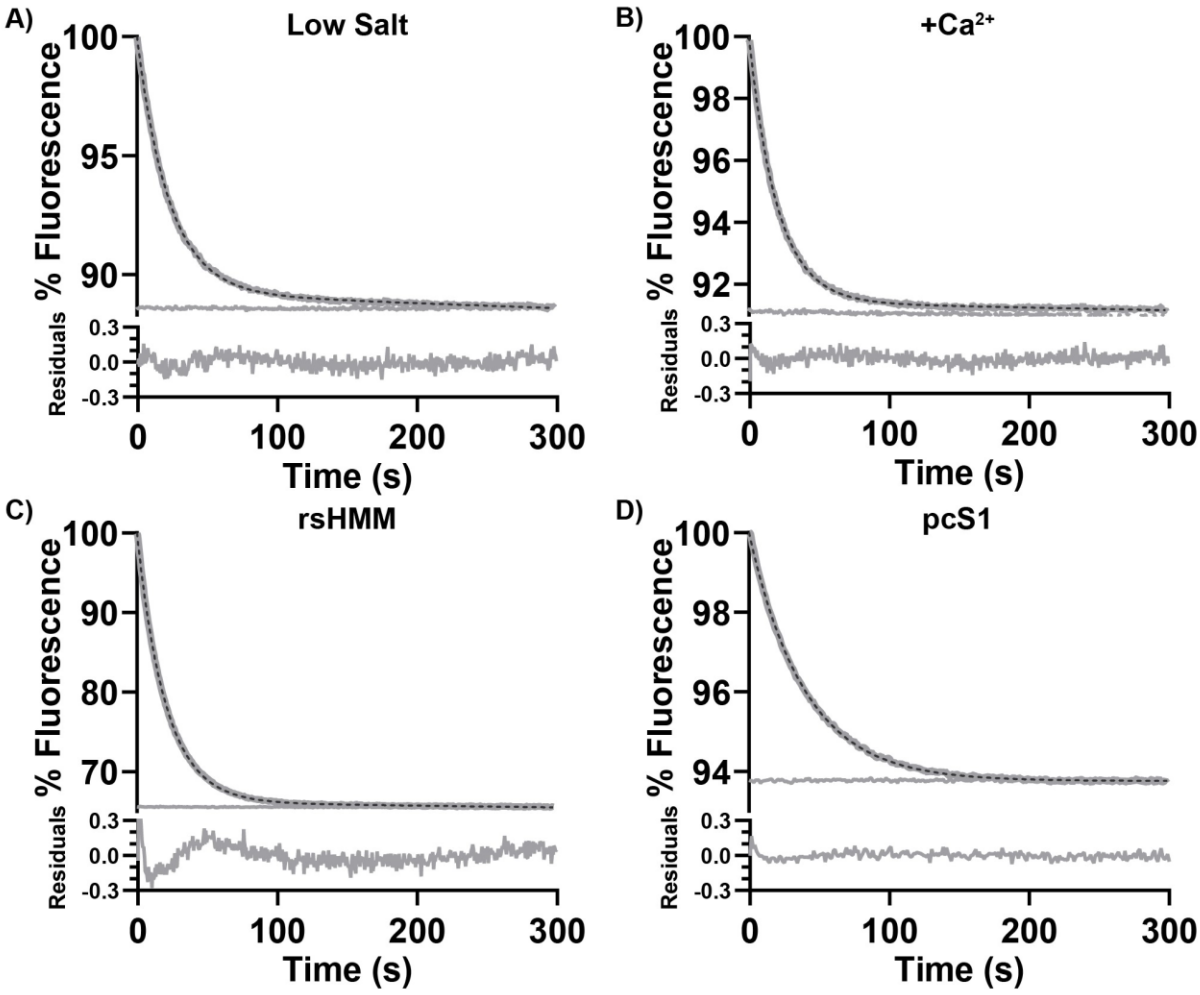

Figure 2. Fluorescence changes following mant ATP displacement from different myosin fragments. (A) pc-HMM at low ionic strength (20 mM KCL) k_{obs} = 0.0261 s^{-1}, **(B)** pC-HMM with excess 2 mM Ca^{2+} k_{obs} = 0.0270 s^{-1}, **(C)** rs-HMM k_{obs} = 0.0282 s^{-1}, **(D)** pc-S1, k_{obs} = 0.0251 s^{-1}.

quality of the data remains the same with no convincing evidence of a slow phase in the reaction. The mean values of k_{obs} are summarized in Table 1.

Mavacamten (Mava) has been widely used as an inhibitor of myosin and is currently in clinical use. Mava inhibits myosin by structurally sequestering the myosin heads along the thick filament (Robert L. Anderson et al., 2018) and by stabilizing the pre-power stroke M.ADP.Pi conformation, increasing the population of myosin in the SRX-state and removing them from the active cycling pool for contraction. In Figure 3A, we examined the effect of 0.5 μM Mava on the mantATP displacement reaction. The presence of 0.5 μM Mava inhibits the turnover of mantATP and slows k_{obs} to 0.0100 ± 0.0006 s^{-1}. This inhibited decay however remained a single exponential. For completeness, we repeated the Mava assay at 3 μM with pc-S1 and observed a single exponential decay. The k_{obs} value was reduced by a factor of ~ 5.

To confirm the K_i values, we repeated the pc-HMM and pc-S1 assays over a range of Mava concentrations from 0 – 30 μM (Fig 3C & E). In all cases, a singe exponential was produced with best fit to a k_{obs} titration curves.

To complete our set of displacement assays we utilized mantdATP to investigate the impact of a myosin activator on nucleotide turnover kinetics. Deoxy-ATP, dATP, is reported to accelerate myosin ATPase activity through alterations to the charges surrounding the nucleotide binding pocket, and displacing the myosin heads off of the thick filament backbone and closer to actin. It is possible therefore that dATP destabilizes the IHM, a suggested component of the SRX. Fig 3B illustrates that replacing mantATP with mantdATP in the assay accelerated the turnover reaction, however, the transient decay remained a single exponential. The mean value for k_{obs} increased by ~50 % for both pc-HMM (to 0.0293 ± 0.0004 s-1) and for pc-S1(to 0.0252 s^{-1}. Titrating mantdATP from 0% to 100% results in a biphasic increase in k_{obs} with a break point at ~50% mantdATP. This may indicate a different behavior of pc-HMM with mantdATP occupying

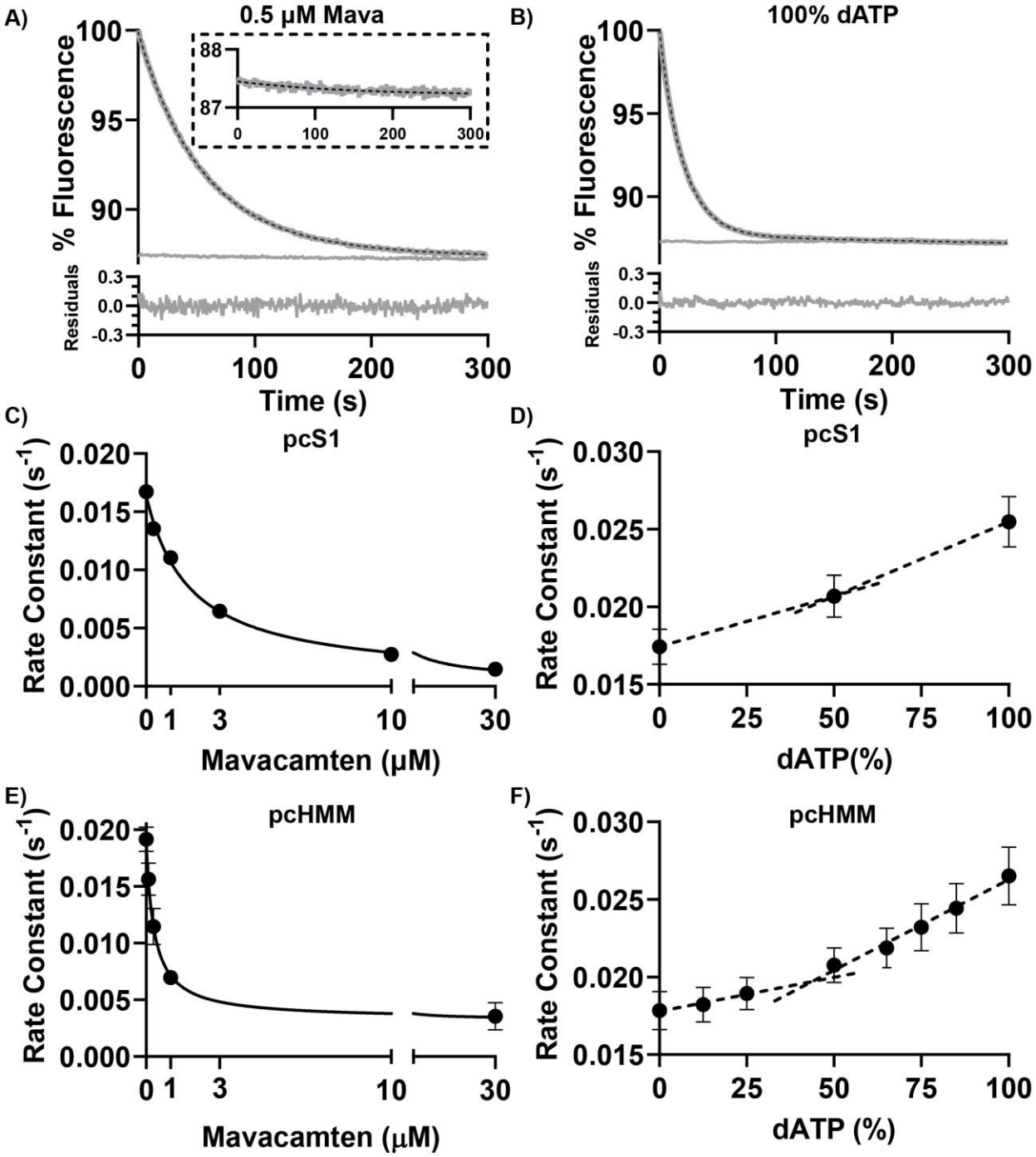

Figure 3. Fluorescence changes of pc-HMM and pc-S1 with Mavacamten or mantdATP.

A) pc-HMM and 0.5 µM Mavacamten, **B)** mantdATP. Titrations of k_{obs} for pc-S1 **(C & D)** or pc-HMM **(E & F)** with Mavacamten **(C & E)** or mantdATP **(D & F)**.

one head compared to two. Repeating the titration with mantdATP for pc-S1 again only showed a single exponential, with a similar 50% increase in k_{obs} (Fig 4D) but little evidence of deviation from a single straight line over the limited concentrations explored.

One of the limitations of much of the literature on the mantATP displacement assays is that a control steady state ATPases alongside the mantATP displacement assays is not presented. Where they are presented the two rarely agree. Furthermore, the effect of Mavacamten on the two assays have different sensitivities. To test k_{cat} in our mantATP displacement assays we performed a multi-turnover experiment where the fluorescence was monitored as HMM turned over a small excess of mantATP (Fig 4). In this case 250 nM pc-HMM was mixed with a 2-fold excess of mantATP. The fluorescence was observed to increase to a short steady-state value and then decayed back to the original signal level (Fig 4A). The addition of a small amount of actin (0.3 μM) to the reaction ensures mantADP is displaced at the end of the reaction to attain the starting fluorescence value. This low actin concentration at 100 mM KCl has an insignificant effect on the turnover rate. The length of time until the fluorescence has returned to 50% of the peak value, tau (τ), gives an estimate of the time taken to hydrolyze the mantATP by the formula $k_{cat} = [mantATP]/([HMM] * \tau)$. Adding 0.5 μM Mava to the assay increased the length of the steady-state (Fig 4B) and replacing mantATP with mantdATP shortened the steady-state (Fig 4C). This provides estimates of k_{cat}, for the control, Mava, and mantdATP of 0.0175 ± 0.0006, 0.0122 ± 0.0004, and 0.0282 ± 0.0014 s^{-1} respectively. These values are consistent with the values of k_{obs} from the single nucleotide turnover assay.

The remarkable conclusion from these assays is that we can find no evidence of a double exponential in any of the assays performed. We conclude that the single nucleotide turnover assay for purified myosin proteins does not correctly calculate the population of the SRX state. This finding does not mean that there is no IHM or SRX state, only that the assay itself is not a reliable resource for reasons discussed above.

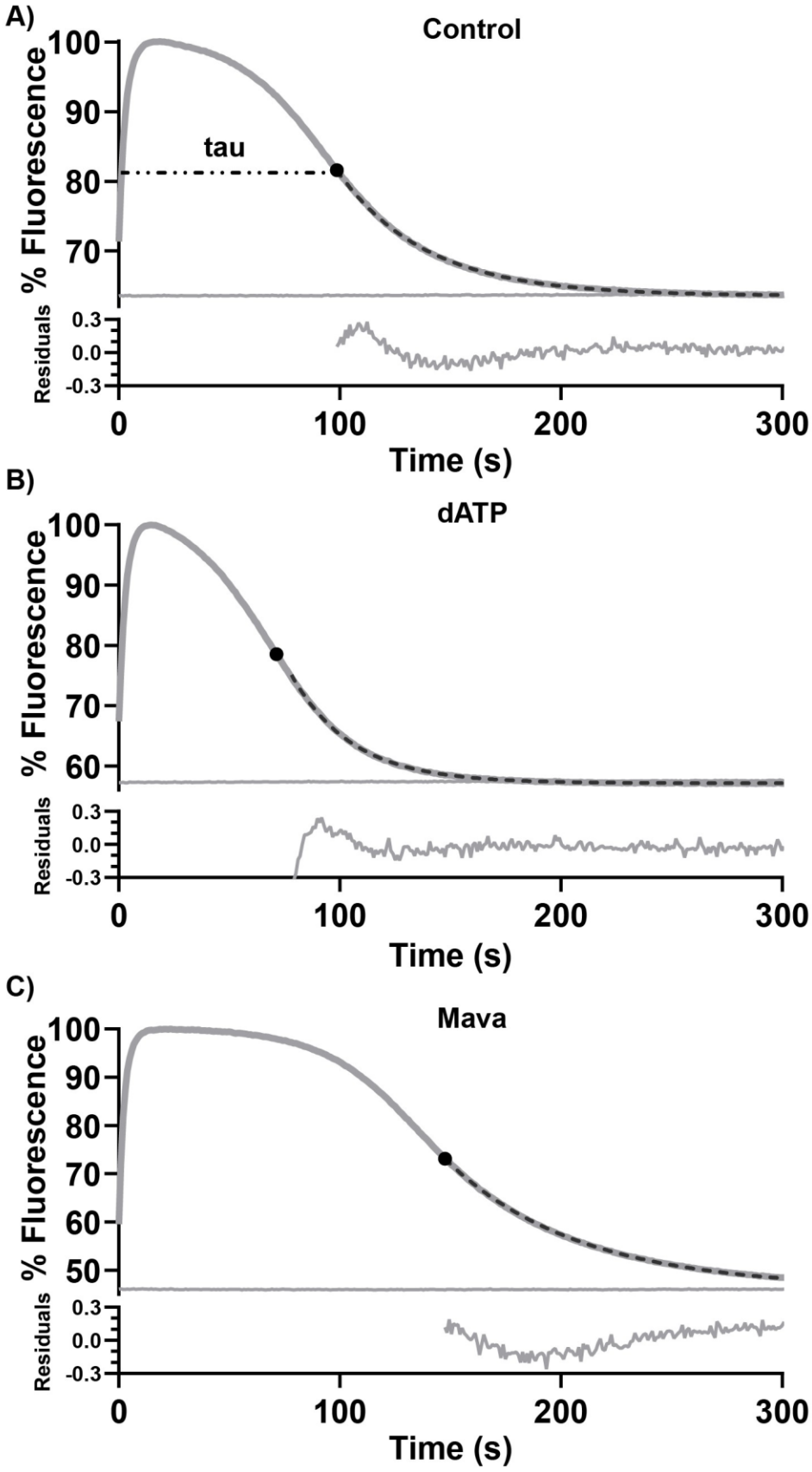
A)
Control
tau
% Fluorescence
100
90
80
70
Residuals
0.3
0.0
-0.3
0
100
200
300
Time (s)
B)
dATP
% Fluorescence
100
90
80
70
60
Residuals
0.3
0.0
-0.3
0
100
200
300
Time (s)
C)
Mava
% Fluorescence
100
90
80
70
60
50
Residuals
0.3
0.0
-0.3
0
100
200
300
Time (s)

Figure 4. Measuring the basal mantATP turnover rate (k_{cat}) using a multiple turnover assay in the stopped flow.

(A) Turnover of mantATP (0.5 μM) by pc-HMM (0.25 μM) followed using excitation at 295 nm and emission at λ> 400 nm. Tau (τ) is the time to turnover the mantATP until the fluorescence increase returns to 50% of its starting value. A single exponential (k_{obs}) is also shown fitted to the final 50% of the transient. **(B)** with mantdATP replacing mantATP. **C)** in the presence of 0.5 μM Mavacamten.

v. Discussion

We have presented a series of single nucleotide displacement assays to evaluate the turnover of mantATP by HMM. As predicted by the theory of thermodynamic equilibrium, we find no evidence of a double exponential relationship, with no secondary slow component in the reaction. All turnover measurements resulted in a clean single exponential which matches the expectations from steady state ATPase assays. We took great care to establish stable base lines and minimize fluorescence bleaching over the long timescale of the reaction. Single exponential displacement reactions were seen for single headed S1 (where no IHM is expected) and for two headed HMMs where the formation of an IHM is possible and have been reported in structural studies of isolated HMM and myosin filaments.

- *Why do we only see a single exponential? Does this mean there is no IHM or SRX in our HMM assays?*

Our results do not mean that there is no IHM or SRX for HMM in solution. They only demonstrate that this mantATP assay is not a feasible tool for evaluating the fraction of myosin in the SRX state in solution. Theoretically, if an SRX is present it should slow down the k_{obs} and not generate a second phase unless the interconversion of SRX and DRX is much slower that turnover. This is the described scenario for the calcium-regulated scallop HMM, where ADP

release is slowed from 15 s^{-1} in the presence of calcium to < 0.1 s^{-1} in its absence. Evidence of a folded back structure for scallop HMM, like the IHM in the absence of calcium, was provided by both negative stain EM and ultracentrifugation analysis.

Why then is the literature full of reports of double exponential, defining an SRX and DRX population ratio for mammalian cardiac myosin? Our studies here are limited to HMM and S1 in solution, so we cannot usefully comment on the data from myofibrils, skinned myocytes, or intact myocytes. Each experimental preparation has its own experimental complexities, and experimentation on the scale larger than isolated single proteins contain many addition protein components that can affect the IHM such as the thick filament backbone, titin, and MyBP-C. However, in our hands, the theory of thermodynamic equilibrium validates our experimental findings. Myosin heads are in either the SRX and DRX states in thermodynamic equilibrium or they are not. If they are in equilibrium, then they must be interchanging on a time scale like, or slower than the turnover of the SRX form of myosin. This is incompatible with measured rates of formation and breakdown of the SRX sate in the mantATP assay.

In the case of the solution studies, apart from the original data from the Cooke laboratory utilizing muscle fibers), too few studies present detailed controls to allow an evaluation of what the issue could be. In many cases, only the percent SRX (%) is reported. Data for this type of analysis of a bi-exponential needs careful evaluation of the quality of the fitting procedure to define two exponentials with precision. Some of the issues were previously discussed (Walklate et al., 2022b). The stability of the baseline and the extent of photobleaching over the extended time of the reaction can seriously affect the data evaluation of the slow component. Similarly, missing information over the first few seconds of the transient can distort the evaluation of the fast phase. Distortion of either the fast or slow phase then has consequences for how the best-fit evaluates the contribution of each phase. Without controls, it is difficult to assess any underlying problem in the data. In addition, it is essential to evaluate the basal turnover reaction by steady state

ATPase assays alongside mantATP displacement assay. The two should be in reasonable agreement, if they do not agree, then there is a problem somewhere in the data or the interpretation.

The data for pc-HMM in Table 1 indicate that presence of calcium has little effect on the k_{obs} of the displacement reaction. This finding suggests little effect of calcium on the steady state basal ATPase of HMM as has been extensively reported in the past. Calcium regulation of the thick filament is one mechanism suggested for controlling the fraction of active myosin heads in a muscle fibre. Perturbation with low ionic strength significantly increased the k_{obs} compared to control, even though previous studies have reported that low IS stabilizes the SRX/IHM. Our data suggest that the differences to the basal ATPase caused by these treatments of HMM are unlikely due to changes in the occupancy of a *switch-off* form of pcHMM, the IHM, or SRX. This may not be the same in a myosin thick filament.

In contrast, Mava inhibits both the S1 and HMM mantATP displacement quite strongly as originally reported. Few studies have reported the Ki of Mava for S1 or HMM basal ATPase, the relevant ATPase for stabilizing the *off state* of myosin. Here, the Ki for pc-S1 and pc-HMM are quite distinct. Mava is thought to stabilize the M.ADP.Pi by inhibiting Pi release. Alternately, Mava itself or the enhanced occupancy of the M.ADP.Pi could stabilize the *off state* of HMM (IHM or SRX). A combination of all three factors could be present. Arguing against this interpretation is the effect of Mava on S1 which has an equivalent degree of inhibition (although with a much weaker Ki) but is not thought to form the IHM or SRX to any significant degree. An explanation of the discrepancy in Ki values could come from cooperative binding of mava to HMM. The high affinity of Mava for HMM makes evaluation of any cooperativity in the binding of Mava difficult to evaluate but a structure like the IHM, where the two heads are interacting, would suggest cooperativity between the heads for any ligand stabilizing the IHM.

Some type of cooperative behavior is implied in the effect of the percent mantdATP present with mantATP, shown in Fig D & E. The effect of mantdATP on k_{obs} is clearly biphasic and is absent from the S1 data although the degree of acceleration of k_{obs} is similar. In this case, the acceleration could again be due to destabilization of M.ADP.Pi by dADP accelerating Pi release or a direct or indirect effect on the switched off IHM (Lundy et al., 2014; Ma et al., 2020; Ma et al., 2023; McCabe et al., 2020; Powers et al., 2019).

Few studies of the mantATP displacement reaction have been reported for the HMM reaction, most have used myofibrils, muscle fibers, or myocytes. The exception is the *25hep HMM*, a human β-cardiac myosin fragment expressed in mouse C2C12 cells. This was initially expressed including some of the light chains (LC) but later work co-expressed the human ELC and purified the HMM using a tag on the human ELC to ensure only HMM with human ELC was isolated. Bacterially expressed human RLC was introduced by exchange. The construct consists of the myosin motor and light chain binding domains followed by 25 heptads repeat which make up the proximal tail and corresponds roughly to HMM. The construct also contained, at the C-terminus, a leucine zipper to ensure correct assembly of the dimer, a GFP, and a peptide to facilitate surface attachment through the flexible linkers of the C-terminus (Adhikari et al Nat Comm 2019).

This construct does show a double exponential for the mantATP displacement reaction and the fraction of slow SRX phase increases with Mava and decreases with several HCM linked mutations. Similar results were reported for the human S1 construct. This leaves the question open if the differences in reported results are due to differences in experimental design or in the protein construct used. This needs parallel studies of the two proteins. Regardless, the problem of the paradoxes in the published assays of the SRX state remain. The two phases cannot be generated if the SRX and DRX states are in thermodynamic equilibrium on anything faster that a 100 s time scale, yet the equilibrium position is modified by mild treatments such as temperature

changes, ionic strength changes, and addition of Mava. Steady state assays of the basal ATPase of the HMM and the influence of these treatments on the ATPase have not been reported and are necessary to resolve the paradoxes.

The parallels between the results presented here and the calcium regulated scallop myosin have been pointed above. Scallop HMM is in rapid equilibrium between *on and off forms* with the equilibrium position modulated by calcium and ionic strength. There is no calcium regulation at 0.5 M KCl and the HMM is fully activated. A clear difference between the scallop and cardiac system is that for scallops, both Pi and ADP release are calcium regulated and both M.ADP and M.ADP.Pi can form the *switched off* form of HMM. This off-state has similarities with the IHM as shown by negative stain EM and sedimentation studies. There is no evidence that pc-HMM can form an IHM in the presence of ADP alone and Mava does not affect ADP release from pc-HMM.

The implications for our results and interpretations for the clinical use of Mava are relatively benign. Mavacamten remains an inhibitor of actomyosin ATPase as reported in the original work (R. Anderson et al., 2018). Whether the mechanism of inhibition is via stabilization of the pre-power stroke conformation (M.ADP.Pi) and inhibition of Pi release and/or the sequestration of myosin heads along the thick filament makes no difference to its use. Separating the two potential effects of Mava is difficult without knowing where and how the compound binds to the protein. Any factor which stabilizes the M.ADP.Pi conformation is also likely to stabilize the IHM if both heads are trapped in the M.ADP.Pi form.

Typically, in the steady state of S1, 80-90% of the myosin heads are in the M.ADP.Pi. If the two heads of HMM or myosin are independent in their ATPase activity, then statistically 64-80% of any myosin will have both heads in the M.ADP.Pi form with potential to form the IHM/SRX. Any treatment that changes the population of M.ADP.Pi will change the probability of forming the IHM/SRX. Low temperature is known to reduce the fraction of myosin as M.ADP.Pi increasing

both M.ATP and M.ADP. If M.ADP.Pi were to be reduced to 50% of the total, then the probability of having both heads simultaneously as M.ADP.Pi reduces to 25%. This is thought to underlie the loss of the ordered thick filament at low temperature. Of significance here is the much tighter Ki for HMM compared to S1 (Fig 4) which implies an additional effect of Mava on HMM compared to S1. Both proteins, however, reach a similar inhibition of the displacement reaction at saturating concentrations of the compound. This is consistent with some form of positive cooperativity between the two heads in each binding a Mava such as for example a higher affinity for the IHM.

vi. Acknowledgments

The authors want to acknowledge Dr Szczesna-Cordary and their laboratory for providing the recombinant RLC.

V. Chapter 3: Danicamtiv increases myosin recruitment and alters cross bridge cycling in cardiac muscle

This chapter represents an accepted co-first author manuscript at Circulation Research

Kristina B. Kooiker†, **Saffie Mohran**†, Kyrah L. Turner, Weikang Ma, Amy Martinson, Galina Flint, Lin Qi, Chengqian Gao, Yahan Zheng, Timothy S McMillen, Christian Mandrycky, Max Mahoney-Schaefer, Jeremy C. Freeman, Elijah Gabriela Costales Arenas, An-Yu Tu, Thomas C. Irving, Michael A. Geeves, Bertrand C.W. Tanner, Michael Regnier, Jennifer Davis, Farid Moussavi-Harami

† Authors contributed equally

Short title: Mechanism and use of myosin activator Danicamtiv

Citation from Circulation Research:

Kooiker, K.B., Mohran, S., Turner, K.L., Ma, W., Martinson, A., Flint, G., Qi, L., Gao, C., Zheng, Y., Mcmillen, T.S., Mandrycky, C., Mahoney-Schaefer, M., Freeman, J.C., Costales Arenas, E.G., Tu, A.-Y., Irving, T.C., Geeves, M.A., Tanner, B.C.W., Regnier, M., Davis, J., Moussavi-Harami, F., 2023. Danicamtiv Increases Myosin Recruitment and Alters Cross-Bridge Cycling in Cardiac Muscle. Circulation Research 133, 430–443.

https://doi.org/10.1161/circresaha.123.322629

i. Abstract

Background: Modulating myosin function is a novel therapeutic approach in patients with cardiomyopathy. Danicamtiv is a novel myosin activator with promising preclinical data that is currently in clinical trials. While it is known that Danicamtiv increases force and cardiomyocyte contractility without affecting calcium levels, detailed mechanistic studies regarding its mode of action are lacking.

Methods: Permeabilized porcine cardiac tissue and myofibrils were used for X-ray diffraction and mechanical measurements. A mouse model of genetic dilated cardiomyopathy was used to evaluate the ability of Danicamtiv to correct the contractile deficient.

Results: Danicamtiv increased force and calcium sensitivity via increasing the number of myosin heads in the “on” state and slowing cross bridge turnover. Our detailed analysis showed that inhibition of ADP release results in decreased cross bridge turnover with cross bridges staying attached longer and prolonging myofibril relaxation. Danicamtiv corrected decreased calcium sensitivity in demembranated tissue, abnormal twitch magnitude and kinetics in intact cardiac tissue, and reduced ejection fraction in the whole organ.

Conclusions: As demonstrated by the detailed studies of Danicamtiv, increasing myosin recruitment and/or altering cross bridge cycling are two mechanisms to increase force and calcium sensitivity in cardiac muscle. Myosin activators such as Danicamtiv can treat the causative hypo-contractile phenotype in genetic DCM.

ii. Introduction

The prevalence of heart failure (HF) continues to rise and despite new and improved treatments, there is still significant morbidity and cost (Tsao et al., 2023). More than half of the HF patients can be categorized by depressed systolic function or contractility (Shah et al., 2017). Traditional inotropic agents improve cardiomyocyte contractility via increased intracellular cyclic adenosine monophosphate (cAMP) and calcium levels but do not improve patient survival (Maack et al., 2019; Teerlink et al., 2009). Directly targeting sarcomeric proteins can overcome adverse effects of traditional inotropes such as arrythmias, increased myocardial oxygen demand and activation of cell death pathways (Maack et al., 2019). Small molecules targeting myosin and modulating its activity have been developed over the last decade for treatment of HF. The strategy for identifying these compounds has been to identify molecules that selectively bind to cardiac myosin and increase or inhibit the myosin ATPase activity.

Omecamtiv Mecarbil (OM) is a first in-class myosin activator that was originally thought to work via increased phosphate release and priming myosin for binding to actin (Malik et al., 2011; Nagy et al., 2015). More detailed biophysical measurements showed that OM inhibits the myosin working stroke and prolongs the detachment of a small population of non-force generating myosin heads (Rohde et al., 2017; Woody et al., 2018). The OM-bound myosin heads activate the thin filament and recruit more myosin heads with the net effect of having more myosin heads that are available for force generation. OM recently completed a phase III clinical trial in HF and was found to result in a modest decrease in HF events or death from cardiovascular causes (Teerlink, Diaz, Felker, McMurray, Metra, Solomon, Adams, et al., 2021; Teerlink, Diaz, et al., 2021b). The successes and challenges of OM show the importance of better understanding of the molecular mechanisms of new sarcomere modulators.

Danicamtiv (Dani) or MYK-491 is a promising novel myosin activator that increases myofibril ATPase activity and calcium sensitivity (Voors et al., 2020). *In vivo* studies demonstrated

improved atrial and ventricular function in a canine HF model as well as patients with HF with reduced ejection fraction (Ráduly et al., 2022; Voors et al., 2020). There is an ongoing clinical trial enrolling patients with genetic dilated cardiomyopathy (DCM) with sarcomeric variants for treatment with Dani. We and others have shown that a reduction in the force and/or kinetics of the cardiac twitch, the tension developed as a function of time, is predictive of diagnosis and severity of DCM in rodent myocytes and humans (Davis et al., 2016; Hinson et al., 2015; Powers et al., 2020). It is logical, therefore, that DCM patients may benefit from treatment with myosin activators.

A recent study in a human engineered heart tissue platform showed that administration of Dani resulted in a larger increase in systolic contraction at a smaller lusitropic cost compared to OM (Shen et al., 2021). While this suggests possible differences in mechanisms, there is limited information available regarding Dani's mechanisms of action other than that Dani increases the number of myosin heads available for force production without altering passive stiffness (Bell et al., 2020).

Here, we present the first detailed mechanistic study of how Dani affects the cross-bridge cycle, cardiac muscle contractile kinetics and myosin structure. We show that Dani increased calcium sensitivity and elevated force mostly at low calcium levels. Using X-ray diffraction, we demonstrate that treatment with Dani under resting conditions repositioned myosin heads closer to the thin filament. In myofibrils under load, Dani slowed the myosin cross bridge cycle and prolonged relaxation kinetics by inhibiting the rate of ADP product release. Lastly, we demonstrate the ability of Dani to recover hypo-contractility at the tissue and organ levels in a rodent DCM model.

iii. Materials and Methods

The data that support the findings of this study are available from the corresponding author upon reasonable request.

- *Animal use and ethics*

All experiments followed protocols approved by both the University of Washington and the Illinois Institute of Technology Institutional Animal Care and Use Committees according to the "Guide for the Care and Use of Laboratory Animals" (National Research Council, 2011). Farm pig hearts were obtained immediately after the animal was euthanized and rinsed in cold oxygenated Tyrode's buffer.

- *Dilated cardiomyopathy mouse model*

We used a previously published rodent genetic DCM model. The I61Q cardiac troponin C (cTnC) is an engineered cTnC variant that desensitizes the myofilament to calcium via altering cTnC calcium binding.(Kreutziger et al., 2011; Wang et al., 2013) Transgenic mice show progressive ventricular dilation and reduced contractility as they age (Davis et al., 2016). Experimental mice were between 3-5 months of age.

- *In vivo mouse echocardiography*

Transthoracic echocardiography was performed using Vevo 3100 high-frequency, high-resolution imaging system (VisualSonics) equipped with MS400 MicroScan Transducer. After an initial m-mode measurement, a 27G butterfly needles was inserted into the tail vein and total 125 µL of N,N-dimethylacetamide (DMA): polyethylene glycol 400 (PEG-400): 30% 2-hydroxypropyl--cyclodextrin (2-HP-CD) (5:25:70) containing 2 mg/kg of Dani or DMSO (vehicle) was delivered. This was followed by a 500 µL of normal saline and removal of the catheter. The mouse continued under sedation and a repeat measurement was performed 10 minutes after the injection.

- *Demembranated tissue mechanics*

Tissue preparation and solutions are described in supplemental methods.

- *Isometric force and rate of tension redevelopment:*

Permeabilized trabeculae (mouse) or thin strips (pig) were dissected and mounted between a force transducer (Aurora Scientific, model 400A) and a motor (Aurora Scientific, model 315C) using aluminum T-clips (Aurora Scientific).(Powers et al., 2020) Sarcomere length (SL) was set to ~2.3 μm for the experiments. Experiments were conducted in physiological solution (pH 7.0) at 15°C (mouse) or 21°C (pig) containing a range of pCa (= $-\log_{10}[Ca^{2+}]$) values from 9.0 to 4.0 with and without 1μM Dani (MedChemExpress). Tissue was allowed to reach stead-state force (F) at each pCa. F-pCa curves were collected and analyzed with custom code using LabView software and fit to the Hill equation. The rate of tension redevelopment (k_{tr}) and high frequency stiffness (HFS) were measured at each pCa (details in the supplement).

- *Quick stretch analysis:*

Permeabilized porcine myocardial strips (~180x700 μm) were mounted between a piezoelectric motor (P841.40, Physik Instrumente, Auburn, MA) and a strain gauge (AE801, Kronex, Walnut Creek, CA) using aluminum T-clips. They were lowered into a 30 μL droplet of relaxing solution (pCa 8.0) maintained at 28°C and set at 2.3 μm SL. Stress (force per cross-sectional area) was recorded following a step-length change of 0.5% muscle length to assess cross-bridge kinetics as a function of [MgATP] as previously described and repeated with varying [MgATP].(Tanner et al., 2015)

- *Myofibril mechanics*

Myofibril activation and relaxation measurements were performed on a custom set up as previously described (Moussavi-Harami et al., 2015; Racca et al., 2016). Briefly, myofibrils were mounted between two glass needles; one which acted as a force transducer and the other as an inflexible motor arm. A dual diode system measures force based on needle deflection, with force transducer needle stiffness measured at 7.98 mm/μN. A double-barreled glass pipette delivered

relaxing (pCa = 9.0) and activating (pCa = 5.8 or 4.0) solutions to the mounted myofibril. Activation and relaxation data were collected at 21 °C and fitted as previously described (Moussavi-Harami et al., 2015).

- *Intact twitch assay*

Unbranched, intact trabeculae or papillary muscles were dissected from the right ventricular wall and mounted between a force transducer (Cambridge Technology, Inc., model 400A) and a rigid post. The tissue was submerged in a chamber continuously perfused with oxygenated modified Krebs buffer (1.8 mM $CaCl_2$) at 33° C. Continuous twitch tension traces were recorded using LabView software at a sampling rate of 1 kHz and analyzed with custom code in MATLAB software (version 2021a, The MathWorks) (Powers et al., 2020).

- *In vitro motility assay*

Myosin and heavy meromyosin (HMM) were purified from pig left ventricular samples as previously described (Moussavi-Harami et al., 2015). *In vitro* motility assays were performed at 30 °C using unregulated Rhodamine Phalloidin labeled F-actin in the presence of 2 mM ATP and either DMSO or 0.5 μM Dani (Moussavi-Harami et al., 2015; Racca et al., 2016). In a subset of experiments, the nucleotide composition was changed to 1 mM ATP and 1 mM ADP. Custom-built software analyzed images of the moving filaments as in our previous publications (Moussavi-Harami et al., 2015; Racca et al., 2016).

- *X-ray diffraction*

Wild type Yucatan mini-pig hearts were provided by Exemplar Genetics LLC. Permeabilized tissue preparation and beamline specifications are described in supplemental methods. X-ray diffraction experiments were performed at the BioCAT beamline 18ID at the Advanced Photon Source, Argonne National Laboratory (Fischetti et al., 2004). Skinned muscle preparations were

mounted in a custom rig allowing for simultaneous X-ray diffraction and force measurements as monitored by an ASI 610A data acquisition and control system (Aurora Scientific). The muscle was incubated in a customized chamber with the solution temperature between 28°C to 30°C. The SL of the muscles was set to 2.3 µm by monitoring the helium-neon laser (633 nm) diffraction pattern on a screen. X-ray fiber diffraction patterns were collected in pCa 8 solution in the absence or presence of 50 µM of Dani. Analysis of x-ray diffraction images were done as described previously (Ma, Gong, Kiss, et al., 2018; Weikang Ma et al., 2021) and provided in the supplemental methods (Ma, Gong, Kiss, et al., 2018; Weikang Ma et al., 2021).

- *Statistical Analysis*

We used GraphPad Prism 9 for data presentation and statistical analysis. The data is presented as mean ± standard error of the mean. We used Shapiro-Wilk test for normality. For data not normally distributed, we used Kruskal-Wallis with Dunn's multiple comparison's test or Wilcoxon matched-pairs signed rank test. For porcine demembranated tissue mechanics, we used a mixed-effect model with Šídák's multiple comparisons test for pCa curves and paired two-tailed t-test for the remaining measures. For myofibrils, we used Welch's unpaired two-tailed t-test (pCa 4.0), or two-way ANOVA followed by Tukey's multiple comparisons test (pCa 5.8 ± ADP). For X-ray diffraction, we used paired two-tailed t-tests. For *in vitro* motility and murine demembranated tissue mechanics, we used two-way ANOVA with Šídák's multiple comparisons. For quick step analysis we used two-way ANOVA with Šídák's multiple comparison for k_{rel} and one-way ANOVA with Tukey's multiple comparisons for the remaining measures. For sinusoidal length-perturbation assays, we used multiple unpaired t-tests. For murine intact mechanics, we used mixed-effect analysis with Dunnett's multiple comparisons.

iv. Results

- *Danicamtiv increased submaximal force and calcium sensitivity while prolonging myofibril relaxation.*

Permeabilized porcine ventricular muscle preparations showed a left-ward shift in the force vs. calcium (pCa) relationship in the presence of 1 μm Dani (Figure 1A). This was quantified by an increase in pCa_{50} (Figure 1B; 5.72±0.02 vs. 5.91±0.05) indicating an increase in the sensitivity of the myofilament to calcium. While there was a slight increase in maximally activated force (Figure 1C), there was a larger increase in force at submaximal calcium levels (Figure 1A). This leads to a reduction in the Hill coefficient (Figure 1D; 3.96±0.31 vs. 2.27±0.29), suggesting an effect of Dani on myofilament cooperativity or recruitment. Force redevelopment rate constants(k_{tr}) were significantly slower at each level of force suggesting that Dani reduced cross bridge cycling kinetics. Incubation in Dani resulted in more than a 50% decrease in maximal k_{tr} (Figure 1E; 1.91±0.14 vs. 0.83±0.08). High-frequency small amplitude oscillation measurements of steady state stiffness showed that Dani increased stiffness to the greatest degree at lower calcium levels. The increased stiffness is proportional to the increase in force, suggesting that the increased stiffness is due to more myosin heads producing force rather than an increase in force per myosin head.

Isolation of sub-cellular myofibrils allow for measurements of force and kinetics of both activation and relaxation (Moussavi-Harami et al., 2015; Racca et al., 2016). Figure 1F shows representative normalized force traces of porcine myofibrils transitioning between maximally activated (high Ca^{2+}) and relaxed (low Ca^{2+}) conditions by rapid solution switching via a double-barreled pipette with and without Dani. Force is developed exponentially with a rate constant (k_{ACT}) that depends on thin filament activation, myosin recruitment, and myosin cross-bridge cycling The rapid switch back to low calcium solution results in a biphasic relaxation relationship with an initial linear phase followed by rapid exponential phase back to baseline.

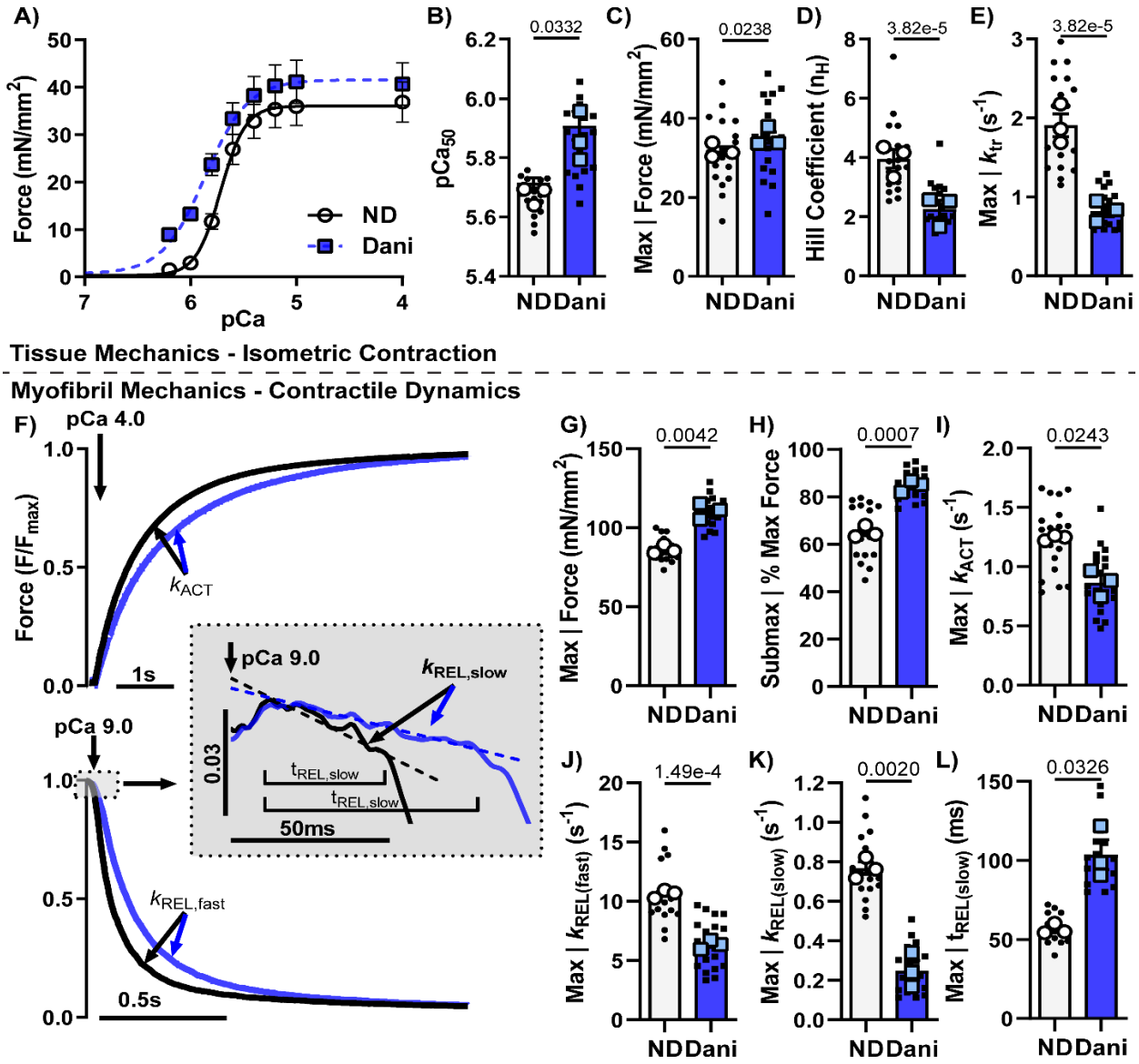

Figure 1. Mechanics in permeabilized porcine cardiac tissue and myofibrils treated with 1 µM Danicamtiv. **(A)** Force-pCa curves from isolated porcine ventricle tissue strips before and after incubation in 1 µM Dani. Summary data for **(B)** pCa_{50}, **(C)** max force generation, **(D)** Hill coefficient and **(E)** max k_{TR}. **(F)** Myofibril mechanics traces at maximum calcium (pCa=4.0) showing activation (top) and relaxation (bottom). Summary myofibril data for **(G)** max force, **(H)** sub-max force, rate constants for **(I)** activation, **(J)** fast phase of relaxation and **(K)** slow phase of relaxation, along with **(L)** duration of the slow phase of relaxation. Data is from 19 paired demembranated tissue preparations (small symbols) and 18 DMSO or 21 Dani treated myofibrils (small symbols) from 3 biological replicates (large symbols). P-values vs. ND.

The rate constant during the linear slow phase of relaxation ($k_{REL(slow)}$) reflects the rate of cross bridge detachment, which is independent of the Ca^{2+} dissociation from troponin C. The duration of the slow phase ($t_{REL(slow)}$) reflects the time it takes for the thin filament to deactivate and has been shown to be influenced by the properties of the thin filament proteins and the level of calcium (Kreutziger et al., 2011; Kreutziger et al., 2008). The subsequent fast exponential phase of relaxation ($k_{REL(fast)}$) reflects inter-sarcomere dynamics and involves both active and passive elements that are influenced by multiple factors.

As in the demembranated tissue preparations, Dani increased myofibril force at maximal (pCa=4) and submaximal calcium (pCa=5.8). The ratio of submaximal to maximal activation was also significantly increased with Dani. (Figure 1G and H). Treatment with Dani resulted in a slight decrease in k_{ACT} (Figure 1I). Relaxation kinetics analysis (Figure 1J) revealed that Dani decreased the fast rate of myofibril relaxation ($k_{REL(fast)}$; 10.64±0.20 vs. 6.34±0.22 s^{-1}), which is consistent with the slowed cellular and organ level kinetics in pre-clinical models (Ráduly et al., 2022). Our analysis also revealed that the initial linear slope ($k_{REL(slow)}$; 0.77±0.03 vs. 0.25±0.05 s^{-1}) of myofibril relaxation decreased while the thin filament deactivation duration ($t_{REL(slow)}$; 56.5±1.9 vs. 103.7±9.4 ms) increased (Figure 1K and L). These results showing prolonged relaxation kinetics suggest that Dani impacts cross bridge turnover kinetics by inhibiting product release, either inorganic phosphate (P_i) or ADP. Previously reported mechanisms of the myosin activator OM showed that slower cross bridge turnover can result in increased force generation and prolonged myosin head activation, requiring more time for the thin filament to transition from an active to an inactive state (S. J. Lehman et al., 2022; Woody et al., 2018). The rate of cross bridge turnover has been previously identified as a critical regulator for transitioning the thin filament from an active to an inactive state (Biesiadecki et al., 2014; Davis et al., 2007).

While it is known that Dani increases myofibril ATPase rate (Voors et al., 2020), a detailed understanding of the exact mechanisms is lacking. Together, our tissue mechanics and myofibril measurements suggest that Dani impacts cardiac function through increased myosin head

recruitment and altered cross bridge cycling kinetics (Figure 2). We will investigate this further through the following reductionist assays.

- *Danicamtiv altered resting myosin thick filament structure and both passive and active elastic and viscous moduli.*

Previous studies have shown that myosin modulators can affect myosin structure (Weikang Ma et al., 2021; Powers et al., 2019). We used small-angle-x-ray diffraction patterns from permeabilized porcine myocardium to study the structural changes induced by Dani under relaxed conditions (pCa8, Figure 3A). The lattice spacing ($d_{1,0}$; Fig 3B, top), directly proportional to inter-filament spacing (Ma & Irving, 2022a) increased after Dani treatment (Fig 3C). The increase of $d_{1,0}$ could be a result of increased electrostatic repulsion between the myofilaments when myosin heads move away from the thick filament backbone towards actin filaments. The equatorial intensity ratio ($I_{1,1}/I_{1,0}$) reflects the proximity of myosin heads to the thin filament (Figure 3B, bottom) (Weikang Ma et al., 2021; Ma & Irving, 2022a; Powers et al., 2019). As seen in Figure 3D, Dani significantly increased $I_{1,1}/I_{1,0}$ under relaxed conditions suggesting that myosin heads moved away from the thick filament backbone and closer to the thin filament.

The meridional reflections arise from axially repeating structures in the myofilaments (Figure 3A) (Ma & Irving, 2022a). The distance of these reflections to the beam center are inversely related to the spacing of the axial periodicities along the myofilaments. When cardiac muscle was exposed to Dani under relaxing conditions, the intensity of the first-order myosin-based layer line (I_{MLL1}; Figure 3E) and the third-order myosin-based meridional reflection (I_{M3}; Figure 3F), both of which correlate with the ordering of myosin heads on the thick filament backbone, decreased by 27% and 35%, respectively. The decrease of I_{M3} and I_{MLL1} reflects a reduction of the number of ordered myosin heads. The intensity of the sixth-order myosin-based meridional reflection (M6)

arises primarily from structures within the thick filament backbone (Ma & Irving, 2022a). The spacing of the M6 reflection (S_{M6}) increased by 0.2% with Dani.

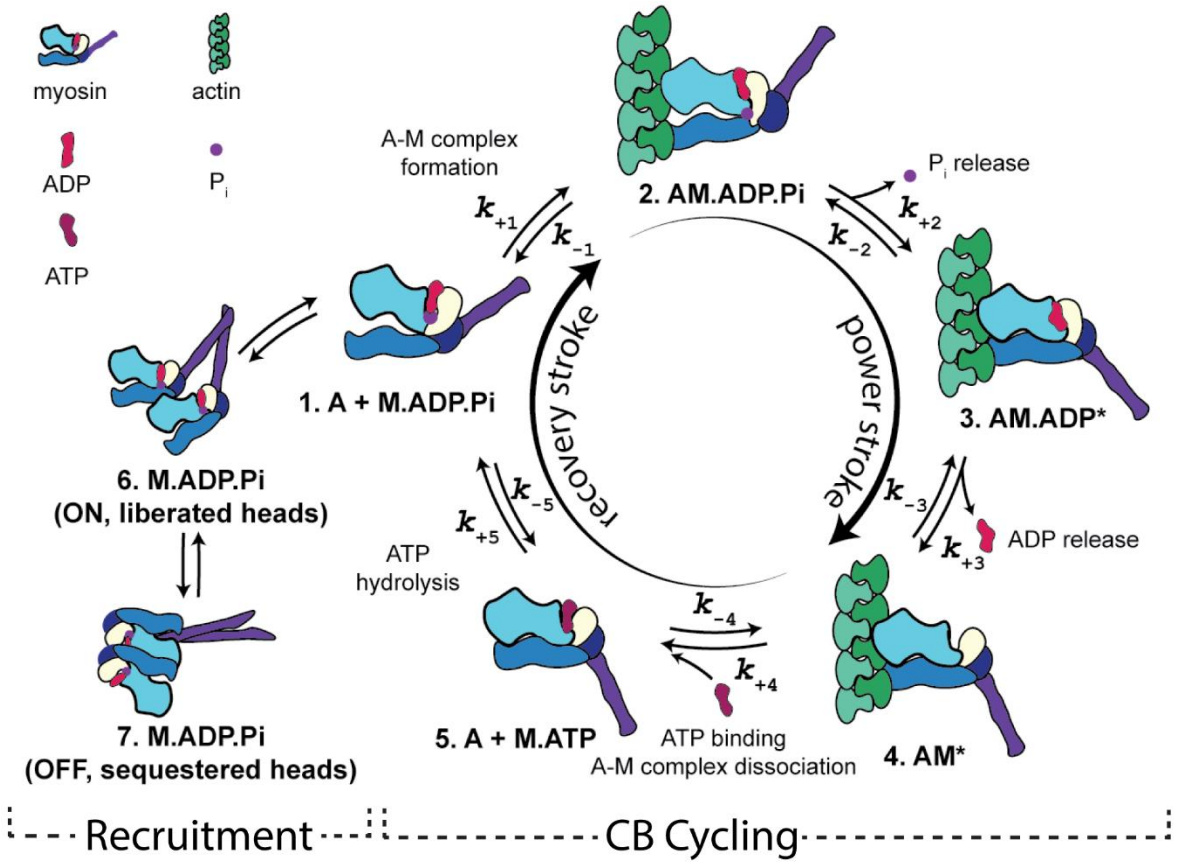

Figure 2. Scheme illustrating a five-step cross-bridge model of contraction. Figure art by Matthew Childers, University of Washington, 2023, licensed under a Creative Commons Attribution-Non-Commercial 4.0 International License.

Both the loss of the helical ordering of the myosin heads and the increase in thick filament backbone periodicity are suggestive of a transition in myosin structure and its position on the thick filament from the OFF to ON state (Linari et al., 2015). It is well recognized that resting thick filaments can be characterized by different structural and biochemical states that can be affected by both disease and small molecules (R. L. Anderson et al., 2018a; Craig & Padrón, 2022; Weikang Ma et al., 2021). Here, the increase in number of ON state thick filaments in the presence

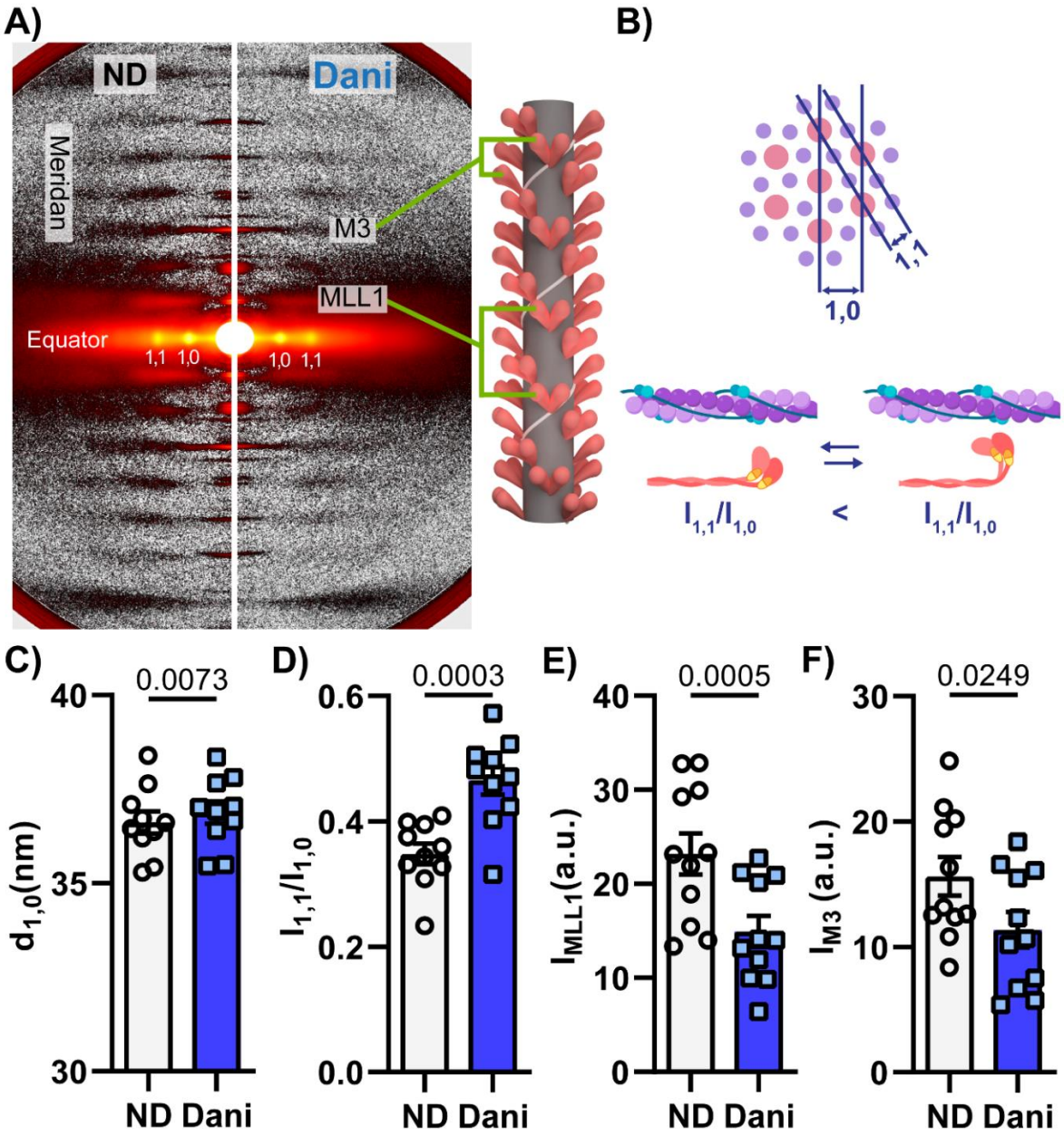

Figure 3. 50 μM Danicamtiv partially activated the thick filament in resting cardiac muscle (pCa=8.0). A) Sample X-ray diffraction patterns of demembranated porcine cardiac tissue exposed to X-ray beams while bathed in low calcium solution (pCa=8.0) containing DMSO (left) or Dani (right). B) Schematics defining how actin and myosin relationships relate to equatorial measurements. (C) Summary data for lattice spacing ($d_{1,0}$), (D) intensity ratio of the primary equatorial reflections ($I_{1,1}/I_{1,0}$), intensity of (E) the first-order myosin-based layer line (I_{MLL1}), and (F) the third-order myosin-based meridional reflection (I_{M3}). Data is from 10 paired tissue preparations. The illustrations created with BioRender.com. a.u., arbitrary units.

of Dani contributes to increased force generation via more myosin motors available for contraction (Powers et al., 2019).

Our x-ray diffraction findings were supported by performing sinusoidal length-perturbation analysis to porcine cardiac tissue with and without Dani under resting and activating conditions. The resultant elastic and viscous moduli responses provide insight into the number of bound cross bridges and characteristics such as kinetics of force generating cross bridges, respectively. As seen in Figure S3, under relaxed conditions (pCa 8.0, 5 mM [MgATP]), elastic moduli were not significantly changed by Dani. There was a significant increase in the viscous moduli at a sub-set of oscillatory frequencies for the Dani-treated strips. Under maximally activated conditions (pCa 4.8, 5 mM [MgATP]) there was an increase in visco-elastic myocardial stiffness for the Dani-treated strips vs. the untreated. Both elastic and viscous moduli values were greater in the presence of Dani across a wide range of frequencies, suggesting greater cross bridge binding in the presence of Dani. The observed leftward-shift towards lower frequencies for the elastic and viscous moduli responses also suggests Dani slowed cross bridge cycling, consistent with the slowed k_{tr} (Figure 1E).

- *Prolonged myofibril relaxation induced by Dani was due to altered ADP release rate.*

Using a combination of reductionistic approaches, we investigated whether Dani affects the product release rates of Pi and ADP during cross bridge cycling. Either of these mechanisms could explain the decreased cross bridge turnover time suggested by the decreased myofibril relaxation kinetics.

It is well accepted that increasing Pi results in decreasing force (Simnett et al., 1998; van Der Velden et al., 2001). As seen in Figure S4, a linear dependence of relative force on Log [P_i] was found in demembranated porcine cardiac tissue. The difference between the slopes was not significant between the Dani and no drug group. Hence, the relation between force and [P_i] was

unchanged with Dani. These results are different than what is reported for OM, where 1μM OM counteracts the inhibitory effects of P_i under similar conditions (Governali et al., 2020).

To test the hypothesis that ADP release is affected by Dani, we quantified myosin cross bridge activity in the presence of elevated ADP conditions. Initial experiments utilized the *in vitro* motility (IVM) assay, which directly measures cross bridge activity (Figure 4A). Previous studies have shown that when ADP levels are elevated, filament velocity is decreased because ADP release is inhibited, promoting the strongly bound actin-myosin state (Godt & Nosek, 1989; Siemankowski et al., 1985). As seen in Figure 4B, Dani also resulted in a substantial (~55%) decrease in filament velocity (2.65±0.17 vs. 1.13± 0.12 μm/s). There was no further decrease in velocity with nucleotide mixtures containing 50% ATP and 50% ADP in the presence of Dani (1.01± 0.05 μm/s), suggesting no additive effect. These results support the hypothesis that Dani slows cross bridge cycling rate through slowed ADP release.

Next, we performed measurements in myofibrils at submaximal calcium (pCa=5.8). Under isometric conditions, ADP release is the rate-limiting step in the cross-bridge cycle and cardiac muscle relaxation kinetics. Furthermore, by increasing ADP levels, there is an increase in maximal force and calcium sensitivity (Godt & Nosek, 1989; Siemankowski et al., 1985; Simnett et al., 1998). To answer the specific question of whether Dani directly affects ADP release from myosin, we made our myofibril measurements with Dani in the presence of increased ADP levels. As expected, ADP (Figure 4C-F, S6) increased force (56.6±3.2 vs. 72.6±2.4 mN/mm^2) and slowed myofibril relaxation rates ($k_{REL(slow)}$: 1.340±0.101 vs. 0.286±0.001 s^{-1}; $k_{REL(fast)}$: 12.81±1.05 vs. 4.34±0.32), while prolonging the duration of the slow phase of relaxation ($t_{REL(Slow)}$: 49.1±1.7 vs. 155.2±3.0 ms). Treatment with Dani at submaximal calcium level (pCa=5.8) resulted in a similar increase in force and slowing of activation and relaxation kinetics that was seen at maximal calcium level (Figure 4C-F and Table S1). Combined treatment with Dani and elevated ADP did not further increase force and minimally decreased cross bridge detachment $k_{REL(slow)}$ compared

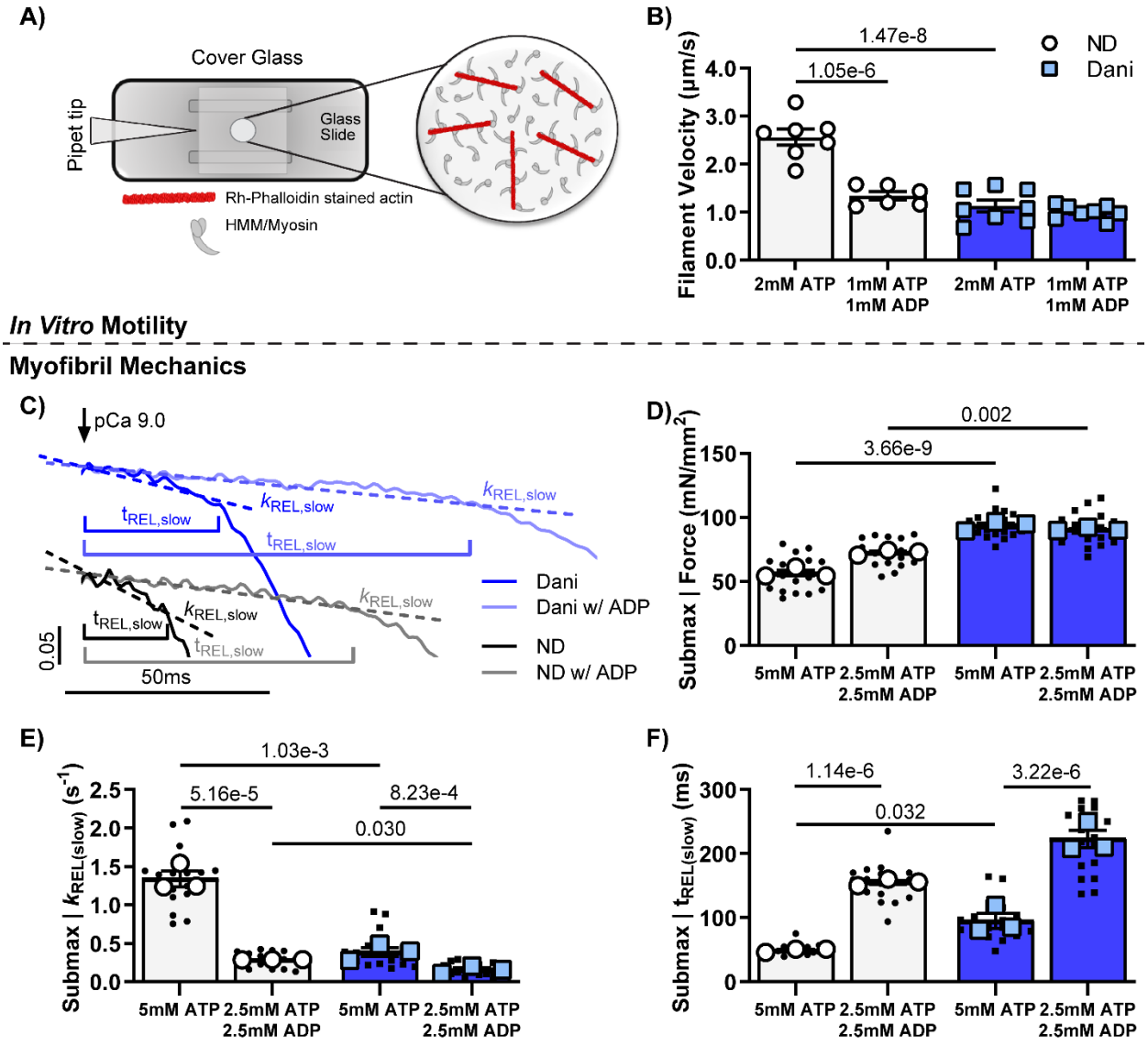

Figure 4. Effect of Danicamtiv and ADP on cross bridge cycling. (A) The *in vitro* motility assay was used to look at cross bridge cycling in isolated myosin and actin. (B), filament sliding velocity with 0.5 µM Dani-treated ATP-bound myosin (left columns), and with (50:50 ADP:ATP)-bound myosin (right columns). (C) Example tracings of the slow phase of myofibril relaxation with and without 1 µM Dani and with ATP or 50:50 ADP:ATP mixture at pCa=5.8. Example tracings are offset for visual clarity. Summary data of the effect of Dani and ADP on (D) submaximal force, and the (E) rate constant and (F) duration for the slow phase of relaxation. Data is from 7-8 slides per condition for *in vitro* motility and 18 DMSO or 21 Dani treated myofibrils (small symbols) from 3 biological replicates (large symbols).

to Dani and no ADP (Figure 4D-E). This suggests that ADP release is the key step in the cross-bridge cycle that is affected by Dani. Interestingly, addition of elevated ADP to Dani treated myofibrils further prolonged thin filament deactivation duration ($t_{REL(Slow)}$: 94.9±12.2 vs. 222.5±13.6 ms), likely due to more strongly-bound cross bridges.

- *Nucleotide handling rates were modified in the presence of Danicamtiv*

To confirm our myofibril results, we measured changes in nucleotide binding and release rates in presence of Dani. We calculated ATP binding and ADP release rates in porcine cardiac tissue using a step-length protocol in the presence of increasing [MgATP] (Figure S7). Cross bridge detachment rates (k_{rel}) increased as [MgATP] increased for the untreated and Dani-treated myocardial strips (Figure 5A, Table S5). k_{rel} was slower for the Dani-treated strips at [MgATP] greater than 0.5 mM. Fits to Eq. 1 suggests that slowed cross bridge detachment stems from a combination of slower cross bridge MgADP release rate (k_{-ADP}) and faster cross bridge MgATP binding rate (k_{+ATP}) in the presence of Dani (Figure 5B-C). Because the rate limiting step of the cross-bridge cycle under load is MgADP dissociation from strongly bound myosin cross bridges in demembranated myocardial strips, it was the slower k_{-ADP} that primarily drove the differences in cross bridge kinetics between the untreated and Dani-treated strips. As seen in Figure 5, k_{+ATP} was significantly faster than k_{-ADP}, and with k_{+ATP} being a second-order nucleotide binding process, the [MgATP] needs to be very low for k_{+ATP} to affect cross bridge detachment rates. Figure 5D shows that the MgATP concentration at half-maximal detachment rate ($[MgATP]_{50}$) was much lower for the Dani-treated strips. This suggests that Dani-treated preparations required less MgATP to reach their maximal cross bridge detachment rate. Using the same approach, we found a similar relationship between k_{rel} and [MgATP] in the presence of 1 μm OM. OM resulted in the same magnitude of k_{-ADP} inhibition and decreased $[MgATP]_{50}$ as Dani, suggesting these small molecules affect similar steps of the cross-bridge cycle.

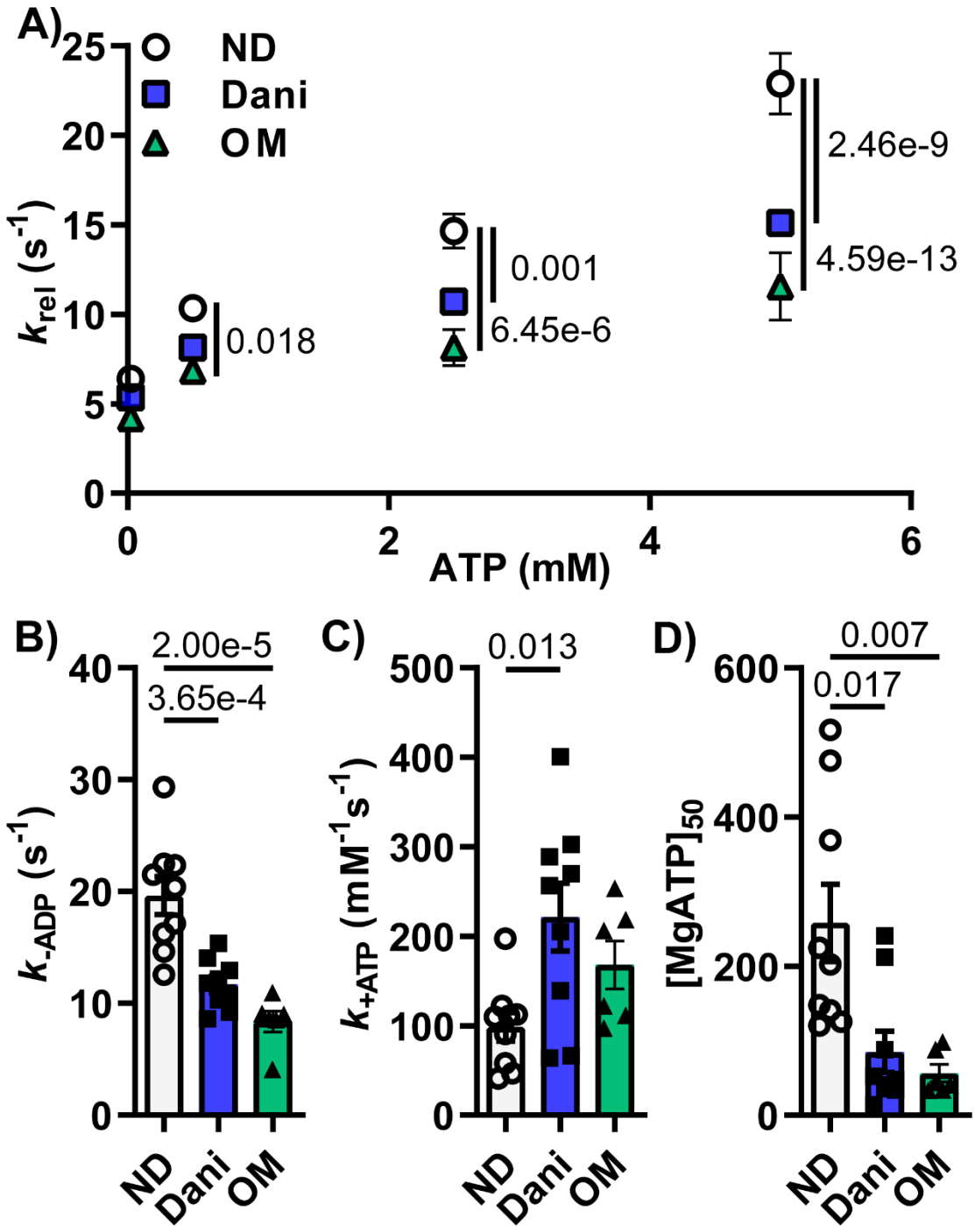

Figure 5. 1 μM Dani and OM increased ATP binding and decreased ADP release in activated porcine cardiac muscle. (A) The cross-bridge detachment rates (k_{rel}) increased with increasing [MgATP] for the untreated, Dani-treated and OM-treated myocardial strips. Treatment with both Dani and OM decreased k_{rel} at [MgATP] greater than 0.5 mM (B). Dani and OM decreased ADP release rate (B, k_{-ADP}) while increasing ATP binding (C, k_{+ATP}). MgATP concentration at half-maximal detachment rate ($[MgATP]_{50}$) was lower for both Dani-treated and OM-treated strips (D). Data is from 9 tissue preparations per condition.

- *Danicamtiv recovered abnormal tension in a rodent DCM model.*

Since Dani is under investigation for treatment of patients with genetic cardiomyopathy, we tested its ability to recover the force deficit in a thin filament DCM mouse model with the characteristic progressive dilation and hypo-contractility of human genetic DCM. Permeabilized muscle preparations showed a right-ward shift in the force vs. pCa relationship in the I61Q cTnC DCM model.(Davis et al., 2016) Additionally, the I61Q cTnC mutant decreased F_{max} and the Hill coefficient. As seen in Figure S8, 1 μm Dani was able to shift the force vs. pCa curves to the left for both control and I61Q cTnC mice with an increase in pCa50 (5.58±0.01 vs. 5.72±0.02 for control, 5.35±0.04 vs. 5.47±0.03 for I61Q cTnC). This increase in pCa50 was significant versus no drug regardless of genotype. Similar to the results in pig cardiac tissue, we found a decrease in the Hill coefficient and maximal k_{tr} but with no increase in maximal force.

Our intact trabecula measurements showed a decrease in peak tension (T_p) and tension index in the I61Q cTnC mice (Figure 6, Table S4) as previously reported.(Davis et al., 2016; Mijailovich et al., 2021) In the presence of Dani, T_p increased in both control and DCM. In control mice, 1 and 3 μM Dani resulted in ~63% and 131% increase in T_p, while the increase is ~87% and ~148% respectively in I61Q cTnC trabecula. While the time to peak is unchanged in presence of Dani, time to 50 and 90% relaxation is increased in presence of Dani (Figure S9, Table S4). We have previously shown that the tension index, the area under the twitch curve that is subtracted from a healthy twitch, is predictive of cardiomyopathy phenotype (Davis et al., 2016; Powers et al., 2020).

While tension index increased with Dani in a dose dependent manner, the increase was greater in the control mice. This is mostly due to the more pronounced relaxation change in the control tissue. Using mixed-effects analysis, the interaction between genotype and Dani is statistically significant, suggesting a different treatment response in control versus I61Q cTnC

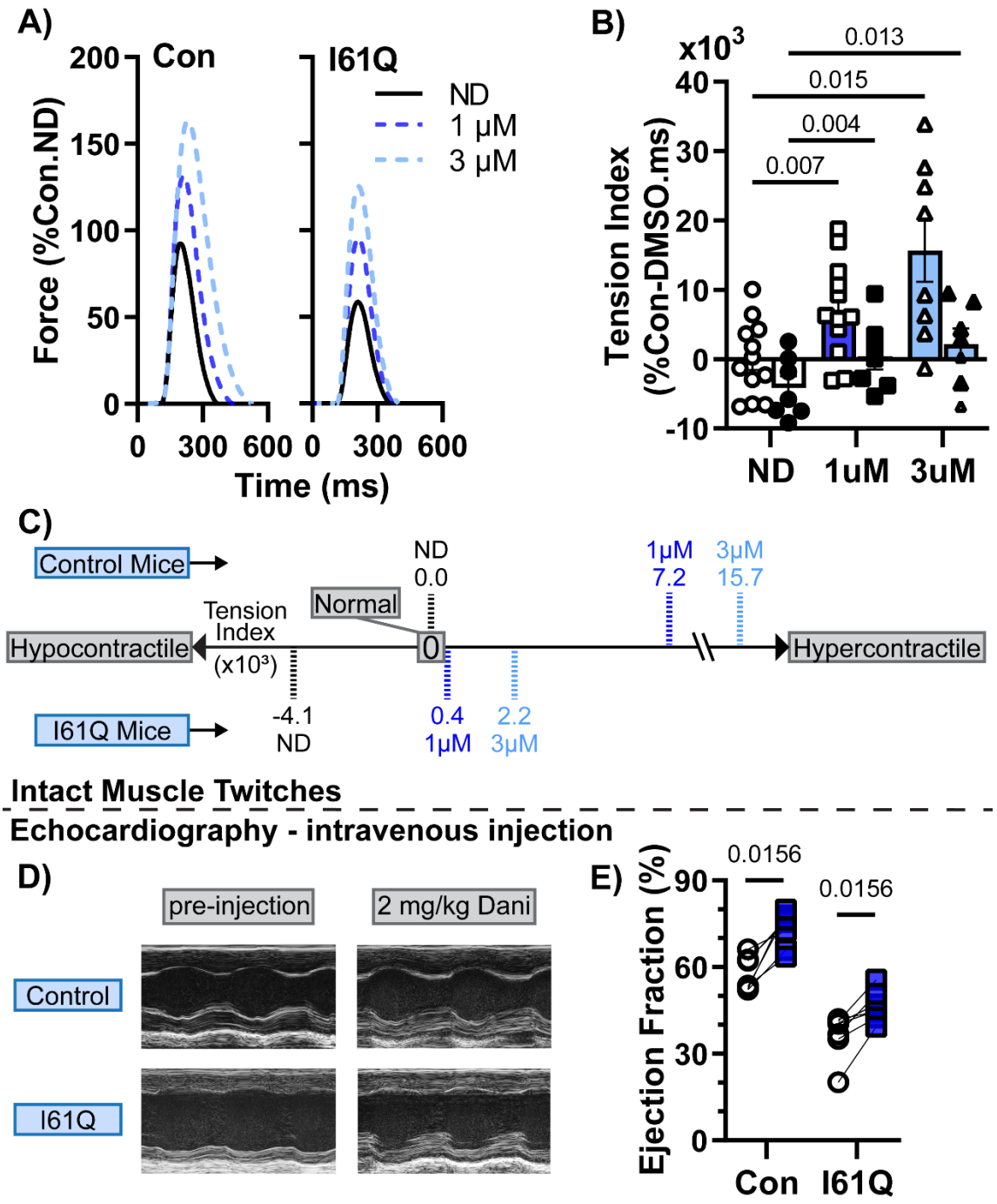

Figure 6. Dani mitigated the contractile abnormalities in a rodent DCM model. (A) Average twitch force-time traces (in % Control-ND T_p) of intact papillary muscle trabeculae from control (left) and I61Q cTnC (right) mice stimulated at 1 Hz. Dani increased Tp (A) and tension index (B and C) in control and I61Q cTnC twitches in a dose dependent manner. (C). Intravenous injection of 2 mg/kg Dani resulted in significant increase in ejection in both control and I61Q cTnC hearts 10 minutes post injection. Data is from 15 control mice and 11 I61Q mice for intact twitches and 7 mice for in each echo group.

tissue. These results suggest that the underlying mechanism of cardiomyopathy might need to be considered when dosing a medication such as Dani. We tested *in-vivo* efficacy of Dani by intravenous injection of 2 mg/kg and saw a significant increase in ejection fraction in both controls (58.1±2.5 vs. 74.7±2.0) and DCM (36.6±2.9 vs. 46.3±2.0) hearts 10 minutes post treatment (Figure 6, Table S6). There was a decrease in heart rate post treatment, which was likely due to sedation. Treatment with vehicle (DMSO) did not significantly increase ejection fraction or heart rate (Table S7).

v. Discussion

We set out to perform a first detailed analysis of the mechanism of action of the myosin activator Danicamtiv. There are several key findings that emerged from this study. First, we showed that treatment with Dani restructured the thick filament of resting muscle to a more ON configuration, where myosin heads are positioned closer to actin. This increased the number of myosin heads available to contribute to contraction, a result that is consistent with more myosin motors binding at lower calcium concentrations. It also suggests reduced reliance on calcium mediated cooperativity of myosin binding, hence an increase in calcium sensitivity with a decreased Hill coefficient. Second, we showed that Dani slowed cross bridge turnover and subsequently decreased rate of myofibril relaxation and prolonged thin filament deactivation. This prolonged relaxation manifested in intact cardiac muscle, which had slower twitch relaxation kinetics. Third, we provided evidence to show that the decrease in myosin ADP release rate is the mechanism for decreased cross bridge turnover and slower relaxation. Fourth, we showed that Dani improved the tissue and organ level hypo-contractility in a genetic DCM model.

- *Danicamtiv restructures myosin in an analogous manner to other myosin activators.*

Myosin activation is a novel way to treat HF. OM, the first in class myosin activator, recently completed a phase 3 clinical trial for treatment of systolic HF (Teerlink, Diaz, Felker, McMurray, Metra, Solomon, Adams, et al., 2021). Studies using fluorescent probes have demonstrated that

OM stabilizes the ON state of the thick filament resulting in more myosin motors available for binding to the thin filament (Teerlink, Diaz, et al., 2021b). Our x-ray diffraction studies also showed partial thick filament activation with Dani under resting conditions. This activation under resting conditions can be expected to result in more myosin motors binding at lower calcium concentrations with less reliance on cooperativity. Results of our sinusoidal length-perturbation analysis further support that Dani increases cross bridge binding and promotes an increase in the ratio of ON to OFF cross bridge populations. Similar changes in myosin structure under resting conditions are induced by 2-deoxy adenosine triphosphate (dATP), a nucleotide known to increase force and calcium sensitivity in rodent, dog, and human cardiac myocardium, (Cheng et al., 2016; Moussavi-Harami et al., 2015; Regnier et al., 2000) that correlate well with active force (Powers et al., 2019).

- *Danicamtiv inhibits cross bridge cycling rate, prolonging thin filament deactivation and relaxation in myofibrils.*

The myofibril kinetics measurements suggest that Dani prolongs thin filament activation, as indicated by the longer $t_{REL(slow)}$ and that this is due to a decreased rate of cross bridge detachment as measured by $k_{REL(slow)}$. A similar mechanism of action involving prolonged actomyosin attachment resulting in cooperative thin filament activation has been proposed as a mechanism for OM.(Nakanishi et al., 2022; Woody et al., 2018) The inhibitor-like mechanism is further supported by decreased ATP turnover in HMM with increasing concentrations of Dani, which was also observed for OM (Figure S5). While both Dani and OM inhibit maximal force at high drug concentrations, OM inhibits to a greater extent and at lower concentration (Figure S4). The duration of the slow phase of relaxation ($t_{REL(slow)}$) is known to be affected by changes in troponin complex calcium affinity(Kreutziger et al., 2011) so we measured the effect of Dani on troponin function. Dani did not change Ca^{2+} binding to cTnC as measured by steady state fluorescence spectroscopy (Figure S10). Therefore, the decreased cross bridge detachment rate is likely

explained by the decreased ADP release rate, and this is supported by myofibril relaxation measurements in the presence of elevated ADP, which mimic relaxation kinetic changes seen with Dani under conditions of load.

- *Danicamtiv corrects abnormal contraction in a genetic DCM mouse model*

Using a rodent model of sarcomeric genetic DCM with decreased thin filament activation, we demonstrated that Dani could normalize the decreased calcium sensitivity of contraction in I61Q cTnC mice. At the lowest calcium levels of our F-pCa curve, there is full recovery of the force deficit to levels of control myocardium. However, the maximum force is still significantly lower in the Dani-treated I61Q cTnC trabeculae. The decreased k_{tr} in mice suggested that slowing of cross bridge kinetics was present in hearts with both myosin heavy chain 6 (MYH6) (mice) and MYH7 (pig). Intact trabecula experiments demonstrated that tension increased in both control and I61Q cTnC mice after treatment with Dani. Control mice consistently achieved a higher peak force and tension index, a summative measure encompassing peak tension and kinetics of both activation and relaxation, compared to I61Q. Control mice also expressed greater sensitivity to Dani treatment with significantly greater time to 50% and 90% relaxation compared to I61Q. An explanation for the difference in relaxation is that Dani normalizes the duration of thin filament deactivation in the I61Q cTnC which are abnormal without treatment. However, in the control mice, the thin filament stays on much longer, resulting in prolonged relaxation. Most of the DCM mice achieved a positive tension index at a dose of 3 μM, which is higher than the reported maximum serum concentrations (Grillo et al., 2021). Our *in vivo* treatment with Dani resulted in about 27% increase in ejection fraction in both control and I61Q hearts. While the cardiac function of the I61Q hearts improved, it did not fully recover to the untreated control levels, which matches the twitch and tension index data.

Our study has some limitations. Our mouse model of genetic DCM is based on an engineered mutation in cTnC and not a known disease-causing mutation. It is also worth noting that MYH6 is

the dominant form of cardiac myosin in mice, while humans express the MYH7 variant. It is possible that our genetic DCM results could be different in organisms with MYH7 as the dominant myosin. Intact twitch measurements were only performed in mice, which expresses the fast form of myosin. Our studies have not assessed the relative affinities of Dani for different cardiac myosin isoforms, however we found comparable results in mouse and pig, which have different predominant isoforms.

In conclusion, we use a variety of tools to demonstrate the biophysical mechanisms of how Danicamtiv works to increase force and calcium sensitivity. This methodological framework can be used to connect information from mechanical measurements to understand how myosin recruitment or the cross-bridge cycle affect cardiac myofibril activation and relaxation. The initial discovery of Dani was based on increased myofibril ATPase activity. Our studies support a more complex process than a simple increase in myosin cycling rate. The inhibition of ADP release leads to slower relaxation kinetics of myofibrils and consequently slower relaxation in intact tissue. In addition, myosin heads are more primed to interact with actin at low levels of calcium, resulting in increased calcium sensitivity and higher contractile forces at levels of calcium the sarcomere experiences during the cardiac cycle. This increase in force production and widening of twitch duration contribute to the increased tension index and augmenting cardiac function.

In addition to providing the mechanism of action, our data may help to identify subsets of patients that may derive the most benefit from Dani. For example, there could be a different response in sarcomeric versus non-sarcomeric DCM or thin filament versus thick filament variants. Genetic variants are being recognized as an increasing cause of heart failure and dilated cardiomyopathy. Myosin activators may provide a treatment that addresses the causative hypo-contractile phenotype. This motivated a current clinical trial of patients with genetic DCM for treatment with Dani. However, there is lack of data regarding the utility of this medication in genetic cardiomyopathy preclinical models. Our study shows that Dani increased cardiac function

in rodent genetic DCM hearts. Future studies will need to look at a diverse group of variants and extend the studies to humans with genetic DCM.

vi. Acknowledgments

The authors acknowledge Mr. Darron Marzolf who provided fresh pig muscle. This project used resources from the University of Washington Center for Translational Muscle Research supported by NIH grant P30AR074990. This research used resources of the Advanced Photon Source; a US Department of Energy (DOE) Office of Science User Facility operated for the DOE Office of Science by the Argonne National Laboratory under Contract DE-AC02-06CH11357. BioCAT is supported by NIH grant P30 GM138395. We acknowledge Dr. David Mack for providing access to BioRENDER.

VI. Chapter 4 Hypertrophic cardiomyopathy mutation R403Q develops mechanical and structural dysfunction in porcine ventricle tissue

This chapter represents a publication style write up of an ongoing project I am leading and currently co-first author on.

Saffie Mohran†, Kristina Kooiker†, Matthew Childers, Timothy McMillen, Christian Mandrycky, Stephanie Neys, Michael Geeves, Thomas Irving, Weikang Ma, Farid Moussavi-Harami, Michael Regnier

† Authors contributed equally

i. Abstract

Missense mutations in human β-cardiac myosin were first reported to cause malignant hypertrophic cardiomyopathy with the discovery of R403Q. Located in the upper 50KDa cardiomyopathy loop of myosin, there are several reports on the impact of R403Q on myosin structure, sarcomere contractile properties, and ATPase activity. Conflicting findings in contractile kinetics between human-patient samples and a transgenic rabbit model motivated us to study a novel MYH7 R403Q porcine model. Preliminary contractile experiments comparing control and R403Q demembranated ventricle strips showed R403Q expresses significantly faster k (1.18s-1 vs 1.89s-1), greater Ca sensitivity (pCa = 5.72 vs 5.89), and a decreased Hill coefficient (4.96 vs 2.57). Small angle x-ray diffraction on R403Q tissues demonstrated greater myosin disorder with decreased intensities in the myosin-based reflections (I = 6.30 vs 0.69, I = 9.35 vs 3.56) compared to WT cardiac muscle. Interestingly, R403Q tissue had blunted structural changes in response to dATP, a myosin activator, while the structural changes in response to Mavacamten, a myosin inhibitor, were increased. These structural changes suggest that R403Q increases the population of ON myosin heads, a potential mechanism of hyper-contractility. To understand the direct impact of R403Q on myosin head structure in the absence of actin, we performed molecular dynamic (MD) simulations of the pre-power stroke state (M.ADP.Pi). Simulations showed the R403Q mutation primarily altered the surface area and electrostatic potential of myosin's actin binding surface. To complement the MD simulations, we isolated S1-subfragments and performed stop-flow measurements of ATP-binding and single nucleotide turnover utilizing Mant-ATP. These actin-absent experiments showed no difference in ATP-binding and single nucleotide turnover kinetics between control and R403Q myosin. Future experiments will utilize S1-subfragments in the absence and presence of actin to assess ADP dissociation and actin-mediated ATP-binding.

ii. Introduction

Hypertrophic cardiomyopathy (HCM) is a complex cardiovascular disorder characterized by myocardial hypertrophy. Among the array of genetic mutations associated with HCM, the first reported familial cardiomyopathy was the R403Q mutation (Geisterfer-Lowrance et al., 1990; Seidman & Seidman, 2001). Expressed in cardiac β-myosin, the mutation has emerged as a central focus of research due to its profound impact on sarcomeric function. The R403Q mutation leads to a single-nucleotide substitution, resulting in the replacement of an arginine (R) with a glutamine (Q) residue at position 403 within the beta-myosin heavy chain protein. This genetic alteration significantly disrupts the interactions between actin and myosin proteins within the sarcomere.

Previous reports focused on β-myosin expressing models of the R403Q mutation showed that myofibril kinetics from human patient myectomy samples (Witjas-Paalberends et al., 2014) were different from measurements collected from a transgenic rabbit model (Susan Lowey et al., 2018). Specifically, activation and relaxation kinetics were described to be faster (when compared to control) in human samples verses slower in the rabbit model. Addition experimentation done in the patient-myectomy study observed tension-cost measurements to assess myosin head cycling efficiency. Reported results showed that the R403Q mutation significantly decreased myosin head efficiency, suggesting that myosin heads were cycling faster and utilizing more ATP to generate lower amounts of force compared to controls (Belus et al., 2008; Witjas-Paalberends et al., 2014).

In addition to the described differences above, both publications showed similarities in how R403Q significantly decreased the maximal tension generation of myocardial tissue preparations, and the significant increase in calcium sensitivity. Separate yet complementary published work assessing the structural perturbations caused by the R403Q mutation regarding myosin head recruitment utilized small angle x-ray diffraction to assess the position and organization of myosin within the myofilament lattice (Robert L. Anderson et al., 2018). Through

the utilization of a novel porcine model expressing the β-myosin version of the R403Q mutation, Anderson et al. discovered that the R403Q significantly disrupted the organization of myosin heads along the thick filament and positioned the myosin heads closer to the actin filament in relaxed conditions. These results suggest that the R403Q mutation structurally positions myosin in a more a “primed” position for cooperative activation and could be a potential mechanism that attributes to the mechanically observed increased calcium sensitivity. In addition to characterizing the structural impact R403Q has on the myofilament architecture, they also reported structural results utilizing the myosin-specific small molecule, Mavacamten. These results suggested that therapeutic intervention could return the dysfunction R403Q myosin head organization back to normal conditions.

The promising results described by Anderson et al. in respect to the structural recovery Mavacamten had on the R403Q porcine tissue introduce significant clinical implications for the treatment of familial cardiomyopathies. There becomes a significant need in the field to understand the exact mechanisms of sarcomeric dysfunction caused by the R403Q mutation in cardiac function, and the implications of treating the disease with Mavacamten and other small molecule therapies. The study presented here utilizes the novel porcine model to not only focuses on the structural dysregulation caused by the mutation, but also the mechanical and biochemical kinetics attributed with the disease and certain therapeutic interventions. By utilizing molecular dynamic (MD) modeling, isolated proteins, myofibril, and tissue preparations, we transcend the limitations of a single experimental scale and provide a cohesive interrogation of the underlying dysfunction sarcomeric mechanisms caused by the R403Q mutation that manifests into the hypertrophic cardiomyopathy observed clinically in affect patients.

iii. Methods

- *X-ray diffraction imaging (Adapted from Chapter 1):*

X-ray fiber diffraction patterns were obtained from permeabilized porcine left ventricular muscle bundles as described previously (Ma, Gong, et al., 2022; Ma, Nag, et al., 2022). Briefly, pieces of frozen porcine left ventricle wall were thawed and permeabilized with 1% Triton-X100 for 3 h at room temperature. Fiber bundles (~5 mm long at ~ 200 µm in diameter) were attached to aluminum T-clips at both ends for the X-ray experiments. X-ray diffraction patterns were collected on a MarCCD 165 detector (Rayonix Inc., Evanston IL) with a 1 s exposure time. Each preparation was done in relaxation (pCa 8.0) conditions with pairwise assessment to either 100% dATP or 30 µM of Mavamten compared to standard ATP control solutions. The X-ray data were analyzed using the MuscleX software package developed at BioCAT (Jiratrakanvong et al., 2018).

- *Isometric force and rate of tension redevelopment (Adapted from Chapter 3):*

Permeabilized trabeculae (mouse) or thin strips (pig) were dissected and mounted between a force transducer (Aurora Scientific, model 400A) and a motor (Aurora Scientific, model 315C) using aluminum T-clips (Aurora Scientific).(Powers et al., 2020) Sarcomere length (SL) was set to ~2.3 µm for the experiments. Experiments were conducted in physiological solution (pH 7.0) or 21°C containing a range of pCa (= $-\log_{10}[Ca^{2+}]$) values from 8.0 to 4.5. Tissue was allowed to reach stead-state force (F) at each pCa. F-pCa curves were collected and analyzed with custom code using LabView software and fit to the Hill equation. The rate of tension redevelopment (k_{tr}) and high frequency stiffness (HFS) were measured at each pCa.

- *Myofibril mechanics (Adapted from Chapter 3):*

Myofibril activation and relaxation measurements were performed on a custom set up as previously described.(Moussavi-Harami et al., 2015; Racca et al., 2016) Briefly, myofibrils were mounted between two glass needles; one which acted as a force transducer and the other as an

inflexible motor arm. A dual diode system measures force based on needle deflection, with force transducer needle stiffness measured at 7.98 mm/µN. A double-barreled glass pipette delivered relaxing (pCa = 8.0) and activating (pCa = 5.6 or 4.5) solutions to the mounted myofibril. Activation and relaxation data were collected at 21 °C and fitted as previously described.(Moussavi-Harami et al., 2015)

- *Porcine S1 protein isolation (Adapted from Chapter 2):*

Porcine cardiac sub-fragment 1 (pc-S1) was isolated as previously described (Mathern & Burke, 1986). Starting with porcine cardiac myosin, add high salt solution (120 mM NaCl, 12.3 mM NaH_2PO_4, 7.7 mM Na_2HPO_4, 1 mM EDTA, pH 7.0) to achieve a myosin concentration of 10 mg/mL. Once dissolved, add chymotrypsin to a 30 µg/mL final concentration. Digest for 15 minutes before stopping with PMSF (0.4 mM final concentration in solution), and then 1.5x volume of BED solution (0.1mM $NaCO_3$, 0.1 mM EGTA, 1 mM DTT, pH 7.0) and 6 mM $MgCl_2$. Centrifuge at 620,000 x g for 20 minutes to isolate the pcS1 from the residual precipitate LMM and undigested myosin and store at -80°C with the addition of 1% sucrose and 1% protease inhibitor.

- *Single nucleotide turnover kinetics (Adapted from Chapter 2):*

All kinetic assays were performed using a HiTech Scientific Stopped Flow system (Bradford upon Avon, UK) equipped with a Hg/Xe lamp and monochromator. Tryptophan fluorescence at 297 nm was utilized as a fluorescence resonance energy transfer (FRET) mechanism to excite mantATP, which was observed at above 400 nm at 90° to the incident light through a KV400 optical filter. 125 nM pc-S1 was mixed with 2 µM mantATP and allowed to react for 1 min to achieve a steady-state before rapidly mixing with an excess of unlabeled ATP (125 µM) in a stopped flow fluorimeter. Data collected over 300 seconds after mixing can be fitted to a single exponential with the best fit superimposed on the data (k_{obs} ~ 0.016 s^{-1}). The residual plot (experimental data subtracted from the best fit line) had random noise of < ± 0.1% of the total

signal strength. The deviation from a flat line was < ±0.2% of the signal or < 1% of the observed fluorescence change (ΔFl).

- *Molecular dynamic (MD) simulation of pre-power stroke M.ADP.Pi state:*

Model Building: Initial structure modeled using the bovine pre-powerstroke cardiac myosin structure (PDB ID: 5N69) (PDB, www.rcsb.org) (Berman et al., 2002; Planelles-Herrero et al., 2017) entry 4DB1 (X-ray crystallography, 2.6 Å resolution). Coordinates for the rigor state actomyosin complex of cardiac myosin and skeletal actin were obtained from the PDB entry 6X5Z (cryo-electron microscopy, 4.2 Å resolution) (Doran et al., 2020). Homology models for R403Q mutation was generated using the structures as templates, sequences downloaded from *Uniprot*, and the *Modeller* homology modelling software. Starting coordinates for the mutant system was obtained via *in silico* modification of the WT structures using the *leap* module of *AMBER (Case et al., 2005)*.

Force Field and Explicit Solvent Molecular Mechanics: All simulations were performed with the AMBER20 package and the ff14SB force field (Maier et al., 2015). Water molecules were treated with the TIP3P force field, metal ions were modeled using the Li and Merz parameter set. ATP molecules were treated with parameters from Meagher *et al.* (Meagher et al., 2003). The SHAKE algorithm was used to constrain the motion of hydrogen-containing bonds and long-range electrostatic interactions were calculated using the particle mesh Ewald (PME) method.

Pre-production protocols: Hydrogen atoms were modeled onto the initial structure using the *leap* module of *AMBER* and each protein was solvated with explicit water molecules in a periodic, truncated octahedral box that extended 10 Å beyond any protein atom. Na^+ and Cl^- counterions were added to neutralize the systems and then 120 mM Na^+ and Cl^- ions were added. Each system was minimized in three stages. First, hydrogen atoms were minimized for 1000 steps in the presence of 100 kcal mol^{-1} restraints on all heavy atoms. Second, all solvent atoms were

minimized for 1000 steps in the presence of 25 kcal mol^{-1} restraints on all protein atoms. Third, all atoms were minimized for 8000 steps in the presence of 25 kcal mol^{-1} restraints on all backbone heavy atoms (N, O, C, and C atoms). After minimization, systems were heated to 310°K during 3 successive stages. In each stage, the system temperature is increased by ~100°K over 100 ps (50,000 steps) using the NVT (constant number of particles, volume, and temperature) ensemble. During all heating stages, 25 kcal mol^{-1} restraints were present on the backbone heavy atoms (N, O, C, and C atoms). After the system temperatures reached 310°K, the systems were equilibrated over 5 successive stages using the NPT (constant number of particles, pressure, and temperature) ensemble. During each stage, the systems were equilibrated for 5.4 ns in the presence of restraints on backbone atoms. The strength of the restraints decreased from 25 kcal mol^{-1} during the first stage to 1 kcal mol^{-1} during the fourth stage. During the final equilibration stage, the systems were equilibrated in the absence of restraints.

Molecular Dynamics Protocol: Production dynamics for conventional molecular dynamics (MD) simulations were then performed using the canonical NVT ensemble with an 8 Å nonbonded cutoff, and 2 fs time step. Coordinates were saved every picosecond. Simulations were run for 500 ns each.

Molecular Dynamics Analysis: The C_α RMSD, C_α RMSF, SASA, interatomic distances, and interatomic contacts were calculated with *cpptraj* (Roe & Cheatham, 2013). The C_α RMSD was calculated after alignment of all The C_α atoms to the minimized structure. The C_α RMSF was calculated about average MD structures for each simulation. Two residues were considered in contact with one another if at least one pair of heavy atoms were within 5 Å of one another. All protein images were prepared using UCSF Chimera (Pettersen et al., 2004; Sanner et al., 1996).

iv. Results

- *X-ray diffraction imaging shows R403Q is less sensitive to dATP but more sensitive to Mavacamten, suggesting the mutation increases the structural ON state of myosin.*

Initial experimentation utilizing the R403Q porcine tissue assessed the structural organization and position of the mutated myosin in permeabilized preparations. Experiments were conducted in relaxed conditions (pCa 8.0). In addition to assessing the structural differences between control and diseased preparations, we also aimed to assess the sensitivity of the myosin population to known positive and negative ionotropic agents. In addition to Mavacamten as a myosin-inhibiting modulator, we selected a known myosin activator, dATP, to induce the opposite effect on myosin organization and structure. Previous reports by us and others have utilized dATP, a naturally occurring nucleotide, as a myosin activator due to the electrostatic perturbations the nucleotide induces on myosin. By utilizing saturating concentrations of both myosin modulators (100% dATP and 30μM Mavacamten), we aimed to assess the structural impact each would have on the R403Q myosin.

Quantification of the intensity ratio (I1,1/I1,0) describes the average mass population of myosin head between the thick and thin filament. Greater intensity values indicate that myosin heads are closer to the thin filament, and potentially in a more primed position for interactions with actin. Conversely, lower intensity ratio values describe myosin heads closer to the thick filament, and potentially sequestered from actin interactions. In paired wise comparisons, we initially took control static images of both WT and R403Q preparations before exchanging the solutions with either 100% dATP or 30μM Mavacamten, respectively. This paired wise experimentation allowed us to normalize the changes caused by the myosin modulators and assess the total change in intensity ratio as a population delta.

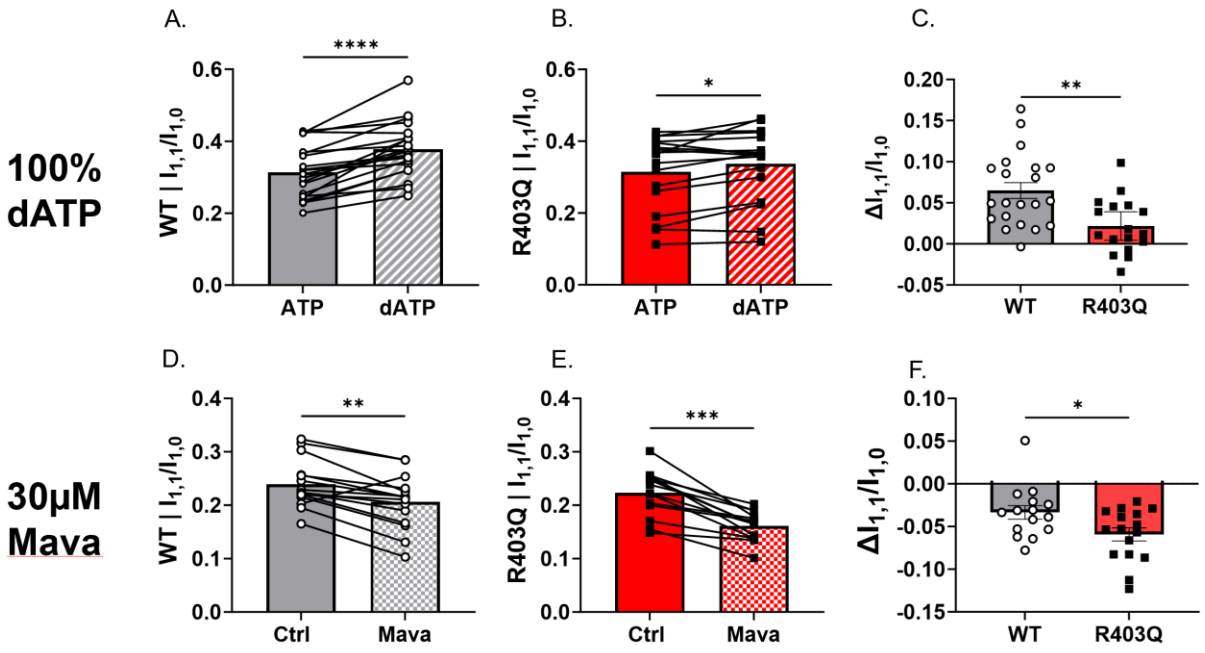

Figure 1. Intensity ratio measurements collected by X-ray diffraction imaging suggests R403Q is less sensitive dATP activation but more sensitive to Mavacamten inhibition.

Pair wise comparisons of WT **(A)** and R403Q **(B)** in 100% dATP treatment shows that R403Q is less sensitive to the myosin activator **(C)** compared to controls. Conversely, WT **(D)** and R403Q **(E)** in the presence of Mavacamten showed that R403Q was significantly more sensitive **(F)** compared to WT.

In 100% dATP conditions, we observed that both WT (Fig 1A) and R403Q (Fig 1B) preparations increased in intensity ratio, suggesting that dATP elevated the myosin population pool closer to actin. Quantification of the total population change caused by dATP however indicates that dATP causing significantly less changes in myosin position in the R403Q tissue compared to control (Fig 1C). Described another way, the already elevated state of R403Q due to the mutation blunted the impact of dATP compared to controls. Conversely, similar analysis of the WT and R403Q with Mavacamten showed that the myosin-inhibiting compound had significantly more impact on the sequestration of myosin heads back to the thick filament

compared to controls (Fig 1F). This suggests that the R403Q myosin population began in a more elevated state, and Mavacamten was able to sequester more heads compared to WT control.

- *R403Q expresses significantly decreased maximal force, increased calcium sensitivity, and decreases hill coefficient value in permeabilized tissue mechanics*

In addition to structural measurements, we performed permeabilized mechanical experiments to assess R403Q contractile dysfunction in steady-state conditions. Control and mutant preparations were exposed to an array of different calcium concentrations, with each tension generation and rate of tension redevelopment assessed at each calcium concentration. Force generation at saturating calcium concentration (pCa 4.5) showed that R403Q preparations

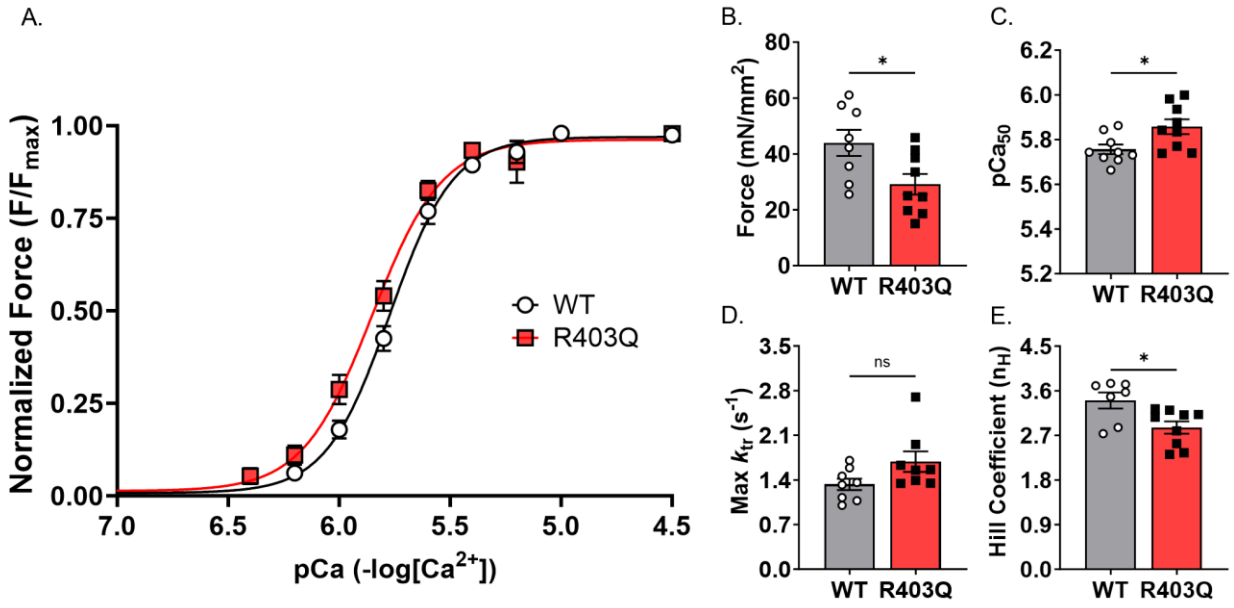

Figure 2. Permeabilized mechanics on R403Q expressed significant contractile dysfunction in steady-state conditions of activation.

Permeabilized tissue mechanics were activated in a range of Ca^{2+} solutions to assess force-pCa **(A)** relationship. R403Q tissues expressed a significant increase in Ca2+ sensitivity **(C)**, along with a decrease in maximal tension generation **(B).** Myosin crossbridge cycling kinetics were unchanged in maximal Ca^{2+} conditions **(D)**, however R403Q showed increased myosin recruitment and activation at lower [Ca^{2+}] with a significantly lower hill coefficient value **(E)**.

produced significantly lower force (Fig 2B) compared to littermate controls. Normalization of the force to calcium concentration relationship produces a sigmoidal relationship, with the EC_{50} value describing the calcium sensitivity of the preparation. Tissues harboring the R403Q mutation showed a significant leftward shift compared to controls (Fig 2A), with quantification of the EC_{50} expressing a significant increase in calcium sensitivity compared to controls (Fig 2C). Assessment of the linear slope portion of the sigmoidal relationship quantifies the hill coefficient (n_H). This value has been previously shown to describe the cooperative recruitment of sarcomeric proteins during activation. The R403Q expressed a significantly lower hill coefficient value, suggesting that more myosin heads are available to bind at lower concentrations of calcium compared to controls (Fig 2E). Interestingly, measurements of the rate of tension redevelopment at maximal calcium concentrations in R403Q showed no significant increase (Fig 2D). A closer investigation at submaximal concentrations may provide a better assessment of the mutations on myosin crossbridge cycling.

- *R403Q significantly decreases maximal force and accelerates both activation kinetics and rate of crossbridge detachment during the initial phase of relaxation in myofibrils*

Myofibril mechanical measurements allow for the quantification of dynamic states of sarcomeric activation and relaxation. Myofibrils isolated from permeabilized R403Q ventricular tissue were activated in maximal (pCa 4.5) and submaximal (pCa5.6) calcium concentrations. Maximal force generation of the R403Q preparations was significantly lower (Fig 3B) compared to controls, validating results collected from steady-state tissue mechanics described above. Assessment of R403Q myofibril kinetics showed that maximally activated force traces expressed significantly faster rate constants of myofibril activation (k_{ACT} | Fig 3D) compared to controls. Assessment of the initial linear phase of relaxation showed that the R403Q mutation significantly increased the rate of crossbridge detachment ($k_{REL,slow}$ | Fig 3F) compared to controls, with no impact on thin filament deactivation time ($t_{REL,slow}$ | Fig 3G). There were no observed differences

in the fast phase of myofibril relaxation ($k_{REL,\ fast}$ | Fig 3E) between R403Q and control myofibrils. These results recapitulate the findings described by (Witjas-Paalberends et al., 2014) from human patient-myectomy samples. With the recapitulated increase in crossbridge detachment rate, our data suggests that R403Q may accelerate product release rate during myosin head cycling.

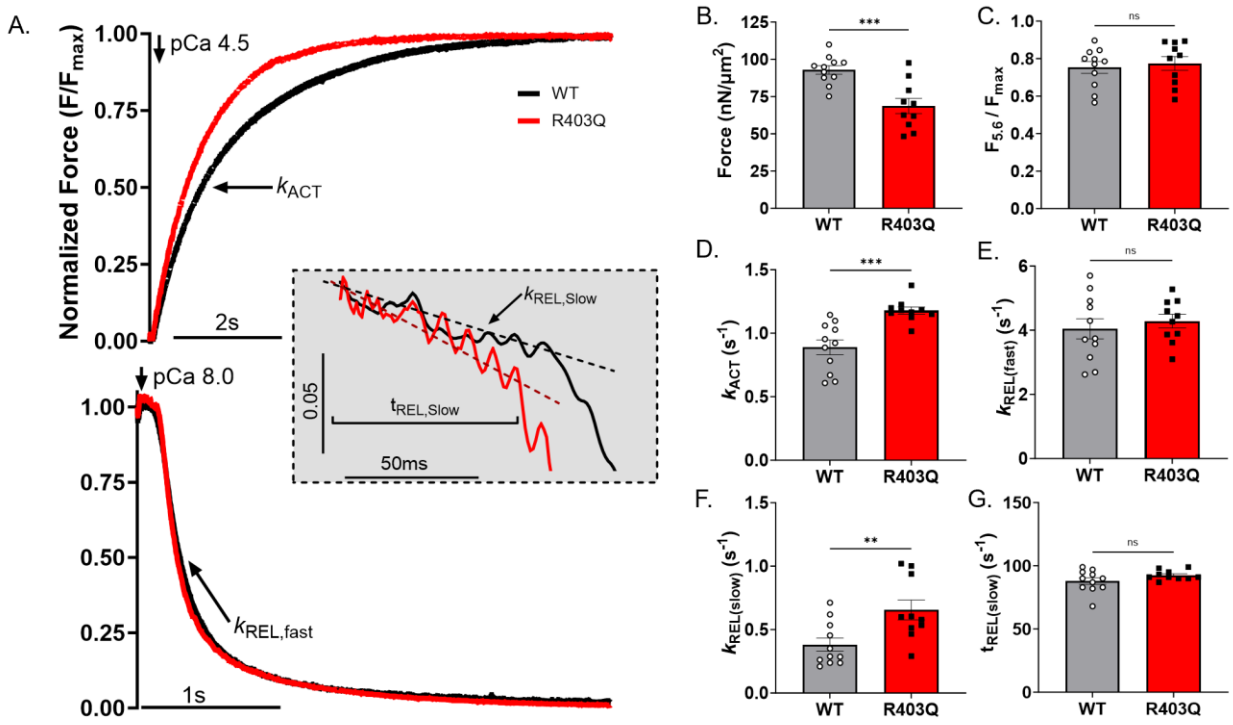

Figure 3. Myofibril activation and relaxation kinetics shows R403Q significantly accelerates activation and crossbridge detachment compared to controls.

Example normalized myofibril activation and relaxation traces **(A)** illustrate the visual kinetic differences between R403Q and WT. Quantification of the maximal tension generation **(B)** and submaximal ratio **(C)** showed similar results to permeabilized tissue mechanics. Fast rate constant values of activation **(D)** and relaxation **(E),** along with the initial linear phase of relaxation describing crossbridge detachment rate **(F)** and thin filament deactivation time **(G)** suggest that the R403Q mutation impacts nucleotide product release.

- *Isolated R403Q cardiac-S1 in the absence of actin showed no difference in stopped-flow single nucleotide turnover rate compared to control*

In addition to accelerated myofibril kinetics, previously reported results from the patient-myectomy samples also described a decrease in tension-cost efficiency, suggesting increased myosin head cycling and nucleotide consumption while producing equivalent or lower tension. To assess if the increased kinetics and decreased contractility is due to the R403Q impacting nucleotide cycling kinetics, we isolated purified porcine cardiac sub-fragment 1 (pc-S1) to perform single nucleotide turnover measurements in the absence of actin. As discussed in Chapter 2, single nucleotide transients were fit by a single-exponential decay. Interestingly, observed rate constant values between R403Q and control preparations showed no significant difference in turnover kinetics. These findings suggested that the structural perturbations caused by the R403Q

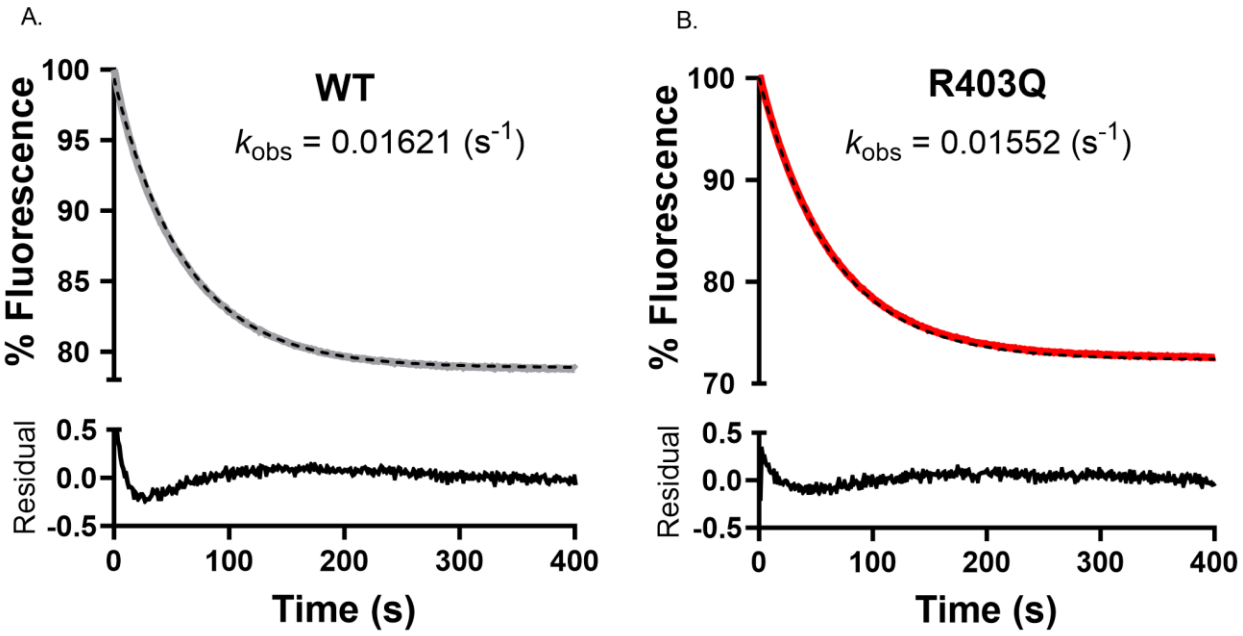

Figure 4. Single nucleotide turnover done with pc-S1 in the absence of actin show no difference between R403Q and control decay rate constants.

Single-exponential decay fits were utilized to quantify the observed rate constants for control **(A)** and R403Q **(B)** preparations. Each recording observed 125nM pc-S1 and 1uM MantATP pushed against 125mM unlabeled ATP.

did not directly impact the nucleotide cycling dynamic of myosin, and that the point mutation alone was not responsible for the accelerated product release observed in the myofibril preparations.

- *Molecular dynamic simulations showed R403Q does not alter the nucleotide binding pocket in the M.ADP.Pi structural conformation*

Results from the single nucleotide turnover measurements suggested that the R403Q mutation had no significant impact myosin's ability to dissociate from mantADP during product release. To validate these results, we decided to utilize molecular dynamic (MD) simulations to

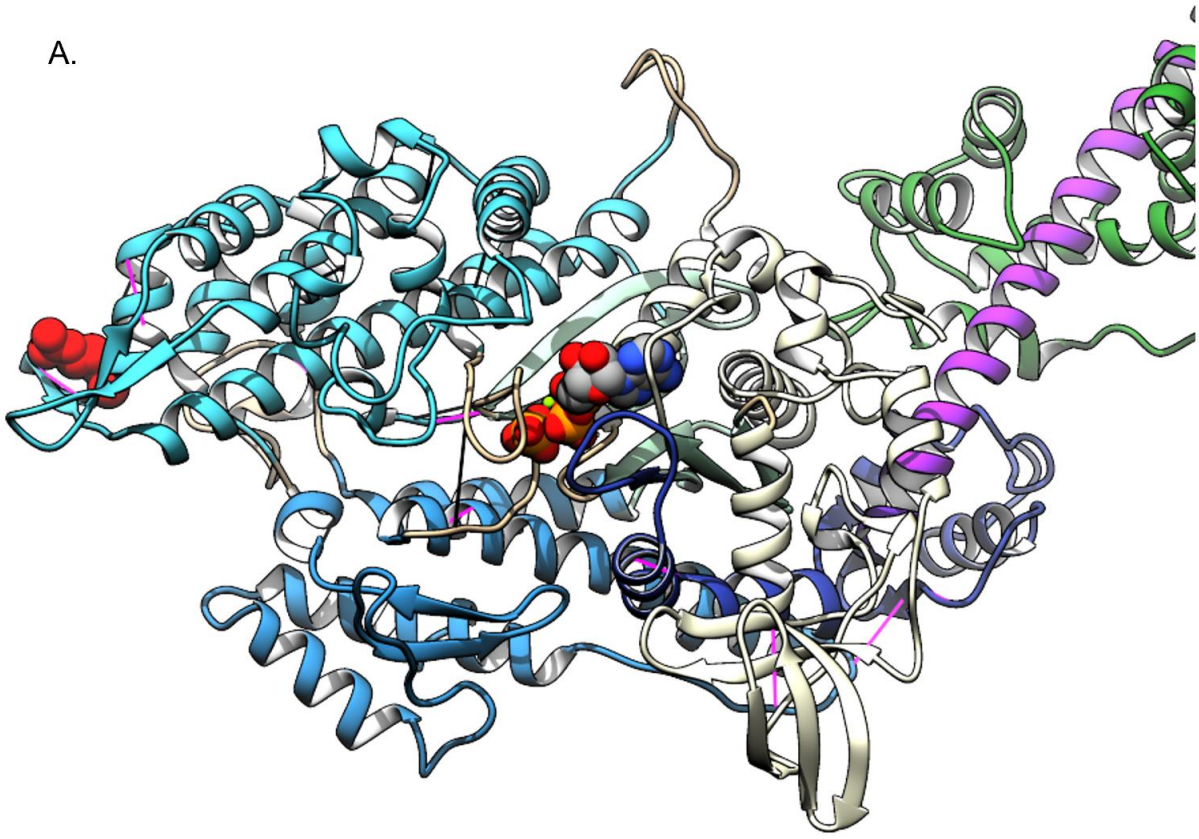

Figure 4. Molecular dynamic illustration of M.ADP.Pi visualizing residue-residue interaction frequency differences with R403Q in myosin.

An illustration highlighting the structural comparison between control and R403Q in a pre-power stroke configuration of myosin. The image shows the residue-residue interactions on myosin that interact more frequently in WT simulations (black bar) compared to simulations run with R403Q (pink bars).

observe the structure of myosin in the M.ADP.Pi (pre-power stroke) conformation. Through homology modeling of known β-cardiac structures, we inserted the R403Q mutation and observed changes in structure caused by different residue interactions. The change from arginine, which is a charged amino acid, to glutamine, an uncharged amino acid, caused a significant amount of structural changes in the residue-residue interactions within the actin-binding site of myosin, which is where the mutation is located. There were no significant changes to the residue interactions near the nucleotide binding site, suggesting that R403Q has no direct impact on nucleotide interactions.

v. Discussion & Future Direction

Since the original discovery of the R403Q mutation, researchers have worked to understand the underlying mechanisms of sarcomeric-associated cardiomyopathies. Recent studies using β-cardiac myosin suggest that many myosin missense HCM mutations causing hypercontractility are due to shifts of the myosin population towards increased heads availability and activity. Throughout the literature, several studies have performed ATPase experiments to assay the population percentage of myosin in the denoted “SRX” state. Although our results in Chapter 2 suggest that these assays are unreliable, it does not mean however that the increased disorganization and IHM formation does not exist. Contrarily, our x-ray diffraction measurements would strongly suggest a shift in myosin head population towards increased activity, as the changes in intensity ratio and myosin organization are significantly changed compared to controls. Specifically, our diffraction results indicate that the myosin organization along the thick filament is significantly reduced. These results suggest that the R403Q mutation impacts the structural stability of the myosin in the IHM conformation and increases the population of myosin readily available to interact with actin.

The results utilizing myosin modulators Mavacamten and dATP further suggest that the R403Q mutation is destabilizing the myosin IHM structure. By expressing a desensitized reaction

to dATP, our results indicate that most of the myosin heads are already in a “primed” actin interacting state, a position that dATP pushes myosin into through increased electrostatic affinity towards actin(Powers et al., 2019). If dATP and R403Q have the same mechanistic pathway, it would make sense that the combination is not additive in structural alteration, and that the change pre- and post- dATP in R403Q preparations would be significantly reduced compared to control. Mavacamten would, by the definition of a myosin inhibitor that stabilizes the IHM state, have a significantly greater impact on R403Q preparations. We see this to be true from our results, where Mavacamten had a significantly greater impact on the R403Q structure compared to controls.

With the R403Q mutation in a unique position on the myosin surface, residing at the tip of a pyramid of the IHM structure, it is suggested to impact the formation of IHM and potential interactions with actin. In addition to the x-ray diffraction measurements assessing myosin structure, we performed mechanical measurements to assess the impact of the mutation on contractility. Several publications studying the mutation have characterized the contractility characteristics in both α- and β-cardiac myosin expressing disease models. For this discussion, we will only focus on β-cardiac myosin in a transgenic rabbit model and patient-myectomy samples. Our observed steady-state tissue mechanics results describe significantly decreased tension generation, a significant increase in Ca^{2+} sensitivity, and a significantly lower hill coefficient value. All these relationships are suggestive of increased myosin activity at submaximal Ca^{2+} concentrations, a hallmark characteristic identified in several myosin associated HCM mutations.

In addition to steady-state mechanics, our data in myofibril contractility kinetics recapitulated the results described in patient myectomy samples. The observed accelerated myofibril activation and crossbridge detachment rates all suggest characteristics of accelerated myosin product release. No observed change in thin filament deactivation duration indicates that

the mutation is not impacting thin filament deactivation, and thus, we hypothesized that any sarcomeric dysfunction should be primarily driven by myosin.

To test this hypothesis, we isolated cardiac S1 from R403Q left ventricular tissue to perform single nucleotide stopped flow in the absence of actin. As described in Chapter 2, our goal for this assay was to not quantify the SRX-DRX population, but to calculate the exponential nucleotide decay rate constant. Interestingly, contrary to our hypothesis, the R403Q did not significantly impact the observed decay rate constant. As a measurement observing the release of MantADP release, we were initially surprised by these results. Preliminary molecular dynamic simulations however support the finds that the R403Q mutation does not impact nucleotide release kinetics alone. Our simulation showed that perturbations caused by the R403Q mutation were localized around the actin-binding domain, with minimal alterations to residue-residue contact frequencies around the nucleotide binding pocket. Since our single nucleotide assay was done in the absence of actin, there should have been no significant differences in nucleotide release.

Future experimentation will utilize unlabeled phalloidin-stabilized actin (as described in Chapter 2) to perform multiple-turnover assessment. This will allow us to observe the binding kinetics, tau, and decay transient of the R403Q compared to control. In addition to multiple turnover measurements, we will also perform standard myofibril ATPase measurements to quantify ATP consumption by the mutation. The goal for these future experiments is to fully understand how R403Q perturbates myosin function. Our current results strongly suggest that R403Q impacts the structural stability of myosin, however more is needed to understand the alterations in myosin cycling kinetics.

vi. Acknowledgements

The authors acknowledge Galina Flint and Kerry Kao for their assistance and expertise in protein isolation and stopped-flow knowledge. The authors also acknowledge Sonette Steczina for her

assistance in tissue mechanic measurements, and her future contributions through single molecule tracking. Finally, the authors acknowledge the significant contribution of Jing Zhao and Jingyuan Yu for their diligent assistance with the x-ray diffraction analysis. The research in this paper was supported by RM1GM131981, P30AR074990, HL128368.

VII. Conclusions and Future Directions

The research presented in this dissertation extends the knowledge of sarcomeric contraction and regulation by leveraging recent advances in structural, mechanical, and biochemical assays utilized in the field of muscle biology. Specifically, the scope of this thesis studies the sarcomeric protein myosin as a regulatory protein of sarcomeric function in conditions of both healthy and diseased states. The mechanistic pathways of thick filament regulation are less understood compared to the thin filament, with recent studies describing both myosin head recruitment and cycling as potential regulatory pathways. The presented studies elucidating the myofilament specific processes that underlie striated muscle function by addressing (1) the underlying regulatory role of myosin through differences in structural recruitment and biochemical cycling, (2) the structural and biochemical pathways that small molecules alter sarcomeric proteins as mechanisms of therapy for individuals with congenital heart failure, and (3) underlying mechanisms of dysfunction in hypercontractile models of striated muscle diseases.

In Chapters 1 & 2, we assessed both the structural organization and biochemical nucleotide turnover kinetics of myosin. Within the field, there are unconfirmed theories that correlate the structural positioning of myosin with the percentage of “inactive” and/or “DRX” myosin within the population pool. In Chapter 1, we prove that the generally assumed null hypothesis “biochemical DRX is equivalent and correlated to the structural OFF state” to be false by measuring both characteristics in the presence of positive inotropic compounds. Our results firmly describe that both characteristics are entirely independent of one another and should not be utilized to describe each other interchangeably. Further investigation of the SRX/DRX quantification In Chapter 2 through single nucleotide turnover assays with isolated myosin proteins showed how unreliable the quantification of the SRX population can be. Our experimentation strongly suggests that significant controls must be instituted and highlighted the importance of data transparency in the field. Although our results showed an inability to quantify

SRX/DRX population percentages due to the myosin heads being in thermos-equilibrium, we do not interpret the data to suggest that no SRX or IHM state exists in myosin. Rather that, the single nucleotide assay for isolated proteins may not be the most reliable assay for the measurement.

For this reason, the main aspect of the future directions following the studies presented in Chapter 1 & 2 centers around the development of more reliable assays to quantify the SRX/DRX population percentages. Chapter 2 highlighted the importance of reference signals and FRET excitation as experimental parameters to collect clean and reliable results. Future work will utilize these experimental factors in the development of a new permeabilized myofibril and/or myocyte assay with fluorescence capabilities to reliable measure the single nucleotide turnover decay under loaded conditions.

In addition to the development of new assays, it is also important to begin investigating other unknown mechanisms of thick filament regulation in sarcomeric function. Current and future work is highlighted by our investigation of Ca^{2+} as a modulator of thick filament activation. Although heavily understood to regulate thin filament activation, preliminary x-ray diffraction measurements in porcine myocardium expressing an engineered cardiac troponin C mutation (D65A) which inhibits Ca^{2+} binding (and thus inhibits thin filament activation even in saturating Ca^{2+} conditions) shows that myosin structure is perturbation by the presence of calcium. Interestingly, there is a location on the RLC that facilitates di-cation binding and could be a mechanism that regulates myosin activation.

In the studies conducted in Chapters 3 & 4, the newly discovered regulatory properties associated with myosin structure and cycling kinetics were utilized to assay the impact myosin mutations and novel myosin-targeting small molecules have on sarcomeric function. In Chapter 3, we show how the novel compound Danicamtiv can modulate myosin cycling and recruitment through product release inhibition. Through reductionist assessment, our study concluded Danicamtiv inhibited the release of ADP during crossbridge detachment, prolonging the strongly

bound interaction of myosin and actin in a force generating state. This mechanistic pathway proved effecting in rescue a transgenic murine model harboring a loss-of-function troponin mutation that causes dilated cardiomyopathy.

Transitioning from small molecules to mutations, Chapter 4 utilized a similar reductionist approach as described in Chapter 3 to assess how the R403Q mutation perturbated sarcomeric function. Utilize a transgenic porcine model harboring the first reported familial hypertrophic cardiomyopathy mutation, we discovered that the mutation not only altered the structural organization of myosin within the sarcomere, but also altered the contractile kinetics in complex myofibril and tissue level preparations. Interestingly, reductionistic assays utilizing purified proteins and molecular dynamic modeling showed that the accelerated kinetics was not due to the mutation impacting myosin-nucleotide interactions. Instead, it seems like the mutation alters the actomyosin interactions that then modulate sarcomeric function.

The work described in Chapter 3 & 4 provides an extensive framework on how to determine mechanistic pathways that can perturb myosin function. By combining a multi-scale assessment, we can determine how alterations in myosin structure impact sarcomeric function. Future work observing new small molecules and mutations can expand the knowledge in the field of muscle biology. Current plans focus on the characterization of a novel myosin inhibitor, Aficamten, as a future direction. In addition to small molecules, this approach can be utilized to assess new disease models. As described in the appendix, a significant portion of my thesis focused on the optimization and utilization of human induced pluripotent stem cells (hiPSC's) for contractile assessment. With the scarcity of human tissue and the developmental problems associated with animal model development (especially in murine models of cardiomyopathies due to the expression of α-cardiac myosin), iPSC's have become a tremendous platform alternative for disease modeling. Future work will focus on the assessment of new disease models through patient-derived, or engineered mutations.

VIII. Appendix: The future of disease modeling: The development and optimization of hiPSC for contractile measurements

In addition to the described thesis work above, a substantial portion of my graduate study was focused on the development and optimization of contractile measurements of myofibrils isolated from human induced pluripotent stem cells (hiPSC's). Currently, a large portion of mechanical assessment of iPSC's in the field utilizes whole cell assays to measure contractility. A generally used technique is through surface deformation tracking, where differentiated cells are cultured on Matrigel surfaces filled with florescent beads. During cell contraction, the Matrigel deforms and is pulled by the cell. This mechanical contraction of the surface can be quantified by measuring the movement of the beads through optical imaging. This measurement technique, although useful, is limiting in both the diseases it can be applied to, as well as the conditions it can be exposed to. Sarcomeric and membrane mutations with significantly depressed tension may be difficult to investigate, while the requirement of keeping the cells intact for electrical stimulation can limit the number of viable assays that can be completed.

By performing permeabilized mechanics, one can get extremely rich information about the sarcomeric dysfunction caused by a mutation and perform measurements at both physiological and maximal calcium concentrations. The myofibril assay provides a technique to determine fundamental sarcomeric function that describes both tension generation and activation/relaxation kinetics. The experimental conditions are done under a uniaxial load, and remove the potential issues caused by membrane anchor proteins on the culture surface. Prior to joining the Regnier research group in 2017, a few publications had successfully utilized iPSC's to report loaded contractile readouts from cardiac myofibrils (Pioner, Fornaro, et al., 2020; Pioner, Guan, et al., 2020; J. M. Pioner et al., 2016; Pioner et al., 2019; Racca et al., 2013; Woulfe et al., 2019). These publications focused on cardiomyocytes, with no utilization of skeletal myotubes yet to be published. Initial conditions for iPSC cardiomyocytes (CM's) provided inconsistent cellular

preparations, with significant limitations in myofibril yield, maturation, and myofibril alignment. Cells were cultured for greater than 80 days in normal maintenance medium, with no myosin isoform optimization protocols.

Through rigorous platform development and incredible diligence with colleagues including Sonette Steczina, Kerry Kao, Dr. Shawn Luttrell, and Dr. Christian Mandrycky, we have been able to generate reliable protocols for iPSC cardiomyocyte and skeletal myotube culturing, myofibril isolation, and contractile assessment. Our platform development of hiPSC's included the incorporation of patterned culturing surfaces, cell type and myosin isoform expression optimization, and physiological Ca^{2+} tolerance. The appendix section consists of **(A)** a methods chapter of how to collect myofibril activation and relaxation measurements from iPSC-CM's, **(B)** an example of my work with iPSC skeletal myotubes and the utilization of the platform to model embryonic diseases, and **(C)** an example of my work with iPSC-CMs through the assessment of a hypertrophic cardiomyopathy disease caused by a mutation in cardiac MYBP-C.

IX. Appendix A: Measuring the contractile kinetics of isolated myofibrils from human-induced pluripotent stem cell derived cardiomyocyte (hiPSC-CM) models of cardiomyopathy

This appendix section represents the submitted version of a first-author methods chapter.

Saffie Mohran, Sonette Steczina, Christian Mandrycky, Kerry Kao, Michael Regnier

i. Abstract

Isolated myofibrils provide biomechanical data at the contractile organelle level that are independent of cellular calcium handling and signaling pathways. These myofibrils can be harvested from animal tissue, human muscle biopsies, or stem cell-derived striated muscle. Here we present our myofibril isolation and rapid solution switching protocols, which allow for precise measurements of activation (kinetics and initial tension generation) and a biphasic relaxation relationship (initial slow isometric relaxation followed by a fast exponential decay in tension). This experiment is generated on a custom-built myofibril apparatus utilizing a two-photodiode array to detect micron level deflection of our forged glass tip force transducers. A complete activation/relaxation curve can be produced from a single myofibril in under 30 minutes.

- *Key Words*

Myofibrils, Muscle Mechanics, Kinetics, Actomyosin, Product Release, ATP Binding, Myofilament, Sarcomere, Thick Filament, Thin Filament, Myosin, Crossbridge Cycling

ii. Introduction

Fundamental mechanisms of thin-filament regulation and actomyosin crossbridge cycling in striated muscle are reliant on the concentration of exposed calcium as well as the composition of sarcomeric proteins within the myofilament. Permeabilized muscle (trabecula and/or single cell) preparations enable precise mechanical experimentation of the myofilament function since all the cellular and sarcoplasmic reticulum (SR) membranes have been removed (Baylor & Hollingworth, 2011; Gordon et al., 2000). These experiments, however, are limited when studying activation and relaxation kinetics due to tissue thickness and diffusion constraints (Marston, 2021). To overcome these limitations in diffusion kinetics, the isolated myofibril assay (Figure 1A) was developed to utilize preparations approximately 3 microns wide, all while retaining the entire filament lattice structure and complete motor protein assembly (Note 1).

Numerous studies have utilized the myofibril apparatus to elucidate fundamental mechanisms on thin-filament regulation and crossbridge cycling of muscle (J. M. Pioner et al., 2016; Piroddi et al., 2007; Racca et al., 2013; Racca et al., 2016; Vitale et al., 2021; Woulfe et al., 2019). Many studies have also investigated how perturbations caused by mutations (Belus et al., 2008; Pioner, Guan, et al., 2020; Josè Manuel Pioner et al., 2016; Racca et al., 2015) and/or small-molecules (Scellini et al., 2021) impact the chemo-mechanical properties of the sarcomere. Changes in kinetics, force production, and passive tension in activated and relaxed conditions provide insights into myofilament (thick, thin, and elastic filaments) function, thin-filament calcium regulation, and actomyosin crossbridge cycling. In activated conditions, myofibril activation kinetics (k_{ACT}), and force production, are all accessible due to the rapid and sustained exposure to high [Ca^{2+}] solutions. Following activation, myofibril relaxation can be assessed with a rapid change back to low [Ca^{2+}] solution and occurs in two phases (Poggesi et al., 2005).

Each portion of the myofibril trace (Figure 1C) can provide an understanding of how different protein variants influence myofibril function. Here we present a protocol for performing

myofibril experimentation on human induced pluripotent stem cell derived cardiomyocytes (hiPSC-CMs). These hiPSC-CMs provide critical disease modeling capabilities including longitudinal disease development studies and a mechanism for therapeutic screening.

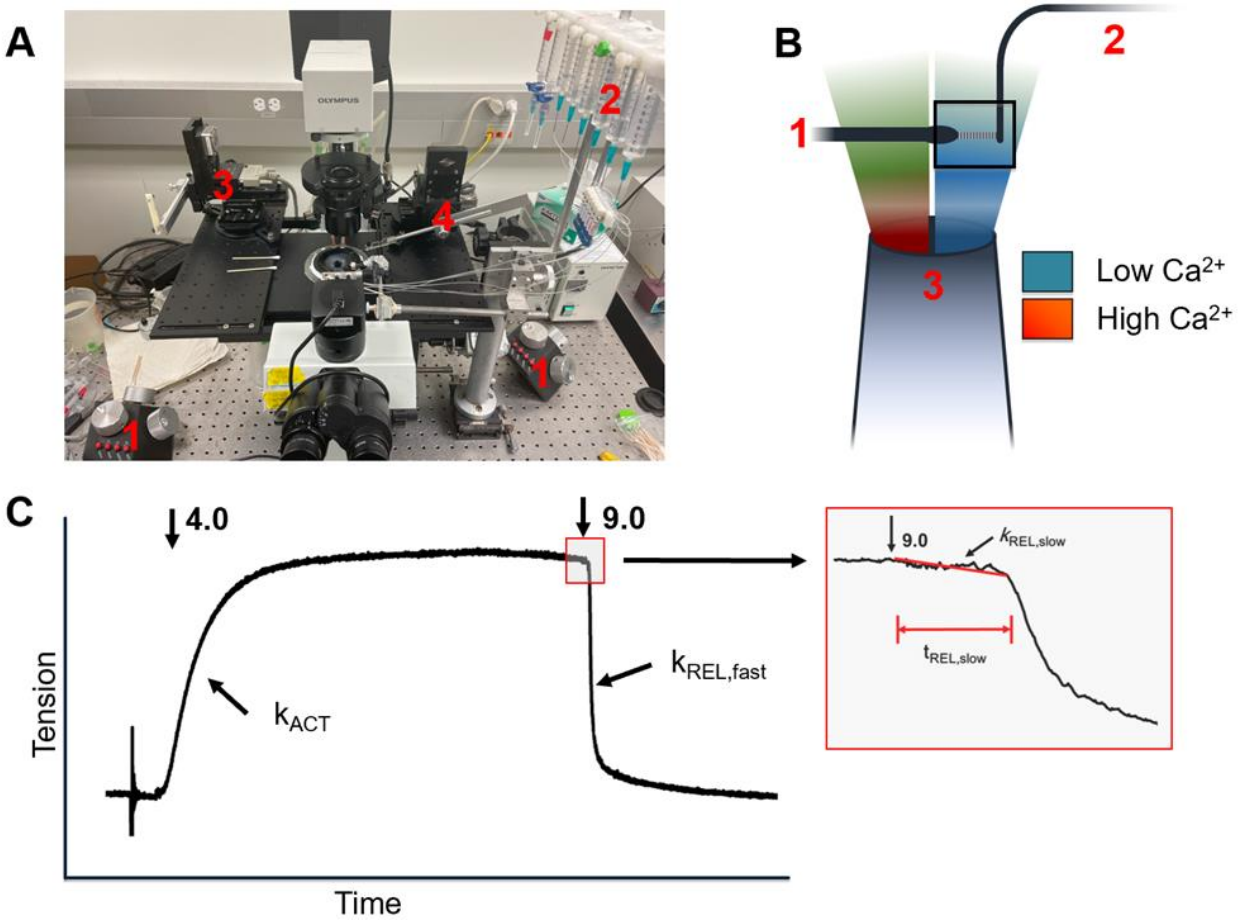

Figure 1. General overview of the myofibril rig and important calculations.

An image **(A)** of the myofibril rig utilized in the Regnier Laboratory in Seattle, WA. Illustration shows the micromanipulators (1), perfusion system (2), motor arm (3), and force transducer holder (4). **B)** Is a cartoon schematic illustrating the experimental procedure, where a myofibril is mounted between a motor arm (1) and force transducer (2) and exposed to high and low Ca^{2+} with a double-barreled pipette. **C)** An example recording of a myofibril activation/relaxation, illustrating the key kinetics and where they are quantified.

iii. Materials

1. Buffers

1.1. Buffer components are listed as the final concentrations [mM] in solution (Note 2).

Component [mM]	**High Ca^{2+}** *pCa 4.0*	**Submaximal Ca^{2+}** *pCa 5.6*	**Low Ca^{2+}** *pCa 9.0*
$CaCl_2$	15.29	12.37	0.03
$MgCl_2$	6.93	6.98	7.19
$K_{2.024}$EGTA	15	15	15
MOPS	80	80	80
Na_2ATP	6.22	6.98	5.98
Creatine Phosphate	15	15	15
KOH	88.26	88.28	88.28
NaOH	55.34	55.36	55.36
HCl	48.77	49.57	49.53
Tris	0.33	0.85	0.76

2. Glass Force Transducer

Making Glass Needles

2.1. Sutter Instrument Model P-27 (Flaming/Brown Micropipette puller)

2.2. Sutter Borosilicate glass #B4100-50-10 (with or without filament | OD: 1.0mm, ID: 0.5mm)

2.3. Narishige MF-900 Micro Forge

2.4. Alcohol based black ink (3084-F black india rapid-dry ink)

Calibration of Needle

2.5. Needle calibration galvanometer

2.6. External sinusoidal signal generator

3. Pattern Fabrication

3.1. 0.004 g/mL Bisacrylamide

3.2. 0.076 g/mL Acrylamide

3.3. 35.32 mM HEPES

3.4. Bind-silane solution:0.3% v/v 3-(Trimethoxysilyl) propyl methacrylate (bindsilane), 95% v/v Ethanol, 5% v/v Acetic Acid (Glacial)

3.5. Corning® Matrigel® Growth Factor Reduced (GFR) Basement Membrane Matrix, Phenol Red-free, LDEV-free

3.6. 100% Ethanol

3.7. Ammonium Persulfate (APS)

3.8. TEMED

3.9. Gibco™ Phosphate buffered saline (PBS), no calcium, no magnesium

3.10. Cellvis 6 Micro-well Glass Bottom Plate 20mm Micro-well, #1.5 Glass (P06-20-1.5-N)

4. Stem cell culture media

4.1. Gibco™ Roswell Park Memorial Institute (RPMI) 1640 Medium

4.2. Gibco™ Dulbecco's Modified Eagle Medium (DMEM) Medium (minus glucose)

4.3. Gibco™ B-27™ Supplement (50X), serum free

4.4. Gibco™ Phosphate buffered saline (PBS), no calcium, no magnesium

4.5. Rock Inhibitor Y-27632 2HCl (Selleck Chemicals Catalog No.S1049)

5. Myofibril Isolation Solution

5.1. Low Ca^{2+} relaxation solution (See 2.1.1)

5.2. Protease Inhibitor Cocktail (Sigma-Aldrich)

5.3. Triton X-100

5.4. Cell Scraper

6. Myofibril Apparatus

6.1. Scope: Olympus IX71 with 10X CPlan FLN & 40X LUCPlan FLN objectives

6.2. Cooling: Lauda RA8

6.3. Photodiode array: Hamamatsu S4204

6.4. Micro-controllers: 2x Sutter MP-225 micromanipulators

6.5. Solution controllers: Warner Instruments Digital Valve Control System

6.6. Double-barreled pipet: Warner instrument borosilicate theta glass OD: 2.0 mm, ID: 1.4 mm, SEP 0.2 mm, Length 10 cm (item # TG200-4)

6.7. Piezo (Fast switch solution changer) (Warner SC-77)

6.8. Computer: Dell OptiPlex 7090 Tower

6.9. NIH DAQ: NI USB-6259

6.10. Acquisition Software (e.g., LabView)

iv. Methods

Preparatory work prior to the day of experimentation includes making the desired buffers (Method 3.1), the forging and calibration of a glass force transducer (Method 3.2), and the culturing of uniformly aligned hiPSC-CM's (Method 3.3). On the day of experimentation, preparatory work involves careful isolation of myofibrils from the hiPSC-CM's (Method 3.4), filling the tubing with calcium solutions (Method 3.5.1), preparing the rig by cleaning the trough (Method 3.5.2), and maintaining the desired temperature (15°C) of the trough. After the isolation and plating of myofibrils, an experiment on a single myofibril consists of: the identification of a myofibril (Method 3.6.2), attachment of the myofibril to the motor arm and force transducer needles (Method 3.6.6 - 3.6.9), positioning the myofibril in front of the double-barreled pipet (Method 3.6.10 – 3.6.13), preparing the myofibril and acquisition software (Method 3.6.14), running the acquisition software and generating an activation/relaxation trace (Method 3.6.15 – 3.6.16), and performing a calibration plot (Method 3.6.17 – 3.6.19). Data analysis involves processing the myofibril traces through semi-automated software, converting the raw voltage trace to tension, and calculating all the kinetic and mechanical values (Method 3.8).

1. Preparing Experimental Solutions

All pCa ($-\log_{10}$ [Ca^{2+}]) solutions can be made and aliquoted prior to experimentation day and stored in -20°C freezer for approximately 6 months. Solutions should then be kept on ice throughout the day ready for use.

2. Creating a Force Transducer Library

Prior to experimentation day, it is important to generate a library of glass force transducers that range between 18-25mm/μN. This range of needle stiffness will provide flexibility to quantify most iPSC-CM based models of hyper- and hypo-contractile disease models.

2.1. Obtain Sutter borosilicate glass and load inside the Sutter P-27 micropipette puller. When loading the glass into the puller, make sure to leave an even length of glass on either side so that the center of the glass is within the center of the filament inside the box. Once the glass is properly loaded close the tinted lid and turn on the P-27. Input the following commands so that the program reads “pressure = 200”, “heat = 620”, “Pull = (blank)”, “Vel = 120”, “time = 100”. Then press pull.

2.2. Once the glass has been pulled apart, the program will alert that the action has been completed. Turn off the P-27, lift the lid, and gently remove one of the needle pieces. Insert the glass needle into the Narishige MF-900 Micro forge holder, with the “floppy” side of the needle protruding outwards. Placing the needle into view, use a pair of micro scissors to cut the “floppy” portion of the pulled needle to approximately 2.5um wide as shown in Figure 2A. Once the glass has been cut, seal the end of the tube with the micro forge at low heat (Figure 2B), making sure to not bend the needle in any direction.

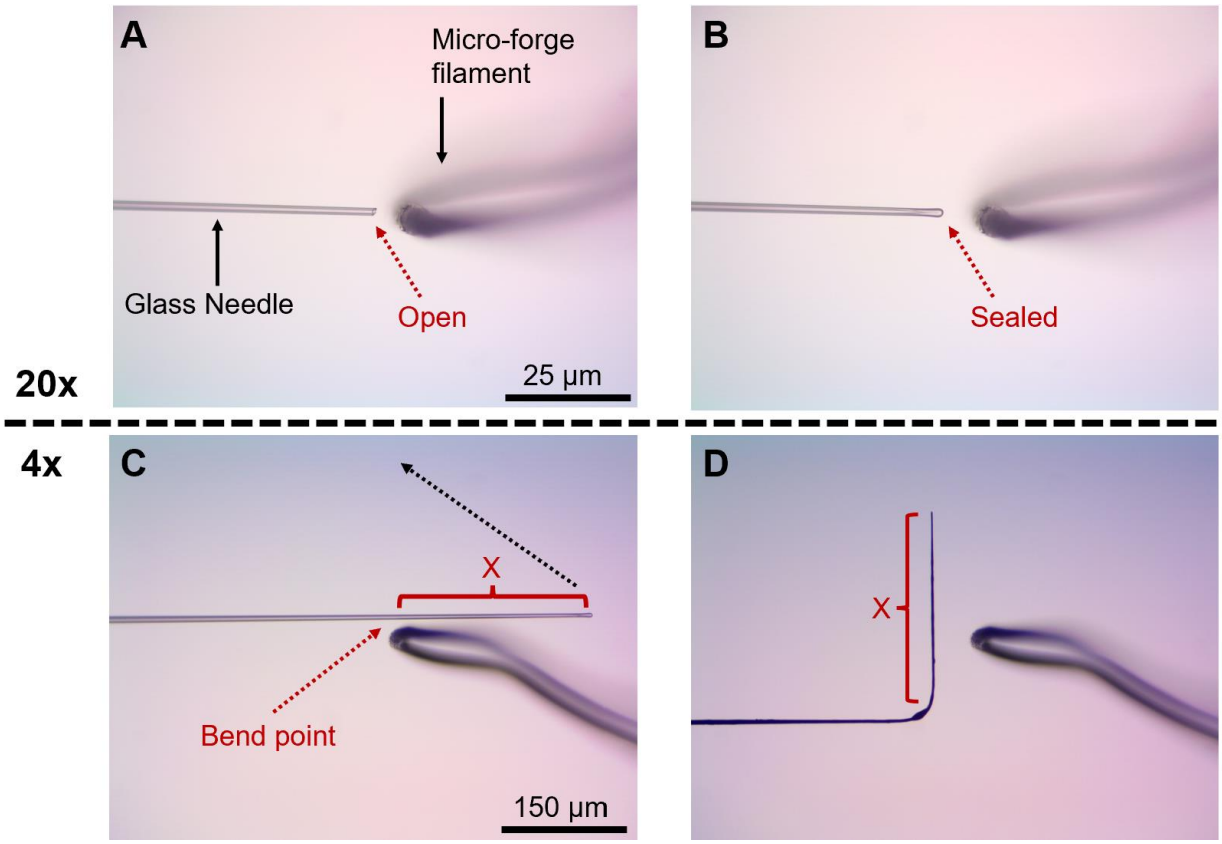

Figure 2. Sequence of images illustrating the fabrication of force transducer needles.

The first step **(A)** is where a freshly pulled needle is cleaned of the floppy tail and mounted on the micro-forge. The needle tip is open, and in focus with the 20x objective. **B)** Utilizing the micro-forge, gently heat the tip of the needle until the glass melts and seals. Take care not to deflect the needle in any direction. *Stopping at B would produce a motor arm, utilizing during the day of experimentation to pick up one end of the myofibril*. **C)** Under the 4x objective, position the sealed needle to overlap the micro forge filament. This overlap length (X) will become the length of the force transducer end. Gently heat the needle, slowly bending the needle upwards and forming a 90° angle. **D)** The finished product, where the needle has been bent and inked. Make sure no black blobs of ink are left on or near the tip of the force transducer during the inking process.

2.3. Once the needle is sealed, force transducers need to be bent to function properly on the rig. Ideally, force transducer lengths (portion that is bent) should be over 125um long and form a 90-degree angle to the bulk of the needle.

Utilizing the 4x objectives on the MF-900, measure the needle ~20 divisions above the microfilament, and then ~35 divisions directly across the microfilament as shown in Figure 2C. Using low heat, bend the needle to the appropriate 90 degrees, bringing the needle down closer to the microfilament and slowly increasing the heat level. (Note 3)

2.4. Once properly bent, force transducers also need to be inked in black alcohol-based ink. To ink the needles, create a small bubble of ink at the nozzle of the 3084-F ink bottle. Slowly move the needle through the bubble, making sure to not leave any large blots of ink on the needle. The final product should be a uniformly black needle with no ink blots as shown in Figure 2D. (Note 4)

2.5. Once the needle is properly inked, it is important to label them for easy identification. Any marking and recording system on the needle itself will be sufficient to enable proper identification of a needle post-calibration (Note 8).

3. Force Transducer Calibration

3.1. Obtain the needle calibration box (galvanometer) and a sinusoidal signal generator. The galvanometer should consist of an extremely sensitive (and fragile) protruding rectangular metal lever of known length and ~100μm in width and height. There should also be a port to connect to the signal generator.

3.2. Remove all material off the myofibril rig including the experimental well and double-barreled pipet (leaving nothing on the black stage (baseplate). Place the galvanometer onto the stage in a position that allows for the protruding lever to be visible under the microscope. Once the lever is visible, place the tip of the lever along the reticle in the eyepiece using the 40x objective. Secure the calibration box in place.

3.3. Plug the galvanometer into the sinusoidal signal generator and run a slow 0.5Hz signal at 0.1V. This should cause the protruding lever on the galvanometer to begin moving side-to-side, following the signal generator. As the voltage increases (amplitude of the sine wave), so does the displacement of the lever from center. Identify a voltage that deflects the lever ~20µm from center. This voltage will be used as the initial amplitude when calibrating force transducer needles.

3.4. Run the signal generator at 0 volts and center the galvanometer lever. This location defines 0um of deflection from center. Turn off the signal generator and mount a force transducer needle for calibration. When mounting the force transducer, place the tip of the needle along the top edge of the galvanometer lever, and make sure that both the needle and lever are touching (Note 5)

3.5. Run the signal generator at the previously identified voltage that deflects the galvanometer lever ~20µm. Record the input voltage and measure the correlated force transducer needle deflection distance three times. Average the observed deflection values and move onto the next voltage. Collect 10 - 15 separate voltage readings where the deflection ranges from 0 - 30 um. (Note 6).

3.6. Once the different voltage values have been recorded, divide each deflection distance by its corresponding recorded voltage (units µm/V). These normalized deflection distances are then multiplied by the galvanometer calibration factor value, calculating the stiffness of the needle at each voltage (unit: µm/µN). These numbers should be approximately the same. By averaging all the different values, one can then calculate the average stiffness of the force transducer needle (Note 7).

4. hiPSC-CM Pattern Fabrication and Cell Seeding

4.1. Preparing patterned culture surfaces is a three-day process. On the first day, prepare PDMS micropattern stamps. The micropattern geometry is lines of 15μm width and 5000μm length and a total stamp area of 1 cm^2 by 1 cm^2. Coat PDMS micropattern stamps with Corning® Matrigel® Growth Factor Reduced (GFR) Basement at a concentration of 1.0 mg/mL. Store stamps overnight at 4 °C to coat.

4.2. On the second day, begin by degassing polyacrylamide gel precursors in a vacuum chamber for at least 1 hour (Note 9).

4.3. Plasma-treat a Cellvis 6 micro-well glass bottom plate at 30W for 30 seconds. Within 5 minutes of plasma treatment, coat the surface of each well with 100uL of Bind-silane Solution. After 1 minute, remove excess Bind-silane Solution. After 10 minutes, rinse wells with 100% ethanol and allow them to dry completely.

4.4. Prepare 18mm coverslips for each well by rinsing with 100% ethanol and allowing them to dry completely. Aspirate excess Matrigel from coated stamps. Dry with a gentle stream of N_2. Immediately, stamp clean 18mm coverslip with dry stamp. Place a 50g weight on top of the stamp for 5 minutes to transfer Matrigel to the 18mm coverslip. After 5 minutes, remove weight and stamp and set aside 18mm coverslip.

4.5. Remove gel precursor solution from vacuum chamber. Start polymerization of gel solution by adding 0.5uL TEMED and 5uL 10% APS. Mix gently, but thoroughly. Add 50uL of gel solution into the center of each well. Immediately, gently place stamped 18mm coverslip over gel solution, ensuring that the

protein-stamped side is face-down. Allow to polymerize in the dark for 30 minutes. Store overnight by filling wells with DPBS and storing wrapped in foil at 4°C.

4.6. On the third day, seed hiPSC-CMs onto prepared patterns. To do so, first prepare a hiPSC-CM cell suspension of at least 1e+6 cells/mL. A cell suspension of up to 2e+6 cells/mL will grant a higher cell patterning yield.

4.7. Next, carefully remove 18mm coverslip from gels using sterile forceps. Aspirate DPBS. Seed 0.5mL of the cell suspension into each well (Note 4.10). Allow to rest in an incubator (5% CO_2, 37°C) for 2 hours before carefully adding pre-warmed re-plating media (RPMI + 1X B27 supplement + 10μM Rock Inhibitor) at 2 mL/well.

5. Culturing Patterned hiPSC-CMs

5.1. 24 hours after plating hiPSC-CMs (day 1 post plating) onto the pattern surface, replace replating media with pre-warmed culture media composed of 50% RPMI:50% DMEM (no glucose) + 1x B27 supplement (Notes 10 – 12).

5.2. Day 3 post plating, replace old media with pre-warmed culture media composed of 25% RPMI:75% DMEM (no glucose) + 1x B27 supplement.

5.3. Continue replacing the media every 48 hours (day 5, 7, etc.) with 25% RPMI:75% DMEM (no glucose) + 1x B27 supplement until day of myofibril isolation.

5.4. Culture cells on the patterned surface for between 8-12 days depending on the chosen timepoints.

6. Isolation of hiPSC-CM myofibrils

6.1. Prepare myofibril isolation solution (1mL of pCa 9.0 relaxation solution per 35mm well of patterned cells + 1% Triton X-100 +1:100 protease inhibitor cocktail) and wash solution (1.5mL of pCa 9.0 relaxation solution per 35mm well of patterned cells +1:100 protease inhibitor cocktail).

6.2. Bring myofibril isolation solution and sterile phosphate buffered saline (PBS) into sterile tissue culture hood. Transfer the 6-well plate with patterned cells into cell culture hood. Gently tilt the plate a few degrees and aspirate the media. Add 1mL of PBS to each well to wash the cells and then aspirate the PBS off. Gently add 1mL of myofibril isolation solution to each, ensuring that the patterned surface is covered with solution.

6.3. Continue this process quickly for all remaining wells. Transfer the plate to a bucket full of ice or 4°C fridge and start a timer for 10 minutes.

6.4. After the 10-minute incubation time, gently tilt the plate and remove the myofibril isolation solution from the first well. Place the supernatant into a labeled tube (Note 13).

6.5. Still on ice, quickly add 0.5mL of wash solution (first wash step) onto the pattern surface and swirl the plate gently to wash off excess Triton X-100. Perform this first wash step for all wells that had been permeabilized with the myofibril isolation solution.

6.6. Once all wells have been washed with 0.5mL of wash solution, repeat step 3.4.5 with 1mL of wash solution (second wash step).

6.7. Use a cell scraper to gently scrape off the myofibrils from the patterned surface so the myofibrils are now floating in the second wash solution. Once you have scraped off the myofibrils from each well, transfer the second wash solution with myofibrils into a clean glass tube and keep the tube on ice. The hiPSC-CM myofibrils are now ready to be pipetted onto the myofibril apparatus.

7. Performing Myofibril Experiments – Solution Preparation

7.1. First, remove the distilled water (ddH_2O) from all the syringes that was left in the system after the previous usage. Turn on the perfusion control box (Warner Instruments), load ~3mL of new ddH_2O into the perfusion syringes and allow 2mL to flow through the tubing. This will ensure that there is no potential debris and/or air bubbles in the tubing. Once sufficient ddH_2O has been flown through, stop the perfusion, and remove all the excess water from the syringe without creating any bubbles at the bottom of the syringe.

7.2. Individually begin loading the different syringes with the correct Ca^{2+} solutions, making sure that all relaxation solutions flow into the right side of the double-barreled pipet, and all activation solutions flow into the left side.

7.3. Once all syringes are loaded, allow the perfusion system to run. This will load the tubing with the Ca^{2+} solutions and be ready for experimentation (Note 14).

8. Performing Myofibril Experiments – Rig Preparation

8.1. Once the Ca^{2+} solutions are properly loaded, turn on both micromanipulator controllers (Sutter MP-285) in the tower, the perfusion piezo motor controller (Warner instruments) (Note 15), the water bath that cools the experimental well (set at 15°C) and the computer.

8.2. On the computer, open the myofibril acquisition software and oscilloscope application. In the acquisition software, load the experimental configuration desired, and input the necessary preliminary information including user initials, myofibril description, number of desired activations (and what pCa), needle stiffness, step function size (Note 16), and directory folder for saving the activation files.

8.3. Mount the desired force transducer needle onto the rig utilizing the needle holder. Under the scope, make sure that the needle is parallel with the bottom of the well.

9. Performing Myofibril Experiments

9.1. Clean the glass surface of the well thoroughly with 70% ethanol and a long-handled cotton Q-tip. Once the surface has been cleaned, use a syringe to remove the EtOH into a waste beaker, and rinse 3x with ddH_2O water. Dry the surface with a Kimwipe.

9.2. Add approximately 100µL of the myofibril solution onto the glass well. Add 750µL of pCa 9.0 solution and examine the glass for myofibrils. Switch to the 10x objective and observe the experimental well. There may be a significant amount of Matrigel pattern material which is okay. Once a myofibril has been identified (Figure 3A | Note 17), gently add 3mL of pCa 9.0 solution to the very edge of the well, taking great care not to disrupt the myofibrils below.

9.3. After confirming that the myofibril is still well adhered to the glass after the addition of 3mL pCa 9.0, raise the objective view 0.5 to 1.5mm (depending on working distance of objective) from the glass. Bring your double-barreled pipet into view. Turn on the perfusion and ensure that there are no bubbles that may

have entered the system. Turn off the perfusion and bring the force transducer needle into view with the double-barreled pipet.

9.4. Once both the force transducer and double-barreled pipet are in view, use the MF-900 micro-forge and carefully fire polish a motor arm (Note 18). Once the motor arm is made, mount the needle onto the manipulator utilizing the motor arm holder, and lock the arm into place. Using the micromanipulator, move the motor arm until it is in view with the force transducer and double-barreled pipet.

9.5. Once the motor arm is in view, drop the focus of the objective until you can see the myofibril again. Slowly move the force transducer and motor arm until they are hovering above the myofibril (not touching yet). On the MP-250 controller box, select the lowest sensitivity program (denoted by pressing “move”, “5”, “move”).

9.6. Change to the 40x objective and focus on the myofibril. Identify the location on the myofibril where the motor arm will attach to the myofibril (Figure 3A), typically somewhere on the left edge where the motor arm has easy access. Using both hands on the motor arm manipulator, very gently press the motor arm down onto the myofibril, pressing down through the myofibril and against the glass. Very slowly move the motor arm side to side along the glass over the width of the myofibril, securing the myofibril to the motor arm.

9.7. Slowly begin to raise the motor arm, taking great care to make sure that the myofibril remails adhered to the motor arm. Maneuver the motor arm so that it begins to gently peel the myofibril off the glass. Do this until ~10μm of the myofibril remains adhered to the glass.

9.8. Set the force transducer sensitivity to the lowest setting (as described in 3.6.5). Move the force transducer needle down so that the tip of the needle sits on the glass, to the left of the myofibril that is still adhered to the glass. Slowly move the force transducer until it contacts the myofibril (in a region similar to the designated spot in Figure 3A | Note 22).

9.9. Manipulate the myofibril with the motor arm so that it lays across the force transducer, and then move the force transducer to the right, underneath the myofibril, adhering to the ~10μm of myofibril that was still adhered to the glass, and lifting it (Note 19).

9.10. Once the myofibril is secured between the motor arm and force transducer (example shown in Figure 3B), use the micromanipulators to bring the myofibril into the plane of the double-barreled pipet (Figure 3C | Note 20). Move the well plate so that the myofibril is in the center of the glass (to ensure the most light is available, you do not want to be on the edge of the well), switch to the 10x objective, and properly position the double-barreled pipet in front of the myofibril (Note 21).

9.11. Once the double-barreled is properly positioned, switch back to the 40x objective. Measure the parameters of the myofibril including myofibril diameter, length, and sarcomere length using the reticle in eye piece and record them in the data acquisition program.

9.12. Once all the information is recorded in the acquisition software, open the oscilloscope program to position the force transducer. Position the motor arm and force transducer so that the myofibril is exactly horizontal (parallel to the glass well), and the force transducer tip is within the boundary of the two-

photodiode system. Switch the light filter to bright field (BF), move the motor arm, myofibril, and force transducer together until the lower and upper voltage limits (-10V to 10V) are found (Note 23).

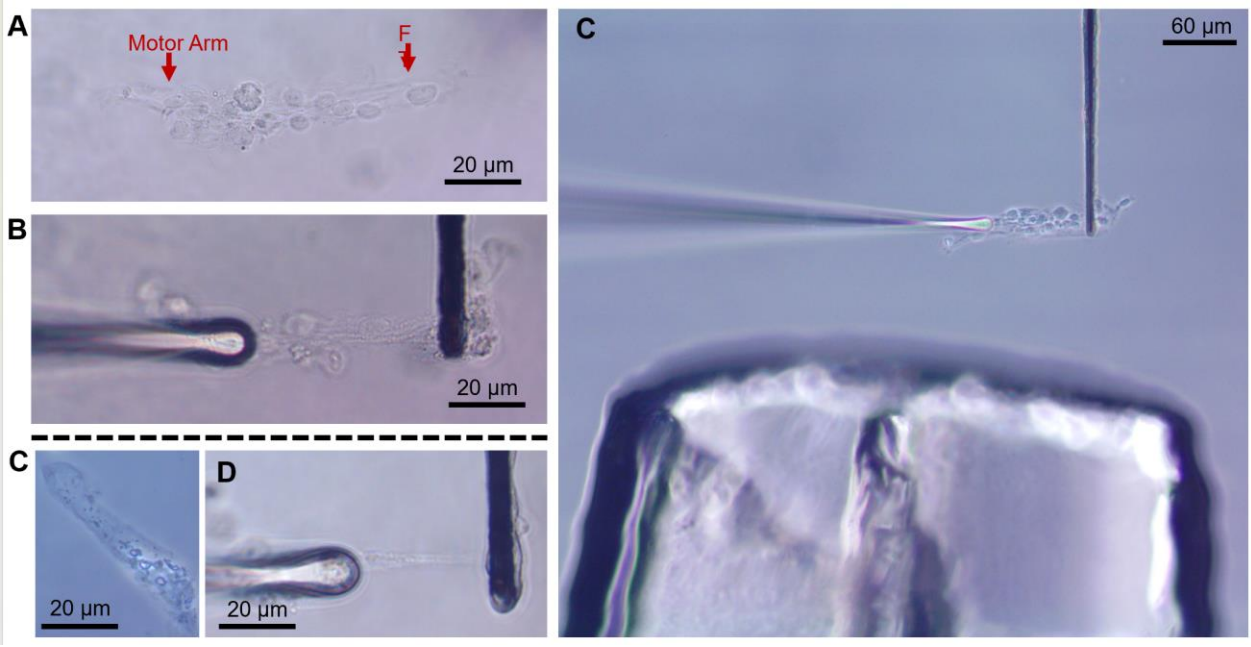

Figure 3. Illustration of an example myofibrils, attachment, and positioning.

A) An example of a day 45 iPSC-CM myofibril bundle differentiated from the WTC-11 background. The myofibril is a representative image of how several myofibrils are covered with nuclei and other cellular debris. The attachment points (labeled as motor arm & FT) on the myofibril, however, are clean and easily accessible. **B)** An example of how the motor arm and force transducer looks when attached to the myofibril bundle. The myofibril is attached to the bottom of the FT, and then looped over the top of the FT. All attachment is achieved through electrostatic adhesion. **C)** Another example of a myofibril, without the cellular debris attached. These myofibrils should be prioritized as the have the greatest chance for proper attachment due to the lack of debris. **D)** An image of the clean myofibril attached to the motor arm and FT. **E)** Myofibril from A, showing the position of the myofibril relative to the double-barreled pipette. Most of the cellular debris attached to the myofibril will be flushed off by the Ca^{2+} solution during experimentation.

9.13. Position the force transducer tip at ~-8V and return the length of the myofibril to the observed length that pulls the sarcomere length to ~2.3µm.

9.14. Turn on the perfusion system and begin perfusion of relaxation solution. Observe the oscilloscope and make sure that the flow of solution has not moved the force transducer position. Begin flowing the activation solution, and again, make sure that the flow does not impact the reading of the oscilloscope (Note 24).

9.15. Set the piezo motor for the double-barreled pipet to “Ext Analog” to allow the computer to control the pipette movement. Click “Acquire Data” on the ‘Acquisition Program’ and record all the myofibril activation measurements (Note 25).

9.16. Once all the myofibril traces have been collected for one myofibril (example trace shown in Figure 4A), slightly slack the myofibril, and turn off the activation solution. Move the slacked myofibril so that the force transducer tip is located slightly out of the 2-photodiode view (reading a -10V value on the oscilloscope). Turn off the relaxation solution.

9.17. Turn the sensitivity of the micromanipulator back up (denoted by pressing “move”, “1”, “move”) and select the pulse button on the controller.

9.18. On the ‘Acquisition Software’ click “Calibrate” and begin slowly pulsing the force transducer from the right side (registering -10V) all the way to the left side (reading +10V). This should generate a staircase pattern (example shown in Figure 4B).

9.19. Once the calibration curve is complete, save the file, and then gently remove the myofibril from the force transducer needle. Avoid leaving any myofibril residue that may impact adhesion of future myofibrils to that location on the force transducer.

10. Myofibril Cleanup

10.1. At the end of the day, lift the force transducer, motor arm, and double-barreled pipet out of the experimental well and aspirate the solution and myofibrils with a syringe. Add 70% EtOH into the well and clean the glass with a long-handled cotton Q-tip.

10.2. Using a separate syringe, remove all the excess pCa solutions from the perfusion system. Fill the perfusion syringes with ddH_2O and allow to perfuse through the system for 10-15 minutes. This will help remove all the salt from the tubing. Every 2-3 weeks, rinse the lines with 10% bleach (for 20-30 minutes) to prevent any bacteria from growing inside the tubing. If cleaning with bleach, rerun ddH_2O afterwards to remove the bleach from the lines.

10.3. Save data files and shut off all equipment including motor arms, piezo motor, microscope light, water bath, MF-900 micro-forge and computer.

11. Data Analysis: Calibrating the myofibril voltage traces

11.1. In any post-experimental analysis software (MatLab, R-Studio, Labview), open the desired myofibril trace file(s) and corresponding calibration plot.

11.2. Myofibril trace file holds the recorded activation trace as a voltage readout (-10V to 10V threshold), time stamp (millisecond resolution), and recorded

experimental parameters including “calibration step size (μm)”, “force transducer calibration value (μm/μN)”, and “myofibril diameter (μm)”.

11.3. Calibration plot file is also a voltage readout indicating the maximal voltage threshold recorded by the photodiode system.

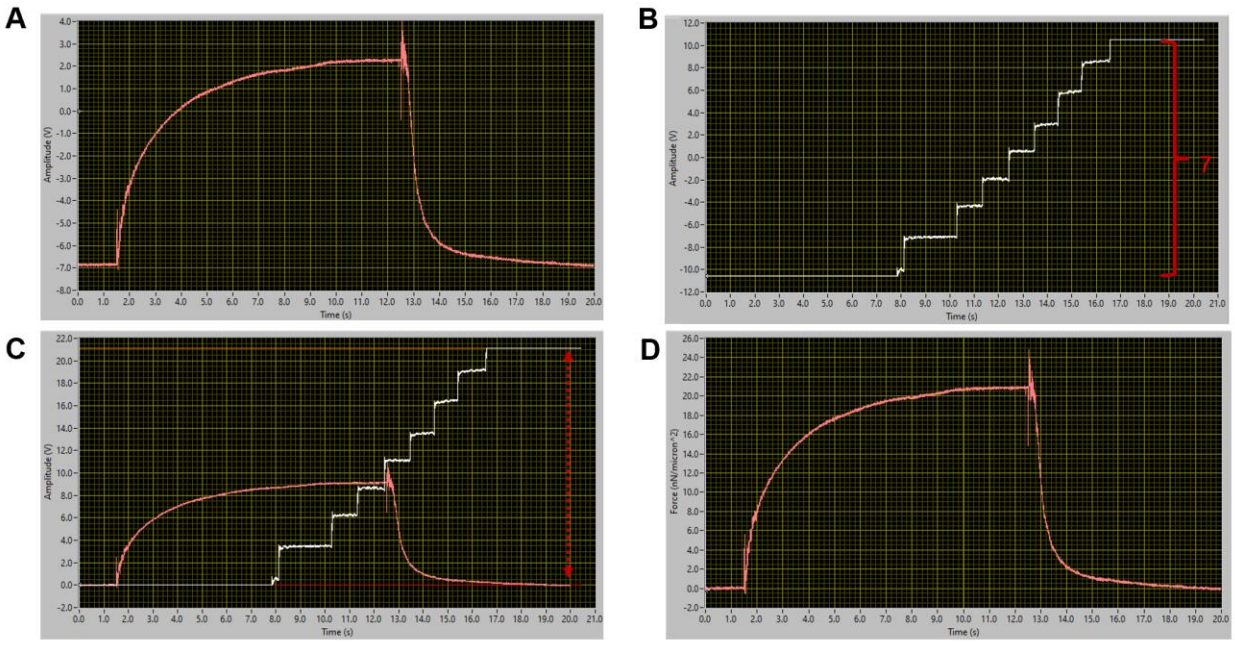

Figure 4. Example recordings from the data acquisition software during experimentation and analysis.

A) An example recording of a day 45 iPSC-CM myofibril bundle differentiated from the WTC-11 background. The noise is very minimal throughout the trace, with both the activation and relaxation phases reaching plateau. **B)** The subsequent calibration plot, illustrating that it took 7 full 1μm steps for the force transducer to move across the photodiode array, generating a staircase function with a minimum reading of -10V and a maximum value of +10V. **C)** In a post-acquisition software, the calibration plot and force trace are overlayed onto each other. **D)** The final product post calibration is the normalized force trace to observed cross-sectional area. This is the specific force of the myofibril.

11.4. Within the calibration plot, identify the minimal and maximal voltage values, along with the number of “steps” that are recorded in the trace.

11.5. Calculate the “average step value” (V) as: $\frac{(\max step\ (V) - minumum\ step\ (V)}{number\ of\ steps}$

11.6. Calculate the “force scaling factor (nN/V)” as: $step\ function\ size/average\ step/force\ transducer\ calibration * 1000$

11.7. Calculate the “scaled myofibril diameter value (μm)” as: $myofibril\ diameter * 0.65$

11.8. Calculate the “cross-sectional area (μm^2)” as: $\pi * \left(\frac{scaled\ myofibril\ diameter}{2}\right)^2$

11.9. Calculate the “normalization factor (nN/V/μm^2)” as: $\frac{force\ scaling\ factor}{cross-sectional\ area}$

11.10. Calculate the “specific force (nN/μm^2) as $force * normalization\ factor$. This specific force value is the force value normalized to the cross-sectional area of the myofibril.

11.11. By identifying the max force value of the myofibril activation file, one can then generate a “normalized trace” relative to the max (where the max force value is equal to 1). This normalized trace will be utilized to quantify kinetics.

12. Data Analysis: Kinetic analysis of the myofibril trace

12.1. On the normalized force trace, identify t_0, t_1, t_2, and t_3 as indicated on Figure 5A and 5B (Note 27).

12.2. To quantify k_{ACT}, calculate the time to 50% (t_{50}) to reach max force during the activation state (t_0 to t_1). Then use $k_{\mathrm{ACT}} = \frac{\ln(2)}{t_{50}}$ to calculate the rate constant (s^{-1}).

12.3. To quantify $k_{REL,Slow}$, identify two points in the slow phase that create the best fit line (X_1,Y_1 & X_2, Y_2). These points are typically the inflection points for the linear phase labeled as points t_1, and t_2 on Figure 5B. Then use $k_{\mathrm{REL,SLow}} = absolute\ value\ (\frac{Y_2-Y_1}{X_2-X_1})$ to linearly interpolate the rate constant (s^{-1}).

12.4. To quantify $t_{REL,Slow}$, use $t_{\mathrm{REL,Slow}} = t_2 - t_1$ (ms).

12.5. To quantify $k_{REL,Fast}$, calculate the time to 50% (t_{50}) baseline of the relaxation state (t_2 to t_3). Then use $k_{\mathrm{REL,Fast}} = \frac{\ln(2)}{t_{50}}$ to calculate the rate constant (s^{-1}).

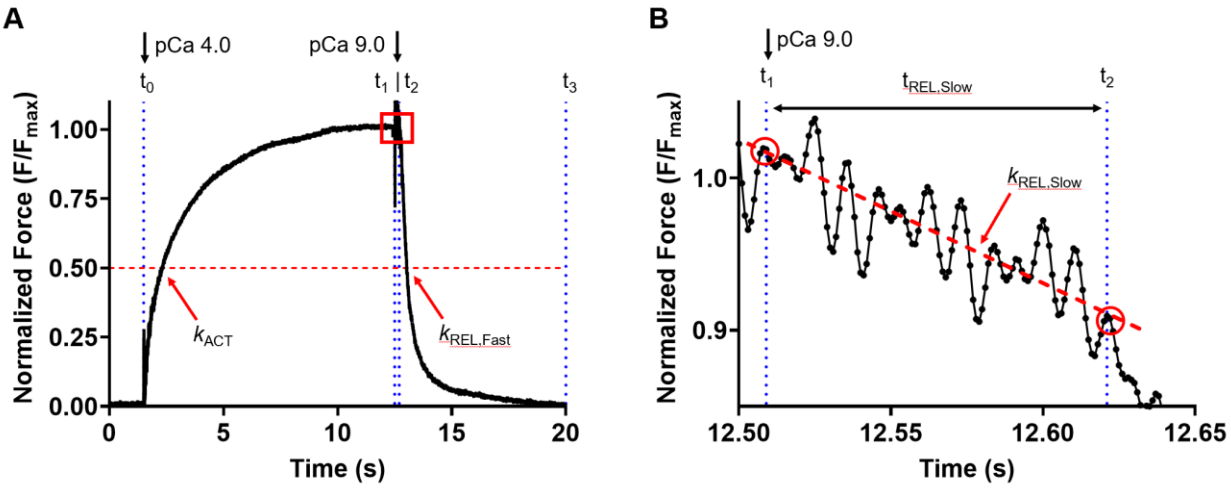

Figure 5. Example normalized trace collected from a day 45 iPSC-CM's differentiated from the WTC-11 background.

(A) The normalized trace with indications for t_0, t_1, t_2, and t_3 (as the blue dot lines) for quantification. Both k_{ACT} and $k_{REL,Fast}$ are quantified as time to 50% (indicated by the red dashed line). Time points t_0 and t_1 indicate the introduction of pCa 4.0 or pCa 9.0 to the myofibril, respectably. The slow phase region is shown by the red box. **(B)** The zoomed in region of the slow phase shows the linear phase of relaxation. Important time points t_1 and t_2 are again highlighted by blue dots. Selecting two points (indicated by the red circles) allows for $k_{REL,Slow}$ to be calculated through linear interpolation. Taking the difference between t_1 and t_2 quantifies $t_{REL,Slow}$. Images plotted on GraphPad Prism 9 for annotation purposes.

v. Notes

1. A myofibril can be rapidly exposed to high Ca^{2+} solutions, instantly oversaturating the thin filament with free Ca^{2+} ions. This instant increase in Ca^{2+} concentration will initiate myofibril contraction and tension development; a mechanism heavily dependent on *both* Ca^{2+} thin-filament activation as well as actomyosin crossbridge cycling. Once fully activated, myofilament activation kinetics (k_{ACT}) and total force generation (F_{max}) can be quantified.

2. All pCa solutions will consist of final concentrations: ionic strength = 0.17M, pMg = 3.0, total EGTA = 0.015M, total MOPS = 0.08M, MgATP = 0.005M, total CP = 0.015M, free K^+ = 0.083M, and free Na^+ = 0.052.

3. When making needles, several attempts are needed to produce properly bent needles. It is important to make a large quantity of needles at the beginning (~15-20) that are properly bent at 90 degrees. This will provide a nice array of needles so that subsequent inking and calibration do not result in needles that are not within the designated range.

4. When inking the force transducers, it is extremely important to prevent and remove any ink blots (especially at the tip of the needle where myofibril attachment will occur). Ink blots will cause significant interference with the photodiode readout, and significantly decrease the sharpness and accuracy of the recorded trace.

5. When positioning the force transducer needle onto the galvanometer needle for calibration, take note of the precise location the force transducer needle touches the galvanometer. It is important to keep this position consistent throughout the entire calibration process. This location on the force transducer should also be the exact location where myofibrils are attached to. All deflection observations should be performed with the 40x objective, as this is the objective utilized during experimentation.

6. When performing the needle calibration, a good check is to observe the voltage-deflection relationship. By plotting the voltage (x-axis) and deflection values (y-axis), one should observe that the relationship is linear.

7. It is important to understand that the calculated needle stiffness is only relevant to the precise location of where the force transducer and galvanometer needle are touching. Traditionally, myofibrils are attached to the tip of the needle, and this calibration at the tip can be sufficient. However, if myofibril adhesion to the same location as calibration is difficult/inconsistent, it would be recommended to perform stiffness measurements along the needle at different points. By measuring the position on the needle that the stiffness measurement is taken, an array of values can be used to reliable calculate myofibril tension.

8. As a method to inventory calibrated needles, we have found using different color sharpies to label works best. For example, a label system with 1 dash, a large space, and then four dashes close together could be labeled needle #14. By using different colors, one could have needles labeled in the library as: Blue 14, Green 23, and Red 45 (all examples of needle numbers).

9. Polyacrylamide gel composition can be changed to modulate gel stiffness. 10 kPa ge mimic native physiological conditions whereas stiffer gels (for example 100 kPa) can be used to simulate diseased states or stress conditions. Gel formulas and techniques are readily available in literature (Denisin & Pruitt, 2016).

10. Plate hiPSC-CMs onto pattern surface in a bubble of 0.5mL of solution. Very slowly, not to disrupt this bubble of media and cells, transfer plate directly into the tissue culture incubator and allow cells to settle down onto the pattern for 2-3 hours as is. This will yield the greatest cell attachment onto the patterned Matrigel surface since cells will not be able

to attach to the plastic surface surrounding the glass bottom surface. After this incubation period, add an additional 1.5mL of replating media to each well, adding to the edge of the well and allowing the media to flow onto the cells on its own to avoid dislodging the newly adhering cells as much as possible.

11. Including this step that slowly ramps up the calcium concentration of the culture media using DMEM (no glucose) will provide the necessary concentration of extracellular calcium required more so by hiPSC-CMs to continue beating after replating onto the pattern surface and will help exercise, elongate, and mature the myofibrils. The 50% RPMI:50% DMEM (no glucose) solution will raise the calcium concentration in the media to 1.1mM calcium and the 25% RPMI:75% DMEM (no glucose) solution will raise the calcium concentration in the media to 1.45mM calcium (Tsan et al., 2021).

12. All wells that have cells on one 6-well plate will have to undergo myofibril isolation at one time since the whole plate will be transferred onto ice for the isolation process. If you want to be able to isolate individual wells on different days, these wells will need to be on a separate plate.

13. Save myofibril solution and first wash solution per cell line in a tube in case you cannot find myofibrils on the surface of the pattern and need to check if myofibrils lifted off the plate during the isolation process. This tube can be spun down at 1000rpm for 5mins and resuspended in wash solution if necessary.

14. If you are unsure if the Ca^{2+} solution has flowed through the entire tubing system, fill the experimental well with water, focus the double-barreled pipet in view, and watch the solution flow. The water based Ca^{2+} solutions will not mix, and the stream should be easily visible.

15. The Piezo controller for the double-barreled pipet should be set to travel 300µm per step. It is important to manually step the controller initially, especially of the rig has not been used for a while. The step distance can sometimes change, and quickly increasing the steps manual will recalibrate the system. This ensures the step distance is correct during experimentation, and that myofibril is being exposed to the correct solutions.

16. The step-function size is the measured distance that the force transducer moves when set to “pulse”. The value should be close to 1µm, but it is important to measure this value initially, as it will be utilized to calibrate the myofibril traces.

17. When looking for myofibrils, it is important to find preparations that are well adhered to the glass (via electrostatic interactions). As a quick check, you can gently shake the table on which the microscope is mounted and watch if the myofibril moves or not. These samples provide the greatest probability for success compared to samples that may just be floating in the well.

18. Motor arms are constructed similar to force transducers, except they do not need to be bent, inked, or calibrated. Using a pulled glass rode, cut the “floppy” part of the needle until the diameter is ~2.5µm, and then gently fire polish the needle closed (Figure 2A, 2B). This will be used as your motor arm. It can be fire-polished multiple times to regain “stickiness”, however, be careful not to inadvertently bend the tip.

19. Once the myofibril has been lifted off the glass, it is important to check how well adhered the preparation is to the motor arm and force transducer. Inducing a slight strain on the myofibril by stretching with the motor arm is a great way to check. As the motor arm pulls on the myofibril, make sure that the force transducer begins to slightly deflect. If the myofibril begins to slide along the force transducer or motor arm, that means it was not

attached properly, and cannot be used for experimentation. This step takes a lot of practice.

20. It is important to elevate the double-barreled pipet (and activation solutions in general) from the bottom of the well to prevent inadvertent activation of other myofibrils that remain on the glass. To bring the myofibril up in the z-plane, use the 40x objective, and slow "walk" the myofibril up with the two manipulators. This process should be done with care, as it can very easily over stretch the myofibril and cause damage or removal from either the motor arm or force transducer.

21. When positioning the double-barreled pipet in front of the myofibril it is important to keep the position consistent between all preps. Measure the distance from the myofibril and pipet tip to ~150µm and that the myofibril is centered within the flow of each solution. Manually trigger the piezo motor from one position to the other (with no flow initially) to make sure the myofibril is positioned correctly in front of the relaxed outlet and activated outlet.

22. One key point is to make note of where the myofibril is attached on the force transducer. Make sure that the myofibril is attached where the calibration happened, and not too far away from the calibration spot. See note 4.14 as incorrect placement further up the force transducer needle may require a different calibration value.

23. Under bright-field conditions, the black force transducer will "cast a shadow" between the 2 photodiodes, and the shadow position is tracked as a voltage. The total amplitude of 20V is the limit that the force transducer can travel while being captured.

24. If turning on the flow of solutions causes the oscilloscope reading to jump or drift, this is most likely due to improper alignment of the motor arm and force transducer. Make sure

that the myofibril is on a singular focal plane, as any misalignment in the z- or y-axis can cause the needles to drift when exposed to solution flow.

25. If you are planning on doing different pCa solutions, it is important to turn on and off the different solution valves once the previous myofibril activation has already completed data acquisition. After the recording, turn on the new pCa, turn off the old pCa, wait ~15 seconds, and run the program again to record the new activation trace.

26. This plot normalizes the variance between preparations as it accounts for how the photodiodes record the needle movement with regards to brightfield brightness, needle shape, needle blackness, and needle position.

27. The locations of t_0, t_1, t_2, and t_3 all describe the time ranges of different components in the myofibril activation/relaxation curve. The initial t_0 observes the exact moment that the myofibril is exposed to high Ca^{2+} solution. The t_1 parameter designates the exact time that the myofibril is exposed to low Ca^{2+} solution. That means the activation period is between t_0 and t_1. The parameter t_2 is the inflection point between the initial linear phase and secondary fast phase of relaxation. That means the range between t_1 and t_2 is the initial linear phase, and then between t_2 and t_3 is the fast exponential phase.

X. Appendix B: Embryonic Myosin Mutation R672C Impacts the Sarcomeric Myosin Expression and Contractile Mechanics in hiPSC Derived Skeletal Myotubes

This appendix section represents a publication style write up of an ongoing project I am co-first author on.

Christian Mandrycky †, **Saffie Mohran** †, Matthew Childers, Shawn Luttrell, Alina Greimel, Elizabeth Choi, Kati Buckingham, Michael Bamshad, Michael Regnier, David L. Mack, Alec Smith

† Authors contributed equally

i. Abstract

Distal arthrogryposis (DA) is a skeletal muscle disorder characterized by joint contractures predominantly localized in the distal extremities. DA associated syndromes like Freeman-Sheldon Syndrome (FSS) are linked to mutations in the MYH3 gene that encodes the embryonic skeletal muscle myosin. To study the mutation and its effect on developing muscle, we generated human induced pluripotent stem cell (hiPSC) lines bearing the R672C MYH3 mutations. hiPSC were differentiated into skeletal muscle and evaluated for differences in the maturation of the contractile unit and its functional performance. Preliminary myofibril mechanics measurements showed R672C myotubes generated greater specific force compared to control myofibrils. Diseased myofibrils also expressed significantly faster rates of relaxation compared to control myofibrils. Myofibril preparations were also used to compare ATP binding rates across conditions. Preliminary results showed homozygous R672C myofibrils have faster ATP binding rates compared to heterozygous and control preparations. Molecular dynamics simulations of R672C mutations in the post rigor state showed greater separation between the β-sheet and SH-Helix than in controls. Mutation also disrupted local salt bridges and hydrogen bond formation in some residues that help stabilize the nucleotide binding pocket and converter-connected helix. Interrupted structural communication between the nucleotide binding pocket and surrounding functional regions may underly the impaired relaxation phenotype. Ongoing studies will further characterize the effect of mutation on actin-myosin binding, crossbridge cycling kinetics, the maturation of skeletal myotubes over time, and myosin isoform switching dynamics.

ii. Introduction

Distal arthrogryposis (DA) syndromes are a group of 10 autosomal dominant disorders characterized by congenital contractures (CC) of the distal appendages and orofacial muscles. With a prevalence rate of ~1 in every 200-500 births, common phenotypic traits in individuals with DA includes clubfoot and camptodactyly (flexion of fingers and/or toes). To date, a significant amount of work by us and others has discovered that DA syndromes are caused by mutations in six different skeletal muscle contractility proteins including troponin I, troponin T, tropomyosin, embryonic myosin (MYH3), fetal myosin (MYH8), and myosin-binding protein C (Sung et al., 2003; Toydemir et al., 2006). Despite the identification of causal protein-mutations, the underlying mechanisms of dysfunction that these mutations cause during development have been poorly investigated.

Under the umbrella of distal arthrogryposis syndromes, two of the most common expressions (Sheldon Hall syndrome (SHS) and the more severe Freeman-Sheldon Syndrome (FSS)) are associated with mutations in MYH3. Specifically, the most common mutations of FSS (R672C, R672H, and T178I) are all located in the motor domain region of myosin, impacting contractility speed due decreased rate constants for ADP release and ADP affinity for actin-myosin complexes (Walklate et al., 2016) in homogenously expressed recombinant proteins. These mutations exhibited dramatic changes in kinetic properties including a notable depression in ATP hydrolysis rates. These findings were later corroborated by tissue and myofibril contractility measurements (Racca et al., 2015) from adult biopsy samples collected from individuals with R672C mutations. Diseased myofibril measurements showed a significant decrease in activation rate constant values (elucidating a decrease in ATP crossbridge cycling) compared to control samples, while also inhibiting both the rate and amount of relaxation. Isometric slow phase mechanics expressed impaired crossbridge detachment and prolonged thin filament deactivation, again indicating dysfunctional ADP release.

The inconsistency in tissue availability however plays an enormous role in the ability of researchers to continue studying DA and identify potential mechanisms of therapy. For this reason, we have generated two induced pluripotent stem cell (iPSC) lines to study DA without the need for patient biopsy. These cell lines were generated through the innovative clustered regularly interspaced short palindromic repeats (CRISPR) gene editing protocol. By generating these cell lines and differentiating them into skeletal myotubes, we can fully investigate the developmental, mechanical, and biochemical dysfunction caused by these mutations at an incredible temporal resolution. By investigating the longitudinal disease progression of the mutation, we aim to identify what underlying mechanisms develop the phenotypical expressions observed in affected individuals. Our reductionist assays will allow us to target various parts of the crossbridge cycle as well as protein isoform expression to determine any significant differences in sarcomeric function during different points of maturation (post differentiation).

iii. Applicable Methods

- *Myofibril isolation and experimentation*

For myofibril isolation, day 9 cells were directly treated with rigor solution (50 mM Tris, 2 mM MgCl, 1 mM EGTA, 100 mM KCl) supplemented with 1:100 PIC and 1% Triton X-100 for 60 min at 4°C. Cells were then washed twice with rigor solution and 1:100 PIC without Triton X-100, gently lifted off the plate with a cell scraper, and solution collected. Myofibrils from iPSC-SkMs were mounted into a custom-built apparatus with rapid Ca^{2+} solution switching (15°C) to measure myofibrillar contraction and relaxation kinetics at the millisecond timescale, as previously described (stiffness of force-transducer needle: 6.99 nN/nm) (Pioner, Guan, et al., 2020; J. M. Pioner et al., 2016). Myofibrils are maximally activated in pCa 4.5 and then subsequently activated in sub-maximal pCa 5.8 and 5.6.

- *Molecular dynamic modeling (Adapted from Chapter 4)*

Model Building: Coordinates for the post-rigor, ATP-bound conformation of human wild type (WT) cardiac β-myosin motor domain were obtained from the Protein Data Bank (PDB, www.rcsb.org) (Berman et al., 2002) entry 4DB1 (X-ray crystallography, 2.6 Å resolution). Coordinates for the rigor state actomyosin complex of cardiac myosin and skeletal actin were obtained from the PDB entry 6X5Z (cryo-electron microscopy, 4.2 Å resolution) (Doran et al., 2020). Homology models for WT human embryonic skeletal myosin (*myh3*) and actomyosin complexes were generated using these structures as templates, sequences downloaded from *Uniprot*, and the *Modeller* homology modelling software. Starting coordinates for the mutant (T178I, R672C) systems were obtained via *in silico* modification of the WT structures using the *leap* module of *AMBER (Case et al., 2005)*.

Force Field and Explicit Solvent Molecular Mechanics: All simulations were performed with the AMBER20 package and the ff14SB force field (Maier et al., 2015). Water molecules were treated with the TIP3P force field, metal ions were modeled using the Li and Merz parameter set. ATP molecules were treated with parameters from Meagher *et al.* (Meagher et al., 2003). The SHAKE algorithm was used to constrain the motion of hydrogen-containing bonds and long-range electrostatic interactions were calculated using the particle mesh Ewald (PME) method.

Pre-production protocols: Hydrogen atoms were modeled onto the initial structure using the *leap* module of *AMBER* and each protein was solvated with explicit water molecules in a periodic, truncated octahedral box that extended 10 Å beyond any protein atom. Na^+ and Cl^- counterions were added to neutralize the systems and then 120 mM Na^+ and Cl^- ions were added. Each system was minimized in three stages. First, hydrogen atoms were minimized for 1000 steps in the presence of 100 kcal mol^{-1} restraints on all heavy atoms. Second, all solvent atoms were minimized for 1000 steps in the presence of 25 kcal mol^{-1} restraints on all protein atoms. Third, all

atoms were minimized for 8000 steps in the presence of 25 kcal mol^{-1} restraints on all backbone heavy atoms (N, O, C, and C atoms). After minimization, systems were heated to 310°K during 3 successive stages. In each stage, the system temperature is increased by ~100°K over 100 ps (50,000 steps) using the NVT (constant number of particles, volume, and temperature) ensemble. During all heating stages, 25 kcal mol^{-1} restraints were present on the backbone heavy atoms (N, O, C, and C atoms). After the system temperatures reached 310°K, the systems were equilibrated over 5 successive stages using the NPT (constant number of particles, pressure, and temperature) ensemble. During each stage, the systems were equilibrated for 5.4 ns in the presence of restraints on backbone atoms. The strength of the restraints decreased from 25 kcal mol^{-1} during the first stage to 1 kcal mol^{-1} during the fourth stage. During the final equilibration stage, the systems were equilibrated in the absence of restraints.

Molecular Dynamics Protocol: Production dynamics for conventional molecular dynamics (MD) simulations were then performed using the canonical NVT ensemble with an 8 Å nonbonded cutoff, and 2 fs time step. Coordinates were saved every picosecond. Simulations were run for 500 ns each.

Molecular Dynamics Analysis: The C_α RMSD, C_α RMSF, SASA, interatomic distances, and interatomic contacts were calculated with *cpptraj* (Roe & Cheatham, 2013). The C_α RMSD was calculated after alignment of all The C_α atoms to the minimized structure. The C_α RMSF was calculated about average MD structures for each simulation. Two residues were considered in contact with one another if at least one pair of heavy atoms were within 5 Å of one another. All protein images were prepared using UCSF Chimera (Pettersen et al., 2004; Sanner et al., 1996).

- *Cellular culture and engineered muscle tissue construction*

Please see (Smith et al., 2022) for the full methods.

iv. Applicable Results

- *Molecular Dynamics modeling demonstrates that R672C causes structural changes to the myosin head structure in rigor and post-rigor states*

Initial measurements to assess how R672C impacts the structure and function of myosin was conducted through molecular dynamics (MD) modeling. Computational simulations were performed in the rigor (M) and post-rigor (M.ATP) states of myosin (Figure 1A) to assess how the mutation R672C impacts nucleotide binding dynamics and affinity. These simulations are able to provide a temporal readout of the probable structural changes caused by the mutation, with results showing that the R672C mutation developed significantly greater distances between the β-sheet and SH Helix when compared to WT in rigor and post-rigor states (Figure 1 B). These

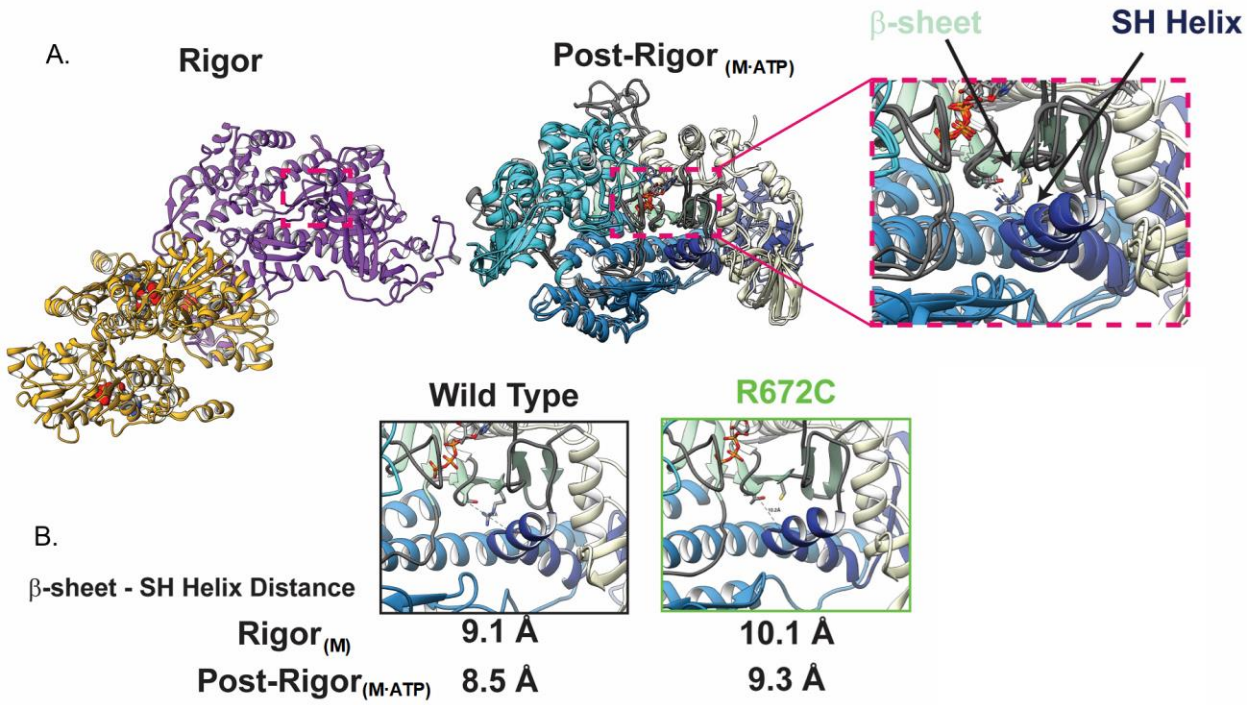

Figure 1. Molecular dynamic simulations show R672C impacts rigor and post rigor states of myosin

Molecular models of the rigor and post rigor states **(A)** of myosin illustrate the specific region of myosin that the R672C is located, and the interaction region between the β-sheet and SH helix. Quantified measurements **(B)** between the two regions showed that the R672C mutation increased distances in both states.

results suggest that the mutation may disrupt the communication between the S2 and the converter domain of myosin.

- *iPSC skeletal myotube differentiation is not impacted by the R762C mutation*

Utilizing a modified approach to the skeletal myotube (SkM) differentiation protocol developed by April Pyle's group (Chal et al., 2015; Hicks & Pyle, 2015; Hicks et al., 2018), our group has successfully generated iPSC-SkM expressing the CRISPR-generated R672C (homozygous and heterozygous expressing) mutations. Initial maturation protocols during primary differentiation are treated with an array of small molecule differentiation mediums and are sorted for Erbb3 at approximately 35 days. During secondary differentiation, myotubes are treated with DMEM

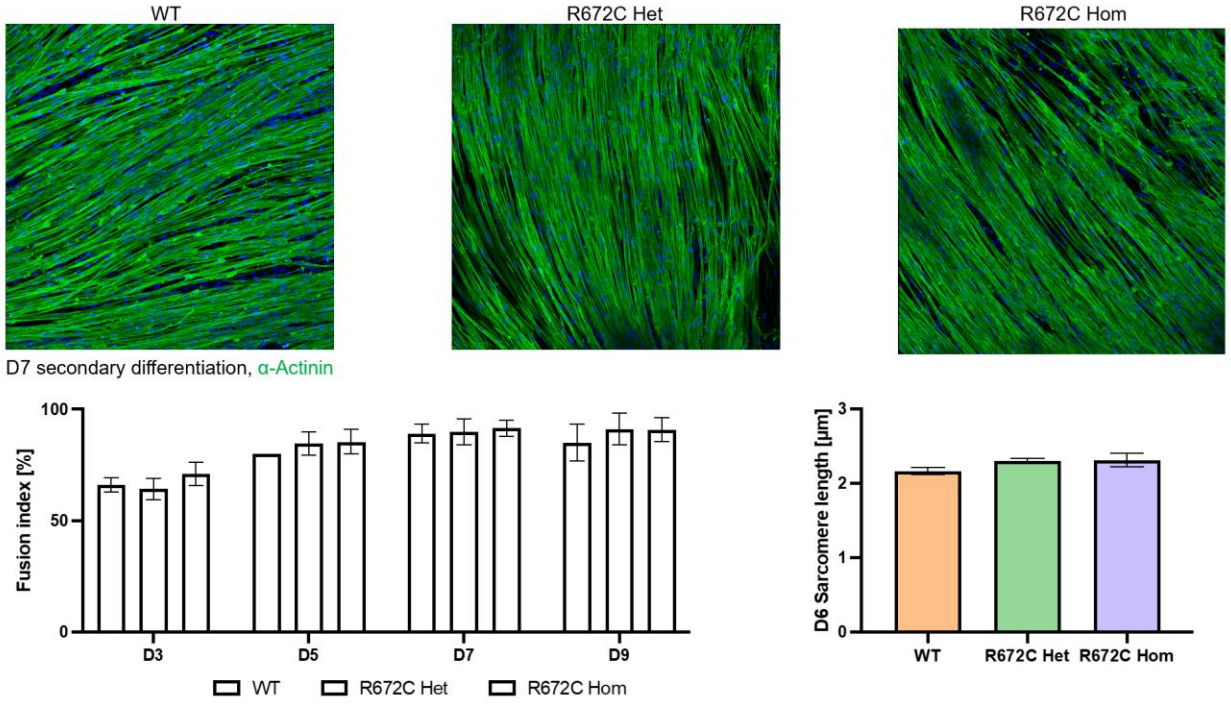

Figure 2. Secondary skeletal muscle differentiation results in striated muscle with and without the R672C mutation

Representative images of iPSC-SkMs on glass surfaces show myotube formation in control WT **(A)**, R672C heterozygous **(B)**, and R672C homozygous **(C)** expressing lines. Assessment of skeletal muscle fusion index percentage **(D)** and computed sarcomere length **(E)** show no difference in differentiation efficiency.

supplemented with horse serum, B27, non-essential amino acids, IGF-1, HGF, and SB431542. All myotube variant (control, homozygous, and heterozygous) cell lines express similar fusion efficiency during secondary differentiation and exhibit similar sarcomere lengths.

- *Myofibril mechanics for homozygous R672C expressing cell lines have altered contractile kinetics*

Initial myofibril isolation experiments occurred on day three post-secondary differentiation in an attempt to assess myofibrils only expressing embryonic myosin. These isolations however expressed low yield cellular mass and produced inconsistent and non-reproducible measurements due to significant immaturity of the cells and sarcomeric formation. To address this limitation, we differentiated the myocytes and isolated myofibrils day 9 post-secondary

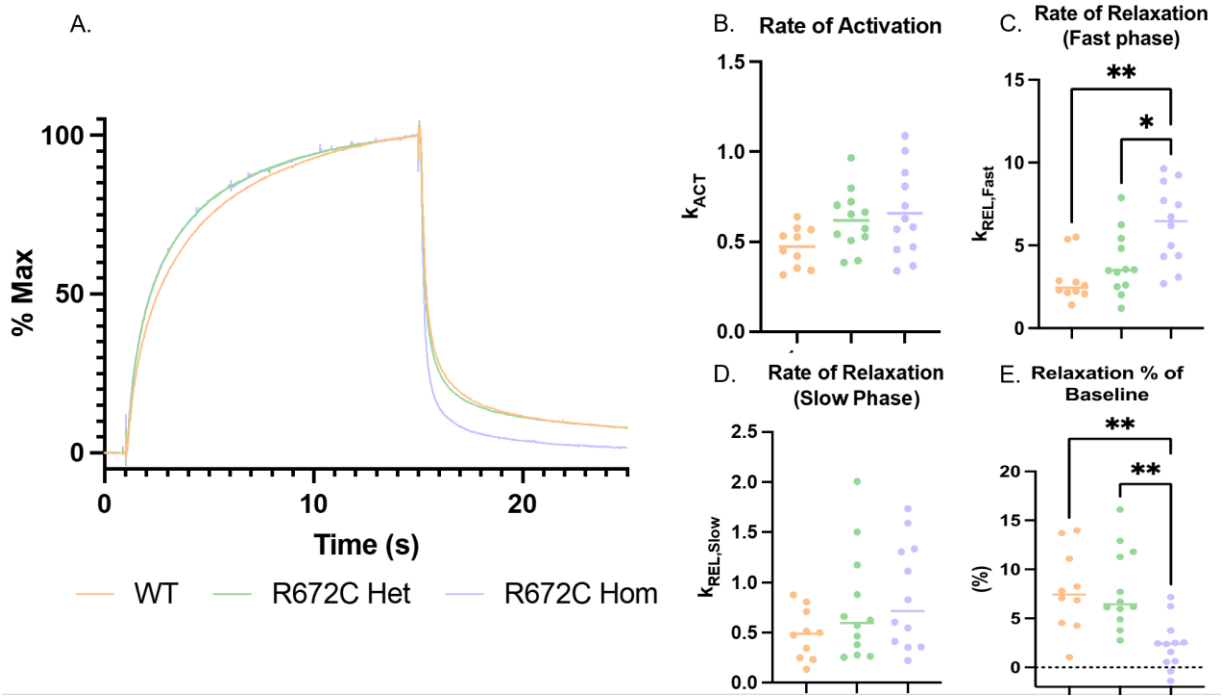

Figure 3. Isolated myofibrils with homozygous expression of R672C embryonic myosin significant accelerated relaxation kinetics compared to control
Normalized myofibril measurements **(A)** show accelerated kinetics of the homozygous expressing R672C line compared to control. Quantified measurements of activation **(B)**, rate of fast phase relaxation **(C)**, rate of crossbridge detachment **(D)**, and ability to relax back down to baseline **(E)**, shows significant differences between the homozygous R672C and control. Measurements were collected from three separate secondary differentiations (N=3 | n =12).

differentiation by permeabilizing the cells with Triton-100X solution for 1 hour at 4°C. Isolated myofibrils from all groups consistently contracted and showed significantly improved sarcomeric formation and contractile function during experimentation.

Data collected from day 9 skeletal muscle myofibrils however showed results inconsistent with previously reported publications. In comparison to control and heterozygous expressing lines, R672C homozygous myofibrils expressed significantly faster rates of fast relaxation (Fig 3C), while also more consistently returning back to baseline (Fig 3E). Previous results published by us and others had demonstrated that the R672C mutation inhibited relaxation through inhibited ADP release. Along with the reported statistical differences, the homozygous line also appears to potentially increase both the rate of myofibril activation (Fig 3B) and cross bridge detachment rate (Fig 3D) compared to control.

- *Engineered muscle tissues from homozygous R672C cells express faster and more complete relaxation dynamics*

In addition to mechanical measurements done on permeabilized isolated myofibrils, we conducted longitudinal mechanical measurements in intact 3D engineered muscle tissue constructs. These preparations provide a platform to assess tension and kinetics of intact muscle cells cast together in a fibrin hydrogel (Fig 4A) between a stiff and flexible post. Since these intact muscle cells retain their membrane, mechanical measurements are conducted through electrical stimulations. Twitch assessment conducted at day 7 post casting showed that the homozygous expressing R672C cells had a shorter time to 90% relaxation (Fig 4B) compared to control and heterozygous conditions. Longitudinal assessment of force at day 5 (Fig 4C), and day 7 (Fig 4D) showed that the homozygous lines also produced significantly lower force compared to the control and heterozygous conditions. It is important to note that these force measurements are described as absolute force and are not normalized to tissue or cell cross-sectional areas.

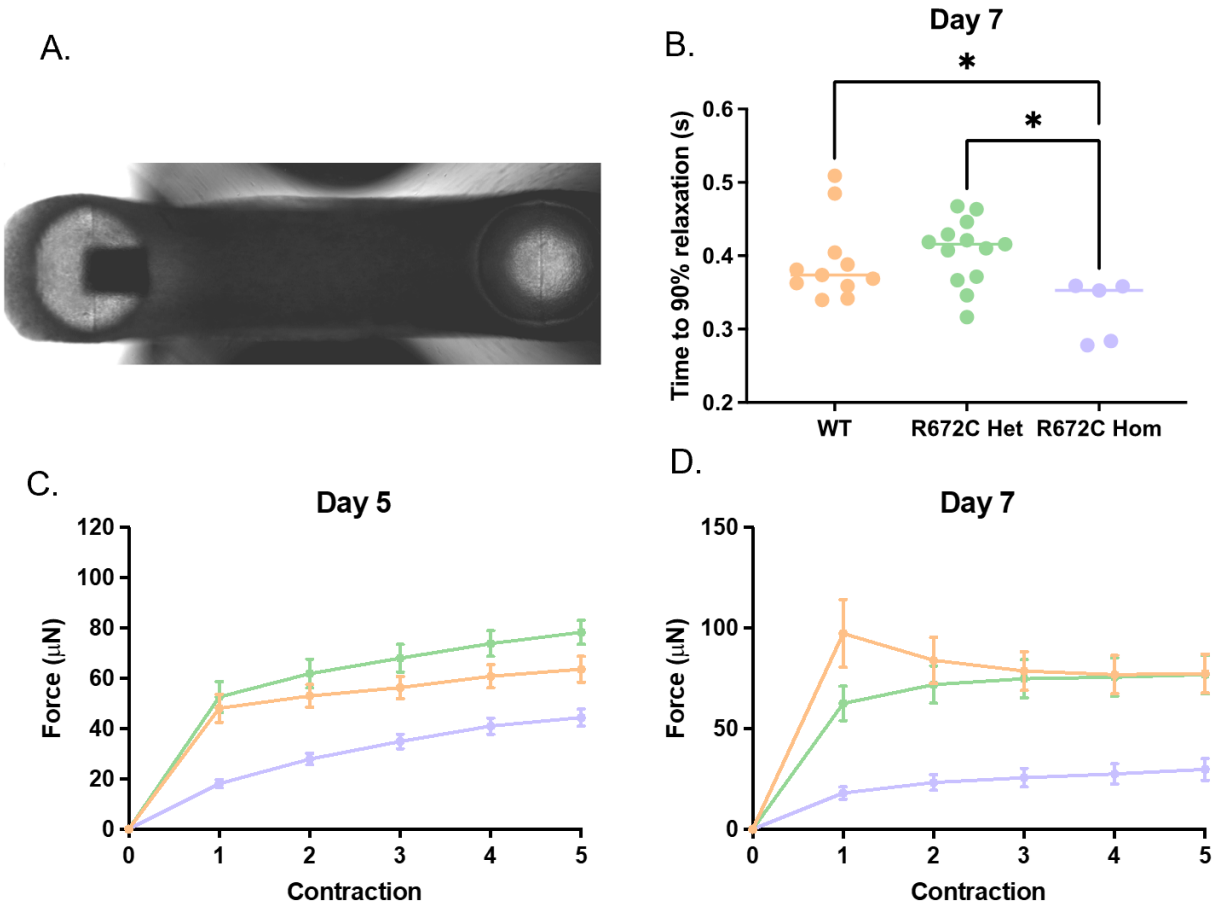

Figure 4. Engineered muscle tissues cast with homozygous R672C cells express faster and more complete

Representative image of a cast engineered muscle tissue **(A)** shows 3D structure of fibrin hydrogel between stiff and flexible post. Cultured R672C homozygous cells expressed shorter time to 90% relaxation **(B)**, and lower absolute force at days 5 **(C)** and 7 **(D)** compared to control and heterozygous preparations.

- *R672C mutant cells have reduced levels of MYH3 proteins and express significantly elevated levels of MYH8 protein*

In addition to mechanical measurements, we assessed the myosin protein expression of the differentiated skeletal myotubes through protein gels. Protein preparations were purified from permeabilized myofibril samples, resulting in quantification of sarcomeric myosin. This means that no myosin potentially dissolved in the cytosol was included. The longitudinal assessment of the

myosin isoform expression was conducted for days 7, 8, and 9, to better understand the mechanical data collected from the permeabilized myofibrils and engineered muscle tissues.

Through protein gel imaging, the R672C mutation significantly altered the expression of the myosin isoforms expressed in the sarcomeric population. In the homozygous expressing lines, the expression of MYH3 from day 7 to day 9 significantly decreases (Fig 5A). This decay is not as significant in either the control or heterozygous expressing lines. In contrast to MYH3 expression, MYH8 expression in the homozygous line increases significantly between days 7 and 9. This relationship, although not as significant in expression level, is similar in the control and heterozygous conditions. In addition to purified protein gels, immunohistochemistry staining of permeabilized skeletal myotubes still attached to the glass culture surface showed significantly

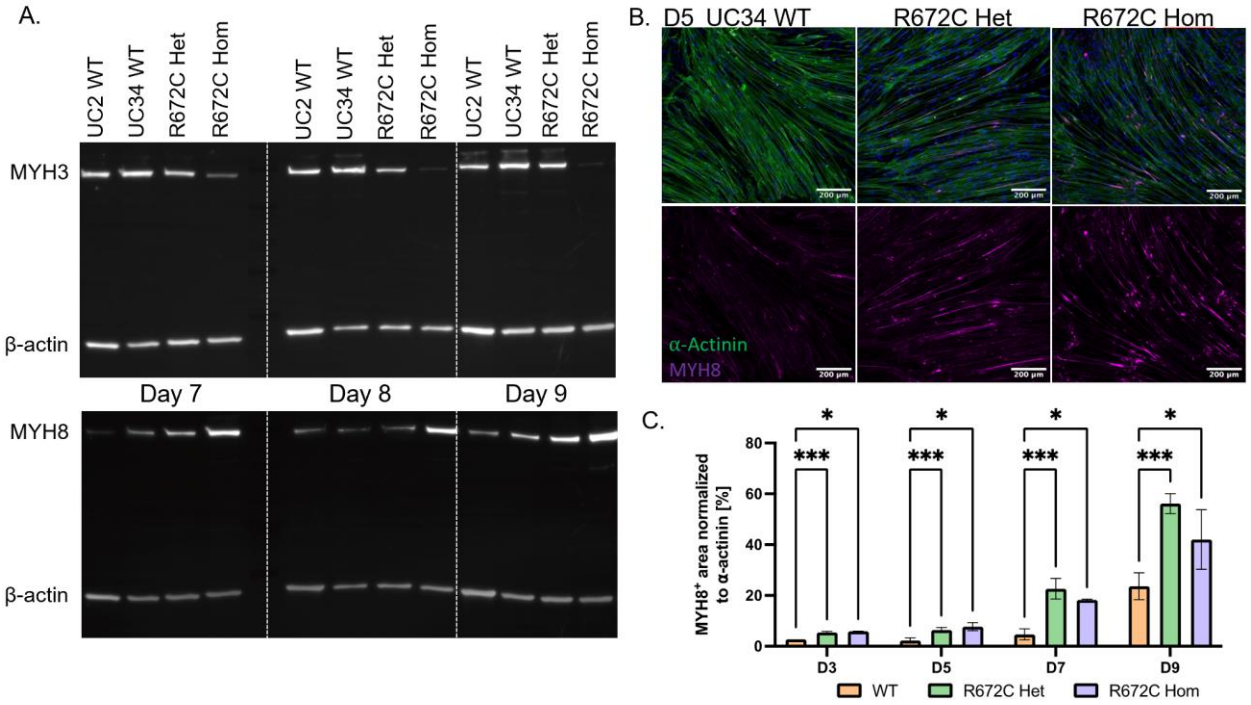

Figure 5. Sarcomeric protein assessment shows R672C reduces MYH3 expression while increasing MYH8 incorporation.

Longitudinal assessment of sarcomeric myosin isoforms 3 and 8 through protein gel **(A)** shows significant difference in expression between cell types and dates. R672C homozygous conditions showed greatest MYH3 silencing and MYH8 expression, which was also confirmed through immunohistochemistry staining **(B)** and quantification **(C)** through positive surface area percentage at day 5.

elevated levels of MYH8 positive staining (Fig 5B). Quantification of the MYH8 positive surface area as a percentage to α-actinin showed that there is a significant increase in MYH8 expression at day 9 in the homozygous and heterozygous lines compared to control, and also compared to younger differentiation days.

v. Discussion & Future Direction

Investigating the accelerated maturation of mutated skeletal myotubes may elucidate developmental mechanisms that promote the disease phenotype expressed in persons with DA. With the rapid degradation of mutant MYH3 being observed, literature in progressive muscle wasting and muscular atrophy have identified a ubiquitin enzyme pathway, Muscle specific RING Finger (MuRF1), as a potential mechanism that regulates myosin protein degradation within cells. In models of skeletal muscle atrophy, MuRF1 is significantly upregulated and is associated with myosin heavy chain protein being depleted from the cell. By isolating cells, and staining for MuRF1, we can assess if there is an upregulation in the MuRF1 expression, potentially degrading the mutant myosin from the cells, and promoting faster myotube maturation. In addition to potential upregulation of MuRF1 expression, another separate study generated a full MYH3 knockout mouse (KO) (Agarwal et al., 2020), which expressed significant developmental dysfunctions including scoliosis. Similar bone deformations are present in severe conditions of DA, potentially correlating that mutations in MYH3 lead to upregulation for protein decay, expediting the expression of MYH8. This accelerated expression of a strong and faster myosin isoform may develop the congenital contractures due to the skeletal bone structure not being ready.

Although our mechanical measurements initially seemed to disagree with previously published results for the R672C mutation by expressing accelerated kinetics, our protein assessment argues that the largest proponent for mechanical differences in our assay was not the mutation in MYH3, but the different myosin isoform expression. To further investigate

difference the contribution of different myosin isoform and the impact they have on our mechanical measurements, we plan on transfecting iPSC-SkM's with siRNA constructs to silence the expression of MYH8 and/or MYH3 to see how it impacts the expression timeline in myofibrils. By suppressing MYH8, we want to observe if MYH3 is potentially preserved, or if more mature myosin's (MYH7 (slow) and MYH2 (fast) are expressed as compensatory mechanisms. In contrast, our desire for MYH3 suppression is to observe if all myotubes progress down the same accelerated timeline, or if MYH3 is a required myosin isoform that is critical for initial myofibril development, fusion, and maturation.

To best assess the mechanical output of the SiRNA treatment, we plan to utilize the 3D engineered muscle platform to conduct longitudinal studies for both contractility and protein expression. This platform removes a significant limitation identified in myofibril experimentation, which is the unknown myosin isoform expression within our preparation. In myofibril measurements, there is no correlation between the isoform expression of the individual myofibril and the averaged percentage of myosin isoform expression from the entire well. This means that the average pooled myosin population may be heavily MYH3 expressing, however, the individually selected myofibril utilized for mechanics may have significantly different expression. The utilization of the engineered muscle tissue allows for mechanical readouts, followed by subsequent protein quantification at any desired stage. The protein quantification is an average myosin isoform value from each construct, while the mechanical measurements are also an averaged calculation from all the cultured cells. This allows us to be more confident that any potential mechanical changes observed in contractility can be normalized for myosin isoform expression.

The engineered muscle tissue platform was also specifically designed for longitudinal assessment of tissues in culture. We will be able to assess changes in contractility, both force generation and kinetics, in relationship to days. With the potential accelerated maturation and

isoform switching occurring in culture, the longitudinal aspect of the study is extremely relevant to modeling this disease. If, after SiRNA treatment, we observed similar myosin isoform expressions, and specifically with conserved MYH3 protein levels, we feel very confident to utilize this platform to assess the contractile dysfunction associated with this disease. If, however, changes in myosin isoform expression is still observed post-SiRNA treatment, the disease model is communicating to us that R672C plays a significant role in myosin isoform expression dysfunction. As previously discussed, myosin isoform switching is a significant mechanism in muscle maturation, it may play a critical role in the phenotypical development associated with DA.

XI. Appendix C: Impaired myofibril function in patient-derived cardiomyocytes with the hypertrophic cardiomyopathy-myosin binding protein-C E258K mutation

This appendix section represents portions of the latest version of a second-author publication in preparation.

Sonette Steczina, **Saffie Mohran**, Logan R.J. Bailey, Timothy S. McMillen, Kristina B. Kooiker, Neil B. Woods, Jennifer Davis, Michael J. Previs, Josè Manuel Pioner, Michael A. Geeves, Corrado Poggesi, Michael Regnier

i. Introduction

Cardiac myosin binding protein C (cMyBP-C, gene: *MYBPC3*) is a regulatory protein in the C-zone of the cardiac muscle sarcomere that spans the thick filament. While tethered to the myosin backbone at its C-terminus, the N-terminus of cMyBP-C interacts with both myosin and actin within the sarcomere and is known to regulate myosin-actin cross-bridge formation and cycling during cardiac muscle contraction (Harris et al., 2002). Mutations in *MYBPC3* are prevalent within the hypertrophic cardiomyopathy (HCM) patient population (Harris et al., 2011) and have been linked to asymmetric thickening of the left ventricular wall, hypercontractility, impaired diastolic function of the heart, and elevated incidence of sudden cardiac death due to arrhythmias (Wijnker & van der Velden, 2020). The specific molecular mechanisms by which cMyBP-C mutations lead to such HCM patient phenotypes, however, is largely unknown and how it affects cross-bridge cycling is not well understood.

Truncation mutations are the most prominent type of mutation identified within the pool of *MYBPC3* HCM-linked mutations (Helms et al., 2020). Haploinsufficiency, or the reduction in full length protein produced compared to wildtype, has been suggested as a unifying factor of *MYBPC3* truncation mutations leading to HCM (Helms et al., 2014). Reductions in full length cMyBP-C in patients and engineered heterozygous *MYBPC3* knock out mouse models have been associated with septal hypertrophy (Carrier et al., 2004), enhanced myofilament sliding velocity (O'Leary et al., 2019), elevated calcium sensitivity (van Dijk et al., 2009), impaired excitation-contraction coupling (Pioner et al., 2023), and acceleration of cross-bridge cycling (Cheng et al., 2013; Desjardins et al., 2012). One such HCM linked *MYBPC3* truncation mutation that has been hypothesized to lead to a haploinsufficiency phenotype is the *MYBPC3*-c.772G>A mutation (Pioner et al., 2023). Compared to other HCM mutations, this mutation is highly penetrant and has a founder effect in the Tuscany region of Italy, where ~13% of the HCM patient cohort in this region of Italy have this specific mutation (Olivotto et al., 2008; Page et al., 2012; Pioner et al.,

2023). Previous work from patient genetic testing data (Singer et al., 2019) and human myectomy samples (Helms et al., 2020) has identified that the c.772G>A leads to a complete exon skipping event of exon 6, inducing a frameshift, and an eventual premature termination codon in exon 9 (Helms et al., 2014).

Our recent publication (Pioner et al., 2023) investigating the *MYBPC3*-c.772G>A mutation in myectomy samples from four independent patients revealed consistently lower expression of full length cMyBP-C, in line with a haploinsufficiency disease mechanism. Isolated sub-cellular contractile organelles (myofibrils) from these myectomy samples indicated accelerated cross-bridge cycling. This was accompanied by a greater energetic cost of tension generation measured in skinned tissue preparations. The acceleration of cross-bridge cycling was compensated for by slower deceleration of excitation-contraction coupling events, such that cardiac twitch mechanics were unaltered. A paired induced pluripotent stem cell (iPSC) line reprogrammed from one patient of the *MYBPC3*-c.772G>A mutation patient cohort was CRISPR/Cas9 edited to generate an isogenic corrected iPSC line. Initial work on these paired iPSC lines supported a potential haploinsufficiency mechanism initiating at around day 60 post initiation of differentiation, accompanied by similar excitation-contraction coupling changes as was seen in the patient myectomy samples (Pioner et al., 2023).

To further study the mechanisms of this mutation, we show in this paper that the c.772G>A mutation induces a splicing event in *MYBPC3*, removing the entirety of exon 6. This exon 6 splicing is present in 20% of the total mRNA transcript at the earliest days of cardiomyocyte maturation and is accompanied by a 20% decline in translated cMyBP-C protein compared to the isogenic line, without any presence of a truncated peptide. Further, myofibrils isolated from patient iPSC-CMs at day 45 exhibited accelerated cross-bridge cycling kinetics during contraction and relaxation compared to the isogenic line, a phenotype consistent with myectomy tissue myofibrils. Mechanistically, we have determined that the reduction in cMyBP-C protein expression in

sarcomeres, due to the c.772G>A HCM mutation, accelerates ADP release from myosin and leads to elevated cMyBP-C phosphorylation, both of which are associated with acceleration of cross-bridge cycling. Our findings validate the usage of iPSC-CMs to model the disease phenotype for this specific *MYBPC3* mutation, providing a readily accessible model to study disease mechanisms and early-stage, mutation specific therapeutic interventions to prevent downstream secondary remodeling.

ii. Applicable Methods

- *Cell patterning, myofibril isolation and kinetics experiments.*

To achieve elongated, mature myofibrils from iPSC-CMs to be able to perform myofibril kinetics experiments, iPSC-CMs were cultured on lined patterns of stamped Matrigel, created using a high-fidelity photoresist double lift-off patterning method (Moeller et al., 2018). Lined patterns for stamping (1 cm x 1 cm area and 15 mm line width) were generated by pouring polydimethylsiloxane (PDMS, Silgard 184, Electron Microscopy Sciences) over a silicon wafer master, a gift from Dr. Beth Pruitt, University of California, Santa Barbara, cured overnight and then gently peeled off. PDMS stamps were then coated in Matrigel overnight.

This Matrigel was then stamped onto an 18 mm cover glass, which was peeled off and then subsequently placed facedown onto a 10 kPa polyacrylamide gel base (0.025 g/mL bis-acrylamide and 0.5 g/mL acrylamide polymerized with 10% APS and TEMED) adhered to plasma treated, glass-bottom 6-well culture dish wells using bind-silane. After hydrating these patterns with phosphate buffered saline (PBS) overnight at 4°C, 300-500k day 33-37 iPSC-CMs per well were replated onto the patterns in replating media (RPMI, 1X B27 supplement, 1:100 pen/strep, and 10 mM rock inhibitor) and allowed to adhere in a concentrated, 0.5 ml bubble only on top of the patterned area for 2 hours in the 37°C incubator. After 2 hours, each well was topped up with replating media for overnight incubation. 24 hours after replating, media was replaced with 50:50

RPMI: DMEM minus glucose media with 1X B27 supplement to begin increasing the concentration of Ca^{2+} from 0.4 mM to 1.1 mM [17]. After 2 days, Ca^{2+} concentration was further increased from 1.1 mM to 1.45 mM by replacing media with 25:75 RPMI: DMEM minus glucose media with 1X B27 supplement. Cells were maintained in this media for 7-8 days (for a total of 10-11 days on the patterned surface).

For myofibril isolation, day 44-47 cells on patterned surfaces were directly treated with pCa 9.0 relaxation solution (170 mM ionic strength, 3 M pMg, 15 mM total EGTA, 80 mM total MOPS, 5 mM MgATP, 15 mM total creatine phosphate, 83 mM free K, and 52 mM free Na) supplemented with 1:100 PIC and 1% Triton X-100 for 10 min on ice. Cells were then washed twice with pCa 9.0 and 1:100 PIC without Triton X-100, gently lifted off the plate with a cell scraper, and solution collected. Myofibrils from iPSC-CMs were mounted into a custom-built apparatus with rapid Ca^{2+} solution switching (15°C) to measure myofibrillar contraction and relaxation kinetics at the millisecond timescale, as previously described (stiffness of force-transducer needle: 23.11 nN/nm) (Pioner, Guan, et al., 2020; J. M. Pioner et al., 2016).

Myofibrils are maximally activated in pCa 4.0 and then subsequently activated in sub-maximal pCa 5.6. To determine changes in adenosine diphosphate (ADP) release from myosin during cross-bridge cycling, 50% of the nucleotide pool in pCa 9.0 and sub-maximal pCa 5.6 solutions were replaced with ADP. For this experiment, each myofibril starting in 100% ATP (5 mM) pCa 9.0 was first exposed pCa 4.0 and pCa 5.6 both with 100% ATP as the nucleotide pool, and then immediately switched to pCa 9.0 and pCa 5.6 solutions with 50% ADP (2.5 mM) and 50% ATP (2.5 mM). For myofibril experiments, *n* equals the number of individual myofibrils analyzed.

iii. Applicable Results

- *Accelerated myofibril cross-bridge cycling and thin filament deactivation are hallmarks of the MYBPC3-c.772G>A mutation both early and later stage of the disease.*

To determine the impact of the reduced cMyBP-C protein expression on contractile function in *MYBPC3*-c.772G>A iPSC-CMs, we measured force during the activation and relaxation of single myofibrils resulting from rapid solution switching between low and high calcium. Myofibril elongation and organization within iPSC-CMs was improved by culturing cells on patterned surfaces, starting at day 38, for one week (Figure 1A) and progressively increasing calcium concentration from 0.4 to 1.45 mM in the culture media to maintain spontaneous contractions and enhance myofibril maturity and organization before myofibril isolation. We consistently isolated myofibrils between 50-100 μm in length from permeabilized iPSC-CMs and mounted them between a glass motor arm and force transducer to assess force generation and kinetics of contraction and relaxation (Figure 3A).

Myofibrils were first maximally activated (pCa 4.0) and relaxed (pCa 9.0), then the activation-relaxation protocol was repeated using a sub-maximal calcium (pCa 5.6) solution, which is more relevant to physiological conditions. Figure 1B shows average force traces at pCa 4.0 for both the patient and isogenic iPSC-CM myofibrils, normalized in amplitude to compare the kinetics for each phase of contraction and relaxation. During myofibril activation, the rate constant estimated from the half time of active force rise (k_{ACT}, s^{-1}) is determined by the rates of myosin recruitment and cross-bridge binding and cycling. Upon switching back to low calcium solution (pCa 9.0) after reaching steady state force, myofibril relaxation is characterized by an initial slow, linear phase then a rapid exponential phase where force returns to baseline, as previously described. The initial, linear phase of relaxation (slow phase) is characterized by two parameters: the normalized slope of force decay ($k_{REL,\ slow}$, s^{-1}) which reflects the rate of cross-bridge detachment under isometric conditions, and the duration of this slow phase ($t_{REL,\ slow}$, ms) that is

dependent on thin filament deactivation resulting from calcium removal from troponins (Kreutziger et al., 2011). The second, fast phase of relaxation, characterized by a rate constant estimated from the half time of the fast force decay ($k_{REL, fast}$, s^{-1}) is dependent on a complex set of factors that includes temporal differences in relaxation of coupled sarcomeres, myofibril elastic properties, crossbridge cycling rates and de-recruitment of myosin.

Figure 1C shows that at day 45, maximal contraction force was slightly elevated in the patient ID3 myofibrils compared to the isogenic cID3 line (pCa 4.0: 33.87 $\pm$ 0.76 vs. 30.37 $\pm$ 1.49, p=0.0452). The elevation of force in the patient ID3 myofibrils was more pronounced at submaximal activations (pCa 5.6: 21.70 $\pm$ 1.34 vs. 15.32 $\pm$ 1.77, p=0.0082). This demonstrates an elevation of specific force when there is 20% less cMyBP-C present. The percentage of force production at submaximal compared to maximal calcium exposure was unchanged between the patient ID3 and isogenic cID3 cell lines (Figure 3D), suggesting no change in calcium sensitivity due to this mutation, consistent with the myectomy tissue data from patients from whom the iPSC-CMs were generated.

Patient ID3 myofibrils exhibited accelerated force development rate during activation at both maximal and submaximal calcium (pCa 4.0: 0.82 $\pm$ 0.05 vs. 0.57 $\pm$ 0.03, p<0.0001 and pCa 5.6: 0.72 $\pm$ 0.03 vs. 0.42 $\pm$ 0.03, p<0.0001; Figure 1E). The rate associated with the initial linear relaxation phase was accelerated in patient ID3 myofibrils compared to the isogenic cID3 line at both maximal and submaximal calcium (pCa 4.0: 1.18 $\pm$ 0.17 vs. 0.64 $\pm$ 0.1, p=0.0104 and pCa 5.6: 1.65 $\pm$ 0.19 vs 0.76 $\pm$ 0.07, p=0.0003; Figure 1F) and the duration of the slow phase of relaxation was shorter in the patient ID3 myofibrils compared to the isogenic cID3 line at both maximal and submaximal calcium solutions (pCa 4.0: 84.67 $\pm$ 5.69 vs. 125.10 $\pm$ 5.87, p<0.0001 and pCa 5.6: 91.33 $\pm$ 5.97 vs. 138.77 $\pm$ 7.29, p<0.0001; Figure 1G). During the fast phase of relaxation, the rate of relaxation was faster in the patient ID3 myofibrils compared to the isogenic

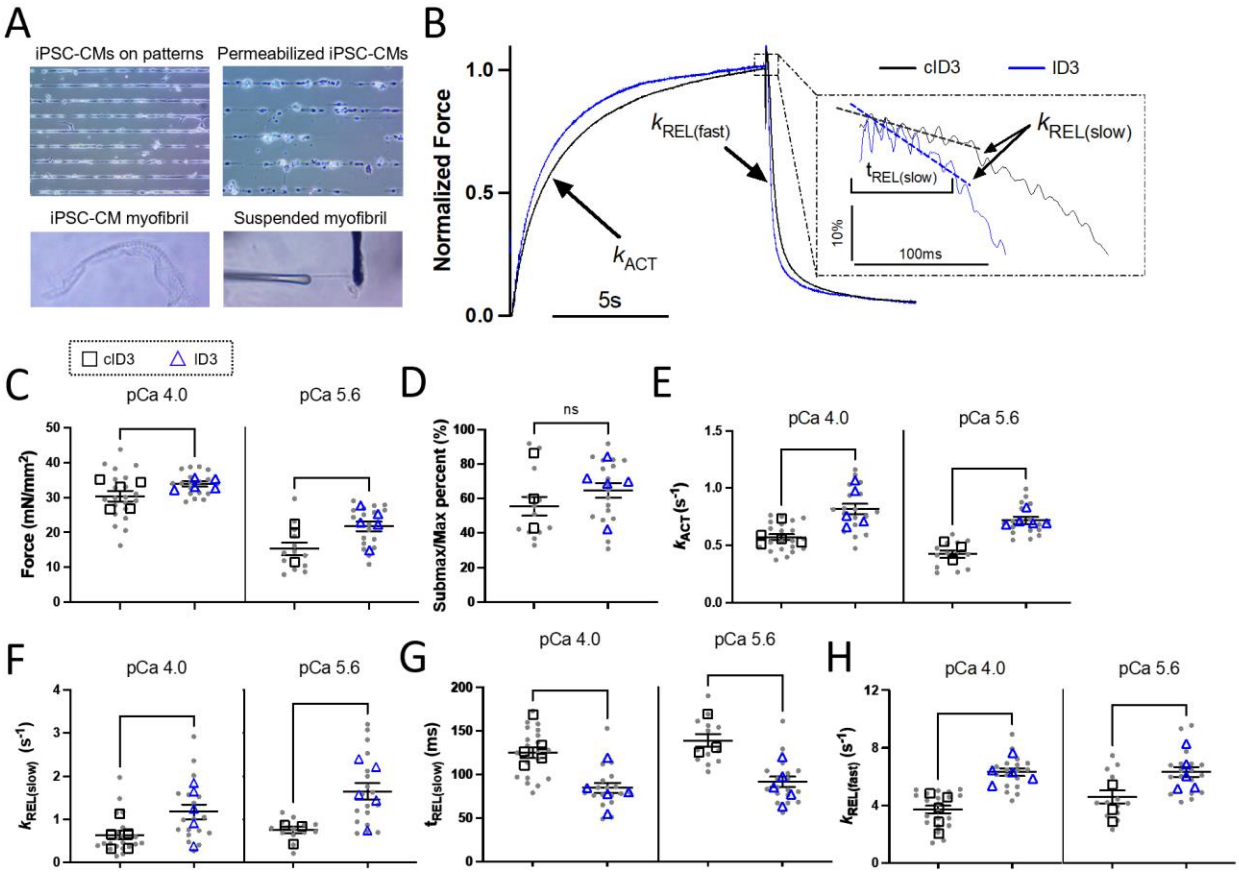

Figure 1. *MYBPC3*-c.772G>A myofibril exhibit accelerated cross-bridge cycling and thin filament deactivation time.

(A) Representative images of iPSC-CMs on patterns before and after skinning with Triton X-100 and a single isolated iPSC-CM myofibril before and after picking up the myofibril between 2 glass needles in preparation for myofibril experiments. (B) Average normalized myofibril kinetics trace highlighting phases of contraction and relaxation for both isogenic cID3 (grey line) and patient ID3 lines (blue line). Contractile dynamics parameters at both maximal pCa 4.0 and sub-maximal pCa 5.6 from day 44-47 isolated iPSC-CM myofibrils include (C) maximal and sub-maximal specific force, (D) ratio of sub-maximal to maximal specific force (%), (E) rate of activation (k_{ACT}), (F) rate of the slow phase of relaxation under isometric length conditions (k_{REL}, slow), (G) duration of the slow phase of relaxation (t_{REL}, slow), and (H) rate of the fast phase of relaxation (k_{REL}, fast) (cID3: pCa 4.0 – *N*=5, *n*=21, pCa 5.6 – *N*=3, *n*=13; ID3: pCa 4.0 – *N*=5, *n*=18, pCa 5.6 – *N*=5, *n*=18). All data are presented as mean ± SEM. Student t-test with Welch Correction, *p<0.05, **p<0.01, ***p<0.001, ****p<0.0001.

cID3 line at both maximal and submaximal calcium concentrations (pCa 4.0: 6.26 ± 0.4 vs. 3.19 ± 0.33, p<0.0001 and pCa 5.6: 6.33 ± 0.35 vs. 4.59 ± 0.44, p=0.0051; Figure 1H). Overall, these results suggest that the patient ID3 iPSC-CM myofibrils exhibit acceleration of cross-bridge

cycling as well as faster thin filament deactivation, compared to the isogenic cID3 iPSC-CM myofibrils.

- Accelerated cross-bridge cycling in isolated myofibrils is due, at least in part, to faster ADP release from myosin*.*

The acceleration in cross-bridge detachment during the slow phase of relaxation in the patient ID3 myofibrils suggests that the c.772G>A mutation may lead to an acceleration of product release. The rate limiting step of cross-bridge detachment during loaded contractions is product release of ADP after the power stroke (Siemankowski et al., 1985). ADP release, specifically during cross-bridge detachment, can be probed by a product inhibition experiment, where the concentration of ADP within the complete nucleotide pool is elevated during the myofibril kinetics assay. By increasing the concentration of ADP in solution, the release of ADP from the nucleotide binding pocket of myosin is slowed, thereby prolonging myosin heads in strongly bound states. For this assay, myofibrils were first activated with submaximal Ca^{2+} (pCa 5.6) with 100% ATP nucleotide (5 mM), and then, in a pairwise fashion, subsequently exposed to pCa 5.6 and pCa 9.0 with 50% of the nucleotide pool replaced with ADP (50:50 ATP:ADP; 2.5 mM of each).

As expected, ADP treatment slowed down both the rates of activation (k_{ACT}) and the fast phase of relaxation ($k_{REL,\ fast}$) (Figure 2A, B). Highlighting the slow phase of relaxation, increasing ADP slows down the kinetics of cross-bridge detachment ($k_{REL,\ slow}$), as can be seen by the decreased $k_{REL,\ slow}$, and increased duration of thin filament deactivation time ($t_{REL,\ slow}$) (Figure 2C-E). Based on a two-way ANOVA analysis of the $k_{REL,\ slow}$ before and after ADP treatment, there is a statistically significant difference between the patient ID3 and isogenic cID3 cell lines in the effect of elevated ADP on relaxation (interaction: $p = 0.0249$, cell line: $p = 0.0008$, ADP: $p<0.0001$) (Figure 1B). For patient ID3 myofibrils, ADP slows down cross-bridge detachment to a greater extent than the isogenic cID3 myofibrils. This is supportive of the phenotype of faster cross-bridge detachment in the patient ID3 myofibrils due to intrinsically faster ADP release from myosin. For

$t_{REL,\ slow}$, ADP treatment lengthens the thin filament deactivation time for both cell lines equally (Figure 1C). While elevation of ADP is also expected to increase myofibril specific force, we did not see a change in specific force for either cell line. This was most likely due to some rundown of the myofibrils with multiple successive activations, which usually does not affect kinetics.

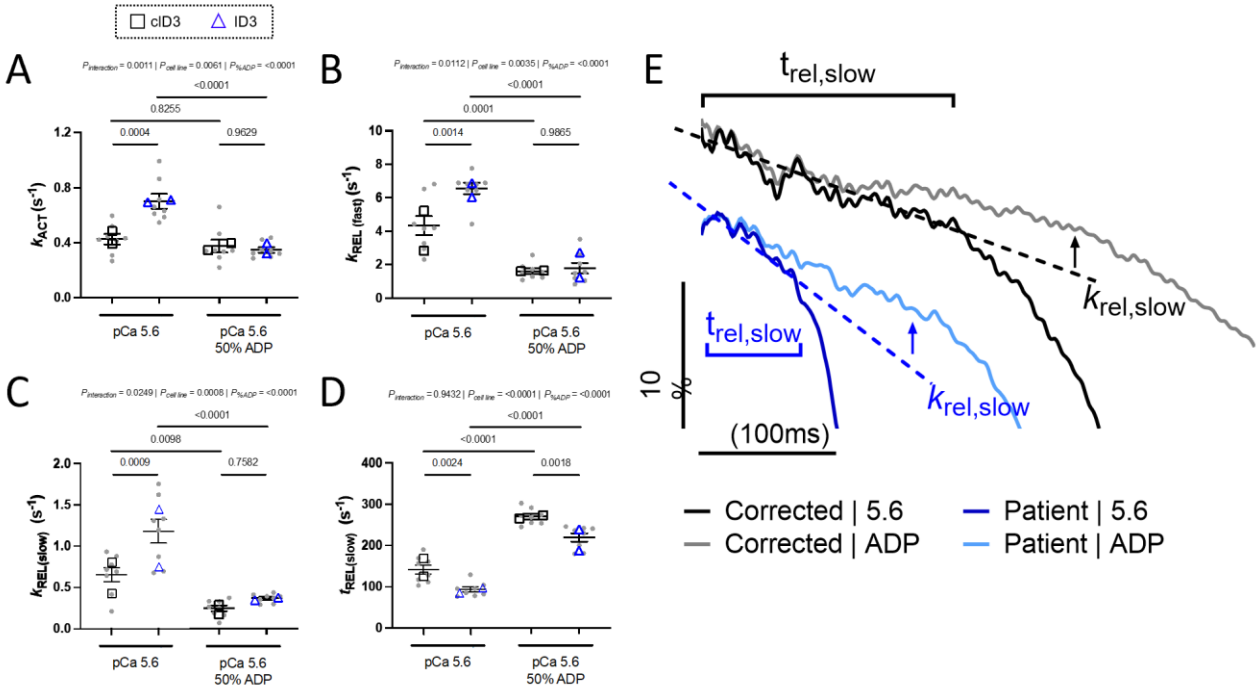

Figure 4. Accelerated cross-bridge cycling in isolated myofibrils is due in part to faster ADP release from myosin.

Quantification of (A) rate of the rate of activation (k_{ACT}), (B) rate of the fast phase of relaxation (k_{REL}, fast), (C) slow phase of relaxation under isometric length conditions (k_{REL}, slow), and (D) duration of the slow phase of relaxation (t_{REL}, slow), paired before and after ADP treatment under submaximal pCa 5.6 activation conditions (cID3: *N*=2, *n*=8; ID3: ID3: *N*=2, *n*=8). (E) Trace highlighting the slow phase of relaxation (with a manual offset between the two cell lines for visualization) before and after the ADP inhibition experiment for both isogenic cID3 (black: 100% ATP, grey: 50% ATP:50% ADP) and patient ID3 (dark blue: 100% ATP, light blue: 50% ATP:50% ADP) lines. All data are presented as mean ± SEM.

iv. Discussion

Much of our current understanding of HCM disease mechanisms have been determined using rodent models or patient cardiac tissue samples at mid- or end-stage of disease

development. The use of iPSC-CMs has now unlocked the ability to investigate the initial time course of the disease phenotype and probe mechanistic questions related to disease initiation. Findings for the *MYBPC3*-c.772G>A mutation from human myectomy samples have now been validated with an *in vitro* iPSC-CM model reprogrammed from a representative HCM patient with the c.772G>A mutation. Using this iPSC-CM model and its CRISPR/Cas9 isogenic line, we have determined that the mutation-induced exon 6 skipping leads to haploinsufficiency and alteration of contractile properties at the earliest stages of iPSC-CM maturation. Myofibrils isolated from patient iPSC-CM recapitulate the cross-bridge kinetics defects found in the myectomy tissue. Using these myofibrils, we provide mechanistic evidence that the cMyBP-C haploinsufficiency, occurring because of the *MYBPC3*-c.772G>A mutation, alters crossbridge induced product release of ADP and PKA mediated phosphorylation at the earliest stages of disease development.

This mutation accelerated myofibril kinetics during contraction and both phases of relaxation, indicative that the myofibrils exhibit faster cross-bridge cycling due to the mutation. The differences in cross-bride cycling kinetics between the patient and isogenic iPSC-CM myofibrils can be attributed specifically to cMyBP-C haploinsufficiency and elevation in cMyBP-C phosphorylation. Our results support that myofibril kinetics changes occur by day 45 of patient iPSC-CM development and are in line with results obtained from patient myectomy tissue. This supports the use of our patient iPSC-CMs as an effective *in vitro* disease model to probe early-stage mechanistic questions. Similar myofibril kinetics changes occur between iPSC-CMs and the myectomy tissue samples even though the force is significantly lower in the iPSC-CM myofibrils compared to the myofibrils isolated from myectomy tissue. These results indicate that the mechanism altering cross-bridge cycling occurs irrespective of the amount of myosin present in the myofibril, since force is relative to number of myosin's recruited for actin binding during myofibril activation.

Utilizing our iPSC-CM isolated myofibrils we aimed to determine how reduced cMyBP-C protein content may be leading to changes in cross-bridge kinetics. ADP release is a rate limiting step of cross-bridge cycling and that rate of ADP release can directly impact how long myosin remains attached to actin. Thus, we performed an ADP inhibition experiment to probe how this mutation impacts ADP release and in turn affect cross-bridge cycling. Our results supported that during the slow phase of relaxation, the rate of cross-bridge detachment was disproportionately impacted by increased ADP concentration on the patient iPSC-CM myofibrils compared to the myofibrils from the isogenic line. These results provide evidence that this mutation results in a faster ADP release from myosin, allowing for accelerated propagation through the cross-bridge cycle. This faster ADP release is likely connected to there being reduced presence of cMyBP-C due to this mutation, consistent with previous work showing that mice with a homozygous *MYBPC3* knock out exhibited enhanced ADP release. This mutation has also been shown to directly impact the interaction between the C1-C2 domain of cMyBP-C and the myosin sub-fragment 2 (De Lange et al., 2013). This disruption in protein-protein interaction between cMyBP-C and myosin could impact product release from myosin during contractility as well as could impact myosin recruitment as was seen in the elevated force capacity of the patient iPSC-CM myofibrils compared to isogenic controls.

XII. References

Adhikari, A. S., Trivedi, D. V., Sarkar, S. S., Song, D., Kooiker, K. B., Bernstein, D., Spudich, J. A., & Ruppel, K. M. (2019). beta-Cardiac myosin hypertrophic cardiomyopathy mutations release sequestered heads and increase enzymatic activity. *Nat Commun*, *10*(1), 2685. https://doi.org/10.1038/s41467-019-10555-9

Agarwal, M., Sharma, A., Kumar, P., Kumar, A., Bharadwaj, A., Saini, M., Kardon, G., & Mathew, S. J. (2020). Myosin heavy chain-embryonic regulates skeletal muscle differentiation during mammalian development. *Development*, *147*(7). https://doi.org/10.1242/dev.184507

Al-Qusairi, L., & Laporte, J. (2011). T-tubule biogenesis and triad formation in skeletal muscle and implication in human diseases. *Skeletal Muscle*, *1*(1), 26. https://doi.org/10.1186/2044-5040-1-26

Alamo, L., Qi, D., Wriggers, W., Pinto, A., Zhu, J., Bilbao, A., Gillilan, R. E., Hu, S., & Padron, R. (2016). Conserved Intramolecular Interactions Maintain Myosin Interacting-Heads Motifs Explaining Tarantula Muscle Super-Relaxed State Structural Basis. *J Mol Biol*, *428*(6), 1142-1164. https://doi.org/10.1016/j.jmb.2016.01.027

Anderson, R., Trivedi, D., Sarkar, S., Henze, M., Ma, W., Gong, H., Rogers, C., Wong, F., Morck, M., Seidman, J., Ruppel, K., Irving, T., Cooke, R., Green, E., & Spudich, J. (2018). Mavacamten stabilizes a folded-back sequestered super-relaxed state of β-cardiac myosin. *bioRxiv*, *266783; doi: https://doi.org/10.1101/266783*.

Anderson, R. L., Trivedi, D. V., Sarkar, S. S., Henze, M., Ma, W., Gong, H., Rogers, C. S., Gorham, J. M., Wong, F. L., Morck, M. M., Seidman, J. G., Ruppel, K. M., Irving, T. C., Cooke, R., Green, E. M., & Spudich, J. A. (2018a). Deciphering the super relaxed state of human beta-cardiac myosin and the mode of action of mavacamten from myosin molecules to muscle fibers. *Proc Natl Acad Sci U S A*, *115*(35), E8143-E8152. https://doi.org/10.1073/pnas.1809540115

Anderson, R. L., Trivedi, D. V., Sarkar, S. S., Henze, M., Ma, W., Gong, H., Rogers, C. S., Gorham, J. M., Wong, F. L., Morck, M. M., Seidman, J. G., Ruppel, K. M., Irving, T. C., Cooke, R., Green, E. M., & Spudich, J. A. (2018b). Deciphering the super relaxed state of human β-cardiac myosin and the mode of action of mavacamten from myosin molecules to muscle fibers. *Proc Natl Acad Sci U S A*, *115*(35), E8143-e8152. https://doi.org/10.1073/pnas.1809540115

Anderson, R. L., Trivedi, D. V., Sarkar, S. S., Henze, M., Ma, W., Gong, H., Rogers, C. S., Gorham, J. M., Wong, F. L., Morck, M. M., Seidman, J. G., Ruppel, K. M., Irving, T. C., Cooke, R., Green, E. M., & Spudich, J. A. (2018). Deciphering the super relaxed state of human β-cardiac myosin and the mode of action of mavacamten from myosin molecules to muscle fibers. *Proceedings of the National Academy of Sciences*, *115*(35), E8143-E8152. https://doi.org/10.1073/pnas.1809540115

Baylor, S. M., & Hollingworth, S. (2011). Calcium indicators and calcium signalling in skeletal muscle fibres during excitation–contraction coupling. *Progress in Biophysics and Molecular Biology*, *105*(3), 162-179. https://doi.org/10.1016/j.pbiomolbio.2010.06.001

Bell, K., Anto, A. R., Anderson, R. L., Del Rio, C. L., & Henze, M. (2020). Cardiac muscle activation; the role of length dependent activation and the novel myosin activator danicamtiv. *European Heart Journal*, *41*(Supplement_2). https://doi.org/10.1093/ehjci/ehaa946.3681

Belus, A., Piroddi, N., Scellini, B., Tesi, C., Amati, G. D., Girolami, F., Yacoub, M., Cecchi, F., Olivotto, I., & Poggesi, C. (2008). The familial hypertrophic cardiomyopathy-associated myosin mutation R403Q accelerates tension generation and relaxation of human cardiac

myofibrils. *The Journal of Physiology*, *586*(15), 3639-3644. https://doi.org/10.1113/jphysiol.2008.155952

Berman, H. M., Battistuz, T., Bhat, T. N., Bluhm, W. F., Bourne, P. E., Burkhardt, K., Feng, Z., Gilliland, G. L., Iype, L., Jain, S., Fagan, P., Marvin, J., Padilla, D., Ravichandran, V., Schneider, B., Thanki, N., Weissig, H., Westbrook, J. D., & Zardecki, C. (2002). The Protein Data Bank. *Acta Crystallogr D Biol Crystallogr*, *58*(Pt 6 No 1), 899-907. https://doi.org/10.1107/s0907444902003451

Biesiadecki, B. J., Davis, J. P., Ziolo, M. T., & Janssen, P. M. L. (2014). Tri-modal regulation of cardiac muscle relaxation; intracellular calcium decline, thin filament deactivation, and cross-bridge cycling kinetics. *Biophys Rev*, *6*(3-4), 273-289. https://doi.org/10.1007/s12551-014-0143-5

Biga, L. (2019). *Anatomy Physiology*. https://open.oregonstate.education/aandp/chapter/10-2-skeletal-muscle/#:~:text=the%20whole%20muscle).-,Figure%2010.2.,the%20cell%20its%20striated%20appearance.

Blanchard, E., Seidman, C., Seidman, J. G., LeWinter, M., & Maughan, D. (1999). Altered crossbridge kinetics in the alphaMHC403/+ mouse model of familial hypertrophic cardiomyopathy. *Circ Res*, *84*(4), 475-483. https://doi.org/10.1161/01.res.84.4.475

Blankenfeldt, W., Thomä, N. H., Wray, J. S., Gautel, M., & Schlichting, I. (2006). Crystal structures of human cardiac β-myosin II S2-Δ provide insight into the functional role of the S2 subfragment. *Proceedings of the National Academy of Sciences*, *103*(47), 17713-17717. https://doi.org/10.1073/pnas.0606741103

Boland, M., Kaur, L., Chian, F. M., & Astruc, T. (2019). Muscle Proteins. In *Encyclopedia of Food Chemistry* (pp. 164-179). Elsevier. https://doi.org/10.1016/b978-0-08-100596-5.21602-8

Brady, A. J. (1967a). Length-tension relations in cardiac muscle. *Am Zool*, *7*(3), 603-610. https://doi.org/10.1093/icb/7.3.603

Brady, A. J. (1967b). The three element model of muscle mechanics: its applicability to cardiac muscle. *Physiologist*, *10*(2), 75-86. https://www.ncbi.nlm.nih.gov/pubmed/6046277

Calderón, J. C., Bolaños, P., & Caputo, C. (2014). The excitation–contraction coupling mechanism in skeletal muscle. *Biophysical Reviews*, *6*(1), 133-160. https://doi.org/10.1007/s12551-013-0135-x

Caremani, M., Brunello, E., Linari, M., Fusi, L., Irving, T. C., Gore, D., Piazzesi, G., Irving, M., Lombardi, V., & Reconditi, M. (2019). Low temperature traps myosin motors of mammalian muscle in a refractory state that prevents activation. *J Gen Physiol*, *151*(11), 1272-1286. https://doi.org/10.1085/jgp.201912424

Carrier, L., Knoll, R., Vignier, N., Keller, D. I., Bausero, P., Prudhon, B., Isnard, R., Ambroisine, M. L., Fiszman, M., Ross, J., Jr., Schwartz, K., & Chien, K. R. (2004). Asymmetric septal hypertrophy in heterozygous cMyBP-C null mice. *Cardiovasc Res*, *63*(2), 293-304. https://doi.org/10.1016/j.cardiores.2004.04.009

Case, D. A., Cheatham, T. E., 3rd, Darden, T., Gohlke, H., Luo, R., Merz, K. M., Jr., Onufriev, A., Simmerling, C., Wang, B., & Woods, R. J. (2005). The Amber biomolecular simulation programs. *J Comput Chem*, *26*(16), 1668-1688. https://doi.org/10.1002/jcc.20290

Chabes, A. L., Pfleger, C. M., Kirschner, M. W., & Thelander, L. (2003). Mouse ribonucleotide reductase R2 protein: a new target for anaphase-promoting complex-Cdh1-mediated proteolysis. *Proc Natl Acad Sci U S A*, *100*(7), 3925-3929. https://doi.org/10.1073/pnas.0330774100

Chal, J., Oginuma, M., Al Tanoury, Z., Gobert, B., Sumara, O., Hick, A., Bousson, F., Zidouni, Y., Mursch, C., Moncuquet, P., Tassy, O., Vincent, S., Miyanari, A., Bera, A., Garnier, J. M., Guevara, G., Hestin, M., Kennedy, L., Hayashi, S., . . . Pourquie, O. (2015).

Differentiation of pluripotent stem cells to muscle fiber to model Duchenne muscular dystrophy. *Nat Biotechnol*, *33*(9), 962-969. https://doi.org/10.1038/nbt.3297
Cheng, Y., Hogarth, K. A., O'Sullivan, M. L., Regnier, M., & Pyle, W. G. (2016). 2-Deoxyadenosine triphosphate restores the contractile function of cardiac myofibril from adult dogs with naturally occurring dilated cardiomyopathy. *Am J Physiol Heart Circ Physiol*, *310*(1), H80-91. https://doi.org/10.1152/ajpheart.00530.2015
Cheng, Y., & Regnier, M. (2016). Cardiac troponin structure-function and the influence of hypertrophic cardiomyopathy associated mutations on modulation of contractility. *Arch Biochem Biophys*, *601*, 11-21. https://doi.org/10.1016/j.abb.2016.02.004
Cheng, Y., Wan, X., McElfresh, T. A., Chen, X., Gresham, K. S., Rosenbaum, D. S., Chandler, M. P., & Stelzer, J. E. (2013). Impaired contractile function due to decreased cardiac myosin binding protein C content in the sarcomere. *Am J Physiol Heart Circ Physiol*, *305*(1), H52-65. https://doi.org/10.1152/ajpheart.00929.2012
Cheung, A., Dantzig, J. A., Hollingworth, S., Baylor, S. M., Goldman, Y. E., Mitchison, T. J., & Straight, A. F. (2002). A small-molecule inhibitor of skeletal muscle myosin II. *Nat Cell Biol*, *4*(1), 83-88. https://doi.org/10.1038/ncb734
Childers, M. C., Geeves, M., Daggett, V., & Regnier, M. (2020). Modulation of post-powerstroke dynamics in myosin II by 2'-deoxy-ADP. *Arch Biochem Biophys*, *699*, 108733. https://doi.org/10.1016/j.abb.2020.108733
Chou, S. Z., & Pollard, T. D. (2019). Mechanism of actin polymerization revealed by cryo-EM structures of actin filaments with three different bound nucleotides. *Proceedings of the National Academy of Sciences*, *116*(10), 4265-4274. https://doi.org/10.1073/pnas.1807028115
Chu, S., Muretta, J. M., & Thomas, D. D. (2021). Direct detection of the myosin super-relaxed state and interacting-heads motif in solution. *Journal of Biological Chemistry*, *297*(4), 101157. https://doi.org/10.1016/j.jbc.2021.101157
Chu, S., Muretta, J. M., & Thomas, D. D. (2021). Direct detection of the myosin super-relaxed state and interacting-heads motif in solution. *J Biol Chem*, *297*(4), 101157. https://doi.org/10.1016/j.jbc.2021.101157
Cooke, R. (2011). The role of the myosin ATPase activity in adaptive thermogenesis by skeletal muscle. *Biophys Rev*, *3*(1), 33-45. https://doi.org/10.1007/s12551-011-0044-9
Cooper, G. M. (2000). *The cell : a molecular approach* (2nd ed.). ASM Press ;

Sinauer Associates. http://www.ncbi.nlm.nih.gov/books/bv.fcgi?rid=cooper
Craig, R., & Padron, R. (2022). Structural basis of the super- and hyper-relaxed states of myosin II. *J Gen Physiol*, *154*(1). https://doi.org/10.1085/jgp.202113012
Craig, R., & Padrón, R. (2022). Structural basis of the super- and hyper-relaxed states of myosin II. *Journal of General Physiology*, *154*(1). https://doi.org/10.1085/jgp.202113012
Crocini, C., & Gotthardt, M. (2021). Cardiac sarcomere mechanics in health and disease. *Biophysical Reviews*, *13*(5), 637-652. https://doi.org/10.1007/s12551-021-00840-7
Davis, J., Davis, L. C., Correll, R. N., Makarewich, C. A., Schwanekamp, J. A., Moussavi-Harami, F., Wang, D., York, A. J., Wu, H., Houser, S. R., Seidman, C. E., Seidman, J. G., Regnier, M., Metzger, J. M., Wu, J. C., & Molkentin, J. D. (2016). A Tension-Based Model Distinguishes Hypertrophic versus Dilated Cardiomyopathy. *Cell*, *165*(5), 1147-1159. https://doi.org/10.1016/j.cell.2016.04.002
Davis, J. P., Norman, C., Kobayashi, T., Solaro, R. J., Swartz, D. R., & Tikunova, S. B. (2007). Effects of Thin and Thick Filament Proteins on Calcium Binding and Exchange with Cardiac Troponin C. *Biophysical Journal*, *92*(9), 3195-3206. https://doi.org/10.1529/biophysj.106.095406
De Lange, W. J., Grimes, A. C., Hegge, L. F., Spring, A. M., Brost, T. M., & Ralphe, J. C. (2013). E258K HCM-causing mutation in cardiac MyBP-C reduces contractile force and

accelerates twitch kinetics by disrupting the cMyBP-C and myosin S2 interaction. *J Gen Physiol*, *142*(3), 241-255. https://doi.org/10.1085/jgp.201311018
Denisin, A. K., & Pruitt, B. L. (2016). Tuning the Range of Polyacrylamide Gel Stiffness for Mechanobiology Applications. *ACS Applied Materials & Interfaces*, *8*(34), 21893-21902. https://doi.org/10.1021/acsami.5b09344
Desjardins, C. L., Chen, Y., Coulton, A. T., Hoit, B. D., Yu, X., & Stelzer, J. E. (2012). Cardiac myosin binding protein C insufficiency leads to early onset of mechanical dysfunction. *Circ Cardiovasc Imaging*, *5*(1), 127-136. https://doi.org/10.1161/CIRCIMAGING.111.965772
Doran, M. H., Pavadai, E., Rynkiewicz, M. J., Walklate, J., Bullitt, E., Moore, J. R., Regnier, M., Geeves, M. A., & Lehman, W. (2020). Cryo-EM and Molecular Docking Shows Myosin Loop 4 Contacts Actin and Tropomyosin on Thin Filaments. *Biophys J*, *119*(4), 821-830. https://doi.org/10.1016/j.bpj.2020.07.006
Dutta, D., Nguyen, V., Campbell, K. S., Padrón, R., & Craig, R. (2023). Cryo-EM structure of the human cardiac myosin filament. *bioRxiv*, 2023.2004.2011.536274. https://doi.org/10.1101/2023.04.11.536274
Eisner, D. A., Caldwell, J. L., Kistamás, K., & Trafford, A. W. (2017). Calcium and Excitation-Contraction Coupling in the Heart. *Circulation Research*, *121*(2), 181-195. https://doi.org/10.1161/circresaha.117.310230
Fatkin, D., Mcconnell, B. K., Mudd, J. O., Semsarian, C., Moskowitz, I. G. P., Schoen, F. J., Giewat, M., Seidman, C. E., & Seidman, J. G. (2000). An abnormal Ca2+ response in mutant sarcomere protein–mediated familial hypertrophic cardiomyopathy. *Journal of Clinical Investigation*, *106*(11), 1351-1359. https://doi.org/10.1172/jci11093
Feher, J. J. (2012). *Quantitative human physiology : an introduction*. Elsevier/Academic Press. Publisher description http://www.loc.gov/catdir/enhancements/fy1606/2012405805-d.html
Fischetti, R., Stepanov, S., Rosenbaum, G., Barrea, R., Black, E., Gore, D., Heurich, R., Kondrashkina, E., Kropf, A. J., Wang, S., Zhang, K., Irving, T. C., & Bunker, G. B. (2004). The BioCAT undulator beamline 18ID: a facility for biological non-crystalline diffraction and X-ray absorption spectroscopy at the Advanced Photon Source. *J. Synchrotron Radiat.*, ***11,***(Pt 5), 399-405. http://www.ncbi.nlm.nih.gov/entrez/query.fcgi?cmd=Retrieve&db=PubMed&dopt=Citation&list_uids=15310956
Garcia-Pavia, P., Kim, Y., Restrepo-Cordoba, M. A., Lunde, I. G., Wakimoto, H., Smith, A. M., Toepfer, C. N., Getz, K., Gorham, J., Patel, P., Ito, K., Willcox, J. A., Arany, Z., Li, J., Owens, A. T., Govind, R., Nunez, B., Mazaika, E., Bayes-Genis, A., . . . Seidman, C. E. (2019). Genetic Variants Associated With Cancer Therapy-Induced Cardiomyopathy. *Circulation*, *140*(1), 31-41. https://doi.org/10.1161/CIRCULATIONAHA.118.037934
Geeves, M. A., Lehrer, S. S., & Lehman, W. (2019). The mechanism of thin filament regulation: Models in conflict? *Journal of General Physiology*, *151*(11), 1265-1271. https://doi.org/10.1085/jgp.201912446
Geisterfer-Lowrance, A. A., Kass, S., Tanigawa, G., Vosberg, H. P., McKenna, W., Seidman, C. E., & Seidman, J. G. (1990). A molecular basis for familial hypertrophic cardiomyopathy: a beta cardiac myosin heavy chain gene missense mutation. *Cell*, *62*(5), 999-1006. https://doi.org/10.1016/0092-8674(90)90274-i
Godt, R. E., & Nosek, T. M. (1989). Changes of intracellular milieu with fatigue or hypoxia depress contraction of skinned rabbit skeletal and cardiac muscle. *The Journal of Physiology*, *412*(1), 155-180. https://doi.org/10.1113/jphysiol.1989.sp017609
Gollapudi, S., Ma, W, Chakravarth, S, Combs, AC, Sa, N, Langer, S, Irving, TC and Nag, S. . (2020). Two classes of myosin inhibitors, blebbistatin and mavacamten, stabilze beta-

cardiac myosin in different structural and functional states. *bioRxiv*. https://doi.org/doi.org/10.1101/2020.12.19.423544
Gollapudi, S. K., Ma, W., Chakravarthy, S., Combs, A. C., Sa, N., Langer, S., Irving, T. C., & Nag, S. (2021). Two Classes of Myosin Inhibitors, Para-nitroblebbistatin and Mavacamten, Stabilize beta-Cardiac Myosin in Different Structural and Functional States. *J Mol Biol*, *433*(23), 167295. https://doi.org/10.1016/j.jmb.2021.167295
Gollapudi, S. K., Yu, M., Gan, Q.-F., & Nag, S. (2021). Synthetic thick filaments: A new avenue for better understanding the myosin super-relaxed state in healthy, diseased, and mavacamten-treated cardiac systems. *Journal of Biological Chemistry*, *296*, 100114. https://doi.org/10.1074/jbc.ra120.016506
Gordon, A. M., Homsher, E., & Regnier, M. (2000). Regulation of contraction in striated muscle. *Physiol Rev*, *80*(2), 853-924. https://doi.org/10.1152/physrev.2000.80.2.853
Gordon, A. M., Huxley, A. F., & Julian, F. J. (1966a). Tension development in highly stretched vertebrate muscle fibres. *The Journal of Physiology*, *184*(1), 143-169. https://doi.org/10.1113/jphysiol.1966.sp007908
Gordon, A. M., Huxley, A. F., & Julian, F. J. (1966b). The variation in isometric tension with sarcomere length in vertebrate muscle fibres. *The Journal of Physiology*, *184*(1), 170-192. https://doi.org/10.1113/jphysiol.1966.sp007909
Governali, S., Caremani, M., Gallart, C., Pertici, I., Stienen, G., Piazzesi, G., Ottenheijm, C., Lombardi, V., & Linari, M. (2020). Orthophosphate increases the efficiency of slow muscle-myosin isoform in the presence of omecamtiv mecarbil. *Nat Commun*, *11*(1), 3405. https://doi.org/10.1038/s41467-020-17143-2
Grillo, M. P., Markova, S., Evanchik, M., Trellu, M., Moliner, P., Brun, P., Perreard-Dumaine, A., Vicat, P., Yang, C., Driscoll, J. P., & Carlson, T. J. (2021). Preclinical in vitro and in vivo pharmacokinetic properties of danicamtiv, a new targeted myosin activator for the treatment of dilated cardiomyopathy. *Xenobiotica*, *51*(2), 222-238. https://doi.org/10.1080/00498254.2020.1839982
Grinzato, A., Auguin, D., Kikuti, C., Nandwani, N., Moussaoui, D., Pathak, D., Kandiah, E., Ruppel, K. M., Spudich, J. A., Houdusse, A., & Robert-Paganin, J. (2023). Cryo-EM structure of the folded-back state of human β-cardiac myosin. *Nature Communications*, *14*(1). https://doi.org/10.1038/s41467-023-38698-w
Gupte, T. M., Haque, F., Gangadharan, B., Sunitha, M. S., Mukherjee, S., Anandhan, S., Rani, D. S., Mukundan, N., Jambekar, A., Thangaraj, K., Sowdhamini, R., Sommese, R. F., Nag, S., Spudich, J. A., & Mercer, J. A. (2015). Mechanistic heterogeneity in contractile properties of alpha-tropomyosin (TPM1) mutants associated with inherited cardiomyopathies. *J Biol Chem*, *290*(11), 7003-7015. https://doi.org/10.1074/jbc.M114.596676
Harris, S. P., Bartley, C. R., Hacker, T. A., McDonald, K. S., Douglas, P. S., Greaser, M. L., Powers, P. A., & Moss, R. L. (2002). Hypertrophic cardiomyopathy in cardiac myosin binding protein-C knockout mice. *Circ Res*, *90*(5), 594-601. https://doi.org/10.1161/01.res.0000012222.70819.64
Harris, S. P., Lyons, R. G., & Bezold, K. L. (2011). In the thick of it: HCM-causing mutations in myosin binding proteins of the thick filament. *Circ Res*, *108*(6), 751-764. https://doi.org/10.1161/CIRCRESAHA.110.231670
Hartner, K.-T., & Pette, D. (1990). Fast and slow isoforms of troponin I and troponin C. Distribution in normal rabbit muscles and effects of chronic stimulation. *European Journal of Biochemistry*, *188*(2), 261-267. https://doi.org/10.1111/j.1432-1033.1990.tb15398.x
Heissler, S. M., Arora, A. S., Billington, N., Sellers, J. R., & Chinthalapudi, K. (2021). Cryo-EM structure of the autoinhibited state of myosin-2. *Science Advances*, *7*(52), eabk3273. https://doi.org/doi:10.1126/sciadv.abk3273

Helms, A. S., Davis, F. M., Coleman, D., Bartolone, S. N., Glazier, A. A., Pagani, F., Yob, J. M., Sadayappan, S., Pedersen, E., Lyons, R., Westfall, M. V., Jones, R., Russell, M. W., & Day, S. M. (2014). Sarcomere mutation-specific expression patterns in human hypertrophic cardiomyopathy. *Circ Cardiovasc Genet*, *7*(4), 434-443. https://doi.org/10.1161/CIRCGENETICS.113.000448

Helms, A. S., Thompson, A. D., Glazier, A. A., Hafeez, N., Kabani, S., Rodriguez, J., Yob, J. M., Woolcock, H., Mazzarotto, F., Lakdawala, N. K., Wittekind, S. G., Pereira, A. C., Jacoby, D. L., Colan, S. D., Ashley, E. A., Saberi, S., Ware, J. S., Ingles, J., Semsarian, C., . . . Day, S. M. (2020). Spatial and Functional Distribution of MYBPC3 Pathogenic Variants and Clinical Outcomes in Patients With Hypertrophic Cardiomyopathy. *Circ Genom Precis Med*, *13*(5), 396-405. https://doi.org/10.1161/CIRCGEN.120.002929

Hernandez, O. M., Jones, M., Guzman, G., & Szczesna-Cordary, D. (2007). Myosin essential light chain in health and disease. *Am J Physiol Heart Circ Physiol*, *292*(4), H1643-1654. https://doi.org/10.1152/ajpheart.00931.2006

Hicks, M., & Pyle, A. (2015). The Path from Pluripotency to Skeletal Muscle: Developmental Myogenesis Guides the Way. *Cell Stem Cell*, *17*(3), 255-257. https://doi.org/10.1016/j.stem.2015.08.017

Hicks, M. R., Hiserodt, J., Paras, K., Fujiwara, W., Eskin, A., Jan, M., Xi, H., Young, C. S., Evseenko, D., Nelson, S. F., Spencer, M. J., Handel, B. V., & Pyle, A. D. (2018). ERBB3 and NGFR mark a distinct skeletal muscle progenitor cell in human development and hPSCs. *Nat Cell Biol*, *20*(1), 46-57. https://doi.org/10.1038/s41556-017-0010-2

Hinson, J. T., Chopra, A., Nafissi, N., Polacheck, W. J., Benson, C. C., Swist, S., Gorham, J., Yang, L., Schafer, S., Sheng, C. C., Haghighi, A., Homsy, J., Hubner, N., Church, G., Cook, S. A., Linke, W. A., Chen, C. S., Seidman, J. G., & Seidman, C. E. (2015). Titin mutations in iPS cells define sarcomere insufficiency as a cause of dilated cardiomyopathy. *Science*, *349*(6251), 982-986. https://doi.org/10.1126/science.aaa5458

Ho, C. Y., Mealiffe, M. E., Bach, R. G., Bhattacharya, M., Choudhury, L., Edelberg, J. M., Hegde, S. M., Jacoby, D., Lakdawala, N. K., Lester, S. J., Ma, Y., Marian, A. J., Nagueh, S. F., Owens, A., Rader, F., Saberi, S., Sehnert, A. J., Sherrid, M. V., Solomon, S. D., . . . Heitner, S. B. (2020). Evaluation of Mavacamten in Symptomatic Patients With Nonobstructive Hypertrophic Cardiomyopathy. *J Am Coll Cardiol*, *75*(21), 2649-2660. https://doi.org/10.1016/j.jacc.2020.03.064

Hodge, T., & Cope, M. J. (2000). A myosin family tree. *J Cell Sci*, *113 Pt 19*, 3353-3354. https://doi.org/10.1242/jcs.113.19.3353

Hong, T., & Shaw, R. M. (2017). Cardiac T-Tubule Microanatomy and Function. *Physiol Rev*, *97*(1), 227-252. https://doi.org/10.1152/physrev.00037.2015

Hooijman, P., Stewart, M. A., & Cooke, R. (2011a). A new state of cardiac myosin with very slow ATP turnover: a potential cardioprotective mechanism in the heart. *Biophys J*, *100*(8), 1969-1976. https://doi.org/10.1016/j.bpj.2011.02.061

Hooijman, P., Stewart, M. A., & Cooke, R. (2011b). A New State of Cardiac Myosin with Very Slow ATP Turnover: A Potential Cardioprotective Mechanism in the Heart. *Biophys J*, *100*(8), 1969-1976. https://doi.org/10.1016/j.bpj.2011.02.061

Huxley, A. F., & Niedergerke, R. (1954). Structural Changes in Muscle During Contraction: Interference Microscopy of Living Muscle Fibres. *Nature*, *173*(4412), 971-973. https://doi.org/10.1038/173971a0

Huxley, H., & Hanson, J. (1954). Changes in the Cross-Striations of Muscle during Contraction and Stretch and their Structural Interpretation. *Nature*, *173*(4412), 973-976. https://doi.org/10.1038/173973a0

Huxley, H. E. (1969). The Mechanism of Muscular Contraction. *Science*, *164*(3886), 1356-1366. https://doi.org/10.1126/science.164.3886.1356

Huxley, H. E. (1971). The Croonian Lecture, 1970 The structural basis of muscular contraction. *Proceedings of the Royal Society of London. Series B. Biological Sciences*, *178*(1051), 131-149. https://doi.org/10.1098/rspb.1971.0057

Huxley, H. E. (1971). Structural changes during muscle contraction. *Biochem J*, *125*(4), 85P. http://www.ncbi.nlm.nih.gov/entrez/query.fcgi?cmd=Retrieve&db=PubMed&dopt=Citation&list_uids=5144244

Huxley, H. E. (1973). Structural changes in actin- and myosin-containing filaments during contraction. *Cold Spring Harbor Symp. Quant. Biol.*, *37*, 361–376.

Huxley, H. E. (2004a). Fifty years of muscle and the sliding filament hypothesis. *Eur J Biochem*, *271*(8), 1403-1415. https://doi.org/10.1111/j.1432-1033.2004.04044.x

Huxley, H. E. (2004b). Recent X-ray diffraction studies of muscle contraction and their implications. *Philos Trans R Soc Lond B Biol Sci*, *359*(1452), 1879-1882. https://doi.org/10.1098/rstb.2004.1556

Huxley, H. E., & Brown, W. (1967). The low-angle x-ray diagram of vertebrate striated muscle and its behaviour during contraction and rigor. *J Mol Biol*, *30*(2), 383-434. https://www.ncbi.nlm.nih.gov/pubmed/5586931

Irving, M. (2017). Regulation of Contraction by the Thick Filaments in Skeletal Muscle. *Biophys J*, *113*(12), 2579-2594. https://doi.org/10.1016/j.bpj.2017.09.037

Jani, V., Qian, W., Yuan, S., Irving, T., & Ma, W. (2022). EMD-57033 Augments the Contractility in Porcine Myocardium by Promoting the Activation of Myosin in Thick Filaments. *Int J Mol Sci*, *23*(23). https://doi.org/10.3390/ijms232314517

Jiratrakanvong, J., Shao, J., Menendez, M., Li, X., Li, J., Ma, W., Agam, G., & Irving, T. (2018). MuscleX: software suite for diffraction X-ray imaging V1.21.0. doi:10.5281/zenodo.1195050. https://doi.org/doi:10.5281/zenodo.1195050

Kawana, M., Spudich, J. A., & Ruppel, K. M. (2022). Hypertrophic cardiomyopathy: Mutations to mechanisms to therapies. *Front Physiol*, *13*, 975076. https://doi.org/10.3389/fphys.2022.975076

Kieu, T. T., Awinda, P. O., & Tanner, B. C. W. (2019). Omecamtiv Mecarbil Slows Myosin Kinetics in Skinned Rat Myocardium at Physiological Temperature. *Biophys J*, *116*(11), 2149-2160. https://doi.org/10.1016/j.bpj.2019.04.020

Kolwicz, S. C., Jr., Hall, J. K., Moussavi-Harami, F., Chen, X., Hauschka, S. D., Chamberlain, J. S., Regnier, M., & Odom, G. L. (2019). Gene Therapy Rescues Cardiac Dysfunction in Duchenne Muscular Dystrophy Mice by Elevating Cardiomyocyte Deoxy-Adenosine Triphosphate. *JACC Basic Transl Sci*, *4*(7), 778-791. https://doi.org/10.1016/j.jacbts.2019.06.006

Kreutziger, K. L., Piroddi, N., McMichael, J. T., Tesi, C., Poggesi, C., & Regnier, M. (2011). Calcium binding kinetics of troponin C strongly modulate cooperative activation and tension kinetics in cardiac muscle. *J Mol Cell Cardiol*, *50*(1), 165-174. https://doi.org/10.1016/j.yjmcc.2010.10.025

Kreutziger, K. L., Piroddi, N., Scellini, B., Tesi, C., Poggesi, C., & Regnier, M. (2008). Thin filament Ca2+ binding properties and regulatory unit interactions alter kinetics of tension development and relaxation in rabbit skeletal muscle. *J Physiol*, *586*(Pt 15), 3683-3700. https://doi.org/10.1113/jphysiol.2008.152181

Lakdawala, N. K., Dellefave, L., Redwood, C. S., Sparks, E., Cirino, A. L., Depalma, S., Colan, S. D., Funke, B., Zimmerman, R. S., Robinson, P., Watkins, H., Seidman, C. E., Seidman, J. G., McNally, E. M., & Ho, C. Y. (2010). Familial dilated cardiomyopathy caused by an alpha-tropomyosin mutation: the distinctive natural history of sarcomeric dilated cardiomyopathy [Research Support, Non-U.S. Gov't

Research Support, U.S. Gov't, Non-P.H.S.]. *J Am Coll Cardiol*, *55*(4), 320-329. https://doi.org/10.1016/j.jacc.2009.11.017

Lamb, G. (2000). Excitation-Contraction Coupling In Skeletal Muscle: Comparisons With Cardiac Muscle. *Clinical and Experimental Pharmacology and Physiology*, *27*(3), 216-224. https://doi.org/10.1046/j.1440-1681.2000.03224.x

Lehman, S. J., Crocini, C., & Leinwand, L. A. (2022). Targeting the sarcomere in inherited cardiomyopathies. *Nature Reviews Cardiology*, *19*(6), 353-363. https://doi.org/10.1038/s41569-022-00682-0

Lehman, S. J., Crocini, C., & Leinwand, L. A. (2022). Targeting the sarcomere in inherited cardiomyopathies. *Nat Rev Cardiol*, *19*(6), 353-363. https://doi.org/10.1038/s41569-022-00682-0

Lehman, W., Craig, R., & Vibert, P. (1994). Ca^{2+} induced tropomyosin movement in *Limulus* thin filaments revealed by three-dimensional reconstruction. *Nature*, ***368,***(6466), 65-67. http://www.ncbi.nlm.nih.gov/entrez/query.fcgi?cmd=Retrieve&db=PubMed&dopt=Citation&list_uids=8107884

Li, M. X., & Hwang, P. M. (2015). Structure and function of cardiac troponin C (TNNC1): Implications for heart failure, cardiomyopathies, and troponin modulating drugs. *Gene*, *571*(2), 153-166. https://doi.org/10.1016/j.gene.2015.07.074

Lin, B. L., Li, A., Mun, J. Y., Previs, M. J., Previs, S. B., Campbell, S. G., Dos Remedios, C. G., Tombe, P. D. P., Craig, R., Warshaw, D. M., & Sadayappan, S. (2018). Skeletal myosin binding protein-C isoforms regulate thin filament activity in a Ca2+-dependent manner. *Scientific Reports*, *8*(1). https://doi.org/10.1038/s41598-018-21053-1

Linari, M., Brunello, E., Reconditi, M., Fusi, L., Caremani, M., Narayanan, T., Piazzesi, G., Lombardi, V., & Irving, M. (2015). Force generation by skeletal muscle is controlled by mechanosensing in myosin filaments. *Nature*, *528*(7581), 276-279. https://doi.org/10.1038/nature15727

Liu, X., Shu, S., & Korn, E. D. (2020). Muscle myosins form folded monomers, dimers, and tetramers during filament polymerization in vitro. *Proceedings of the National Academy of Sciences*, *117*(27), 15666-15672. https://doi.org/10.1073/pnas.2001892117

Liu, Y., White, H. D., Belknap, B., Winkelmann, D. A., & Forgacs, E. (2015). Omecamtiv Mecarbil modulates the kinetic and motile properties of porcine beta-cardiac myosin. *Biochemistry*, *54*(10), 1963-1975. https://doi.org/10.1021/bi5015166

Lowey, S., Bretton, V., Joel, P. B., Trybus, K. M., Gulick, J., Robbins, J., Kalganov, A., Cornachione, A. S., & Rassier, D. E. (2018). Hypertrophic cardiomyopathy R403Q mutation in rabbit beta-myosin reduces contractile function at the molecular and myofibrillar levels. *Proc Natl Acad Sci U S A*, *115*(44), 11238-11243. https://doi.org/10.1073/pnas.1802967115

Lowey, S., Bretton, V., Joel, P. B., Trybus, K. M., Gulick, J., Robbins, J., Kalganov, A., Cornachione, A. S., & Rassier, D. E. (2018). Hypertrophic cardiomyopathy R403Q mutation in rabbit β-myosin reduces contractile function at the molecular and myofibrillar levels. *Proceedings of the National Academy of Sciences*, *115*(44), 11238-11243. https://doi.org/10.1073/pnas.1802967115

Lowey, S., Lesko, L. M., Rovner, A. S., Hodges, A. R., White, S. L., Low, R. B., Rincon, M., Gulick, J., & Robbins, J. (2008). Functional Effects of the Hypertrophic Cardiomyopathy R403Q Mutation Are Different in an α- or β-Myosin Heavy Chain Backbone. *Journal of Biological Chemistry*, *283*(29), 20579-20589. https://doi.org/10.1074/jbc.m800554200

Lu, F., & Pu, W. T. (2020). The architecture and function of cardiac dyads. *Biophys Rev*, *12*(4), 1007-1017. https://doi.org/10.1007/s12551-020-00729-x

Lundy, S. D., Murphy, S. A., Dupras, S. K., Dai, J., Murry, C. E., Laflamme, M. A., & Regnier, M. (2014). Cell-based delivery of dATP via gap junctions enhances cardiac contractility. *J Mol Cell Cardiol*, *72*, 350-359. https://doi.org/10.1016/j.yjmcc.2014.04.010

Lymn, R. W., & Taylor, E. W. (1971). Mechanism of adenosine triphosphate hydrolysis by actomyosin. *Biochemistry*, *10*(25), 4617-4624. https://doi.org/10.1021/bi00801a004

Ma, W., Childers, M., Murray, J., Moussavi-Harami, F., Gong, H., Weiss, R., Daggett, V., Irving, T., & Regnier, M. (2020). Myosin dynamics during relaxation in mouse soleus muscle and modulation by 2'-deoxy-ATP. *J Physiol*. https://doi.org/10.1113/JP280402

Ma, W., Duno-Miranda, S., Irving, T., Craig, R., & Padron, R. (2021). Relaxed tarantula skeletal muscle has two ATP energy-saving mechanisms. *J Gen Physiol*, *153*(3). https://doi.org/10.1085/jgp.202012780

Ma, W., Gong, H., & Irving, T. (2018). Myosin Head Configurations in Resting and Contracting Murine Skeletal Muscle. *Int J Mol Sci*, *19*(9). https://doi.org/10.3390/ijms19092643

Ma, W., Gong, H., Jani, V., Lee, K. H., Landim-Vieira, M., Papadaki, M., Pinto, J. R., Aslam, M. I., Cammarato, A., & Irving, T. (2022). Myofibril orientation as a metric for characterizing heart disease. *Biophys J*, *121*(4), 565-574. https://doi.org/10.1016/j.bpj.2022.01.009

Ma, W., Gong, H., Kiss, B., Lee, E. J., Granzier, H., & Irving, T. (2018). Thick-Filament Extensibility in Intact Skeletal Muscle. *Biophys J*, *115*(8), 1580-1588. https://doi.org/10.1016/j.bpj.2018.08.038

Ma, W., Henze, M., Anderson, R. L., Gong, H., Wong, F. L., Del Rio, C. L., & Irving, T. (2021). The Super-Relaxed State and Length Dependent Activation in Porcine Myocardium. *Circ Res*, *129*(6), 617-630. https://doi.org/10.1161/CIRCRESAHA.120.318647

Ma, W., Henze, M., Anderson, R. L., Gong, H., Wong, F. L., Del Rio, C. L., & Irving, T. (2021). The Super-Relaxed State and Length Dependent Activation in Porcine Myocardium. *Circulation Research*, *129*(6), 617-630. https://doi.org/10.1161/circresaha.120.318647

Ma, W., & Irving, T. C. (2022a). Small Angle X-ray Diffraction as a Tool for Structural Characterization of Muscle Disease. *Int J Mol Sci*, *23*(6), 3052. https://doi.org/10.3390/ijms23063052

Ma, W., & Irving, T. C. (2022b). Small Angle X-ray Diffraction as a Tool for Structural Characterization of Muscle Disease. *Int J Mol Sci*, *23*(6). https://doi.org/10.3390/ijms23063052

Ma, W., McMillen, T. S., Childers, M. C., Gong, H., Regnier, M., & Irving, T. (2023). Structural OFF/ON transitions of myosin in relaxed porcine myocardium predict calcium-activated force. *Proc Natl Acad Sci U S A*, *120*(5), e2207615120. https://doi.org/10.1073/pnas.2207615120

Ma, W., Nag, S., Gong, H., Qi, L., & Irving, T. (2022). Cardiac myosin filaments are directly regulated by calcium. *J Gen Physiol*, *154* (12), e202213213. https://doi.org/https://doi.org/10.1085/jgp.202213213

Ma, W, McMillen, T., Childers, M., Gong, H., Regnier, M., & Irving, T. (2023). Structural OFF/ON transitions of myosin in relaxed porcine myocardium predict calcium activated force. *Proc Natl Acad Sci U S A*, *120*(5), e2207615120. https://doi.org/10.1073/pnas.2207615120

Maack, C., Eschenhagen, T., Hamdani, N., Heinzel, F. R., Lyon, A. R., Manstein, D. J., Metzger, J., Papp, Z., Tocchetti, C. G., Yilmaz, M. B., Anker, S. D., Balligand, J. L., Bauersachs, J., Brutsaert, D., Carrier, L., Chlopicki, S., Cleland, J. G., de Boer, R. A., Dietl, A., . . . Mebazaa, A. (2019). Treatments targeting inotropy. *Eur Heart J*, *40*(44), 3626-3644. https://doi.org/10.1093/eurheartj/ehy600

Maier, J. A., Martinez, C., Kasavajhala, K., Wickstrom, L., Hauser, K. E., & Simmerling, C. (2015). ff14SB: Improving the Accuracy of Protein Side Chain and Backbone Parameters from ff99SB. *J Chem Theory Comput*, *11*(8), 3696-3713. https://doi.org/10.1021/acs.jctc.5b00255

Malik, F. I., Hartman, J. J., Elias, K. A., Morgan, B. P., Rodriguez, H., Brejc, K., Anderson, R. L., Sueoka, S. H., Lee, K. H., Finer, J. T., Sakowicz, R., Baliga, R., Cox, D. R., Garard, M., Godinez, G., Kawas, R., Kraynack, E., Lenzi, D., Lu, P. P., . . . Morgans, D. J. (2011). Cardiac myosin activation: a potential therapeutic approach for systolic heart failure [Research Support, N.I.H., Extramural

Research Support, Non-U.S. Gov't]. *Science*, *331*(6023), 1439-1443. https://doi.org/10.1126/science.1200113
Mamidi, R., Li, J., Gresham, K. S., Verma, S., Doh, C. Y., Li, A., Lal, S., Dos Remedios, C. G., & Stelzer, J. E. (2017). Dose-Dependent Effects of the Myosin Activator Omecamtiv Mecarbil on Cross-Bridge Behavior and Force Generation in Failing Human Myocardium. *Circ Heart Fail*, *10*(10). https://doi.org/10.1161/CIRCHEARTFAILURE.117.004257
Markandran, K., Poh, J. W., Ferenczi, M. A., & Cheung, C. (2021). Regulatory Light Chains in Cardiac Development and Disease. *International Journal of Molecular Sciences*, *22*(9), 4351. https://doi.org/10.3390/ijms22094351
Marston, S. (2021). Force Measurements From Myofibril to Filament. *Front Physiol*, *12*, 817036. https://doi.org/10.3389/fphys.2021.817036
Mathern, B. E., & Burke, M. (1986). Stability and substructure of cardiac myosin subfragment 1 and isolation and properties of its heavy-chain subunit. *Biochemistry*, *25*(4), 884-889. https://doi.org/10.1021/bi00352a022
McCabe, K. J., Aboelkassem, Y., Teitgen, A. E., Huber, G. A., McCammon, J. A., Regnier, M., & McCulloch, A. D. (2020). Predicting the effects of dATP on cardiac contraction using multiscale modeling of the sarcomere. *Arch Biochem Biophys*, 108582. https://doi.org/10.1016/j.abb.2020.108582
McNally, E. M., & Mestroni, L. (2017). Dilated Cardiomyopathy: Genetic Determinants and Mechanisms. *Circ Res*, *121*(7), 731-748. https://doi.org/10.1161/CIRCRESAHA.116.309396
Mcnamara, J. W., Li, A., Dos Remedios, C. G., & Cooke, R. (2015). The role of super-relaxed myosin in skeletal and cardiac muscle. *Biophysical Reviews*, *7*(1), 5-14. https://doi.org/10.1007/s12551-014-0151-5
McNamara, J. W., Li, A., Lal, S., Bos, J. M., Harris, S. P., van der Velden, J., Ackerman, M. J., Cooke, R., & Dos Remedios, C. G. (2017). MYBPC3 mutations are associated with a reduced super-relaxed state in patients with hypertrophic cardiomyopathy. *PLoS One*, *12*(6), e0180064. https://doi.org/10.1371/journal.pone.0180064
McNamara, J. W., Li, A., Smith, N. J., Lal, S., Graham, R. M., Kooiker, K. B., van Dijk, S. J., dos Remedios, C. G., Harris, S. P., & Cooke, R. (2016). Ablation of cardiac myosin binding protein-C disrupts the super-relaxed state of myosin in murine cardiomyocytes. *J Mol Cell Cardiol*, *94*, 65-71. https://doi.org/http://dx.doi.org/10.1016/j.yjmcc.2016.03.009
Mcnamara, J. W., Li, A., Smith, N. J., Lal, S., Graham, R. M., Kooiker, K. B., Van Dijk, S. J., Remedios, C. G. D., Harris, S. P., & Cooke, R. (2016). Ablation of cardiac myosin binding protein-C disrupts the super-relaxed state of myosin in murine cardiomyocytes. *Journal of Molecular and Cellular Cardiology*, *94*, 65-71. https://doi.org/10.1016/j.yjmcc.2016.03.009
Meagher, K. L., Redman, L. T., & Carlson, H. A. (2003). Development of polyphosphate parameters for use with the AMBER force field. *J Comput Chem*, *24*(9), 1016-1025. https://doi.org/10.1002/jcc.10262
Mijailovich, S. M., Prodanovic, M., Poggesi, C., Powers, J. D., Davis, J., Geeves, M. A., & Regnier, M. (2021). The effect of variable troponin C mutation thin filament incorporation on cardiac muscle twitch contractions. *J Mol Cell Cardiol*, *155*, 112-124. https://doi.org/10.1016/j.yjmcc.2021.02.009
Moeller, J., Denisin, A. K., Sim, J. Y., Wilson, R. E., Ribeiro, A. J. S., & Pruitt, B. L. (2018). Controlling cell shape on hydrogels using lift-off protein patterning. *PLoS One*, *13*(1), e0189901. https://doi.org/10.1371/journal.pone.0189901
Morck, M. M., Bhowmik, D., Pathak, D., Dawood, A., Spudich, J., & Ruppel, K. M. (2022). Hypertrophic cardiomyopathy mutations in the pliant and light chain-binding regions of

the lever arm of human β-cardiac myosin have divergent effects on myosin function. *Elife*, *11*. https://doi.org/10.7554/elife.76805
Mortara, A., Oliva, F., Metra, M., Carbonieri, E., Di Lenarda, A., Gorini, M., Midi, P., Senni, M., Urso, R., Lucci, D., Maggioni, A. P., Tavazzi, L., & Investigators, I.-H. O. (2014). Treatment with inotropes and related prognosis in acute heart failure: contemporary data from the Italian Network on Heart Failure (IN-HF) Outcome registry. *J Heart Lung Transplant*, *33*(10), 1056-1065. https://doi.org/10.1016/j.healun.2014.05.015
Moussavi-Harami, F., Razumova, M. V., Racca, A. W., Cheng, Y., Stempien-Otero, A., & Regnier, M. (2015). 2-Deoxy adenosine triphosphate improves contraction in human end-stage heart failure. *J Mol Cell Cardiol*, *79*, 256-263. https://doi.org/10.1016/j.yjmcc.2014.12.002
Mukund, K., & Subramaniam, S. (2020). Skeletal muscle: A review of molecular structure and function, in health and disease. *WIREs Systems Biology and Medicine*, *12*(1). https://doi.org/10.1002/wsbm.1462
Mun, J. Y., Previs, M. J., Yu, H. Y., Gulick, J., Tobacman, L. S., Beck Previs, S., Robbins, J., Warshaw, D. M., & Craig, R. (2014). Myosin-binding protein C displaces tropomyosin to activate cardiac thin filaments and governs their speed by an independent mechanism. *Proceedings of the National Academy of Sciences*, *111*(6), 2170-2175. https://doi.org/10.1073/pnas.1316001111
Muthu, P., Liang, J., Schmidt, W., Moore, J. R., & Szczesna-Cordary, D. (2014). In vitro rescue study of a malignant familial hypertrophic cardiomyopathy phenotype by pseudo-phosphorylation of myosin regulatory light chain. *Archives of Biochemistry and Biophysics*, *552-553*, 29-39. https://doi.org/10.1016/j.abb.2013.12.011
Nag, S., & Trivedi, D. V. (2021). To lie or not to lie: Super-relaxing with myosins. *Elife*, *10*. https://doi.org/10.7554/eLife.63703
Nag, S., Trivedi, D. V., Sarkar, S. S., Adhikari, A. S., Sunitha, M. S., Sutton, S., Ruppel, K. M., & Spudich, J. A. (2017). The myosin mesa and the basis of hypercontractility caused by hypertrophic cardiomyopathy mutations. *Nat Struct Mol Biol*, *24*(6), 525-533. https://doi.org/10.1038/nsmb.3408
Nagy, L., Kovacs, A., Bodi, B., Pasztor, E. T., Fulop, G. A., Toth, A., Edes, I., & Papp, Z. (2015). The novel cardiac myosin activator omecamtiv mecarbil increases the calcium sensitivity of force production in isolated cardiomyocytes and skeletal muscle fibres of the rat. *Br J Pharmacol*, *172*(18), 4506-4518. https://doi.org/10.1111/bph.13235
Nakanishi, T., Oyama, K., Tanaka, H., Kobirumaki-Shimozawa, F., Ishii, S., Terui, T., Ishiwata, S., & Fukuda, N. (2022). Effects of omecamtiv mecarbil on the contractile properties of skinned porcine left atrial and ventricular muscles. *Front Physiol*, *13*, 947206. https://doi.org/10.3389/fphys.2022.947206
Nayak, A., Wang, T., Franz, P., Steffen, W., Chizhov, I., Tsiavaliaris, G., & Amrute-Nayak, M. (2020). Single-molecule analysis reveals that regulatory light chains fine-tune skeletal myosin II function. *J Biol Chem*, *295*(20), 7046-7059. https://doi.org/10.1074/jbc.RA120.012774
O'Leary, T. S., Snyder, J., Sadayappan, S., Day, S. M., & Previs, M. J. (2019). MYBPC3 truncation mutations enhance actomyosin contractile mechanics in human hypertrophic cardiomyopathy. *J Mol Cell Cardiol*, *127*, 165-173. https://doi.org/10.1016/j.yjmcc.2018.12.003
Olivotto, I., Girolami, F., Ackerman, M. J., Nistri, S., Bos, J. M., Zachara, E., Ommen, S. R., Theis, J. L., Vaubel, R. A., Re, F., Armentano, C., Poggesi, C., Torricelli, F., & Cecchi, F. (2008). Myofilament protein gene mutation screening and outcome of patients with hypertrophic cardiomyopathy. *Mayo Clin Proc*, *83*(6), 630-638. https://doi.org/10.4065/83.6.630

Olivotto, I., Oreziak, A., Barriales-Villa, R., Abraham, T. P., Masri, A., Garcia-Pavia, P., Saberi, S., Lakdawala, N. K., Wheeler, M. T., Owens, A., Kubanek, M., Wojakowski, W., Jensen, M. K., Gimeno-Blanes, J., Afshar, K., Myers, J., Hegde, S. M., Solomon, S. D., Sehnert, A. J., . . . investigators, E.-H. s. (2020). Mavacamten for treatment of symptomatic obstructive hypertrophic cardiomyopathy (EXPLORER-HCM): a randomised, double-blind, placebo-controlled, phase 3 trial. *Lancet*, *396*(10253), 759-769. https://doi.org/10.1016/S0140-6736(20)31792-X

Padron, R., Dutta, D., & Craig, R. (2023). Variants of the myosin interacting-heads motif. *J Gen Physiol*, *155*(1). https://doi.org/10.1085/jgp.202213249

Padron, R., Ma, W., Duno-Miranda, S., Koubassova, N., Lee, K. H., Pinto, A., Alamo, L., Bolanos, P., Tsaturyan, A., Irving, T., & Craig, R. (2020). The myosin interacting-heads motif present in live tarantula muscle explains tetanic and posttetanic phosphorylation mechanisms. *Proc Natl Acad Sci U S A*. https://doi.org/10.1073/pnas.1921312117

Page, S. P., Kounas, S., Syrris, P., Christiansen, M., Frank-Hansen, R., Andersen, P. S., Elliott, P. M., & McKenna, W. J. (2012). Cardiac myosin binding protein-C mutations in families with hypertrophic cardiomyopathy: disease expression in relation to age, gender, and long term outcome. *Circ Cardiovasc Genet*, *5*(2), 156-166. https://doi.org/10.1161/CIRCGENETICS.111.960831

Palmer, S., & Kentish, J. C. (1994). The role of troponin C in modulating the Ca2+ sensitivity of mammalian skinned cardiac and skeletal muscle fibres. *J Physiol*, *480 (Pt 1)*, 45-60. https://doi.org/10.1113/jphysiol.1994.sp020339

Parker, F., & Peckham, M. (2020). Disease mutations in striated muscle myosins. *Biophysical Reviews*, *12*(4), 887-894. https://doi.org/10.1007/s12551-020-00721-5

Pettersen, E. F., Goddard, T. D., Huang, C. C., Couch, G. S., Greenblatt, D. M., Meng, E. C., & Ferrin, T. E. (2004). UCSF Chimera--a visualization system for exploratory research and analysis. *J Comput Chem*, *25*(13), 1605-1612. https://doi.org/10.1002/jcc.20084

Pilagov, M., Heling, L. W. H. J., Walklate, J., Geeves, M. A., & Kad, N. M. (2023). Single-molecule imaging reveals how mavacamten and PKA modulate ATP turnover in skeletal muscle myofibrils. *Journal of General Physiology*, *155*(1). https://doi.org/10.1085/jgp.202213087

Pinotsis, N., Abrusci, P., Djinovic-Carugo, K., & Wilmanns, M. (2009). Terminal assembly of sarcomeric filaments by intermolecular beta-sheet formation. *Trends Biochem Sci*, *34*(1), 33-39. https://doi.org/10.1016/j.tibs.2008.09.009

Pioner, J. M., Fornaro, A., Coppini, R., Ceschia, N., Sacconi, L., Donati, M. A., Favilli, S., Poggesi, C., Olivotto, I., & Ferrantini, C. (2020). Advances in Stem Cell Modeling of Dystrophin-Associated Disease: Implications for the Wider World of Dilated Cardiomyopathy. *Front Physiol*, *11*, 368. https://doi.org/10.3389/fphys.2020.00368

Pioner, J. M., Guan, X., Klaiman, J. M., Racca, A. W., Pabon, L., Muskheli, V., Macadangdang, J., Ferrantini, C., Hoopmann, M. R., Moritz, R. L., Kim, D. H., Tesi, C., Poggesi, C., Murry, C. E., Childers, M. K., Mack, D. L., & Regnier, M. (2020). Absence of full-length dystrophin impairs normal maturation and contraction of cardiomyocytes derived from human-induced pluripotent stem cells. *Cardiovasc Res*, *116*(2), 368-382. https://doi.org/10.1093/cvr/cvz109

Pioner, J. M., Racca, A. W., Klaiman, J. M., Yang, K.-C., Guan, X., Pabon, L., Muskheli, V., Zaunbrecher, R., Macadangdang, J., Jeong, M. Y., Mack, D. L., Childers, M. K., Kim, D.-H., Tesi, C., Poggesi, C., Murry, C. E., & Regnier, M. (2016). Isolation and Mechanical Measurements of Myofibrils from Human Induced Pluripotent Stem Cell-Derived Cardiomyocytes. *Stem Cell Reports*, *6*(6), 885-896. https://doi.org/10.1016/j.stemcr.2016.04.006

Pioner, J. M., Racca, A. W., Klaiman, J. M., Yang, K. C., Guan, X., Pabon, L., Muskheli, V., Zaunbrecher, R., Macadangdang, J., Jeong, M. Y., Mack, D. L., Childers, M. K., Kim, D.

H., Tesi, C., Poggesi, C., Murry, C. E., & Regnier, M. (2016). Isolation and Mechanical Measurements of Myofibrils from Human Induced Pluripotent Stem Cell-Derived Cardiomyocytes. *Stem Cell Reports*, *6*(6), 885-896. https://doi.org/10.1016/j.stemcr.2016.04.006

Pioner, J. M., Santini, L., Palandri, C., Martella, D., Lupi, F., Langione, M., Querceto, S., Grandinetti, B., Balducci, V., Benzoni, P., Landi, S., Barbuti, A., Ferrarese Lupi, F., Boarino, L., Sartiani, L., Tesi, C., Mack, D. L., Regnier, M., Cerbai, E., . . . Coppini, R. (2019). Optical Investigation of Action Potential and Calcium Handling Maturation of hiPSC-Cardiomyocytes on Biomimetic Substrates. *Int J Mol Sci*, *20*(15). https://doi.org/10.3390/ijms20153799

Pioner, J. M., Vitale, G., Steczina, S., Langione, M., Margara, F., Santini, L., Giardini, F., Lazzeri, E., Piroddi, N., Scellini, B., Palandri, C., Schuldt, M., Spinelli, V., Girolami, F., Mazzarotto, F., van der Velden, J., Cerbai, E., Tesi, C., Olivotto, I., . . . Poggesi, C. (2023). Slower Calcium Handling Balances Faster Cross-Bridge Cycling in Human MYBPC3 HCM. *Circ Res*, *132*(5), 628-644. https://doi.org/10.1161/CIRCRESAHA.122.321956

Piroddi, N., Belus, A., Scellini, B., Tesi, C., Giunti, G., Cerbai, E., Mugelli, A., & Poggesi, C. (2007). Tension generation and relaxation in single myofibrils from human atrial and ventricular myocardium. *Pflugers Arch*, *454*(1), 63-73. https://doi.org/10.1007/s00424-006-0181-3

Planelles-Herrero, V. J., Hartman, J. J., Robert-Paganin, J., Malik, F. I., & Houdusse, A. (2017). Mechanistic and structural basis for activation of cardiac myosin force production by omecamtiv mecarbil. *Nat Commun*, *8*(1), 190. https://doi.org/10.1038/s41467-017-00176-5

Poggesi, C., Tesi, C., & Stehle, R. (2005). Sarcomeric determinants of striated muscle relaxation kinetics. *Pflugers Arch*, *449*(6), 505-517. https://doi.org/10.1007/s00424-004-1363-5

Powers, J. D., Kooiker, K. B., Mason, A. B., Teitgen, A. E., Flint, G. V., Tardiff, J. C., Schwartz, S. D., McCulloch, A. D., Regnier, M., Davis, J., & Moussavi-Harami, F. (2020). Modulating the tension-time integral of the cardiac twitch prevents dilated cardiomyopathy in murine hearts. *JCI Insight*, *5*(20). https://doi.org/10.1172/jci.insight.142446

Powers, J. D., Yuan, C. C., McCabe, K. J., Murray, J. D., Childers, M. C., Flint, G. V., Moussavi-Harami, F., Mohran, S., Castillo, R., Zuzek, C., Ma, W., Daggett, V., McCulloch, A. D., Irving, T. C., & Regnier, M. (2019). Cardiac myosin activation with 2-deoxy-ATP via increased electrostatic interactions with actin. *Proc Natl Acad Sci U S A*, *116*(23), 11502-11507. https://doi.org/10.1073/pnas.1905028116

Previs, M. J., Previs, S. B., Gulick, J., Robbins, J., & Warshaw, D. M. (2012). Molecular Mechanics of Cardiac Myosin-Binding Protein C in Native Thick Filaments. *Science*, *337*(6099), 1215-1218. https://doi.org/10.1126/science.1223602

Racca, A. W., Beck, A. E., McMillin, M. J., Korte, F. S., Bamshad, M. J., & Regnier, M. (2015). The embryonic myosin R672C mutation that underlies Freeman-Sheldon syndrome impairs cross-bridge detachment and cycling in adult skeletal muscle. *Hum Mol Genet*, *24*(12), 3348-3358. https://doi.org/10.1093/hmg/ddv084

Racca, A. W., Beck, A. E., Rao, V. S., Flint, G. V., Lundy, S. D., Born, D. E., Bamshad, M. J., & Regnier, M. (2013). Contractility and kinetics of human fetal and human adult skeletal muscle. *J Physiol*, *591*(Pt 12), 3049-3061. https://doi.org/10.1113/jphysiol.2013.252650

Racca, A. W., Klaiman, J. M., Pioner, J. M., Cheng, Y., Beck, A. E., Moussavi-Harami, F., Bamshad, M. J., & Regnier, M. (2016). Contractile properties of developing human fetal cardiac muscle. *J Physiol*, *594*(2), 437-452. https://doi.org/10.1113/JP271290

Ráduly, A. P., Sárkány, F., Kovács, M. B., Bernát, B., Juhász, B., Szilvássy, Z., Porszász, R., Horváth, B., Szentandrássy, N., Nánási, P., Csanádi, Z., Édes, I., Tóth, A., Papp, Z., Priksz, D., & Borbély, A. (2022). The Novel Cardiac Myosin Activator Danicamtiv Improves Cardiac Systolic Function at the Expense of Diastolic Dysfunction In Vitro and In Vivo: Implications for Clinical Applications. *International Journal of Molecular Sciences*, *24*(1), 446. https://doi.org/10.3390/ijms24010446

Ranu, N., Laitila, J., Dugdale, H. F., Mariano, J., Kolb, J. S., Wallgren-Pettersson, C., Witting, N., Vissing, J., Vilchez, J. J., Fiorillo, C., Zanoteli, E., Auranen, M., Jokela, M., Tasca, G., Claeys, K. G., Voermans, N. C., Palmio, J., Huovinen, S., Moggio, M., . . . Ochala, J. (2022). NEB mutations disrupt the super-relaxed state of myosin and remodel the muscle metabolic proteome in nemaline myopathy. *Acta Neuropathol Commun*, *10*(1), 185. https://doi.org/10.1186/s40478-022-01491-9

Reconditi, M. (2006). Recent improvements in small angle x-ray diffraction for the study of muscle physiology. *Reports on Progress in Physics*, *69*(10), 2709-2759. https://doi.org/10.1088/0034-4885/69/10/r01

Reconditi, M., Linari, M., Lucii, L., Stewart, A., Sun, Y. B., Narayanan, T., Irving, T., Piazzesi, G., Irving, M., & Lombardi, V. (2005). Structure-function relation of the myosin motor in striated muscle. *Ann N Y Acad Sci*, *1047*, 232-247. https://doi.org/10.1196/annals.1341.021

Regnier, M., Rivera, A. J., Chen, Y., & Chase, P. B. (2000). 2-deoxy-ATP enhances contractility of rat cardiac muscle [Research Support, Non-U.S. Gov't

Research Support, U.S. Gov't, P.H.S.]. *Circ Res*, *86*(12), 1211-1217. https://www.ncbi.nlm.nih.gov/pubmed/10864910

Risi, C. M., Pepper, I., Belknap, B., Landim-Vieira, M., White, H. D., Dryden, K., Pinto, J. R., Chase, P. B., & Galkin, V. E. (2021). The structure of the native cardiac thin filament at systolic Ca(2+) levels. *Proc Natl Acad Sci U S A*, *118*(13). https://doi.org/10.1073/pnas.2024288118

Roe, D. R., & Cheatham, T. E., 3rd. (2013). PTRAJ and CPPTRAJ: Software for Processing and Analysis of Molecular Dynamics Trajectory Data. *J Chem Theory Comput*, *9*(7), 3084-3095. https://doi.org/10.1021/ct400341p

Rohde, J. A., Roopnarine, O., Thomas, D. D., & Muretta, J. M. (2018). Mavacamten stabilizes an autoinhibited state of two-headed cardiac myosin. *Proc Natl Acad Sci U S A*, *115*(32), E7486-E7494. https://doi.org/10.1073/pnas.1720342115

Rohde, J. A., Thomas, D. D., & Muretta, J. M. (2017). Heart failure drug changes the mechanoenzymology of the cardiac myosin powerstroke. *Proc Natl Acad Sci U S A*, *114*(10), E1796-E1804. https://doi.org/10.1073/pnas.1611698114

Rossi, D., Pierantozzi, E., Amadsun, D. O., Buonocore, S., Rubino, E. M., & Sorrentino, V. (2022). The Sarcoplasmic Reticulum of Skeletal Muscle Cells: A Labyrinth of Membrane Contact Sites. *Biomolecules*, *12*(4), 488. https://doi.org/10.3390/biom12040488

Sanner, M. F., Olson, A. J., & Spehner, J. C. (1996). Reduced surface: an efficient way to compute molecular surfaces. *Biopolymers*, *38*(3), 305-320. https://doi.org/10.1002/(SICI)1097-0282(199603)38:3%3C305::AID-BIP4%3E3.0.CO;2-Y

Sarkar, S. S., Trivedi, D. V., Morck, M. M., Adhikari, A. S., Pasha, S. N., Ruppel, K. M., & Spudich, J. A. (2020). The hypertrophic cardiomyopathy mutations R403Q and R663H increase the number of myosin heads available to interact with actin. *Science Advances*, *6*(14), eaax0069. https://doi.org/10.1126/sciadv.aax0069

Sarkar, S. S., Trivedi, D. V., Morck, M. M., Adhikari, A. S., Pasha, S. N., Ruppel, K. M., & Spudich, J. A. (2020). The hypertrophic cardiomyopathy mutations R403Q and R663H increase the number of myosin heads available to interact with actin. *Sci Adv*, *6*(14), eaax0069. https://doi.org/10.1126/sciadv.aax0069

Saxton, A., Tariq, M. A., & Bordoni, B. (2022). Anatomy, Thorax, Cardiac Muscle. In *StatPearls*. https://www.ncbi.nlm.nih.gov/pubmed/30570976
Scellini, B., Piroddi, N., Dente, M., Vitale, G., Pioner, J. M., Coppini, R., Ferrantini, C., Poggesi, C., & Tesi, C. (2021). Mavacamten has a differential impact on force generation in myofibrils from rabbit psoas and human cardiac muscle. *Journal of General Physiology*, *153*(7). https://doi.org/10.1085/jgp.202012789
Schmid, M., & Toepfer, C. N. (2021). Cardiac myosin super relaxation (SRX): a perspective on fundamental biology, human disease and therapeutics. *Biology Open*, *10*(2), bio057646. https://doi.org/10.1242/bio.057646
Seidman, J. G., & Seidman, C. (2001). The Genetic Basis for Cardiomyopathy. *Cell*, *104*(4), 557-567. https://doi.org/10.1016/s0092-8674(01)00242-2
Shadrin, I. Y., Khodabukus, A., & Bursac, N. (2016). Striated muscle function, regeneration, and repair. *Cellular and Molecular Life Sciences*, *73*(22), 4175-4202. https://doi.org/10.1007/s00018-016-2285-z
Shah, K. S., Xu, H., Matsouaka, R. A., Bhatt, D. L., Heidenreich, P. A., Hernandez, A. F., Devore, A. D., Yancy, C. W., & Fonarow, G. C. (2017). Heart Failure With Preserved, Borderline, and Reduced Ejection Fraction: 5-Year Outcomes. *J Am Coll Cardiol*, *70*(20), 2476-2486. https://doi.org/10.1016/j.jacc.2017.08.074
Shen, S., Sewanan, L. R., Jacoby, D. L., & Campbell, S. G. (2021). Danicamtiv Enhances Systolic Function and Frank-Starling Behavior at Minimal Diastolic Cost in Engineered Human Myocardium. *J Am Heart Assoc*, *10*(12), e020860. https://doi.org/10.1161/JAHA.121.020860
Siemankowski, R. F., Wiseman, M. O., & White, H. D. (1985). ADP dissociation from actomyosin subfragment 1 is sufficiently slow to limit the unloaded shortening velocity in vertebrate muscle. *Proceedings of the National Academy of Sciences*, *82*(3), 658-662. https://doi.org/10.1073/pnas.82.3.658
Simnett, S. J., Johns, E. C., Lipscomb, S., Mulligan, I. P., & Ashley, C. C. (1998). Effect of pH, phosphate, and ADP on relaxation of myocardium after photolysis of diazo 2. *Am J Physiol*, *275*(3), H951-960. https://doi.org/10.1152/ajpheart.1998.275.3.H951
Singer, E. S., Ingles, J., Semsarian, C., & Bagnall, R. D. (2019). Key Value of RNA Analysis of MYBPC3 Splice-Site Variants in Hypertrophic Cardiomyopathy. *Circ Genom Precis Med*, *12*(1), e002368. https://doi.org/10.1161/CIRCGEN.118.002368
Smerdu, V., Karsch-Mizrachi, I., Campione, M., Leinwand, L., & Schiaffino, S. (1994). Type IIx myosin heavy chain transcripts are expressed in type IIb fibers of human skeletal muscle. *Am J Physiol*, *267*(6 Pt 1), C1723-1728. https://doi.org/10.1152/ajpcell.1994.267.6.C1723
Smith, A. S., Luttrell, S. M., Dupont, J.-B., Gray, K., Lih, D., Fleming, J. W., Cunningham, N. J., Jepson, S., Hesson, J., Mathieu, J., Maves, L., Berry, B. J., Fisher, E. C., Sniadecki, N. J., Geisse, N. A., & Mack, D. L. (2022). High-throughput, real-time monitoring of engineered skeletal muscle function using magnetic sensing. *Journal of Tissue Engineering*, *13*, 204173142211221. https://doi.org/10.1177/20417314221122127
Sogah, V. M., Serluca, F. C., Fishman, M. C., Yelon, D. L., Macrae, C. A., & Mably, J. D. (2010). Distinct troponin C isoform requirements in cardiac and skeletal muscle. *Developmental Dynamics*, *239*(11), 3115-3123. https://doi.org/10.1002/dvdy.22445
Sommese, R. F., Sung, J., Nag, S., Sutton, S., Deacon, J. C., Choe, E., Leinwand, L. A., Ruppel, K., & Spudich, J. A. (2013). Molecular consequences of the R453C hypertrophic cardiomyopathy mutation on human beta-cardiac myosin motor function. *Proc Natl Acad Sci U S A*, *110*(31), 12607-12612. https://doi.org/10.1073/pnas.1309493110
Spudich, A., James. (2014). Hypertrophic and Dilated Cardiomyopathy: Four Decades of Basic Research on Muscle Lead to Potential Therapeutic Approaches to These Devastating

Genetic Diseases. *Biophysical Journal*, *106*(6), 1236-1249. https://doi.org/10.1016/j.bpj.2014.02.011
Spudich, J. A. (2019). Three perspectives on the molecular basis of hypercontractility caused by hypertrophic cardiomyopathy mutations. *Pflugers Arch*, *471*(5), 701-717. https://doi.org/10.1007/s00424-019-02259-2
Squire, J. M. (2009). Muscle myosin filaments: cores, crowns and couplings. *Biophysical Reviews*, *1*(3), 149-160. https://doi.org/10.1007/s12551-009-0017-4
Stewart, M. A., Franks-Skiba, K., Chen, S., & Cooke, R. (2010). Myosin ATP turnover rate is a mechanism involved in thermogenesis in resting skeletal muscle fibers. *Proc Natl Acad Sci U S A*, *107*(1), 430-435. https://doi.org/10.1073/pnas.0909468107
Sung, S. S., Brassington, A. M., Grannatt, K., Rutherford, A., Whitby, F. G., Krakowiak, P. A., Jorde, L. B., Carey, J. C., & Bamshad, M. (2003). Mutations in genes encoding fast-twitch contractile proteins cause distal arthrogryposis syndromes. *Am J Hum Genet*, *72*(3), 681-690. https://doi.org/10.1086/368294
Szent-GyöRgyi, A. G. (2004). The Early History of the Biochemistry of Muscle Contraction. *Journal of General Physiology*, *123*(6), 631-641. https://doi.org/10.1085/jgp.200409091
Tang, W., Ge, J., Unrath, W. C., Desetty, R., & Yengo, C. M. (2021). Cardiomyopathy mutations impact the actin-activated power stroke of human cardiac myosin. *Biophys J*, *120*(11), 2222-2236. https://doi.org/10.1016/j.bpj.2021.04.007
Tanner, B. C., Breithaupt, J. J., & Awinda, P. O. (2015). Myosin MgADP release rate decreases at longer sarcomere length to prolong myosin attachment time in skinned rat myocardium. *Am J Physiol Heart Circ Physiol*, *309*(12), H2087-2097. https://doi.org/10.1152/ajpheart.00555.2015
Teerlink, J. R., Diaz, R., Felker, G. M., McMurray, J. J. V., Metra, M., Solomon, S. D., Adams, K. F., Anand, I., Arias-Mendoza, A., Biering-Sorensen, T., Bohm, M., Bonderman, D., Cleland, J. G. F., Corbalan, R., Crespo-Leiro, M. G., Dahlstrom, U., Echeverria, L. E., Fang, J. C., Filippatos, G., . . . Investigators, G.-H. (2021). Cardiac Myosin Activation with Omecamtiv Mecarbil in Systolic Heart Failure. *N Engl J Med*, *384*(2), 105-116. https://doi.org/10.1056/NEJMoa2025797
Teerlink, J. R., Diaz, R., Felker, G. M., McMurray, J. J. V., Metra, M., Solomon, S. D., Biering-Sorensen, T., Bohm, M., Bonderman, D., Fang, J. C., Lanfear, D. E., Lund, M., Momomura, S. I., O'Meara, E., Ponikowski, P., Spinar, J., Flores-Arredondo, J. H., Claggett, B. L., Heitner, S. B., . . . Investigators, G.-H. (2021a). Effect of Ejection Fraction on Clinical Outcomes in Patients treated with Omecamtiv Mecarbil in GALACTIC-HF. *J Am Coll Cardiol*. https://doi.org/10.1016/j.jacc.2021.04.065
Teerlink, J. R., Diaz, R., Felker, G. M., McMurray, J. J. V., Metra, M., Solomon, S. D., Biering-Sorensen, T., Bohm, M., Bonderman, D., Fang, J. C., Lanfear, D. E., Lund, M., Momomura, S. I., O'Meara, E., Ponikowski, P., Spinar, J., Flores-Arredondo, J. H., Claggett, B. L., Heitner, S. B., . . . Investigators, G.-H. (2021b). Effect of Ejection Fraction on Clinical Outcomes in Patients Treated With Omecamtiv Mecarbil in GALACTIC-HF. *J Am Coll Cardiol*, *78*(2), 97-108. https://doi.org/10.1016/j.jacc.2021.04.065
Teerlink, J. R., Metra, M., Zaca, V., Sabbah, H. N., Cotter, G., Gheorghiade, M., & Cas, L. D. (2009). Agents with inotropic properties for the management of acute heart failure syndromes. Traditional agents and beyond [Review]. *Heart Fail Rev*, *14*(4), 243-253. https://doi.org/10.1007/s10741-009-9153-y
Toepfer, C., Caorsi, V., Kampourakis, T., Sikkel, M. B., West, T. G., Leung, M.-C., Al-Saud, S. A., Macleod, K. T., Lyon, A. R., Marston, S. B., Sellers, J. R., & Ferenczi, M. A. (2013). Myosin Regulatory Light Chain (RLC) Phosphorylation Change as a Modulator of Cardiac Muscle Contraction in Disease. *Journal of Biological Chemistry*, *288*(19), 13446-13454. https://doi.org/10.1074/jbc.m113.455444

Toepfer, C. N., Garfinkel, A. C., Venturini, G., Wakimoto, H., Repetti, G., Alamo, L., Sharma, A., Agarwal, R., Ewoldt, J. F., Cloonan, P., Letendre, J., Lun, M., Olivotto, I., Colan, S., Ashley, E., Jacoby, D., Michels, M., Redwood, C. S., Watkins, H. C., . . . Seidman, C. E. (2020). Myosin Sequestration Regulates Sarcomere Function, Cardiomyocyte Energetics, and Metabolism, Informing the Pathogenesis of Hypertrophic Cardiomyopathy. *Circulation*, *141*(10), 828-842. https://doi.org/10.1161/CIRCULATIONAHA.119.042339

Toepfer, C. N., Garfinkel, A. C., Venturini, G., Wakimoto, H., Repetti, G., Alamo, L., Sharma, A., Agarwal, R., Ewoldt, J. F., Cloonan, P., Letendre, J., Lun, M., Olivotto, I., Colan, S., Ashley, E., Jacoby, D., Michels, M., Redwood, C. S., Watkins, H. C., . . . Seidman, C. E. (2020). Myosin Sequestration Regulates Sarcomere Function, Cardiomyocyte Energetics, and Metabolism, Informing the Pathogenesis of Hypertrophic Cardiomyopathy. *Circulation*, *141*(10), 828-842. https://doi.org/10.1161/circulationaha.119.042339

Toepfer, C. N., Wakimoto, H., Garfinkel, A. C., McDonough, B., Liao, D., Jiang, J., Tai, A. C., Gorham, J. M., Lunde, I. G., Lun, M., Lynch, T. L., McNamara, J. W., Sadayappan, S., Redwood, C. S., Watkins, H. C., Seidman, J. G., & Seidman, C. E. (2019). Hypertrophic cardiomyopathy mutations in MYBPC3 dysregulate myosin. *Science Translational Medicine*, *11*(476), eaat1199. https://doi.org/10.1126/scitranslmed.aat1199

Tolkatchev, D., Elnatan, D., Nogara, L., Ly, T., Naber, N., Haak, K., Meech, R., Cooke, R., & Kostyukova, A. S. (2018). Piperine, an alkaloid inhibiting the super-relaxed state of myosin, binds to the myosin regulatory light chain. *Arch Biochem Biophys*, *659*, 75-84. https://doi.org/10.1016/j.abb.2018.09.027

Toydemir, R. M., Rutherford, A., Whitby, F. G., Jorde, L. B., Carey, J. C., & Bamshad, M. J. (2006). Mutations in embryonic myosin heavy chain (MYH3) cause Freeman-Sheldon syndrome and Sheldon-Hall syndrome. *Nature Genetics*, *38*(5), 561-565. https://doi.org/10.1038/ng1775

Tripathi, A. K., Ray, A. K., & Mishra, S. K. (2022). Molecular and pharmacological aspects of piperine as a potential molecule for disease prevention and management: evidence from clinical trials. *Beni Suef Univ J Basic Appl Sci*, *11*(1), 16. https://doi.org/10.1186/s43088-022-00196-1

Trivedi, D. V., Adhikari, A. S., Sarkar, S. S., Ruppel, K. M., & Spudich, J. A. (2018). Hypertrophic cardiomyopathy and the myosin mesa: viewing an old disease in a new light. *Biophys Rev*, *10*(1), 27-48. https://doi.org/10.1007/s12551-017-0274-6

Tsan, Y.-C., Depalma, S. J., Zhao, Y.-T., Capilnasiu, A., Wu, Y.-W., Elder, B., Panse, I., Ufford, K., Matera, D. L., Friedline, S., O'Leary, T. S., Wubshet, N., Ho, K. K. Y., Previs, M. J., Nordsletten, D., Isom, L. L., Baker, B. M., Liu, A. P., & Helms, A. S. (2021). Physiologic biomechanics enhance reproducible contractile development in a stem cell derived cardiac muscle platform. *Nature Communications*, *12*(1). https://doi.org/10.1038/s41467-021-26496-1

Tsao, C. W., Aday, A. W., Almarzooq, Z. I., Anderson, C. A. M., Arora, P., Avery, C. L., Baker-Smith, C. M., Beaton, A. Z., Boehme, A. K., Buxton, A. E., Commodore-Mensah, Y., Elkind, M. S. V., Evenson, K. R., Eze-Nliam, C., Fugar, S., Generoso, G., Heard, D. G., Hiremath, S., Ho, J. E., . . . Stroke Statistics, S. (2023). Heart Disease and Stroke Statistics-2023 Update: A Report From the American Heart Association. *Circulation*. https://doi.org/10.1161/CIR.0000000000001123

Tyska, M. J., & Warshaw, D. M. (2002). The myosin power stroke. *Cell Motility and the Cytoskeleton*, *51*(1), 1-15. https://doi.org/10.1002/cm.10014

Ujfalusi, Z., Vera, C. D., Mijailovich, S. M., Svicevic, M., Yu, E. C., Kawana, M., Ruppel, K. M., Spudich, J. A., Geeves, M. A., & Leinwand, L. A. (2018). Dilated cardiomyopathy myosin

mutants have reduced force-generating capacity. *J Biol Chem*, *293*(23), 9017-9029. https://doi.org/10.1074/jbc.RA118.001938

van Der Velden, J., Klein, L. J., Zaremba, R., Boontje, N. M., Huybregts, M. A., Stooker, W., Eijsman, L., de Jong, J. W., Visser, C. A., Visser, F. C., & Stienen, G. J. (2001). Effects of calcium, inorganic phosphate, and pH on isometric force in single skinned cardiomyocytes from donor and failing human hearts. *Circulation*, *104*(10), 1140-1146. https://doi.org/10.1161/hc3501.095485

van der Velden, J., & Stienen, G. J. M. (2019). Cardiac Disorders and Pathophysiology of Sarcomeric Proteins. *Physiol Rev*, *99*(1), 381-426. https://doi.org/10.1152/physrev.00040.2017

van Dijk, S. J., Dooijes, D., dos Remedios, C., Michels, M., Lamers, J. M., Winegrad, S., Schlossarek, S., Carrier, L., ten Cate, F. J., Stienen, G. J., & van der Velden, J. (2009). Cardiac myosin-binding protein C mutations and hypertrophic cardiomyopathy: haploinsufficiency, deranged phosphorylation, and cardiomyocyte dysfunction. *Circulation*, *119*(11), 1473-1483. https://doi.org/10.1161/CIRCULATIONAHA.108.838672

Van Heerebeek, L., Hamdani, N., Handoko, M. L., Falcao-Pires, I., Musters, R. J., Kupreishvili, K., Ijsselmuiden, A. J. J., Schalkwijk, C. G., Bronzwaer, J. G. F., Diamant, M., BorbéLy, A., Van Der Velden, J., Stienen, G. J. M., Laarman, G. J., Niessen, H. W. M., & Paulus, W. J. (2008). Diastolic Stiffness of the Failing Diabetic Heart. *Circulation*, *117*(1), 43-51. https://doi.org/10.1161/circulationaha.107.728550

Vander Roest, A. S., Liu, C., Morck, M. M., Kooiker, K. B., Jung, G., Song, D., Dawood, A., Jhingran, A., Pardon, G., Ranjbarvaziri, S., Fajardo, G., Zhao, M., Campbell, K. S., Pruitt, B. L., Spudich, J. A., Ruppel, K. M., & Bernstein, D. (2021). Hypertrophic cardiomyopathy beta-cardiac myosin mutation (P710R) leads to hypercontractility by disrupting super relaxed state. *Proc Natl Acad Sci U S A*, *118*(24). https://doi.org/10.1073/pnas.2025030118

Vitale, G., Ferrantini, C., Piroddi, N., Scellini, B., Pioner, J. M., Colombini, B., Tesi, C., & Poggesi, C. (2021). The relation between sarcomere energetics and the rate of isometric tension relaxation in healthy and diseased cardiac muscle. *Journal of Muscle Research and Cell Motility*, *42*(1), 47-57. https://doi.org/10.1007/s10974-019-09566-2

Voors, A. A., Tamby, J. F., Cleland, J. G., Koren, M., Forgosh, L. B., Gupta, D., Lund, L. H., Camacho, A., Karra, R., Swart, H. P., Pellicori, P., Wagner, F., Hershberger, R. E., Prasad, N., Anderson, R., Anto, A., Bell, K., Edelberg, J. M., Fang, L., . . . Solomon, S. D. (2020). Effects of danicamtiv, a novel cardiac myosin activator, in heart failure with reduced ejection fraction: experimental data and clinical results from a phase 2a trial. *Eur J Heart Fail*, *22*(9), 1649-1658. https://doi.org/10.1002/ejhf.1933

Walklate, J., Kao, K., Regnier, M., & Geeves, M. A. (2022a). Exploring the Super-relaxed State of Myosin in Myofibrils from Fast-twitch, Slow-twitch and Cardiac Muscle. *J Biol Chem*, 101640. https://doi.org/10.1016/j.jbc.2022.101640

Walklate, J., Kao, K., Regnier, M., & Geeves, M. A. (2022b). Exploring the super-relaxed state of myosin in myofibrils from fast-twitch, slow-twitch, and cardiac muscle. *J Biol Chem*, *298*(3), 101640. https://doi.org/10.1016/j.jbc.2022.101640

Walklate, J., Vera, C., Bloemink, M. J., Geeves, M. A., & Leinwand, L. (2016). The Most Prevalent Freeman-Sheldon Syndrome Mutations in the Embryonic Myosin Motor Share Functional Defects. *Journal of Biological Chemistry*, *291*(19), 10318-10331. https://doi.org/10.1074/jbc.m115.707489

Wang, D., McCully, M. E., Luo, Z., McMichael, J., Tu, A. Y., Daggett, V., & Regnier, M. (2013). Structural and functional consequences of cardiac troponin C L57Q and I61Q Ca(2+)-desensitizing variants. *Arch Biochem Biophys*, *535*(1), 68-75. https://doi.org/10.1016/j.abb.2013.02.006

Wijnker, P. J. M., & van der Velden, J. (2020). Mutation-specific pathology and treatment of hypertrophic cardiomyopathy in patients, mouse models and human engineered heart tissue. *Biochim Biophys Acta Mol Basis Dis*, *1866*(8), 165774. https://doi.org/10.1016/j.bbadis.2020.165774

Wilson, C., Naber, N., Pate, E., & Cooke, R. (2014). The Myosin Inhibitor Blebbistatin Stabilizes the Super-Relaxed State in Skeletal Muscle. *Biophys J*, *107*(7), 1637-1646. https://doi.org/10.1016/j.bpj.2014.07.075

Witjas-Paalberends, E. R., Ferrara, C., Scellini, B., Piroddi, N., Montag, J., Tesi, C., Stienen, G. J., Michels, M., Ho, C. Y., Kraft, T., Poggesi, C., & van der Velden, J. (2014). Faster cross-bridge detachment and increased tension cost in human hypertrophic cardiomyopathy with the R403Q MYH7 mutation. *J Physiol*, *592*(15), 3257-3272. https://doi.org/10.1113/jphysiol.2014.274571

Woody, M. S., Greenberg, M. J., Barua, B., Winkelmann, D. A., Goldman, Y. E., & Ostap, E. M. (2018). Positive cardiac inotrope omecamtiv mecarbil activates muscle despite suppressing the myosin working stroke. *Nat Commun*, *9*(1), 3838. https://doi.org/10.1038/s41467-018-06193-2

Woulfe, K. C., Ferrara, C., Pioner, J. M., Mahaffey, J. H., Coppini, R., Scellini, B., Ferrantini, C., Piroddi, N., Tesi, C., Poggesi, C., & Jeong, M. (2019). A Novel Method of Isolating Myofibrils From Primary Cardiomyocyte Culture Suitable for Myofibril Mechanical Study. *Front Cardiovasc Med*, *6*, 12. https://doi.org/10.3389/fcvm.2019.00012

Xu, H., & Van Remmen, H. (2021). The SarcoEndoplasmic Reticulum Calcium ATPase (SERCA) pump: a potential target for intervention in aging and skeletal muscle pathologies. *Skeletal Muscle*, *11*(1). https://doi.org/10.1186/s13395-021-00280-7

Xu, S., Offer, G., Gu, J., White, H. D., & Yu, L. C. (2003). Temperature and ligand dependence of conformation and helical order in myosin filaments. *Biochemistry*, *42*(2), 390-401. https://doi.org/10.1021/bi026085t

Yang, S., Tiwari, P., Lee, K. H., Sato, O., Ikebe, M., Padron, R., & Craig, R. (2020). Cryo-EM structure of the inhibited (10S) form of myosin II. *Nature*, *588*(7838), 521-525. https://doi.org/10.1038/s41586-020-3007-0

Yuan, C. C., Kazmierczak, K., Liang, J., Ma, W., Irving, T. C., & Szczesna-Cordary, D. (2022a). Molecular basis of force-pCa relation in MYL2 cardiomyopathy mice: Role of the super-relaxed state of myosin. *Proc Natl Acad Sci U S A*, *119*(8). https://doi.org/10.1073/pnas.2110328119

Yuan, C. C., Kazmierczak, K., Liang, J., Ma, W., Irving, T. C., & Szczesna-Cordary, D. (2022b). Molecular basis of force-pCa relation in MYL2 cardiomyopathy mice: role of the super relaxed state of myosin. *Proc Natl Acad Sci U S A*

119(8), e2110328119.

VITA

Saffie E. Mohran (Saffie-Alrahman E. Mohran) was born in Tucson, AZ in 1995. He received his Bachelor of Science degree in biomedical engineering from the University of Arizona in 2017. During his undergraduate education, he had the opportunity to work under the mentorship of Dr. Steven Goldman, Dr. Elizabeth Juneman, and Dr. Jordan Lancaster. Following his undergraduate degree, Saffie pursued graduate school under the co-mentorship of Dr. Michael Regnier and Dr. David Mack as he pursued his interests in striated muscle disease-modelling and therapeutic discovery. With experience in cardiac and skeletal muscle biology, Saffie has focused his studies on sarcomeric mutations and small molecule intervention. He earned his Ph. D in Bioengineering from the University of Washington in 2023.